DISS. ETH Nr. 27456

Analysis of Lunar Rockfalls

A dissertation submitted to attain the degree of
DOCTOR OF SCIENCES of ETH ZURICH
(Dr. sc. ETH Zurich)

presented by
VALENTIN TERTIUS BICKEL
MSc. Earth Sciences, ETH Zurich

born
15 August 1990
citizen of Munich, Germany

Accepted on the recommendation of

Prof. Dr. Simon Loew
Dr. Andrea Manconi
Dr. Urs Mall
Prof. Dr. Mathieu Lapôtre



(Prof. Dr. Simon Loew)

2021

ETH
Eidgenössische Technische Hochschule Zürich
Swiss Federal Institute of Technology Zurich

DERDW
EARTH SCIENCES

Valentin Tertius Bickel

Analysis of Lunar Rockfalls

Doctoral Thesis

Chair of Engineering Geology
Geological Institute
Swiss Federal Institute of Technology (ETH) Zurich

International Max Planck Research School for Solar System Science
Department Planets and Comets
Max Planck Institute for Solar System Research (MPS) Goettingen

Supervision

First Supervisor
Prof. Dr. Simon Loew

Co-Supervisor
Dr. Andrea Manconi

Co-Supervisor
Dr. Urs Mall

May 2021

15-288-946

Acknowledgements

This thesis accumulates the work performed over 3 years and 4 months, a journey that started in 2017 — during a period of increasing excitement about lunar science and exploration as fanned by the announcement of NASA's Artemis program — and ended in 2021, a year which might see more than a dozen of national and commercial spacecraft embarking on a journey to the Moon. Some of the research presented in this thesis has been conducted at the Lunar and Planetary Institute, Houston, TX, USA, and the NASA Ames Research Center, Mountain View, CA, USA. Other aspects have been developed in cooperation with NASA's Jet Propulsion Laboratory, Pasadena, CA, USA. The research conducted for, in support of, and inspired by this thesis has been published in 7 journal contributions, where 4 additional contributions are currently undergoing peer-review or are in preparation (9 contributions are presented here). Our methods and results have been shared with the community through participation in 21 conferences and workshops, via a total of 8 oral and more than 25 poster presentations - with a few more to come in 2021.

I would like to acknowledge the contributions, endorsement, and support of a large number of people who allowed me to succeed on my journey and, thus, represent a fundamental part of this thesis. I would like to thank my Thesis Advisory Committee, Simon Loew, Andrea Manconi, and Urs Mall, for their continued trust and the incredible amount of creative freedom they offered - I have been able to shape the research scope of this thesis since day one; Jordan Aaron for his invaluable support across the years and projects; Mathieu Lapôtre and Maria Schönbächler for participating in the assessment of this thesis; and Emily Law, Brian Day, as well as the Solar System Trek Team for their unique and steady support. I am grateful for the inspiring and productive discussions and collaborations I got to conduct with outstanding scientists such as David Carrier; David Kring; Susan Conway; Nicolas Thomas; Jean-Pierre Williams, Paul Hayne, and the Diviner Team; Mark Shirley; Pascal Lee; and Ingrid Daubar. I would like to particularly thank JPL's COSMIC team, Lukas Mandrake, Gary Doran, Kiri Wagstaff, Umaa Rebbapragada, and Steven Lu for welcoming me amid a global pandemic and for letting me contribute to NASA technology and science. Many of the mentioned collaborations have been supported by scholarships and fellowships, issued by the German Academic Exchange Service, the Lunar and Planetary Institute, the Frontier Development Lab, Google Cloud, and NVIDIA.

Further, I would like to thank the many excellent graduate student and PostDoc-level colleagues I got to work with over the years, such as Ben Moseley, Nicole Relatores, Jerome Burelbach, Hendrik Kolvenbach, Ariel Deutsch, Pierre-Antoine Tesson, Charis Lanaras, Hannah Sargeant, Casey Honniball, Sabrina Martinez, and Alex Rogaski - here is to the future! In addition, I am grateful for my friends and companions at the Max Planck Institute for Solar System Research, ETH Zurich, and ASC Göttingen, who made it easier for me to endure the less straightforward periods of this journey.

Finally, I would like to thank my family for their continuous support and excitement about the work I have been conducting over the years (and decades). And, last but not least, Lisa, thank you for pulling me back to reality from the Moon every once in a while.

Ad astra, the author **Göttingen, May 3rd, 2021**

Contents

Zusammenfassung v

Summary vi

Nomenclature vii

List of Figures ix

List of Tables xiii

1 Introduction 1

2 Detection and Mapping of Rockfalls 5
2.1 Automated Detection of Lunar Rockfalls Using a Convolutional Neural Network 5
2.2 Deep Learning-Driven Detection and Mapping of Rockfalls on Mars 17
2.3 Transfer Learning for Rockfall Mapping in Known and Unknown Planetary Domains 27
2.4 A Dataset for Deep Learning-driven Rockfall Detection on the Moon and Mars 41

3 Drivers of Rockfalls 45
3.1 Impacts drive Lunar Rockfalls over Billions of Years 45
3.2 Global Drivers and Transport Mechanisms of Lunar Rockfalls 55

4 Exploration Applications of Rockfalls 77
4.1 Analysis of Lunar Boulder Tracks: Implications for Trafficability of Pyroclastic Deposits 77
4.2 Lunar South Pole Boulders and Tracks: Implications for Crew and Rover Traverses 95

5 Conclusion 111

A Supplementary Information 129
A.1 Using Boulder Tracks as a Tool to understand the Bearing Capacity of lunar PSRs 129
A.2 SUP: Detection and Mapping of Rockfalls 143
A.3 SUP: Drivers of Rockfalls 165
A.4 SUP: Exploration Applications of Rockfalls 183

B Declaration of Originality 211

Zusammenfassung

Vergangene und gegenwärtige Raumfahrtmissionen haben gezeigt, dass die Oberfläche des Mondes durch Hangbewegungen wie Felsstürze erodiert wird, ähnlich wie auf der Erde. Trotz der überwältigenden Anzahl der verfügbaren Satellitenbilder und anderer Daten bleiben viele Fragen unbeantwortet: Warum ereignen sich Felsstürze auf dem Mond? Welche endo- und exogenen Prozesse stecken hinter lunaren Felsstürzen? Was können uns diese Prozesse über die geologische Aktivität und Evolution des Mondes erzählen? Was können uns die Spuren von Felsstürzen über den Mondregolith und seine Interaktion mit dem Weltraum verraten? Um diesen Fragen nachzugehen entwickeln wir Deep Learning-basierte Algorithmen, die uns ermöglichen die Erkennung und Extraktion von Felsstürzen in dem Peta-byte-großen Bildarchiv des Lunar Reconnaissance Orbiters zu automatisieren - einer einzigartigen Ressource, die bisher nur oberflächlich genutzt wurde. Unsere Convolutional Neural Networks erreichen ein menschenähnliches Leistungsniveau, aber benötigen nur einen Bruchteil der Zeit von menschen-gestützten Verfahren. Durch die Anwendung von Transfer Learning Prinzipien erreichen wir eine zusätzliche Steigerung des Leistungsniveaus unserer Detektoren und machen sie robust genug, um Felsstürze auf Körpern im gesamten Sonnensystem zu erkennen, so wie auf dem Mars, Ceres, oder dem Kometen 67P. Mit diesen Multi-Domain Detektoren führen wir den ersten vollständigen, globalen Scan der gesamten Mondoberfläche durch und kartieren eine Population von mehr als 130.000 Felsstürzen, die sehr unregelmäßig über den Mond verteilt ist. Die überwiegende Mehrheit aller Felsstürze befindet sich in jungen Einschlagkratern und auf Äquator-zugewandten Hängen mit besonders ausgeprägten Temperaturschwankungen. Diese Beobachtung legt nahe, dass Felsstürze vorwiegend von Prozessen wie erratischen Impakten und kontinuierlicher, thermaler Degradierung von Gestein verursacht und angetrieben werden. Wir beobachten Felsstürze sogar in den ältesten, pränektarischen Gebieten des Mondes, was zeigt, dass diese treibenden Prozesse - in älteren Gebieten speziell kleine, meteoritische Impakte - über Milliarden von Jahren aktiv sind. Wir beobachten keine signifikanten Ansammlungen von Felsstürzen in der Nähe von sichtbaren vulkanischen und tektonischen Strukturen, was darauf hindeutet, dass seismische Aktivität kein wichtiger, globaler Auslöser von Felsstürzen in der jüngeren geologischen Geschichte des Mondes war. Um die voranschreitende Erkundung und Erforschung des Mondes weiter zu unterstützen und zukünftigen Bodenmissionen den Weg zu ebnen, entwickeln wir eine Methode, um mit Satellitenbildern von Felsstürzen und deren Spuren die lokale Bodenfestigkeit bisher unerforschter Gebiete abzuschätzen, zum Beispiel von pyroklastischen Feldern und den permanenten, polaren Schattengebieten. Diese Dissertation demonstriert das enorme Potential von modernen Deep Learning-basierten Verfahren für die Planetenforschung und vermittelt neue Erkenntnisse über die Verwitterung, Erosion und Evolution von atmosphärenlosen Körpern in unserem Sonnensystem.

Summary

Past exploration missions have revealed that the lunar topography is eroded through mass wasting processes such as rockfalls, similar to Earth. Despite the abundance of remote sensing and in–situ data many questions about the occurrence and characteristics of lunar rockfalls remain unanswered: Why do lunar rockfalls occur? What endo- and exogenic processes drive lunar rockfalls? What can these processes tell us about the geologic activity and evolution of the Moon? What can rockfall tracks teach us about the shallow lunar regolith and its interaction with the space environment? To help address these questions, we develop deep learning-driven algorithms that allow us to automate the detection and mapping of rockfalls in Lunar Reconnaissance Orbiter's Petabyte-scale image archive - a uniquely rich resource that has barely been exploited by previous work. Our convolutional neural networks achieve human-level detection performance while reducing the required processing time by several orders of magnitude. By applying transfer learning principles we further boost the performance of our detectors and make them robust enough to map rockfalls on other bodies across the Solar System as well, such as Mars, Ceres, and comet 67P. Using such multi-domain trained algorithms we conduct the first-ever, global scan of the lunar surface and derive the global distribution of rockfalls on the Moon, identifying more than 130,000 individual rockfalls. The global distribution of rockfalls is highly heterogeneous, where the vast majority as well as the highest spatial concentrations of rockfalls occur in young impact craters and on equator-facing slopes with large thermal gradients. This indicates that rockfall occurrence is mainly controlled by erratic impacts and continuous solar-driven thermal fatigue. We discover that rockfalls occur even in the oldest, pre-Nectarian lunar terranes, indicating that the identified processes - particularly small-scale meteoritic impacts - drive erosion over billions of years. We do not observe significant clusters of rockfalls in the proximity of visible volcanic and tectonic features which suggests that seismic activity has not been a major, global driver of lunar rockfall in the Moon's recent geologic past. Using satellite images of rockfall boulders and their tracks, we further develop a method to estimate the regolith surface strength and geomechanical properties of yet unexplored regions, such as the polar permanently shadowed regions and large pyroclastic deposits, directly supporting humanity's current efforts to continue the exploration of the Moon and beyond. This dissertation demonstrates the enormous potential of deep learning-driven applications for planetary science and reveals new insights about the weathering, erosion and evolution of airless planetary bodies in our solar system.

Nomenclature

Symbols

q_p	bearing pressure	$[kN/m^2]$
q_f	ultimate bearing capacity	$[kN/m^2]$
g_M	lunar gravitational acceleration	$[1.63\ m/s^2]$

Acronyms and Abbreviations

AP	Average Precision
AoI	Area of Interest
ASU	Arizona State University
CT	Confidence Threshold
CCD	Charged Coupled Device
CDR	Calibrated Data Record
CNN	Convolutional Neural Network
CPU	Central Processing Unit
DEM	Digital Elevation Model
DTM	Digital Terrain Model
EDR	Experimental Data Record
ESA	European Space Agency
FC	Framing Camera
FN	False Negative
FP	False Positive
GIS	Geographic Information System
GPU	Graphical Processing Unit
GSD	Ground Sampling Distance
GSFC	Goddard Space Flight Center
HiRISE	High Res. Imaging Science Experiment
IoU	Intersection over Union
ISRU	In/Situ Resource Utilization
JPL	Jet Propulsion Laboratory
LO	Lunar Orbiter
LER	Lunar Electric Rover
LPD	Lunar Pyroclastic Deposit
LPI	Lunar and Planetary Institute
LRO	Lunar Reconnaissance Orbiter
LROC	Lunar Reconnaissance Orbiter Camera
LRV	Lunar Roving Vehicle
MRO	Mars Reconnaissance Orbiter
NAC	Narrow Angle Camera
NaN	Not-a-Number
NMS	Non Maximum Suppression
NASA	National Aeronautics and Space Agency
PRE	Precision
PSR	Permanently Shadowed Region
PTIF	Pyramid tif
REC	Recall
RP	Resource Prospector
SETI	Search for Extraterrestrial Intelligence
SEV	Space Exploration Vehicle
SSR	Seasonally Shadowed Region
TP	True Positive
USGS	United States Geological Survey
VIPER	Volatiles Invest. Polar Exploration Rover
WAC	Wide Angle Camera

List of Figures

1.1 Examples of rockfall in LO (1969) and LRO images (2010) . . . 2
1.2 Apollo 17 panorama of Station 6 in Taurus Littrow valley . . . 3
1.3 Oblique LROC image of Taurus Littrow valley . . . 4

2.1 Rockfall in Nicholson crater . . . 7
2.2 Visualization of the rockfall feature mask . . . 8
2.3 Example RetinaNet rockfall detections . . . 11
2.4 RetinaNet performance visualization . . . 13
2.5 RetinaNet performance visualization II . . . 14
2.6 RetinaNet-based estimate of rockfall diameter . . . 15
2.7 Examples of lunar and martian rockfalls . . . 18
2.8 Example RetinaNet rockfall detections II . . . 21
2.9 RetinaNet validation visualization . . . 22
2.10 Comparison of different neural networks . . . 24
2.11 RetinaNet performance visualization III . . . 25
2.12 RetinaNet-based estimate of rockfall diameter II . . . 26
2.13 A selection of extraterrestrial rockfalls . . . 28
2.14 Example RetinaNet rockfall detections III . . . 29
2.15 Results for research question 1) . . . 32
2.16 Results for research question 2) . . . 33
2.17 Results for research question 3) . . . 34
2.18 RetinaNet example detections on Ceres . . . 35
2.19 RetinaNet example detections on 67P . . . 36
2.20 Results for research question 4) . . . 37
2.21 Examples of lunar and martian rockfalls II . . . 42
2.22 Visual representation of RMaM-2020 dataset characteristics . . . 44

3.1 Global lunar rockfall distribution heatmap . . . 47
3.2 Regional rockfall distribution maps and rockfall diameter distribution . . . 48
3.3 Statistics about rockfall distribution in space and time . . . 49
3.4 Conceptual model of lunar rockfall . . . 50
3.5 Oblique LROC image of a rockfall in Taurus Littrow valley . . . 57
3.6 AoI overview map . . . 60
3.7 Geophysical, global characteristics of lunar rockfall I . . . 62
3.8 Geophysical, global characteristics of lunar rockfall II . . . 63
3.9 Geophysical, global characteristics of lunar rockfall III . . . 64
3.10 Geophysical, global characteristics of lunar rockfall IV . . . 65
3.11 Geophysical, global characteristics of lunar rockfall V . . . 66
3.12 Comparison of rockfall distribution and lunar tectonic regions & activity . . . 67
3.13 Statistical analysis of rockfall distribution and tectonic activity . . . 68
3.14 Lunar rockfall source regions . . . 69
3.15 Lunar rockfall fact sheet . . . 70
3.16 Improved conceptual model of lunar rockfall . . . 73

4.1 Boulder track appearance across the terranes . . . 83
4.2 Bearing capacity as function of slope angle . . . 86
4.3 Bearing capacity as function of depth . . . 87
4.4 Comparison of bearing capacity values from different sources . . . 89

4.5 Trafficability analysis of different rover types . . . 90
4.6 Correction of apparent track depth . . . 99
4.7 Map of all detected south polar sunlit rockfalls . . . 100
4.8 South pole boulder track fact sheet . . . 101
4.9 South polar bearing capacity as function of depth . . . 102
4.10 South polar bearing capacity as function of depth and slope angle . . . 103
4.11 Map of south polar surface bearing capacity as function of topography . . . 104
4.12 Map of potentially challenging south polar terrain . . . 105
4.13 Detailed map of potentially challenging south polar terrain . . . 106
4.14 Photograph of Apollo 15 LRV on-slope slippage . . . 108

5.1 Rockfalls across the Solar System. . . . 112

A.1 Seeing into PSRs . . . 131
A.2 Map of south polar PSR AoIs . . . 132
A.3 Example of a rockfall in a PSR . . . 133
A.4 Schematic illustration of PSR secondary illumination . . . 134
A.5 Rockfall that crosses the penumbral/umbral border . . . 135
A.6 Examples of boulder tracks across various terranes . . . 136
A.7 PSR bearing capacity as function of slope angle . . . 137
A.8 PSR bearing capacity as function of depth . . . 138
A.9 RetinaNet augmentation . . . 143
A.10 Map of used training and testing images . . . 144
A.11 Additional RetinaNet example detections . . . 144
A.12 Testing images used . . . 145
A.13 Negative testing images used . . . 146
A.14 Effect of CT on performance . . . 147
A.15 Effect of target size on performance . . . 148
A.16 Effect of illumination on performance . . . 148
A.17 Example of RetinaNet performance in complex environments . . . 149
A.18 Map of the distribution of all available HiRISE images . . . 151
A.19 Map of all training and testing images used . . . 151
A.20 RetinaNet augmentation II . . . 152
A.21 Examples of label types used . . . 152
A.22 Selection of testing images used . . . 153
A.23 Examples of rockfall detections . . . 154
A.24 Examples of rockfall detections II . . . 155
A.25 Example of a full-scene scan with RetinaNet . . . 156
A.26 FP examples on Mars . . . 156
A.27 Images used for testing on Mars . . . 159
A.28 Images used for testing on the Moon . . . 160
A.29 Images used for testing on Ceres . . . 161
A.30 Rockfall diameter as function of terrane age . . . 165
A.31 Examples of impact-induced rockfalls . . . 166
A.32 Rockfalls in varying geomorphic contexts . . . 167
A.33 Example of rockfalls in Nectarian terranes . . . 168
A.34 Examples of potentially mis-classified rockfalls . . . 168
A.35 CNN-driven rockfall detection pipeline . . . 169
A.36 Showcase I of used geophysical maps . . . 172
A.37 Showcase II of used geophysical maps . . . 173
A.38 Showcase III of used geophysical maps . . . 174
A.39 Showcase IV of used geophysical maps . . . 175
A.40 Showcase V of used geophysical maps . . . 176
A.41 Overview of AoIs . . . 177
A.42 Relation of rockfall size and terrane properties . . . 178
A.43 Photograph of rockfall source region in Taurus Littrow valley . . . 178
A.44 Distribution of global and local slope angles . . . 179
A.45 Impact-induced and -ejected rockfalls in Vavilov crater . . . 180
A.46 Ellipsoidal boulder volume vs track length for all thirteen investigated AoIs. . . . 180

A.47 Example rockfall trajectories. . . . 181
A.48 Relation between track length and elevation drop . . . 181
A.49 Map of all studied boulder and track locations . . . 183
A.50 Isis3 processing pipeline . . . 184
A.51 Determination of boulder track characteristics . . . 184
A.52 Rover-soil contact types . . . 185
A.53 Studied rover concepts . . . 185
A.54 Overview of boulder track measurements . . . 186
A.55 Boulder track characterization . . . 187
A.56 Comparison of Terzaghi and Hansen equations . . . 188
A.57 Derived N-factors for Terzaghi and Hansen . . . 188
A.58 Regolith thickness literature values . . . 189
A.59 Bearing capacity as function of geomorphic context and slope . . . 190
A.60 Bearing capacity as function of geomorphic context and depth . . . 190
A.61 Photographs of LRV tracks across the terranes . . . 191
A.62 Isis3 processing pipeline II . . . 199
A.63 Characterization of boulders and boulder tracks . . . 200
A.64 Effective incidence angle and estimation uncertainty . . . 200
A.65 PSR bearing capacity as function of slope angle with varying soil bulk density . . . 201
A.66 Estimates of PSR ice depth . . . 201
A.67 Soil mechanical input parameters as used for this study . . . 205
A.68 Characterization of south polar rockfalls . . . 206
A.69 Rockfalls on Mons Malapert . . . 207
A.70 Rockfalls in Shackleton crater at the south pole . . . 207
A.71 Terzaghi bearing capacity vs slope angle . . . 208
A.72 Studied rover concepts II . . . 208
A.73 Shear failure surface on level and inclined terrain . . . 208

List of Tables

2.1 RetinaNet validation results . . . 12
2.2 RetinaNet validation results II . . . 23
2.3 Summary of domain characteristics . . . 29
2.4 Summary of trained rockfall detectors . . . 31

3.1 AoI overview table . . . 61

A.1 Estimated PSR bearing capacity values . . . 137
A.2 List of images used for RetinaNet testing . . . 150
A.3 Images used for training . . . 157
A.4 Images used for testing . . . 157
A.5 All HiRISE image IDs used for RMaM–2020. . . . 163
A.6 All NAC image IDs used for RMaM–2020. . . . 164
A.7 Summary of used all geophysical datasets. . . . 171
A.8 Regions of interest and their resource potential . . . 193
A.9 Rover and lander technical specifications . . . 194
A.10 Regolith density values . . . 194
A.11 Details of produced DEMs . . . 194
A.12 Regolith thickness determination methods . . . 195
A.13 Details of statistical analysis . . . 195
A.14 Report of estimated bearing capacity . . . 196
A.15 List of all images used . . . 197
A.16 Noise exaggeration kernel filter weights . . . 202
A.17 Interpolation kernel filter weights . . . 202
A.18 DEM spatial resolution and intersection error . . . 202
A.19 List of all identified in-PSR boulders and tracks . . . 203
A.20 Details of the statistical analysis . . . 203
A.21 Annual maximum temperature in AoIs . . . 204
A.22 Bearing capacity estimates with associated, soil density-related uncertainty . . . 204
A.23 Details of the statistical analysis II . . . 204
A.24 Images used for this study . . . 209
A.25 Soil input parameters as used for this study . . . 210
A.26 Rover technical specifications . . . 210

Chapter 1

Introduction

Lunar rockfalls have first been discovered in the high–resolution imagery returned by NASA's Lunar Orbiter (LO) missions in the pre–Apollo era (1960s) (Filice, 1967; Eggleston et al., 1968; Moore, 1970). The LOs were actually looking for landing sites that would allow the Apollo crewed missions to maximize operation safety and scientific return, but also discovered curious boulders that moved downslope, across the lunar surface — dubbed "rolling boulders" at the time (Eggleston et al., 1968). Figure 1.1 showcases one of these boulders with its associated track in Vitello crater, next to a present–day photograph by NASA's Lunar Reconnaissance Orbiter (LRO). The track is an important characteristic that proves the boulder has 1) in fact moved and 2) moved in the recent geologic past, assuming that tracks erode in the course of a few million years (Hurwitz, Kring, 2016) — geologically speaking, a very short amount of time.

Pre- and co–Apollo–era scientists used the tracks of rockfalls to estimate the angle of internal friction, the cohesion, as well as the bearing capacity of lunar regolith (Hovland, Mitchell, 1973; Filice, 1967; Moore, 1970). Their idea was to convince skeptics who argued that the lunar soil would not be able to bear any kind of load and to help inform the engineers who were designing the landing gear of the Apollo landers (Carrier et al., 1991). The results of these remote sensing studies were well aligned with in–situ data collected by NASA's Surveyor missions (Carrier et al., 1991), which consisted of seven robotic landers that touched down on the lunar nearside between 1966 and 1968. In 1972, Apollo 17 astronaut Harrison Schmitt even sampled a rockfall boulder and track at station 6 on the slope of the North Massif in Taurus Littrow valley, returning rock and regolith samples to Earth. Schmitt and Apollo 17 commander Eugene Cernan recognized and commented on the enormous dimensions and energy of this particular rockfall event that carved a ∼10 m wide track:

> **165:02:13 Schmitt:**
> *Hey, I'm standing on a boulder track. (To Cernan) How does that make you feel?*
>
> **165:02:17 Cernan:**
> *That makes me feel like I'm coming over to do some sampling. (Pause) Think how it would have been if you were standing there before that boulder came by!*
>
> **165:02:33 Schmitt:**
> *I'd rather not think about it.*[1]

The dimensions of the boulder track deeply impressed Eugene Cernan, who kept referring to it as the astronauts were operating around station 6:

> **165:37:18 Cernan:**
> *Man, I tell you, these slopes are great. I wouldn't mind being up on top coming down, but...Hey, that boulder track is quite a trench!*
>
> **165:59:39 Cernan:**
> *Okay. I'm going to power up and see if I can't come down and get you. (Pause) It's fun walking downhill! Boy, that boulder track is impressive.*

Figure 1.2 shows a panoramic photograph of the rockfall–deposited boulders that carved the tracks that impressed the Apollo 17 astronauts. Figure 1.3 features an oblique LRO photograph of another rockfall on the opposite side of the valley, on the north–facing slope of the South Massif, illustrating the significant

[1] from the Apollo 17 Lunar Surface Journal: https://www.hq.nasa.gov/alsj/a17/a17.sta6.html

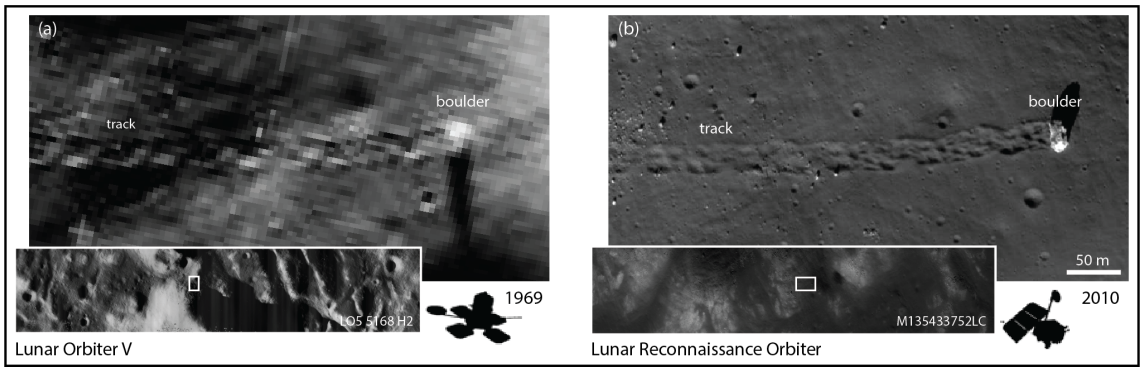


Figure 1.1: Lunar Orbiter (a) and Lunar Reconnaissance Orbiter (b) images of the identical rockfall in Vitello crater, taken in 1969 and 2010, respectively. The direct comparison reveals the differences in image spatial resolution and quality. LO and LRO parent frames are shown as well. LO image credits to NASA/USGS; LRO image credits to LROC/GSFC/ASU.

topographic relief of the lunar surface, i.e., the environment in which lunar rockfalls occur. During the Apollo-era, Hovland, Mitchell (1973) looked at potential drivers of these rolling boulders, identifying erratic processes like meteoritic impacts and moonquakes, as well as continuous processes like micro–impacts and thermal breakdown. However, the LOs only returned ∼1600 images — where most have insufficient spatial resolution and quality to resolve rockfalls — that only covered a very small fraction of the lunar surface, thus, strongly limiting the expressivity of the observations of rockfall drivers made locally.

After the end of the Apollo program in 1972, no new high–resolution imagery (<∼10 m/pix) of the Moon was available, resulting in a data hiatus more than ∼40 years long. Then, in 2009, NASA's LRO started to downlink high–resolution imagery from the Moon (Robinson et al., 2010). As of today, the remarkable downlink rate of LRO resulted in a unique image archive with more than 2.6 million acquisitions and a size of more than 1 Peta–byte (PB, i.e. 1,000 TB or 1,000,000 GB), and growing, covering the entire surface of the Moon multiple times over. The unique LRO dataset not only attracted scientists but also motivated the public as well as citizen scientists to become involved in the analysis of the lunar surface. Among other things, this lead to quaint "discoveries" related to rockfalls, such as boulders that got confused with alien battle tanks and boulder tracks that were confused with alien roads or tunnels[2]. Since 2009, scientists have been using LRO's massive image archive to investigate lunar rockfalls in more detail: Xiao et al. (2013) identified ∼50 rockfalls in various locations on the surface of the Moon and argued that seismic activity in combination with meteoritic impacts are the main drivers of lunar rockfalls and mass wasting in general. Kumar et al. (2013) and Kumar et al. (2016) mapped rockfalls in the Schrödinger impact basin on the lunar farside and suggested that the identified rockfall events were triggered by tectonic activity as well as impacts. Subsequently, Kumar et al. (2019b) and Mohanty et al. (2020) used the apparent spatial proximity of rockfalls in Laue crater and Mare Orientale to two extrapolated (approximated) Apollo–era shallow moonquake epicenter locations from January 3rd, 1975 and December 9th, 1972 to strengthen their earlier findings, arguing that tectonic activity in these regions is responsible for the occurrence of rockfalls. Building on these local observations and findings, other work used the abundance of rockfalls in the proximity of visible tectogenetic features, such as faults and graben, in other lunar regions as one argument for present–day lunar seismic activity that could potentially pose a threat to future surface exploration efforts in these regions (Watters et al., 2010, 2019; Mohanty et al., 2020).

This means that the current literature, in contrast to the Apollo–era literature, is converging on the hypothesis that lunar seismic activity has been the main driver of lunar rockfalls in the recent geologic past and still is, with potentially hazardous effects on future ground exploration missions. It is important to note that all these previous studies exclusively relied on human–driven rockfall recognition and mapping and thus have been limited to a few small geographic regions, strongly limiting their sensitivity for region- and global–scale causal relationships. The LRO image archive is simply too large to be manually processed by human operators: Assuming an expert–level processing time of 30 minutes per image and a 40 hour work week it would take 100 experts roughly 6.25 years to look at all images. This means that as of today,

[2]see e.g.: https://www.popularmechanics.com/military/weapons/a26480/alien-tank-on-the-moon/

more than 50 years after their discovery — despite the abundance of image data — the global and local drivers of lunar rockfalls are still unknown. Numerous questions remain unanswered:

- How many rockfalls are there on the Moon?
- Where exactly do rockfalls occur?
- Do rockfalls still occur today?
- Why do rockfalls occur?
- What can the drivers of rockfalls tell us about the geologic activity of the Moon?
- What can lunar rockfalls teach us about the erosion of airless planetary bodies in general?
- Can we use rockfalls to aid future exploration efforts to the Moon and other planetary bodies?

Before we can address these important science questions, we need to first solve the fundamental challenge researchers are currently facing: the massive LRO image archive. Is there a way to quickly process large portions of this dataset (weeks instead of years) while maintaining a human–level mapping performance? We turn to cutting–edge algorithms developed and used by research fields like computer vision and robotics, specifically convolutional neural networks (CNN), to automate the detection of rockfalls in LRO imagery, i.e., to perform a task very similar to e.g. face recognition, but with the goal of studying lunar geomorphology. CNNs are the drivers behind the deep learning revolution that took place in the past decade (Goodfellow et al., 2016). Their main strength is the processing of spatial data, i.e., images, specifically their ability to recognize spatial properties and prominent feature characteristics across a large range of image scales and orientations, while being robust versus variations in image geometry, scene illumination, sensor and environment noise, as well as artifacts (Russakovsky et al., 2015; Pierson, Gashler, 2017).

Chapter 2 describes how we customized, trained, and tested these deep learning–based algorithms on lunar rockfalls and LRO imagery. Chapter 2 goes on to describe how we then merged satellite image data from the Moon with imagery of other planetary bodies that also host rockfalls, such as planet Mars, dwarf–planet Ceres, and comet 67P, to create multi–domain rockfall detectors that achieve improved mapping performance on the Moon as well as on all other bodies considered. All developed rockfall detectors only require a few seconds to scan one complete image (vs ∼30 minutes by a human expert) and thus have the potential to process the entire or large portions of the LRO image archive. Some aspects of the work presented in chapter 2 have been performed as part of the NASA Jet Propulsion Laboratory (JPL) Visiting Student Research Program (JVSRP) in cooperation with JPL's Machine Learning and Instrument Autonomy (MLIA[3]) group led by Dr. Lukas Mandrake. Chapter 3 discusses how we combined our novel algorithms with big computational resources provided by the Google Cloud Platform to scan the entire surface of the Moon for rockfalls, deriving the first global map of lunar rockfalls and turning the challenging LRO dataset into a great science opportunity. Chapter 3 then describes how we combined this rockfall map with a large variety of existing global, geophysical lunar datasets to address the research questions posed above, identifying and characterizing the dominant global and local drivers of lunar rockfall and overcoming some of the limitations of past work. Some of the relevant, auxiliary datasets used throughout chapter 3 have been produced in cooperation with NASA's Frontier Development Lab (FDL[4]), hosted by

[3] https://ml.jpl.nasa.gov/
[4] https://frontierdevelopmentlab.org/



AS17-141-21575 to 21603

Figure 1.2: Panorama of the (small and large) rockfall–deposited boulders located at the Apollo 17 station 6 site; the boulders originated from a source region on the left side of the frame. The South Massif is in the background. LRV and astronaut to scale. LRO image credits to USGS/NASA.

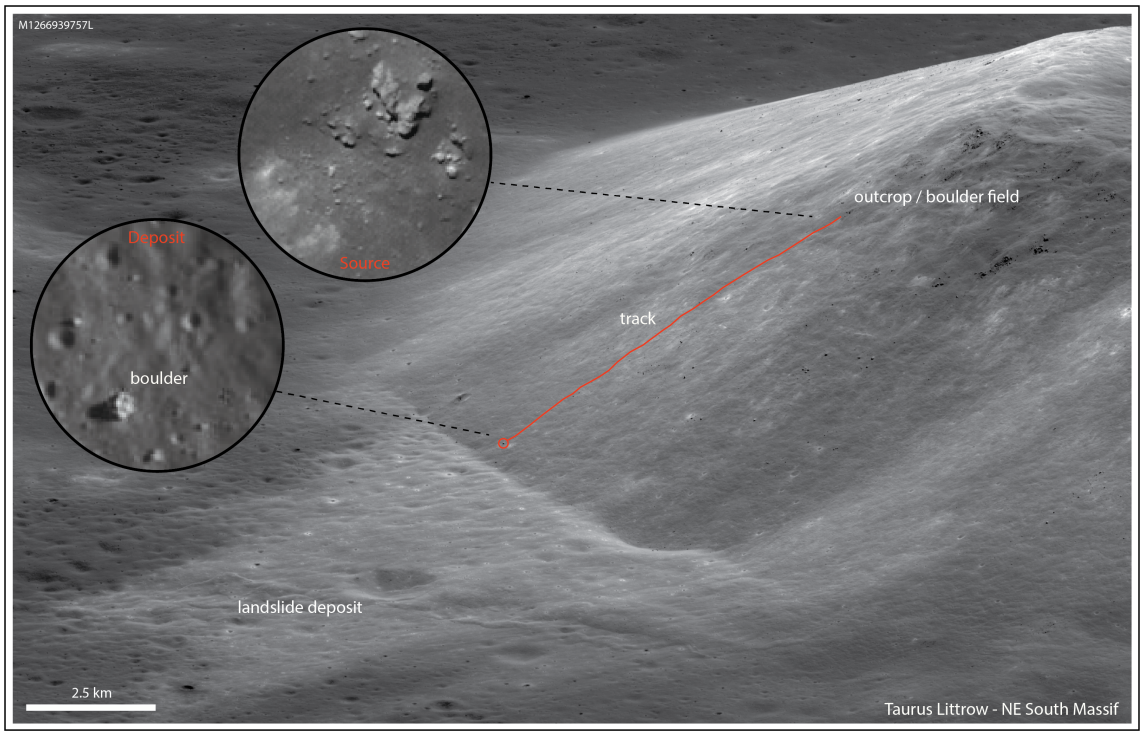


Figure 1.3: Oblique LRO image of a rockfall on the north–facing slope of the South Massif; the boulder track is indicated in red. The insets show the rockfall source and deposition regions. A bright landslide deposit is highlighted as well. The South Massif is ∼2,300 m tall, i.e., ∼500 m higher than the Grand Canyon is deep. LRO image credits to LROC/GSFC/ASU.

the SETI Institute and the NASA Ames Research Center. Chapter 4 focuses on the exploration–relevant aspects of rockfalls. Inspired by the work performed in the pre–Apollo era (Carrier et al., 1991; Filice, 1967; Eggleston et al., 1968; Moore, 1970), we develop an LRO–based method to estimate the surface strength of yet unexplored lunar regions - including pyroclastic deposits and polar sunlit and shadowed regolith - by using only rockfall tracks, informing the currently ongoing efforts to plan and design the missions and hardware for the continued exploration of the Moon. The majority of the research presented in chapter 4 has been conducted as part of the Exploration Science Summer Internship Program at the Lunar and Planetary Institute (LPI[5]), supervised by Dr. David Kring. Chapter 5 closes this dissertation with a conclusion and an outlook: We discuss the parallels and differences between terrestrial and extraterrestrial rockfall, debate how rockfalls could threaten or impact future lunar exploration, and reason what our observations could teach us about the erosion of planetary surfaces across our Solar System in general. The exploration of the Moon and our solar system is very much ongoing and future missions, landed as well as orbiting, will create a large array of science opportunities related to planetary geomorphology and geologic activity — including rockfalls. The Conclusion gazes ahead, at how future science opportunities could look like and how they could be used, on the Moon and beyond.

[5] https://www.lpi.usra.edu/

Chapter 2

Detection and Mapping of Rockfalls

This chapter describes in exceeding detail how we adopted and applied cutting–edge deep learning algorithms to automatically detect and map rockfalls on the Moon and on other planetary bodies. We further report testing and validation metrics, as well as benefits and limitations of the developed algorithms.

2.1 Automated Detection of Lunar Rockfalls Using a Convolutional Neural Network

Published 2018 in IEEE Transactions on Geoscience and Remote Sensing
Bickel, V.T., Lanaras, C., Manconi, A., Loew, S., Mall, U., 2018
https://doi.org/10.1109/TGRS.2018.2885280

Abstract
This paper implements a novel approach to automatically detect and classify rockfalls in Lunar Reconnaissance Orbiter narrow angle camera (NAC) images using a single-stage dense object detector (RetinaNet). The convolutional neural network has been trained with a data set of 2932 original rockfall images. In order to avoid overfitting, the initial training data set has been augmented during training using random image rotation, scaling, and flipping. Testing images have been labelled by human operators and have been used for RetinaNet performance evaluation. Testing shows that RetinaNet is capable to reach recall values between 0.98 and 0.39, precision values between 1 and 0.25, and average precisions ranging from 0.89 to 0.69, depending on the used confidence threshold and intersection-over-union values. Mean processing time of a single NAC image in RetinaNet is around 10 s using a GeForce GTX 1080 Ti and GeForce Titan Xp, which is in orders of magnitudes faster than a human operator. The processing speed allows to efficiently exploit the currently available NAC data stack with more than 1 million images in a reasonable timeframe. The combination of speed and detection performance can be used to produce lunar rockfall distribution maps on large spatial scales for utilization by the scientific and engineering community.

Introduction

Lunar rockfalls and their traces have been investigated by researchers since the Lunar Orbiter Program sent back the first high-resolution images of the lunar surface in 1966 (Filice, 1967; Eggleston et al., 1968; Moore, 1970; Moore et al., 1972; Pike, 1971; Hovland, Mitchell, 1971, 1973). In addition to images taken from orbital platforms, astronauts Eugene Cernan and Harrison Schmitt were able to directly sample and photograph boulder and track remnants of rockfalls in the Taurus-Littrow valley during the Apollo 17 mission in 1972 (Lyndon, 1973). Since the arrival of NASA's Lunar Reconnaissance Orbiter (LRO) in orbit around the Moon in 2009 (Robinson et al., 2010), a growing repository of high-resolution images taken by LRO's Narrow Angle Camera (NAC) is available that enables the studies of geomorphological processes and small-scale features such as rockfalls in unprecedented detail. Various investigations use NAC imagery to identify and study lunar rockfalls as a tool to, e.g., estimate local seismic activity and shaking intensity in Schrödinger Crater (Kumar et al., 2016) or to investigate the topographic evolution of the Moon (Xiao et al., 2013). Besides that these studies show that rockfalls are a widespread phenomenon and occur in

various geologic settings.

A crucial point in lunar studies that use rockfalls is the identification of these small-scale features in NAC images. Usually, manual mapping of rockfall features is performed by human operators, which is difficult, inefficient, and time consuming. Further, the total count of available NAC images that can be used for mass wasting feature mapping passed the one million mark already in 2016 (Witze, 2018), i.e., manual processing of the entire NAC archive appears unrealistic. These limitations result in a lack of detected and mapped rockfall features on large spatial or even global scales that would be useful to draw solid conclusions for scientific questions such as the general spatial rockfall distribution, the geomorphological evolution of the Moon, or the potential connection between structural geologic features and surficial mass wasting. Further, the global analysis of rockfalls could potentially contribute to resolve some of the main lunar science priorities that have been established by the U.S. National Research Council of the National Academies in 2007, such as the determination of the variety, age, distribution, and origin of lunar rock types (science goal 3b) or the spatial complexity of the crust (science goal 3d) (NRC, 2007).

Recent advances in computer vision and deep learning allow computer-executed detection and localization of objects in images (Lin et al., 2017; Girshick et al., 2016; Ren et al., 2015; He et al., 2015) that is being used i.a. for face detection and autonomous driving. Amongst the available state-of-the-art techniques, single-stage dense object detectors, such as RetinaNet, have proven to perform best in terms of classification precision and speed (Lin et al., 2017). In general, such a convolutional neural network (CNN) is being trained with a large amount of images that contain realistic representations of the object of interest. Subsequently, the trained network can be used to find and classify the object of interest in previously unseen images in a relatively quick and efficient way (Girshick et al., 2016). This paper presents a way to automatize the detection of lunar rockfalls using a single-stage dense object detector and to exploit the available archive of NAC image big data. The developed tool is capable of producing large-scale lunar rockfall maps with optimized efficiency and speed, potentially supporting scientific and engineering applications and investigations in the future.

The first chapter of this paper provides an introduction to lunar rockfalls, their geomorphological appearance, and how they are physically represented in high-resolution imagery. Subsequently, the available data for studies of the lunar surface are presented, followed by a description of the common human operator-based mapping techniques. The next chapter contains information about the used hard and software, their implementation, as well as the training, inference, and application of the used neural network. Further, the used testing and evaluation methods are described. Finally, the derived results are presented and the benefits and limitations of the technique are discussed.

A. Lunar Rockfall Characterization

Rockfall features have been identified all across various lunar regions with different surface ages and geologic settings, respectively, units, such as mare, highland, and pyroclastic deposit regions (Kumar et al., 2016; Xiao et al., 2013). Hungr et al. (2014) generally characterize rockfalls as the falling, rolling, and bouncing of single or clusters of ice or rock fragments with limited total volume which mainly interact with the underlying slope substrate. This interaction with the slope substrate can cause the characteristic boulder tracks that can be detected from orbit (Figure 2.1) and is a distinct indicator for a past active displacement of a boulder, i.e., a rockfall. Xiao et al. (2013) note that there exist rockfalls without visible traces on the lunar surface, e.g., on the Western wall of Rima Hadley. While this subtype of rockfall can be inferred from ground-based imagery, it is difficult to detect in satellite imagery with sufficient confidence, as distinct traces are missing and as spatial resolution of the available orbital imagery is often insufficient. Due to these limitations, the subset of trace-less rockfalls is not being considered in this paper. General factors that could increase the probability for rockfalls and mass wasting to occur are rock or soil type, its structure, slope topography and lateral constraints (Corominas et al., 2018). Potential triggers for rockfall in particular and mass wasting events in general on the Moon have been identified i.a. by Kumar et al. (2016), Xiao et al. (2013), and Carrier et al. (1991) as recent seismic activity and impact events, while shear outgassing and thermal fluctuations in rock outcrops during lunar diurnal periods could contribute as well. With dominant terrestrial erosional processes such as fluvial, aeolian, or biologic processes being absent on the Moon, boulder tracks conserve their pristine shape for very long time periods. This allows observers to detect and trace rockfalls back to either a distinct or diffuse source area such as a rock face, outcrop, or upslope boulder field (Figure 2.1). Furthermore, the absence of vegetation facilitates the detection of these features from orbit. While the form, track shape, and runout distances of boulders alter, their overall appearance in images taken from orbit is relatively uniform. Kumar et al. (2016) and Xiao et al. (2013)

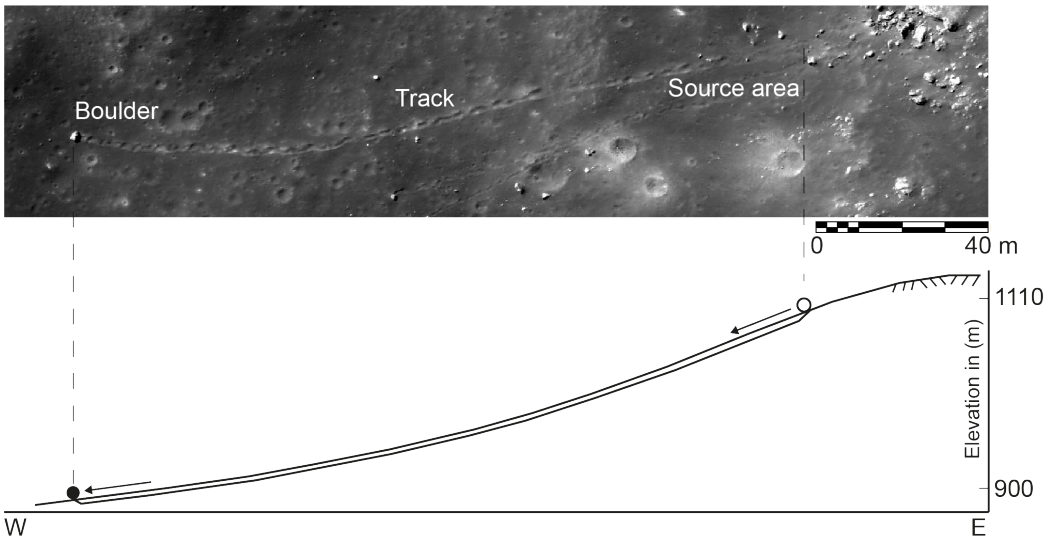


Figure 2.1: Example for a lunar rockfall in Northeastern Nicholson Crater: (Top) Source outcrop on the right side, characteristic boulder track strikes right left, boulder itself is deposited downslope. (Bottom) Cross section through crater slope, topography is derived using the global WAC DEM by Scholten et al. (2012), elevation difference between source (hollow shape) and deposition area (filled shape) is ∼200 m. Detail of M138107059LC. Vertical axis is exaggerated for visualization purposes. North is up.

report typical boulder diameters of less than a meter up to 25 m and track lengths from meters up to a few kilometer.

The major components of a typical lunar rockfall that can be observed in NAC images are: 1) a boulder that usually has a higher albedo than the surrounding regolith; 2) a shadow that is cast by the boulder and appears right next to its parent boulder; and 3) a nearly linear boulder track with light shadows at its deepest point and potentially along its rims (Figure 2.2). A computer can use such evident features (here called feature mask) as well as more subjacent information in the images to identify rockfalls. The process of object detection and classification in RetinaNet is in fact much more complex than described here, but the concept of using evident features such as illustrated in Figure 2.2 aids to understand the neural network's processing routines. Using the same simplification, the feature mask also allows a computer to distinguish rockfalls from other features with similar appearances such as static boulders without traces or small impact craters which might meet one or two of the mentioned criteria, but not all three (Figure 2.2). This feature mask is the simplified basis for the automatization of lunar rockfall detection and is used to illustrate the description of object detector training and its application.

B. Available Data

Rockfalls and individual boulder tracks are meter-scale mass wasting features that can only be recognized and studied in image data with sufficient spatial resolution in the order of meters per pixel or less. In addition, a data set for rockfall detection on large spatial scales should provide global and multitemporal coverage, as well as a constant level of quality. Multitemporal coverage is useful, because it enables to view sites of interest with alternating illumination and viewing conditions, facilitating detections. Currently, these criteria are only being met in the data set that is being generated by NASA's LRO NAC that is in operation since 2009 (Robinson et al., 2010) and was able to take more than one million images so far (Witze, 2018) with mean ground sampling distances (GSD) of around 0.5 m/pixel from its nominal orbit in 50 km altitude (Robinson et al., 2010). So far, the vast majority of the lunar surface has been covered, while the majority of the surface has been acquired several times.

Access to the imagery is possible via the planetary data system and related sites such as the LRO Camera (LROC) image search page. Images can be retrieved as 12 bit experimental data records (EDRs) level 0, calibrated data records level 1 (CDR), and reduced data records level 2 (Robinson et al., 2010). In addition,

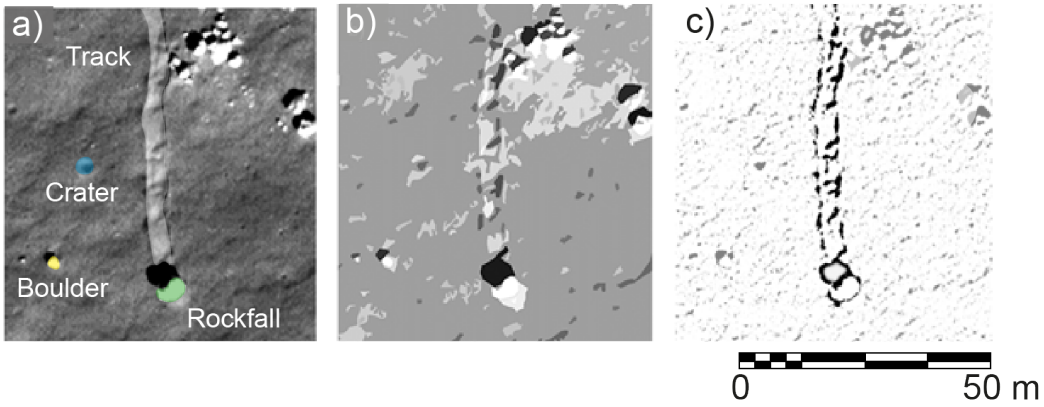


Figure 2.2: Simplified visualization of lunar rockfall feature mask. (a) original detail of NAC M111422030LC showing a rockfall (green) with its track as well as static boulders (yellow) and small craters (blue). (b) Median filter highlights the occurrence of characteristic high-intensity features (boulders, illuminated crater slopes) and low-intensity features (boulder shadows, crater shadows) right next to each other. (c) Highpass filter highlights the paired straight edges of the track which are characteristic for rockfalls. North is up.

advanced data products such as mosaics or digital elevation models (DEMs) are available for specific sites of increased interest, such as Apollo or future landing sites (Robinson et al., 2010). For a global analysis, EDR and CDR data have to be used, as the other products do not exist on a global scale (Robinson et al., 2010). Along with the EDR and CDR data, the LROC team distributes preprocessed pyramid tiff files (CDR PTIFs) that provide full spatial resolution, but are reduced to 8 bit, corresponding to a joint photographic experts group quality level of 75 (N. Estes, 2018, pers. comm.). Their reduced size enables a faster processing of the data, while providing identical spatial resolution and sufficient image quality. Due to the optimal compromise between spatial resolution and file size, the CDR PTIF data set has been used for machine learning and prediction with the single-stage dense object detector. The vast majority of LRO's NAC observations are subnadir looking, with emission angles ranging from 0° to 35°; oblique images with emission angles of more than 35° are available as well, but their extreme distortions and GSD variations make them unattractive for automated mapping purposes. Other global data sets include LRO wide angle camera (WAC) images and the Lunar Orbiter Laser Altimeter (LOLA) measurements; however, their spatial resolutions of ∼75 m/pixel for the visible bands and ∼118 m/pixel, respectively, render them impractical for rockfall mapping and analysis, as boulders have much smaller dimensions (LOLA, n.d.; WAC, n.d.). Products with potentially sufficient GSDs are, e.g., images taken by the Lunar Orbiters from 1966 to 1967 or by the Apollo Metric Camera during the Apollo 15, 16, and 17 missions, but their coverage is limited to a small number of orbits during the missions' timespan, while quality is not consistent (USRA, n.d.; USGS, n.d.).

Methods

A. Classic Manual Mapping

On Earth, large-scale manual slope instability mapping campaigns are only possible due to the contribution of a high number of involved institutes and professionals, such as being conducted, e.g., for the Italian Landslide Inventory since 1997 within the frame of the IFFI project (IFFI, 2018). Such projects run over years or decades and rely on information that is collected in situ as well as in air- or spaceborne imagery to create maps and inventories (IFFI, 2018). On the Moon, however, identification of slope instabilities is limited to the utilization of space borne imagery, while available resources are reduced. The available image products can be accessed using either web-based or desktop-based image viewers. Due to download and processing speed as well as storage limitations the web-based method is usually more efficient. Several tools allow to load, view, and analyze georeferenced image data from space missions, such as Moon Trek that is being developed by the NASA Jet Propulsion Laboratory (JPL) at Caltech (https://moontrek.jpl.nasa.gov/), QuickMap that is operated by the Arizona State University (ASU)

(https://quickmap.lroc.asu.edu/), or JMars which is operated and developed by the Mars Space Flight Facility at ASU (https://jmars.asu.edu/). As slope instabilities require relief, the search for rockfalls could often be limited to areas with slope gradients that can be retrieved from DEM-based global slope maps, either based on WAC DEMs (Scholten et al., 2012) or an LOLA-DEM (LOLA, n.d.). However, previous studies show that rockfalls usually detach, respectively, occur on slopes with angles reaching from around 15° up to 40° (Xiao et al., 2013), suggesting that rockfalls could also be deposited at slope gradients lower than 15°. Therefore, a limitation to areas with substantial relief might reduce the number of areas to look at, but also might bias the mapping itself, as rockfalls on particularly shallow slopes might be systematically excluded. With the regions of interest selected, high-resolution NAC images from the designated areas have to be visually examined by an experienced human operator in order to identify regions that host mass wasting processes such as rockfalls.

Due to the large amount of available NAC images and of lunar terrain with substantial relief and the irregular distribution of mass wasting features, manual search and mapping of rockfalls is very time consuming; a single operator is able to detect and map around 50 features per day, based on the experiences of the authors. In addition, manual mapping is biased, as: 1) the quality which is provided by human operators is directly connected to their experience, motivation, and awareness and tends to drop significantly over time and 2) human operators might overlook rockfalls with unexpected appearances or dimensions. Using this approach an effective and extensive analysis of large areas or the production of large-scale rockfall maps is significantly aggravated.

B. Automated Object Detection, Implementation, and Hardware Setup

Several of the limitations of manual mapping can be avoided using an automated detection approach, which can be performed in various ways. Region-based CNNs (R-CNNs) use multilayer CNNs to derive invariant and discriminative features that finally produce bounding boxes (bboxes) or segmented masks around detections (Girshick et al., 2016). This means that R-CNNs operate in a two-step architecture: 1) scanning an input image and identifying candidate regions in the image where detections of features appear possible, so called region proposals and 2) classifying the proposals (Girshick et al., 2016). Region proposals can be produced with a variety of different methods, such as objectness (Alexe et al., 2012), selective search (Uijlings et al., 2013), or constrained parametric min-cuts (Endres, Hoiem, 2010). Subsequently, all region proposals get classified by the CNN (Girshick et al., 2016). Various studies optimized the present computational region proposal determination bottleneck and significantly improved R-CNN training and prediction speed, called Fast (Girshick et al., 2016) and Faster R-CNNs (Ren et al., 2015). Residual Networks (ResNets) have been introduced in He et al. (2015) who applied a deep residual learning framework to deep learning applications to address the degradation problem of deep CNNs, i.e., vanishing gradients for increasing network depth. Lin et al. (2017) reduced the common two-stage architecture of R-CNNs to a faster single-stage architecture (RetinaNet) that uses a novel focal loss training method, which is a reshaped standard cross-entropy loss that reduces the weight assigned to well-classified examples (Lin et al., 2017). The focal loss approach addresses the foreground-background imbalance during single-stage detector training, which used to overwhelm the detector during training, degenerating the model and reducing its accuracy. RetinaNet has proven to outperform state-of-the-art two-stage architectures in terms of accuracy and speed (Lin et al., 2017). For this paper, the single-stage dense object detector "RetinaNet" (Lin et al., 2017) has been used that relies on the ResNet50 in He et al. (2015). RetinaNet has been implemented in Python3 using the machine learning library Keras v2.2.0 ("Keras RetinaNet" by Fizyr) (Fizyr, 2018) and a TensorFlow backend v1.7.0. For network training and evaluation two desktop computers with advanced GPU-based computation capabilities (GeForce GTX 1080 Ti and GeForce Titan Xp) are used.

C. RetinaNet Training

The neural network requires a specific format of the training data, e.g., information about training image IDs and the location of bboxes that mark features for training (Fizyr, 2018). A manual and global search has been performed that identified 104 NAC images with rockfall features in various lunar regions, including various emission angles and illumination conditions, as well as image spatial resolutions and image qualities. Imagery with rockfall features has been downloaded as CDR PTIF, incorporated into QGIS v2.18.14, where the NAC images have been subtiled into smaller patches. Subsequently, the detected features are marked with rectangular bboxes and their image coordinates are extracted for further use using MATLAB vR2018a or Python3, as illustrated in Figure A.9 in the Appendix. Bboxes have been placed in a way to allow the trained network to detect rockfalls not only based on the deposited boulders, but also using the end of their tracks to avoid confusion of actual rockfalls with static boulders and small craters. Still,

bboxes are small enough to prevent the environment (small craters, scattered static boulders) to influence the training by altering the underlying feature mask. Using this approach, a total of 2932 individual lunar rockfalls have been identified, marked, and extracted. The location of each used NAC image is plotted in Figure A.10).

In order to make the network rotation and scale invariant, Keras RetinaNet's build-in augmentation techniques have been applied to increase the size and complexity of the produced training database. In particular, all used images for training are rotated, up- or downsampled, as well as randomly flipped during each epoch of the training (Figure A.9). During training, RetinaNet learns the optimal filter weights for the targeted objects on its own and performs an internal image enhancement, thus, pre-CNN image processing, such as contrast enhancement or edge detection, are not required and have not been performed. Validation has been performed using the default RetinaNet training-validation split. In total, training involved 82 epochs and 2932 iterations per epoch, while the drop of loss, classification loss, and regression loss have been monitored. Here, the loss describes the combination of classification and regression loss, which denote the class label prediction loss and the initial anchor bbox correction loss, respectively. Due to convergence of overall loss drop and an increase in the classification loss between epoch 75 and 161, training has been stopped. To prevent influence through overfitting, i.e., a too strong focus of the trained network on the restricted training data set, epoch 82 has been selected as being most representative for the desired purpose. The number of epochs in combination with the performed iterations per epoch results in an actual number of 240,424 different augmented images that have been used for training and validation.

D. RetinaNet Testing

The results derived with the trained neural network are tested against a data set of 70 image patches that contain a total of 126 rockfalls that have not been used for network training or validation. These image patches contain rockfalls and tracks in different lunar regions such as mare and highland areas, as well as pyroclastic deposits. The used NAC images have been patched to dimensions suitable for processing in RetinaNet, i.e., 844 by 844 pixel, usually corresponding to 366 patches per NAC image. No patch overlap has been used, as the neural network has proven to detect features very close to or right at the edges of input patches (Figure 2.3 and Figure A.11). Fifty patches were selected semirandomly from a total of 18 individual NAC images with different viewing geometries and illumination conditions, all containing rockfalls with a variety of shapes and sizes, as well as displacement methods, i.e., track shapes created by either rolling, sliding, or jumping boulders. The selection has been semirandomly, because the selection of patches had to cover the entire bandwidth of available viewing geometries, spatial resolutions, illumination conditions, and lunar regions for testing to be representative. Within these hard constrains, testing patch selection has been random. In addition, 20 patches taken from 19 NAC images that do not contain any rockfalls have been manually selected and used to enhance the analysis of network performance in relation to false positives. This additional set of patches is expected to simulate the fact that a specific portion of the lunar surface lacks any rockfall features and thus minimize a potential testing bias in relation to the absolute number of used testing patches. Care has been taken that these negative patches cover a wide range of lunar surface types. An application of the trained network to such a diverse testing data set provides the setup for an accurate evaluation of the performance of the network under realistic conditions. All testing images and important details are listed in Table A.2 and all used patches are displayed in Figure A.12 and Figure A.13. Figure A.10 in the Appendix illustrates the spatial distribution of the used rockfall features across the lunar surface that have been used for testing.

Testing has been performed using the built-in evaluation routines of RetinaNet, Keras, and TensorFlow, using the described data set that has previously been labelled by an experienced human operator. The used routines count the predictions of the trained network in unseen images, i.e. true positives (TP, correct classifications), false negatives (FN, rockfalls that have not been detected by the network), and false positives (FP, mis-classifications). These counts are used to calculate the recall and the precision of the prediction, respectively. Recall describes the number of rockfalls that have been detected out of all the present ones (e.g., 82/126 rockfalls have been detected), precision expresses how many of the detections are actually correct and how many are incorrect (e.g., 20/102 detections are false positives). These two ratios can be used to derive the average precision (AP) that expresses the development of the precision in relation to the recall, i.e., the average of the maximum precisions at different recall values, here derived for recall values ranging from 0 to 1 in 0.1-wise recall steps. AP is the standard metric to evaluate the performance of object detection routines such as RetinaNet (Lin et al., 2017; Girshick et al., 2016) and has been used for this work as well. The recall and precision values are previously derived using different confidence thresholds (CTs), i.e., the confidence level in percent the network must have in order to mark

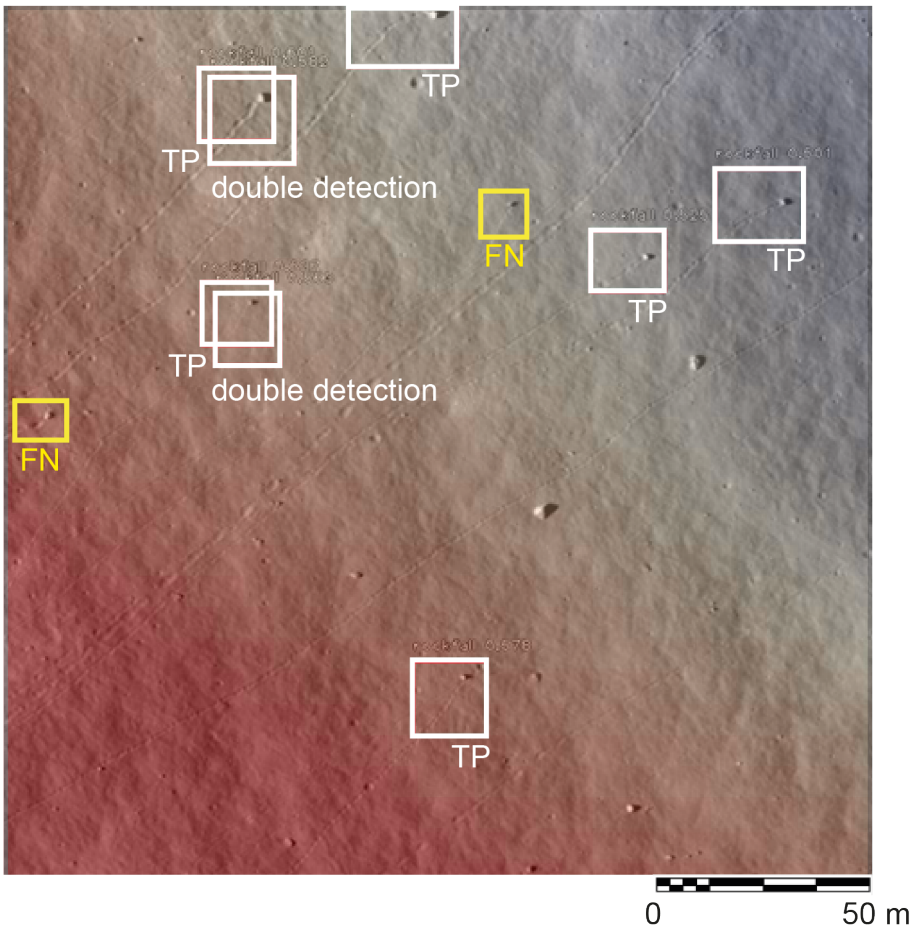


Figure 2.3: Example of RetinaNet detections (white rectangles, TP) in testing patch, the trained network is able to detect features that are situated directly at the edge of the patched NAC images (e.g. Top of figure). Yellow bboxes indicate rockfalls that have not been recognized by the network (false negatives, FN). Red background colors indicate high terrain, blue background colors represent low terrain, detail taken from M113242798RC, DEM taken from Scholten et al. (2012). Double detections occur locally and require an application of postprocessing algorithms, such as NMS (not performed here for visualization purposes). North is up.

and classify a feature as rockfall. Higher thresholds require that the network has a high classification confidence in a potential detection, which has two important effects: 1) the neural network will generally pick up less features, as potential detections with lower confidences are dismissed and 2) the number of mis-classifications is reduced. Lower CTs allow the acceptance of more features but increase the probability to detect wrong features. For this paper, CTs ranging from 20% (0.2) to 60% (0.6) have been assessed. A visual comparison of the effect of different CTs is displayed in Figure A.14. AP, recall, and precision have been computed using intersection-over-union (IoU) values ranging from the default value 0.5 (50% bbox overlap) to a relatively loose value of 0.1 (10% bbox overlap). IoU is a measure for the overlap of labelled and predicted bboxes, and thus for the quality of the bbox placement by the network. Bbox placement precision on the order of pixels and meters (i.e., close to 1) is not vital for the task of creating large-scale rockfall abundance maps and a loose IoU value enables the network to include detections with non-optimal bbox placement as TPs. RetinaNet's built-in non-maximum-suppression filter (NMS) has been applied using default values (score threshold 0.05 and IoU threshold 0.5) to remove multiple detections of identical features. An NMS uses the network's confidence in a detection (score) to prefilter overlapping detection boxes, and then performs the suppression based on an IoU threshold, removing redundant detections with low scores that cover the same or almost the same area as the respective strongest detection in the scanned image (Fizyr, 2018). Additional examples of successful rockfall detections in the used patches that have been filtered with NMS are displayed in Figure A.11.

CT	AP_{10}	REC_{10}	PRE_{10}	AP_{25}	REC_{25}	PRE_{25}	AP_{50}	REC_{50}	PRE_{50}
0.2	0.89	0.98	0.45	0.84	0.96	0.35	0.69	0.88	0.25
0.3	0.89	0.90	0.63	0.84	0.88	0.54	0.69	0.82	0.35
0.4	0.89	0.77	0.86	0.84	0.77	0.84	0.69	0.75	0.60
0.5	0.89	0.69	0.98	0.84	0.69	0.95	0.69	0.65	0.79
0.6	0.89	0.44	1	0.84	0.44	0.96	0.69	0.39	0.85

Table 2.1: Results of RetinaNet validation, reported as AP, recall (REC), and precision (PRE) for IoU values of 0.1(10), 0.25(25), and 0.5(50).

Results

Processing time per NAC PTIF image (i.e., ∼366 patches) is around 10 s for the described hardware setup. Performance of the neural network for all used confidence thresholds and IoUs is summarized in Table 2.1. Lower CTs generally produce higher recall values, but lower precisions. Lower IoUs improve both, recall and precision. One of the sites used for RetinaNet testing in South-Eastern Mare Frigoris has been used to demonstrate the ability of the trained neural network to create rockfall abundance maps, as displayed in Figure 2.4.

Discussion

The results indicate that a trained single-stage dense object detector such as RetinaNet is able to automatically detect lunar rockfalls with traces in the available NAC imagery. Processing times are orders of magnitude shorter compared to a human operator. This allows to process a significantly higher number of NAC images in the same amount of time, while generally receiving acceptable recall, precision, and AP values. As expected, higher CTs deliver more reliable (precise) results, but are not able to detect all visible rockfall features. For the purpose of creating large-scale lunar rockfall abundance maps, the precision has to be close to 1 to avoid mapping FPs, which could bias the resulting products and interpretations. Therefore, a CT of 0.4 or 0.3 would provide a promising compromise between recall and precision. CT could also be locally adapted (in- or decreased), e.g., if prediction results proof to be insufficient. Usage of lower IoU values also enhances network prediction performance. The fact that the bbox placement accuracy is dropping with increasing IoUs could be caused by the fact that the data set used for training is not as extensive as normally desired for deep learning applications. However, bbox placement precision is not the main concern for RetinaNet as a tool to create large-scale rockfall abundance maps, where placement accuracy of a single bbox on a meter scale is less important than the general correctness of a detection and its position in a larger geomorphological or even global context.

A direct comparison of RetinaNet's performance to other object detection architectures and applications is difficult, because the application and used training data set is different in terms of size, type, and quality of data compared to usual data sets used for object recognition, such as available, e.g., on PASCAL VOC or MS COCO (Girshick et al., 2016; Ren et al., 2015). In addition, this neural network is being trained and operated with single band images in contrast to the common three band (red-green-blue) images. Despite these differences, the performance (e.g., the AP) of the trained network appears to fit to state-of-the-art AP values for other object detection applications ranging from ∼0.21 to ∼0.82 (Girshick et al., 2016; Ren et al., 2015)

A visual assessment of RetinaNet's performance reveals that missing or wrong detections can be caused by three factors: 1) insufficient NAC image spatial resolution or particularly small boulder and track size; 2) particularly poor illumination conditions causing long shadows or shallow pixel intensity gradients; and 3) properties of the immediate neighborhood of rockfalls (Figure 2.5). Errors introduced by the first two factors can be limited by using input NAC imagery with appropriate solar incidence angles, camera emission angles, as well as spatial resolution. However, for rockfalls with particularly small dimensions (<∼3m mean diameter) an ambiguity will remain, potentially inhibiting a successful detection. This spatial resolution-dependent limitation is equally relevant for both, human and computer-controlled operators, as very small rockfall features cannot be identified with sufficient confidence anymore, as illustrated in Figure A.15. A main focus during training has been to enhance the ability of the neural network to pick up small-scale features, but as such features are represented by fewer amounts of pixels, training is generally more difficult

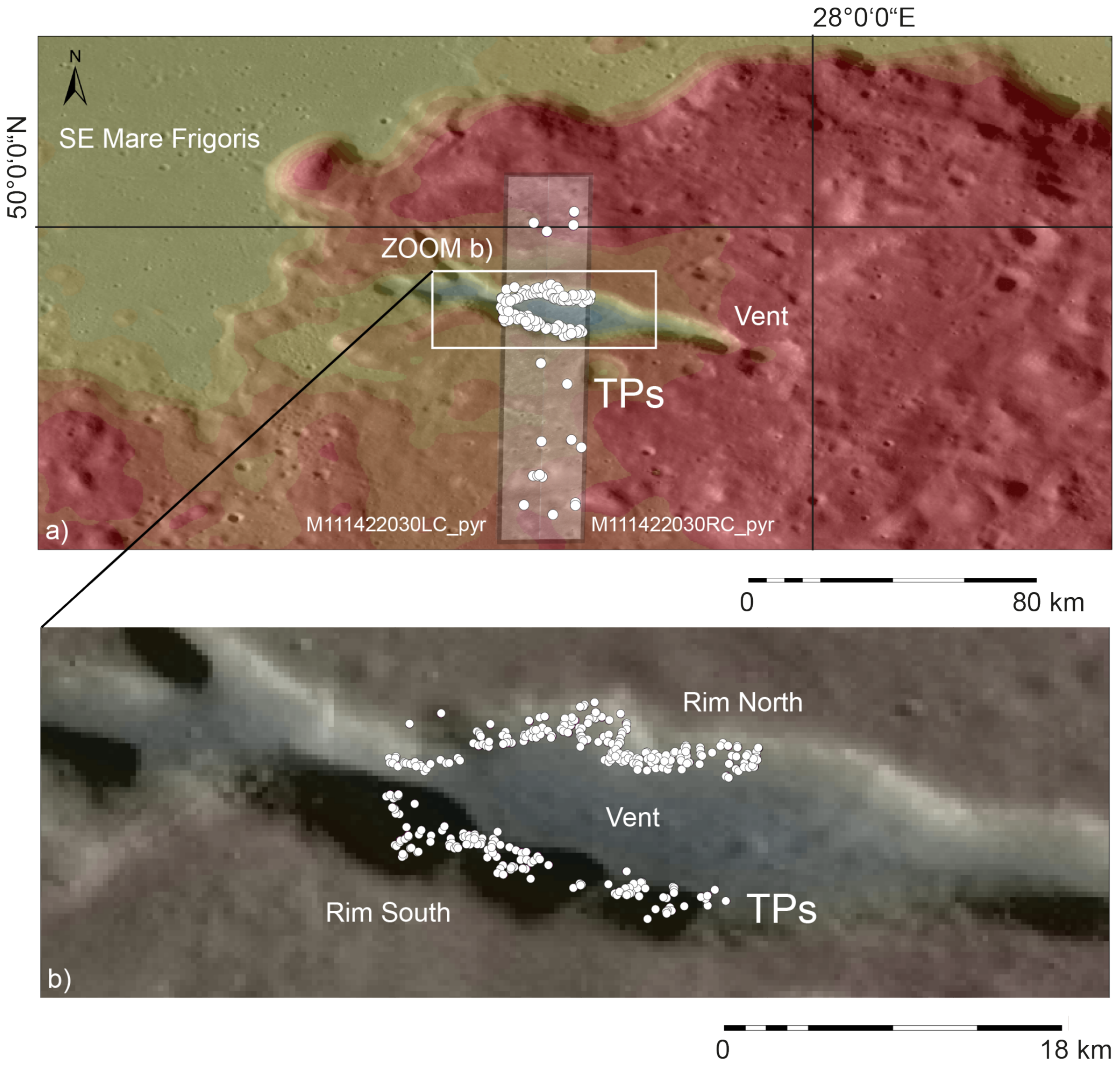


Figure 2.4: RetinaNet performance illustration. (a) Location of a pyroclastic vent between craters Aristoteles and Baily in SE Mare Frigoris in a global lunar WAC mosaic, NAC images M111422030LRC are overlain (whitish area). (b) Rockfall detections along the E-W striking slopes of the vent in NAC images M111422030LRC. White shapes mark the network's confirmed positive rockfall detections (TPs), FNs are not displayed. Original bboxes have been manually changed to shapes that mark the detected features to improve visibility of individual detections. The origin of these boulders lies in outcrops along the rim of the pyroclastic vent, but the trigger or rockfall frequency is unknown. Map indicates that not all rockfalls are necessarily associated with prominent topographic features [see TPs north and south of the vent in (a)]. Reddish indicate higher terrain, blue lower terrain; topography taken from Scholten et al. (2012).

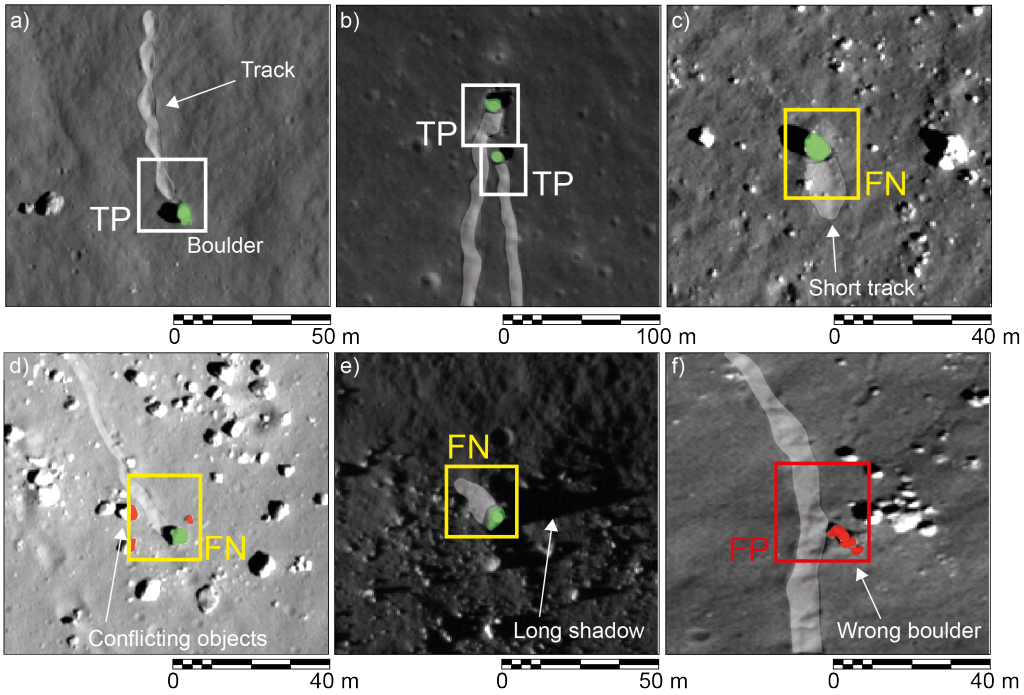


Figure 2.5: Examples for influence of NAC image features and rockfall neighborhood on detection. (a) Optimal setting, successful detection (TP). (b) Suboptimal setting as two boulders are close to each other, successful detection of both. (c) Track is very short, no detection (FN). (d) Numerous boulders closeby, no detection. (e) Difficult illumination conditions with long shadows and confusing contrast, no detection. (f) Boulder at track-kink, misclassified as rockfall (FP). North is up.

and the rate of mis-matching and classification is also rising. In areas of the Moon where the illumination conditions are difficult around the year, particularly at the poles as well as in (semi) permanently shadowed regions, the applicability of the neural network is reduced to a similar extent as human operator-based mapping is. Despite the limitations concerning the spatial resolution and illumination conditions of the available imagery, the CNN is able to detect rockfalls over a wide range of resolutions and solar incidence angles, as further illustrated by Figure A.16.

The third factor is caused by the lunar surface itself, e.g., in cases where a rockfall comes at rest directly next to other boulders which have not been moving or in cases where a static boulder is situated on a kink of an actual boulder trail [Figure 2.5(d) and (f)]. The modification of the direct environment of the object of interest by the presence of other objects or via obscuring is a known limitation of CNNs. The presence of too many other close boulders [Figure 2.5(d)] will reduce the confidence of the trained network in the detection, as it has been mainly trained with ideal rockfall examples and clean surroundings as usually encountered on the Moon. As a consequence of the reduced confidence, the detection might fall below the used CT and, thus, might not be classified. As a result, the ability of the trained CNN to detect boulders that come at rest directly next to other static boulders or objects might be occasionally reduced or limited. Figure A.17 displays two case studies of typical lunar rockfall sites to further illustrate the CNN performance in these cases.

The second example is rare and is very difficult to avoid, as the feature mask geometry is very similar to a real rockfall, with the exemption that the track kinks and continues downslope [Figure 2.5(f)]. Results show that the network produces reduced confidences while looking at such special settings, i.e., mis-classifications only occur as long as lower CTs are being applied. In addition, such an apparent misclassification would still point the attention of a human operator toward an actual rockfall feature, even if the moving boulder itself is missed. Even in the absence of fast erosional processes, boulder tracks might eventually disappear as a consequence of micrometeorite impacts (space gardening). As the tracks are a

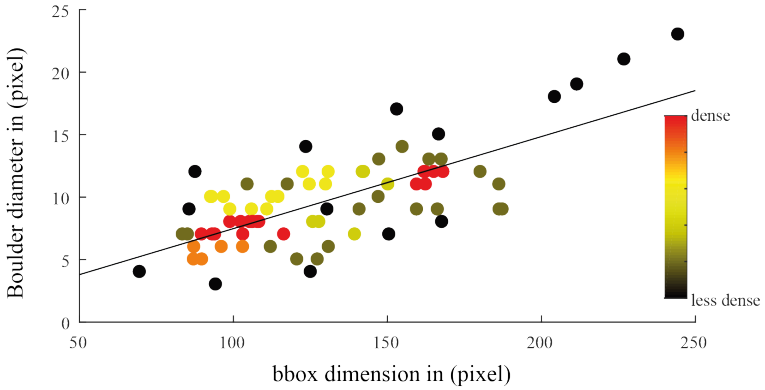


Figure 2.6: Relation between dimension (diameter) of detected boulder on the x axis and its bbox diameter on the y axis. The least-squares fit illustrates the linear-type relation, further supported by the scatter density indication. Using the spatial resolution of the used NAC image, the boulder diameter can be inferred in (meters) for further analysis.

vital part of the feature mask used by RetinaNet, boulders with eroded tracks would not be detected as rockfalls, although they might have been displaced in the distant past. This implies that a CNN might not be able to recognize ancient lunar rockfalls. However, a human operator would face the exact same limitation, thus this is not a limit of the used method but a limit governed by the observed features and the conditions of their environment.

RetinaNet creates multiple detection-proposals per patch, occasionally resulting in multiple, slightly different detections of the same rockfall feature, i.e., with slightly different confidence scores, as well as locations and dimensions of the marking bboxes (e.g., Figure 2.3). This is caused by the imperfect ability of an object detector to localize the concept of interest and is a common situation in computer vision and object detection scenarios (Rothe et al., 2014). The up- and downsampling of the used training imagery using the build-in augmentation generator favors the occurrence of these multiple detections, because the network recognizes features at different levels. This is probably a by-product of the scale invariance of the network, which is vital however to boost the general network performance (Figure A.16). RetinaNet's built-in NMS filter has been applied to remove multiple detections. Known shortcomings of NMS algorithms are well-known and include the selection of non-representative bboxes and the suppression of detections of other close-by objects (Rothe et al., 2014). During testing and evaluation, these shortcomings have net been observed, however.

Visual assessment during testing of the CNN revealed that the size of the assigned bboxes is related to the size of the detected boulders. This observation can be used to establish a linear relation between bbox diameter and boulder diameter (Figure 2.6) and will be used in the future to retrieve not only the locations of boulders but also their magnitude, enabling an analysis of potential rockfall distribution-magnitude relationships. Utilization of advanced computer vision methods as presented in this paper could be also applied to routinely scan through acquired imagery from lunar or other planetary missions "on the fly" to attach tags to images that indicate the occurrence of specific features of interest in them, such as specific geomorphological features, e.g., cave skylights or crater types. The resulting image catalog could then be efficiently filtered by the scientific community using these tags. As missions continue, quality of scanning and tagging would steadily improve as the neural networks improve. Such an approach would help to deal with the ever increasing amount of data being returned by current and future space exploration missions.

Conclusion

This paper shows that single-stage dense object detectors such as RetinaNet can be trained and applied to automatically localize and classify lunar rockfalls with trails in available LRO NAC images. The implemented Keras RetinaNet network achieves recall values between 0.98 and 0.39, precision values between 1 and 0.25, as well as AP values between 0.89 and 0.69, dependent on the used confidence threshold and

IoU. The average processing time of a single NAC PTIF is around 10 s using either a GeForce GTX 1080 Ti or a GeForce Titan Xp. Wrong classifications are caused by either: 1) insufficient NAC image spatial resolution respectively small boulder or track dimensions; 2) poor illumination conditions; or 3) unfavorable appearance of the rockfalls' immediate neighborhood. Local occurrence of multiple detections of the same rockfall feature can be effectively removed using RetinaNet's built-in NMS filter.

Due to its performance and processing speed, the neural network enables the production of large-scale lunar rockfall or rockfall density maps for utilization by the scientific and engineering community, while being able to exploit the entire available NAC image archive. If the locations of the majority of lunar rockfalls are known, their spatial distribution would allow to draw conclusions about, e.g., the Moon's endo- and exogenic activity as well as other relevant scientific questions.

While data processing within the implemented RetinaNet is fast, the provision of the vast amounts of input images as well as the collection of the produced results is still challenging. As the amount of available image data is immense, a neural network could best operate per an on-demand basis that brings the user to the data, not the data to the user, thus avoiding image download, processing, and storage issues. In addition, handling of a CNN as well as the extraction of the required information from the network is complex. The implementation of a single-stage dense object detector as an advanced tool in an existing web-based infrastructure such as Moon Trek (https://moontrek.jpl.nasa.gov/) would lift all these limitations, allowing the community to use the capabilities and advantages of the neural network in the most efficient way. Moon Trek is a sophisticated web-based data viewing and interpretation site for lunar data sets, operated and developed by NASA JPL at Caltech in California, U.S. If implemented amongst the existing advanced tools with similar data processing pipelines such as the crater or boulder detection tool, the dense object detector for rockfalls would be accessible for the entire scientific and engineering community in a user-friendly environment while bridging current technical limitations.

Acknowledgment

The authors would like to thank Emily Law and the Moon Trek team at NASA JPL for their support and the offer to implement this tool in Moon Trek. They would like to thank Prof. E. Baltsavias and S. Galliani from the Chair of Photogrammetry and Remote Sensing, ETH Zurich, Hoenggerberg, as well as Julie Stopar from the LROC team for her support. They would also like to thank the editor and the two anonymous reviewers for their valuable and constructive feedback and the NVIDIA Academics Team for their support with a Titan Xp GPU grant for this project. Data can be made available upon request to the authors. The workflow is entirely based on open source software. The developed tool will potentially be accessible online on the Moon Trek platform that is being developed by NASA JPL, Caltech, USA. This research did not receive any specific grant from funding agencies in the public, commercial, or not-for-profit sectors.

2.2 Deep Learning-Driven Detection and Mapping of Rockfalls on Mars

Published 2020 in IEEE Journal of Selected Topics in Applied Earth Observations and Remote Sensing
Bickel, V.T., Conway, S., Tesson, P.-A., Manconi, A., Loew, S., Mall, U., 2020
https://doi.org/10.1109/JSTARS.2020.2991588

Abstract
The analysis of rockfall distribution and magnitude is a useful tool to study the past and current endogenic and exogenic activity of Mars. At the same time, tracks left by rockfalls provide insights into the mechanical properties of the Martian surface. While a wealth of high-resolution spaceborne image data are available, manual mapping of displaced boulders with tracks is inefficient and slow, resulting in: 1) a small total number of mapped features; 2) inadequate statistics; and 3) a sub-optimal utilization of the available big data. This study implements a deep learning-driven approach to automatically detect and map Martian boulders with tracks in high resolution imaging science experiment (HiRISE) imagery. Six off-the-shelf neural networks have been trained either on Martian or lunar rockfall data, or a combination of both, and are able to achieve a maximum overall recall of up to 0.78 and a maximum overall precision of up to 1.0, with a mean average precision of 0.71. The fusion of training data from different planets and sensors results in an increased detection precision, highlighting the value of domain generalization and multidomain learning. Average processing time per HiRISE image is ∼45 s using an NVIDIA Titan Xp, which is more than one order of magnitude faster than a human operator. The developed deep learning-driven infrastructure can be deployed to map Martian rockfalls on a global scale and within a realistic timeframe.

Introduction

Mars is a dynamic planet and recent surface activity has been shown by a large number of studies using data returned from ground-borne and spaceborne missions, such as the Mars Science Laboratory (MSL or Curiosity) or the Mars Reconnaissance Orbiter (MRO). While Mars is host to a variety of active processes, mass wasting and aeolian processes are particularly relevant for this study. Dynamic aeolian features include dunes (Bourke et al., 2008; Bridges et al., 2012) and dust devils (Balme, Greeley, 2006; Lorenz, Reiss, 2005) that migrate across the Martian surface. Observed mass wasting processes include polar ice and dust avalanches (Russell et al., 2008; Schorghofer et al., 2002), rockfalls (Roberts et al., 2012; Kumar et al., 2019a; Haas de et al., 2015), slope streaks (Aharonson et al., 2003; Schorghofer et al., 2007; Brusnikin et al., 2016) and potentially recurring slope lineae (RSL) (Dundas et al., 2017; Schmidt et al., 2017; Stillman et al., 2019). As for RSL, other mass wasting phenomena are potentially related to the action of volatiles, such as flows in gullies (Dundas et al., 2017; Pasquon et al., 2016; Raack et al., 2015) and flows over CO2 ice (Gardin et al., 2010).

The occurrence, frequency, and magnitude of mass wasting phenomena, and rockfalls in particular can be indicative of seismic activity of planetary bodies or moons in general, as several recent studies have shown (Roberts et al., 2012; Kumar et al., 2019a; Taylor et al., 2013; Kumar et al., 2016, 2019b). Thus, suspected regions of increased seismic activity inferred from rockfall frequency patterns could be priority targets for the deployment of future geophysical networks. The tracks created by extraterrestrial rockfalls, i.e., boulder tracks, are also a valuable tool to estimate the basic mechanical properties of the surface substrate present (Bickel et al., 2019; Sargeant et al., 2020).

However, the manual detection and mapping of Martian rockfalls (boulders with tracks, here also called feature of interest) in satellite imagery remains a challenging task. Since 2010, MRO's high resolution imaging science experiment (HiRISE) (McEwen et al., 2007) has returned tens of thousands of high-resolution images of the Martian surface. While image data are abundant, traditional mapping of rockfalls is slow and inefficient - a human operator has to spend a substantial amount of time to scan through a single HiRISE image, which is a tiring and arduous process, particularly when mapping is performed over large regions using an increased number of images. In addition, the mapping of rockfalls on non-terrestrial surfaces is complicated by limitations of the used image data (resolution and coverage). However, a high number of rockfall detections is required to establish a robust statistical analysis, which in turn is the basis for

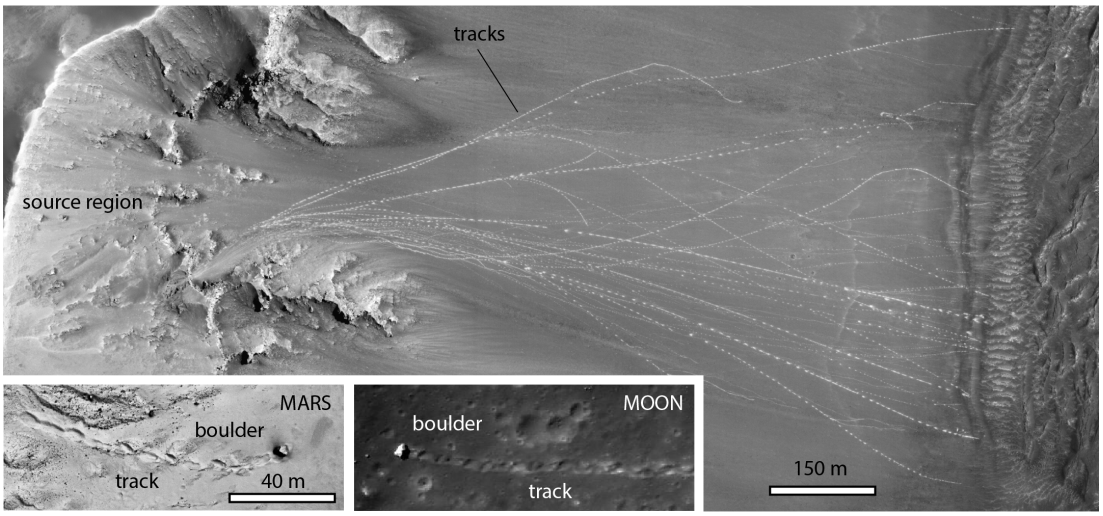


Figure 2.7: Example of Martian and lunar rockfalls with their associated boulders and tracks ("feature of interest"). Overview image shows numerous rockfalls that detached from a bedrock outcrop near an impact crater rim on Mars. During their displacement, the boulders bounce and roll leaving tracks on the slope's substrate. The downslope direction is towards the right. North is down. Detail of HiRISE image ESP_031280_1705. Bottom insets feature a close up of a Martian boulder with its track in HiRISE image ESP_039901_1665 and a lunar boulder with track in NAC image M138107059LC. Image credits: NASA/JPL/UofA/LROC/ASU.

scientifically robust conclusions. Previous studies on Martian rockfalls, such as those performed in Kumar et al. (2019a) and Tesson et al. (2020), would greatly benefit from an increased number of detected and mapped boulders with tracks.

Here, we describe how we implemented and applied a deep learning-based approach to automatically detect and map Martian rockfalls (boulders with tracks) in HiRISE imagery, to significantly enhance the statistical relevance of state-of-the-art geomorphological analyses on Mars. Deep learning-driven rockfall mapping in satellite imagery has first been demonstrated by Bickel et al. (2018) on the Moon, where other surface activity is limited. For the lunar environment, a convolutional neural network (CNN) was able to achieve near-human detection performance while reducing the required processing time (human versus machine) by more than one order of magnitude. On Mars, Fanara et al. (2020) developed a method to automatically detect ice falls in HiRISE images of the northern polar caps, using support vector machines. Due to its atmosphere and dynamic geologic environment, Mars generally poses additional challenges for the detection and mapping of rockfalls from orbit. Combining experience from previous work with a novel multidomain learning approach, this study shows how deep learning and off-the-shelf CNNs can be used to extract new and valuable information from underexploited, but challenging Martian datasets, given the limitations of the available data. In addition, this study is relevant in light of spacecraft autonomy, where similar neural networks and infrastructures could be deployed to optimize mission procedures, e.g., by using AI for onboard selection of image data to improve utilization of the available data transfer bandwidth from remote regions of the solar system.

This article is organized as follows. Section I-A introduces Martian rockfalls and their physical appearance in high-resolution images taken by HiRISE. Next, the available and used datasets are described (Section I-B), followed by a description of the applied deep learning approach (Section II). Finally, results are presented and discussed (Sections "Results" and "Discussion"), with a focus on the limitations of the developed method and its value for the exploration of the red planet. Section "Conclusion" concludes this article.

I-A. Martian Rockfalls

Repeat coverage and high-resolution images (better than 0.5 m/pix (McEwen et al., 2007)) have revealed terrestrial-like rockfall (or boulder fall) present-day activity on Mars. Images show meter-scale blocks (here called boulders) which have detached from a bedrock cliff or boulder field, and have rolled/bounced downslope, leaving a visible track on the surface behind them (see Figure 2.7). As aeolian processes are active on Mars (Bourke et al., 2008), tracks left by rockfalls infill or erode over time, meaning, visible

tracks are recent, forming during the Late Amazonian period (conservatively the last few tens of millions of years). They have been found on the walls of long, linear fissures (e.g., Cerberus Fossae) (Roberts et al., 2012), valleys (e.g., Valles Marineris) (Kumar et al., 2019a), as well as impact craters (Haas de et al., 2015). Rockfalls can be produced by weathering (e.g., solar-induced thermal stress) (Tesson et al., 2020) followed by fracture propagation in the exposed rock (i.e., fatigue) at the top of a slope. In impact craters, loose blocks could also be formed by impact events (ejecta blocks) or could detach from ejecta blankets that have previously been emplaced on the crater walls (Krishna, Kumar, 2016). Once formed, boulders move under the influence of gravity, while their displacement can also be driven by external factors such as nearby marsquakes or meteoritic impacts. Recently, the spatial distribution of boulder tracks has been used to highlight the possibility of recent marsquakes in potentially active regions (Roberts et al., 2012). As energy is increased closer to a seismic event, rockfall frequency and size should also increase (Keefer, 1984). On a larger scale, spatial distribution of rockfalls can be used to study active weathering processes responsible for rock breakdown on Mars (Tesson et al., 2020), as well as to estimate weathering rates. Besides their implications for weathering processes and seismic activity of Mars, rockfalls and their tracks can be used to infer the mechanical properties of regolith, as demonstrated on the Moon by, e.g., Moore (1970) during the Apollo era and recently by Bickel et al. (2019) and Sargeant et al. (2020), directly informing future surface exploration efforts. A deep learning-enabled global study of rockfall distribution on Mars could provide valuable information for a wide variety of relevant scientific and exploration-related applications.

I-B. Available Datasets

The surface of Mars has been imaged and is currently being imaged by numerous spacecrafts. While many instruments provide datasets with near-global coverage, such as ESA's Mars Express High Resolution Stereo Camera (HRSC, ∼15 m/pix), and MRO's Context Camera (CTX, ∼6 m/pix), their spatial resolution is insufficient to detect and map small geomorphological features such as boulders with tracks. The highest resolution is currently offered by MRO's HiRISE camera that takes subnadir images in the range from 0.25 to 0.75 m/pix with swath widths of about 6 km (McEwen et al., 2007). HiRISE is a pushbroom sensor comprised of 14 CCDs that provides data products with information in three different channels, covering the spectral range from 400 to 1000 nm (visual to near infrared wavelength). However, full multispectral coverage is only available for the central portion of each swath (roughly a 1.2-km wide footprint on the ground, i.e., approximately one-fifth of the entire image). The rest of the image is only available in a single channel, the red channel (550 to 850 nm). As the scope of this work is the detection and mapping of rockfalls on a large spatial scale; the utilization of imagery with maximum ground coverage has the highest priority. For this reason, network training and inference has been limited to the red channel, i.e., the full image swath. It has to be noted that despite its superior spatial resolution, HiRISE has not yet been able to cover a large portion of the Martian surface (around 3.56% as of February 14th 2020) due to its small footprint. Any analysis of rockfalls is therefore limited to regions that have been observed by the camera — for humans as for a CNN. Despite the reduced coverage, numerous targets of high scientific value across all regions and latitudes have been imaged, as illustrated by Figure A.18 in the Appendix. HiRISE's coverage might not be complete, but most geomorphological contexts are represented in the data stack.

We used nonmap-projected, full-resolution .jp2 HiRISE images for this work. These data have undergone standard radiometric calibration routines and the data from the 9 or 10 red channel CCDs have been stitched to produce a single rectangular image. The perfect rectangular, upright orientation of nonmap projected HiRISE images helps to minimize the number of tiles when an image is cut into smaller pieces to fit into the RAM of the used GPUs, directly optimizing processing speeds. They have the additional advantage that because no resampling of the data has been performed in order to map-project the data, these images represent the highest fidelity and resolution products. By using the available metadata for these images, in particular the coordinates of the image corners, the real-world coordinates of the detections in an image can be reconstructed using their respective image coordinates. Map-projected and, thus, rotated images result in more and potentially empty (NaN) tiles, larger file sizes, and consequently, longer processing times, which is not optimal for machine learning applications. The used nonmap projected .jp2s have been reduced to 8 bit to further improve processing speeds and to enable the utilization of off-the-shelf machine learning toolboxes and libraries. One limitation of the nonmap projected products is that the stitching of these products is performed considering only the spacecraft pointing information and no postprocessing is done to improve the match between the CCDs in the overlapping area (as is done for the map-projected products). This means that there are visible seams caused by CCD mismatch on these products. Besides image data, the laser altimeter (MOLA) onboard the Mars Global Surveyor (MGS) provides information about the Martian topography and relief. The United States Geological Survey (USGS) combined more

than 600 million laser pulses in a global map product with a resolution of 463 m/pix (MOLA, 2014). Using MOLA and HRSC data, (Fergason et al., 2017) blended a new DEM with a resolution of 200 m/pix. We include both products as potential auxiliary data for this study.

Methods

II-A. Deep Learning-Driven Object Detection

Recent advances in machine and deep learning have overcome some of the issues in computer and machine vision, such as the detection and classification of objects in images. An important milestone was the development of two-stage region-based CNNs (R-CNNs) (Girshick et al., 2016), and their subsequent improvements, i.e., fast and faster R-CNNs (Girshick et al., 2016; Ren et al., 2015). Recently, He et al. (2015) introduced the so-called residual networks (ResNets) that solved the problem of vanishing gradients during training, enabling deeper and more powerful networks. Then, Lin et al. (2017) established a much faster single-stage architecture (RetinaNet) while adding a new loss function (focal loss) that improves the training efficiency by minimizing the weight assigned to well-classified examples. RetinaNet consists of two main networks, a ResNet for deep feature extraction and a feature pyramid network (FPN) (Lin et al., 2018) for the construction of rich, multiscale convolutional feature pyramids, as well as two subnetworks, an anchor classification network and an anchor regression network (Lin et al., 2017). RetinaNet is outperforming other off-the-shelf state-of-the-art detectors in terms of classification accuracy and speed (Lin et al., 2017), is robust, and well established (Douillard, 2018; Singh, 2019; Weinstein et al., 2019). The combination of simplicity, reliability, recognition, speed, and performance is the reason why we chose RetinaNet for this study. We run RetinaNet with both ResNet50 and ResNet101 backbones (He et al., 2015), where the number refers to the layers of the network, i.e., its depth. In theory, a deeper neural network would yield better results, see, e.g., Eigen et al. (2014). We used RetinaNet — with open-source software only — in Python3, using Keras (v2.2.0, RetinaNet implementation by Fizyr) (Fizyr, 2018) and TensorFlow (v1.7.0). For the training and inference, we used two GPU-enabled desktop computers (NVIDIA GeForce GTX 1080 Ti and GeForce Titan Xp).

II-B. RetinaNet Labeling, Training, and Testing

Labels for training have been created by three experienced human operators (with domain knowledge) following the workflow of Bickel et al. (2018), using 136 full-swath HiRISE images with varying spatial resolutions and solar incidence angles, taken over different Martian regions (see Table A.3 and Figure A.19 in the Appendix). Each label represents a classification and localization of a rockfall by a human operator that can be used by RetinaNet for training, validation, and testing. We placed the labels in a way to train the CNNs on the combination of boulder and track, to avoid detections of tracks without boulders and boulders without tracks (see Figure A.20 for details). The problem of how to label such irregular features, such as rockfalls and tracks, is interesting and is further discussed in Section "Discussion". The used images are from a wide range of longitudes and latitudes and represent a variety of geomorphological contexts, i.e., crater slopes, fissures (graben), and valleys (see Figure A.19).

We trained and tested six different CNNs. Their names indicate the origin of the main training data (Ma for Mars and M for Moon), the level of complexity of the training data (basic or complex), and the ResNet backbone depth (either 50 or 101). Four CNNs are exclusively trained with Martian image data while two CNNs are trained with a combination of Martian and lunar rockfall labels, where lunar labels were taken from Bickel et al. (2018), using NAC images [narrow angle camera, PTIF (pyramid tif) single band 8bit, see Bickel et al. (2018). The level of complexity loosely describes the "difficulty" of the used training labels: "Basic" labels contain very clear examples of rockfalls with distinct tracks in a noncomplex environment (bare regolith); "Complex" labels feature more challenging environments such as debris fields. Examples of both levels are displayed in Figure A.21. All "Complex" networks utilize the labels from "Basic," but further add complex examples, as described above. In addition, we included a series of "negative" examples (1024 labels) in the training data to highlight morphologic features that mimic the feature of interest, such as sand ripples, etc., but that must not be classified as rockfalls. The six trained CNNs are: (I) Ma Basic_{50}, (II) Ma Basic_{101}, (III) Ma Complex_{50}, (IV) Ma Complex_{101}, (V) Ma/M Complex_{50}, and (VI) Ma/M Complex_{101}. We trained (I) and (II) with 2340 labels over 74 and 48 epochs; (III) and (IV) with 4969 labels over 85 and 66 epochs; (V) and (VI) with 13964 labels over 75 and 111 epochs. Here, (V) and (VI) have been trained with 4969 Martian and 8995 lunar labels, making (V) and (VI) the first cross-planet multicamera CNNs for rockfall detection. The term epoch describes one complete pass of all labels and images through the network. Training has been performed with RetinaNet's focal loss function

and a default 80-20 split for validation. At each epoch, the entire training data stack has been augmented using various affine transformations, such as image flipping and rotation, as well as up- and down-sampling (see Figure A.20). Due to the augmentation, the effective number of training labels was (I) 173,160, (II) 112,320, (III) 422,365, (IV) 327,954, (V) 1,047 300, and (VI) 1,550,004. Training was stopped as soon as the regression of the loss stagnated after multiple learning rate reductions, i.e., as soon as the validation accuracy converged.

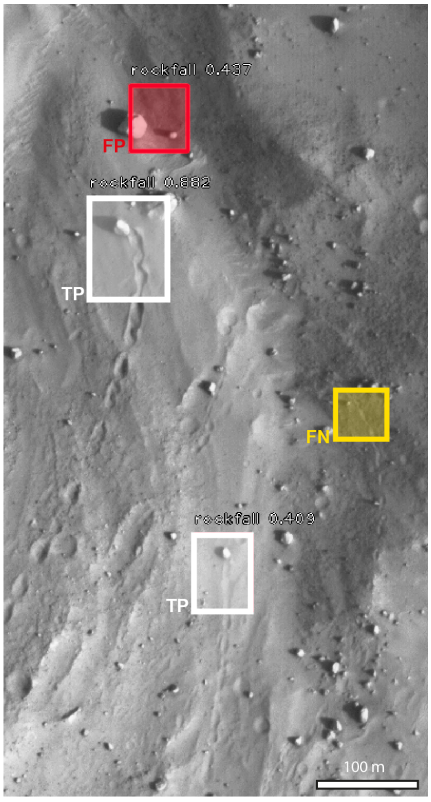


Figure 2.8: Rockfall detections using Ma/M Complex$_{50}$: One high (88.2%) and one low (40.9%) confidence TP (white boxes), one FN (yellow box), and one low confidence FP (43.7%) (red box). Note that the general potential for FPs is substantial due to the amount of morphology that mimics the feature of interest (boulder with track), like sand ripples, other aeolian features, boulders without tracks, craters, and shadows. The downslope direction is towards the top. Detail of HiRISE image ESP_036624_1720. Image credits: NASA/JPL/UofA.

We tested the performance of all six convolutional neural networks with a test set of four full-swath HiRISE images — a total of 5048 image patches — taken over different geographic and geomorphic contexts: Zunil crater, a graben near Grjota Valles, a slope of a large crater in Terra Meridiani, and a crater in Syrtis Major (Table A.4). The testing data have been labeled by an experienced human operator and testing data have not been used for training. The patches contain a total of 274 rockfalls. All testing images used have spatial resolutions ranging from 25 to 50 cm/pixel and solar incidence angles ranging from 51° to 59°. The vast majority of the used patches do not feature any rockfalls, representing a realistic testing scenario. A selection of the used patches is displayed in the Appendix (see Figure A.22) and a general example of rockfall detections is shown in Figure 2.8. For assessing the performance, we applied four different standard metrics: 1) recall (r); 2) precision (p); 3) average precision (AP); and 4) the F1 score. These metrics are calculated based on three numbers measured during testing: 1) true positives (TPs, correct detections); 2) false negatives (FNs, missed targets); and 3) false positives (FPs, wrong detections). All metrics describe different portions or aspects of CNN performance and can be used to quantify the general CNN detection behavior. Recall represents the percentage of rockfalls detected (e.g., 25/32 rockfalls have been detected). In the best case, recall would be 1, meaning that a CNN has found all rockfalls in the test set. Precision describes the percentage of rockfalls that have been detected and classified correctly (8/10 detections are correct). Precision is therefore a measure for the reliability of a CNN. AP is a metric that describes the stability of the relation between recall and precision along varying network confidence levels (here, the average of the precision at recall levels of 0 to 0.8, in 0.1 steps) and is therefore, a measure for the overall robustness of a CNN. The AP applied here is described by

$$AP = \frac{[p(r_0) + p(r_{0.1}) + \cdots + p(r_m)]}{n} \tag{2.1}$$

where index m is the maximum applicable/reached recall level (limited by the assessed networks' performance) and n is the number of the applied steps or p(r) values. The F1 score is the harmonic mean of the recall and precision and is another tool to assess the relation between the two inputs, particularly in the presence of high numbers of false negatives (FNs). We performed the entire assessment for varying network confidence thresholds (CT), i.e., the confidence of the CNN in a detection (the posterior probability output of the CNN). Usually, the application of lower CTs will result in more detections, increasing recall and decreasing precision. In turn, the application of higher confidences would result in lower recall and higher precisions. For this study, CT values ranging from 0.2 to 0.8 have been investigated. The applied intersection over union value ($IoU_{testing}$) for testing has been defined as 0.5. $IoU_{testing}$ describes the required overlap between a CNN predicted bounding box and the labeled ground truth to count a detection as a TP during testing. Where required, a standard nonmaximum suppression filter

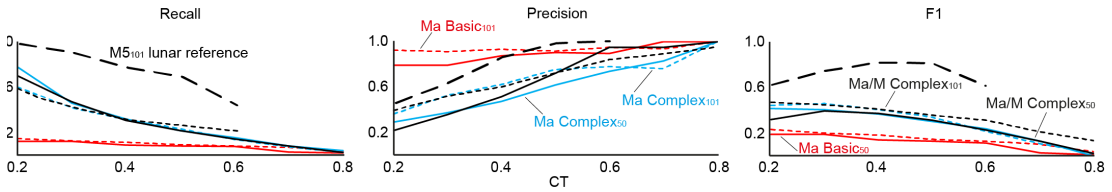


Figure 2.9: Graphical visualization of the networks' performance, from left to right: Recall, precision, and F1 score. The colors indicate the different CNNs and the dashed line represents a cross-planet reference derived with $M5_{101}$ (a lunar network) on lunar NAC data, see Bickel et al. (2018). The x-axis represents the confidence threshold (CT).

(NMS) adapted from Malisiewicz (2011) has been applied to remove double detections. We used this NMS with $IoU_{inference} = 0.3$ during inference. Depending on the application, a user might be interested in optimizing a CNN for either maximum recall (missing fewer targets, while having many FPs), for maximum precision (few mistakes, even if many targets are missed), or for a compromise between the two extremes.

II-C. Domain Generalization and Multidomain Learning

One of the main limitations of supervised learning is the access to large quantities of high-quality labels that adequately describe the feature of interest (rockfall). As lunar and Martian rockfalls share a common overall physical appearance (see Figure 2.7) and as there are large numbers of labels (8995) available from a previous study of rockfall detection on the Moon (Bickel et al., 2018), we included them for the training of two CNNs, (V) and (VI). The subtle differences in the appearance of rockfalls as well as in the radiometric properties of the images (HiRISE and NAC) could be expected to help the resulting CNNs to better generalize, potentially minimizing any present bias, e.g., related to a geomorphic setting or to label background. In addition, a better domain generalization might enable a hybrid-CNN to achieve a more robust performance (increased AP). We investigated whether the result of such a multidomain learning approach is beneficial for the detection performance of a CNN or rather reduces it.

Results

The performance of one of the CNNs (Ma/M $Complex_{50}$) is visualized for one exemplary image (see Figure 2.8), showing two TPs, one FN, and one FP. More examples of detections in more complex environments, such as dune fields, debris fields, and slopes with cross-cutting rockfall tracks, are shown in Figure A.23 and Figure A.24 in the Appendix. Average processing time per HiRISE nonmap projected image (i.e., ∼950 patches) is around 45 s using a Titan Xp. Performance of all investigated neural networks for all used confidence thresholds is summarized in Table 2.2 and visualized in Figure 2.9. Lower CTs generally produce higher recall values but lower precisions, while higher CTs generally produce lower recall values but higher precisions (as expected). The "Basic" CNNs (I) and (II) achieve very high average precisions (0.91 and 0.97) but to the cost of a significantly reduced recall. Figure 2.9 suggests that deeper networks (ResNet 101) generally produce a lower number of FPs, but to the cost of a slightly reduced recall. Interestingly, multidomain learning with Martian and lunar data appears to potentially help the CNNs (V) and (VI) to better generalize, improving the detection precision, particularly for higher CT values. However, the potentially improved generalization does not appear to improve the recall of the respective CNNs. The performance of all tested CNNs is showcased for one test patch in Figure 2.10. (bounding boxes), while Figure 2.11 and Figure A.25 report the results of the testing on full-swath HiRISE image for a graben in the Grjota Valles area and a slope in Terra Meridiani, where TPs and FPs are displayed as points. To place the performance of CNN (VI) in context, Figure 2.11 additionally shows all detections that were made by an experienced human operator.

Discussion

Testing of all trained networks demonstrates the potential of automated CNN-based mapping of Martian rockfalls (boulders with tracks) in full HiRISE swaths and on large spatial scales. The CNNs' processing speed is about 60-100 times faster than that of a human operator (for the tested images). The performance of the trained and implemented CNNs in combination with the associated processing times allow for the

Ma Basic$_{50}$					Ma Basic$_{101}$				
CT	**AP$_{50,\ n=2}$**	**REC$_{50}$**	**PRE$_{50}$**	**F1**	**CT**	**AP$_{50,\ n=2}$**	**REC$_{50}$**	**PRE$_{50}$**	**F1**
0.2	0.905	0.11	0.79	0.19	0.2	0.97	0.14	0.93	0.24
0.3	0.905	0.11	0.79	0.19	0.3	0.97	0.11	0.91	0.20
0.4	0.905	0.08	0.88	0.14	0.4	0.97	0.10	0.93	0.18
0.5	0.905	0.07	0.90	0.13	0.5	0.97	0.08	0.92	0.15
0.6	0.905	0.06	0.89	0.12	0.6	0.97	0.07	0.95	0.13
0.7	0.905	0.01	1	0.03	0.7	0.97	0.05	0.94	0.10
0.8	0.905	0.00	1	0.01	0.8	0.97	0.02	1	0.04
Ma Complex$_{50}$					Ma Complex$_{101}$				
CT	**AP$_{50,\ n=9}$**	**REC$_{50}$**	**PRE$_{50}$**	**F1**	**CT**	**AP$_{50,\ n=7}$**	**REC$_{50}$**	**PRE$_{50}$**	**F1**
0.2	0.51	0.78	0.29	0.42	0.2	0.65	0.60	0.36	0.45
0.3	0.51	0.45	0.37	0.41	0.3	0.65	0.41	0.52	0.46
0.4	0.51	0.31	0.47	0.37	0.4	0.65	0.31	0.62	0.41
0.5	0.51	0.20	0.62	0.31	0.5	0.65	0.22	0.75	0.36
0.6	0.51	0.14	0.74	0.24	0.6	0.65	0.13	0.78	0.22
0.7	0.51	0.07	0.83	0.13	0.7	0.65	0.06	0.76	0.11
0.8	0.51	0.03	1	0.05	0.8	0.65	0.01	1	0.02
Ma/M Complex$_{50}$					Ma/M Complex$_{101}$				
CT	**AP$_{50,\ n=8}$**	**REC$_{50}$**	**PRE$_{50}$**	**F1**	**CT**	**AP$_{50,\ n=7}$**	**REC$_{50}$**	**PRE$_{50}$**	**F1**
0.2	0.555	0.70	0.21	0.32	0.2	0.68	0.61	0.39	0.48
0.3	0.555	0.46	0.35	0.40	0.3	0.68	0.41	0.52	0.45
0.4	0.555	0.30	0.51	0.38	0.4	0.68	0.31	0.60	0.41
0.5	0.555	0.20	0.72	0.32	0.5	0.68	0.24	0.73	0.36
0.6	0.555	0.13	0.95	0.23	0.6	0.68	0.19	0.84	0.31
0.7	0.555	0.07	0.95	0.13	0.7	0.68	0.12	0.89	0.21
0.8	0.555	0.01	1	0.02	0.8	0.68	0.07	0.95	0.14

Table 2.2: Performance results for all trained and tested CNNs: Ma Basic$_{50}$ and Ma Basic$_{101}$ (Mars), Ma Complex$_{50}$ and Ma Complex$_{101}$ (Mars), as well as Ma/M Complex$_{50}$ and Ma/M Complex$_{101}$ (Mars and Moon); IoU is 0.5 (shown in the header as IoU$_{50}$.

utilization of the entire HiRISE image archive to rapidly and effectively scan for rockfalls on a global scale — and through newly acquired data, as MRO's mission continues. Interestingly, the utilization of "Basic" and more "Complex" rockfall labels is clearly represented in the performance (e.g., Figure 2.9). In general, the CNNs trained with more diverse — and potentially more problematic or less clear — labels achieve significantly higher recall values, but appear to be more easily confused by features that mimic rockfalls. In turn, the newly implemented utilization of labels from two different planetary bodies (domains) appears to enables the respective networks (V) and (VI) to counter the drawback of a reduced precision, as encountered by the "Complex" single-domain networks (III) and (IV). Besides the training on multidomain labels, the generally increased number of labels could have a positive impact on the overall performance as well. We will continue to systematically investigate these observations in future work to explore and exploit the potential of multiplanetary and multisensor (rockfall) detectors (multidomain learning).

The placement of feature labels, i.e., their position and size, for training and testing is a challenging problem, as rockfalls have a highly variable appearance and as the background within each bounding box is part of the label itself, although it might not represent the actual feature of interest. In order to avoid confusion with static boulders and tracks without boulders, we draw relatively large boxes to capture the entire rockfall (boulder with associated track). It has to be noted that these relatively large boxes also result in an increased background content (as shown in Figure A.20), such as small boulders, sand ripples, and other nonsignal features. In small datasets or in datasets with limited variation, this background can become dominant and can negatively influence the filter weights during training, making it harder for a CNN to identify the actual rockfall during inference (see "Basic" versus "Complex"). The potential negative influence of the increased background is very hard to quantify and remains an interesting subject for future studies with relevant applications for computer vision in general.

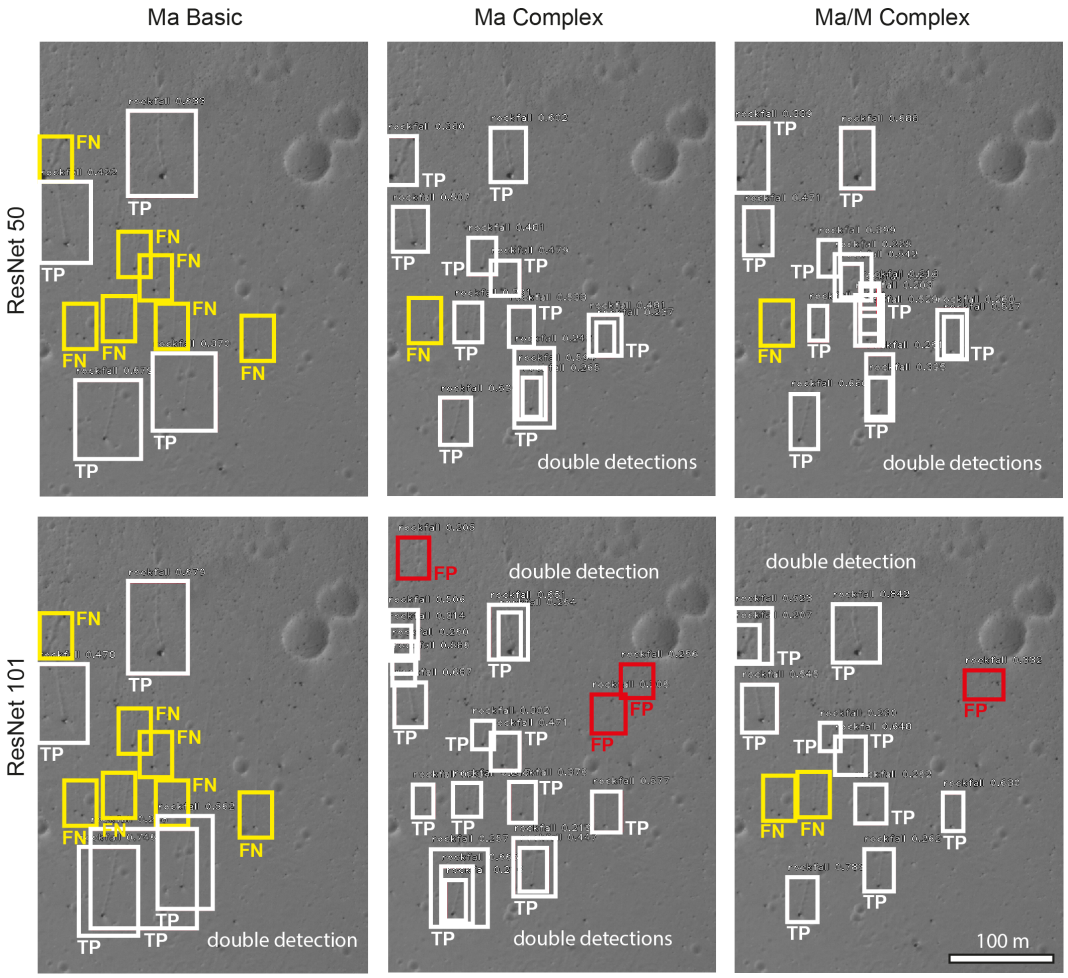


Figure 2.10: Visual, exemplary comparison of CNN performance, showing detections with CTs > 0.2. The Ma Basic networks draw larger bounding boxes and have a significantly lower recall. Detail of HiRISE image ESP_03770_1710. Image credits: NASA/JPL/UofA.

In contrast to rockfall mapping on the Moon, automated mapping on Mars is affected by the more dynamic Martian environment, particularly by its atmosphere. This is obvious from the difference in recall and precision for the lunar reference (Bickel et al., 2018) and Martian detectors (this study), highlighted by Figure 2.9. Aeolian processes deposit sand ripples and scour, occasionally in the lee of static boulders. As sand ripples tend to be rather linear features, the combination of boulder and ripple can mimic the appearance of a rockfall with track, as shown in Figure A.26. During training, we took care to include a significant number of negative "boulder and ripple" examples to sensitize the CNNs for the subtle differences in their physical appearance. The vast majority of aeolian FPs have very low confidence scores, usually lower than 0.3 (see Figure A.26), which facilitates their removal (e.g., in Figure 2.11). Occasionally, some CNNs assign higher confidence scores (∼0.4 to ∼0.6) to aeolian FPs by mistake, which is reflected in the nonperfect (i.e., <1.0) precision scores of some CNNs in the respective CT range (∼0.4 to ∼0.6). An additional limitation is created by the spatial resolution of the used HiRISE images and by the size of the target features, respectively: When GSD (ground sampling distance) and target size converge, detection and classification ambiguities are the result — affecting CNNs in a similar way to experienced human operators. These ambiguities are a fundamental problem of automated as well as human-based mapping and will always remain (although being "shifted in scale"), even if imagery with better spatial resolution becomes available in the future. In order to enhance the overall mapping performance and reliability of the trained detectors, an additional postprocessing step could be implemented using auxiliary MOLA DEM-derived slope angle maps (e.g., based on MOLA (2014) and Fergason et al. (2017)). As rockfalls are features

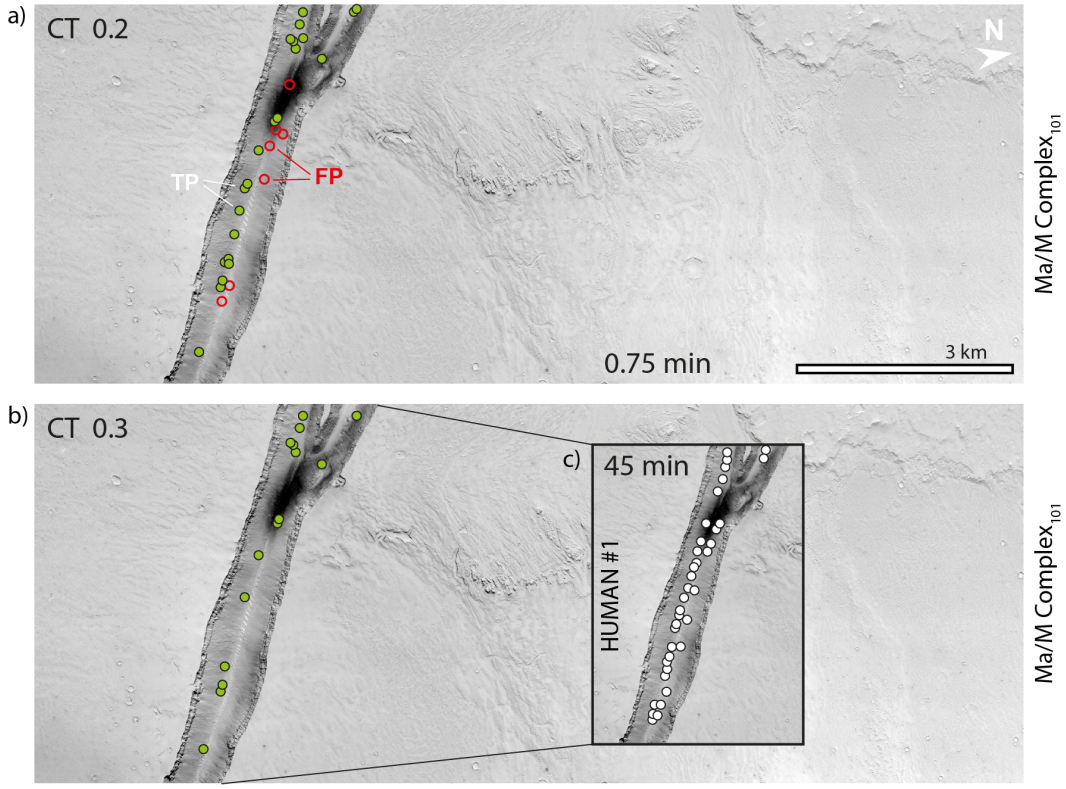


Figure 2.11: CNN-driven rockfall mapping with a full–scene HiRISE image in a graben (Grjota Valles area) by Ma/M Complex$_{101}$ with (a) CT 0.2 and (b) 0.3. Rockfalls mapped by a human operator are shown in the inset in (c) (white dots). Green dots are TPs, red indicates FPs. The increase of the CT by 0.1 effectively removes all FPs from the output, while slightly reducing the recall. The majority of FPs is related to aeolian deposits. Processing times are ∼45 min (human) versus 45 s (CNN). Note that the human processing time would be much longer if not only the graben itself would have been searched. Full HiRISE image ESP_025156_1965. Image credits: NASA/JPL/UofA.

that are usually connected to topography gradients, the slope maps could be used to discard detections in flat terrain, which are likely FPs caused by aeolian processes. However, MOLA-guided postfiltering would need to consider: 1) the spatial resolution of the underlying DEMs (200 and 463 m/pix) that could misrepresent slope conditions and angles of very small topographic features; 2) local inconsistencies in the DEMs; and 3) the user-defined cutoff slope angle (rockfall area versus non-rockfall area).

Fully automated mapping of Martian boulders with tracks, either as stand-alone process or in combination with MOLA-based postfiltering, is feasible and will produce reliable map products, depending on the selected network and CT criteria. It has to be kept in mind that the produced rockfall distribution maps might not be representative of the entire Martian rockfall population due to the limited recall (<1.0) of all CNNs. Still, their output can serve as big data foundation for statistical analyses and can directly inform and focus future mapping efforts that can perform follow up investigations in greater detail. For example, human operators could focus their attention on areas highlighted by the CNN, not scour the whole image. As the CNN-driven mapping proceeds, the neural networks will collect more and more rockfall examples (labels), which will help us to train new generations of CNNs with enhanced capabilities, increasing the value of the produced output as time passes.

As observed in a previous study (Bickel et al., 2018), the diameter of the CNN-placed bounding boxes is related to the physical diameter of the detected boulders (see Figure A.21). This relation has been quantified with the testing dataset and is plotted in Figure 2.12. This additional information further enriches the value of the produced data, as it enables, e.g., rockfall magnitude and spatial frequency analyses, which are useful to investigate the relation between rockfall abundance and proximity to tectonic

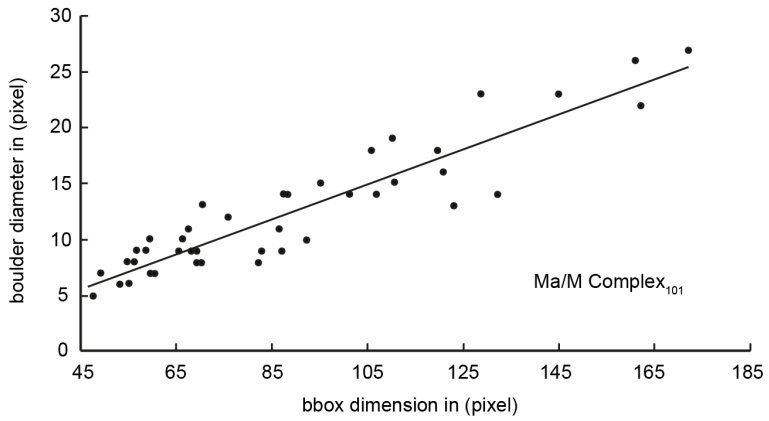


Figure 2.12: Relation of the CNN–predicted bounding box diameter in pixel (x–axis) and the respective boulder diameter in pixel (y–axis). The linear relation is highlighted with a least square fit (R2 is 0.851). This first-order approximation can be applied to estimate rockfall diameters in (meters), using the bounding box diameter in combination with the spatial resolution of the respective HiRISE image.

features, among others. It has to be noted that this relation strongly depends on the quality and consistency of the labels placed by the human operators and only represents a first-order approximation.

Conclusion

This study demonstrates the feasibility of using off-the-shelf CNNs in combination with a novel multidomain learning approach to efficiently extract new and yet unexplored information from the growing HiRISE big data stack. The trained CNNs are capable of mapping Martian rockfalls orders of magnitude faster than a human operator, and achieve inference performances that can be deployed to produce statistically relevant products.

Testing of six different CNNs showed that training data complexity and network depth directly affect the detection performance, where "Complex" CNNs achieve significantly higher recall, but slightly reduced precision values, potentially caused by the more complex label background. The application of deeper networks, such as a ResNet 101, has proven to generally benefit the average precision of all tested CNNs. The novel application of multidomain learning principles, using a combination of rockfall labels from the Moon and Mars, resulted in an apparent, further improvement of detection precision values, particularly for higher confidence scores. In summary, deep multidomain networks trained on more complex data achieved the peak overall performance in this study. Future work will elaborate on the beneficial impact of multidomain training and domain generalization, as well as on the influence of label size, shape, and background.

MOLA slope map-based postfiltering could be used to effectively remove FPs and to further improve the reliability of the CNN output for subsequent applications. The trained and tested CNNs represent a capable tool that will support the scientific community in characterizing Mars' past and current endogenic and exogenic activity, among other highly relevant research questions.

Acknowledgment

The authors would like to thank E. Law, N. Gallegos, and the Solar System Treks team at NASA JPL and NASA Ames for their support and the offer to implement this tool in Mars Trek. The authors would like to thank S. Kumar for sharing a list of HiRISE images that contain rockfalls. Data can be made available upon request to the authors. The workflow is entirely based on open source software. The developed tool will eventually be accessible online on the Mars Trek platform that is being developed by NASA JPL at Caltech, USA. This research did not receive any specific grant from funding agencies in the public, commercial, or not-for-profit sectors.

2.3 Transfer Learning for Enhanced Rockfall Mapping in Known and Unknown Planetary Domains

Submitted to the ISPRS Journal of Photogrammetry and Remote Sensing
Bickel, V.T., Mandrake, L., Doran, G., in review - might be subject to change

Abstract
Rockfalls are small–scale mass wasting events that have been observed across the solar system. They provide valuable information about the endo- and exogenic activity of their host body, but are difficult to identify and map in satellite imagery, especially on global scales and in big data sets. Past work implemented convolutional neural networks to automate rockfall mapping on the Moon and Mars with the caveat of 1) achieving sub–optimal performance and 2) requiring substantial manual image labeling efforts. Mixing image data from the Moon and Mars while keeping the total number of labels constant, we show that including a small number (10%) of rockfall labels from a foreign domain during detector training (e.g. Moon) can increase performance in another domain (e.g. Mars) by up to 6% Average Precision (AP). We additionally show that using a large number of foreign domain training examples (90%) in combination with a small number (10%) of home domain labels can be as powerful or more powerful as exclusively (100%) using home labels in the home domain. We further observe that rockfall detectors trained on multiple domains outperform single–domain trained detectors in completely unknown domains by up to 16% AP, using image data from Ceres and comet 67P. We conduct an experiment varying only image resolution on a single planetary body (Mars) to test whether the improvement was due to training on differing resolutions specifically and show that none of the improvement can be explained by this effect alone. This means that the benefits of multi–domain training mostly draw from either variations in lighting condition, differing physical appearance/backgrounds around the target of interest for generalization purposes, or both. Our findings have important applications such as ML–enabled science discovery in legacy and new planetary datasets. The used dataset of martian and lunar rockfalls including a detailed description is available here: https://doi.org/10.3389/frsen.2021.640034

Introduction

The surfaces of planetary bodies across the inner and outer solar system are shaped by a large variety of endogenic and exogenic processes, such as impact cratering, volcanic activity, and mass wasting. The spatial distribution and frequency of occurrence of the resulting morphological features is indicative of, for example, the relative or absolute ages of surfaces (Benedix et al., 2019), the evolution of the interior and exterior of a body (Needham, Kring, 2017), and the seismic and erosional activity of a planet or moon (Xiao et al., 2013), respectively.

Mass wasting processes have been observed on different planetary bodies, such as on Mars (Tesson et al., 2020), Earth's Moon (Xiao et al., 2013), Mercury (Wright et al., 2020), Venus (Malin, 1992), comet 67P (Lucchetti et al., 2019), dwarf planet Ceres (Duarte et al., 2019), and asteroid Vesta (Otto et al., 2013), among others. Some mass wasting processes appear to be unique to a specific body, for example martian Recurring Slope Lineae (RSL) (Dundas et al., 2017) and martian polar ice avalanches (Russell et al., 2008), but other processes occur on numerous bodies, such as rockfalls (Xiao et al., 2013; Tesson et al., 2020). The term rockfall describes a process where meter–sized blocks of rock detach from a topographic high and rapidly roll, bounce, and slide to a topographic low, usually leaving behind a distinct track (Figure 2.13) (Hungr et al., 2014). The characteristic combination of deposited block and track (referred to as 'rockfall' throughout this work) is proof of the dynamic displacement and allows for an unambiguous detection of rockfall events in satellite imagery (Bickel et al., 2018). Besides providing physical evidence of the influence of solar insulation on rock breakdown (Tesson et al., 2020) and potentially indicating seismically active regions and their geographic shift over time (Bickel et al., 2020a), rockfalls allow for the remote analysis of the geomechanical properties of a surface, directly informing future exploration efforts (Hovland, Mitchell, 1973; Bickel et al., 2019; Sargeant et al., 2020; Bickel, Kring, 2020).

The identification and mapping of rockfalls in planetary satellite imagery is challenging, however, and requires a large amount of time and diligence. Previous studies have shown how the procedure of mapping rockfalls on the Moon and on Mars can be automated using convolutional neural network–based object detectors (Bickel et al., 2018, 2020b), resulting in a first global map of more than 136,000 lunar rockfalls

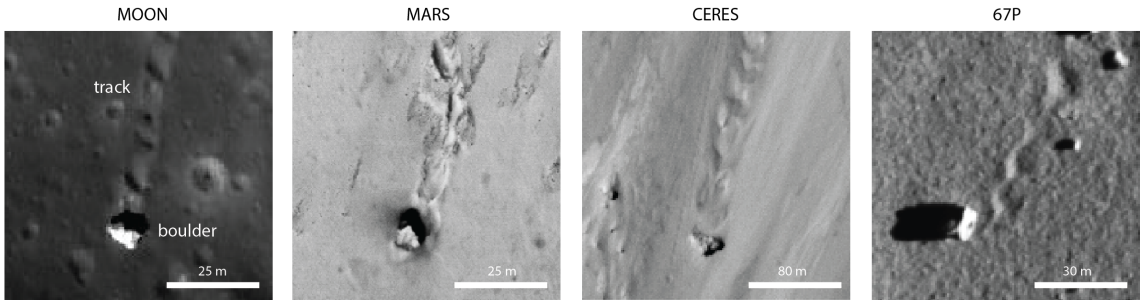


Figure 2.13: Examples of rockfalls (boulder and track) from the Moon (NAC), Mars (HiRISE), Ceres (FC), and comet 67P (OSIRIS) showcasing similarities and differences in physical appearance; details of M138107059LC, ESP_039901_1665, FC11B0005064_18168115057F1G, and N20160605T150621617ID30F22.

(Bickel et al., 2020a). However, the same studies also outlined the difficulties and limitations of automated rockfall mapping, such as missed or incorrect detections that bias all subsequent analyses. These studies also showed that thousands of labels are required to train rockfall detectors with a sufficient level of performance and robustness, requiring months of labelling work. Previous work found some indication that transfer learning, i.e. training of detectors on multi–planetary (or multi–domain) datasets (e.g. Moon and Mars), potentially helps to improve the performance of rockfall detectors (Bickel et al., 2020b), an observation we seek to address systematically in this work. The potential benefits of multi–domain learning are not unique to planetary science and are being studied in different contexts. For example, Wang et al. (2019) show that one single (universal) detector that is trained on 11 different domains that contain a variety of natural images, such as VOC (objects like bicycles, cars, etc.), COCO (animals and common objects), and KITTI (street scenes), is competitive with single–domain detectors trained specifically for each of those individual domains. Prakash et al. (2021) show that terrestrial landslide detectors trained on multiple different geomorphic regions achieve better detection performance in unknown regions than detectors which have been trained on fewer regions. One objective of this study is to investigate whether these findings are applicable to the planetary science use case as well, given differences in data type, volume, quality, as well as the physical appearance of the objects studied.

This work seeks to answer four main scientific questions: (1) does multi–domain training help to improve the performance of object (rockfall) detectors in a planetary science context?; (2) can we substitute the majority of labels from a domain of interest with labels from a foreign domain while maintaining detector performance in the domain of interest?; (3) are multi–domain detectors more suited for application in completely unknown domains?; and (4) what aspect of domain mixing is driving the observed improvement? The first three research questions are of an applied nature and directly inform a series of immediate actions such as building detectors that improve our ability to perform science discovery in legacy datasets and in new image datasets and pipelines (in unknown domains, i.e., future missions), among other applications. The fourth research question is of a theoretical nature and aims to advance our general understanding of how training data heterogeneity and mixing influence the performance of object detectors — a problem that is not unique to the planetary sciences, but fundamental to computer vision, with potential applications across a large number of fields. In this work the term ‘domain’ describes a satellite image observation dataset that is characterized by three domain parameters: a) the physical nature and appearance of the planetary body photographed (geomorphology), b) the illumination characteristics, and c) the range of scale and spatial resolution, as controlled by a spacecraft’s orbit, instrument (camera) properties, and other factors. Throughout this paper, four domains appear: the Moon domain (M), the Mars domain (Ma), the comet 67P domain (67P), and the dwarf planet Ceres domain (C). Depending on the experiment performed, domains are either “known” — domains that have been used to train a specific detector — or “unknown” — domains that have not been used to train a specific detector. The total number of labels used has been equal for all experiments.

For the applied research questions (1) through (3) the original (full) spectrum of domain parameter variability has been used, i.e., the complete range of illumination conditions (described by the solar incidence and phase angle), and spatial resolutions present in the respective labelled datasets. The intention is to keep the parameters and scope of the experiments as close as possible to a real world application — where datasets from different domains can be heterogeneous — as the derived insights are intended to directly

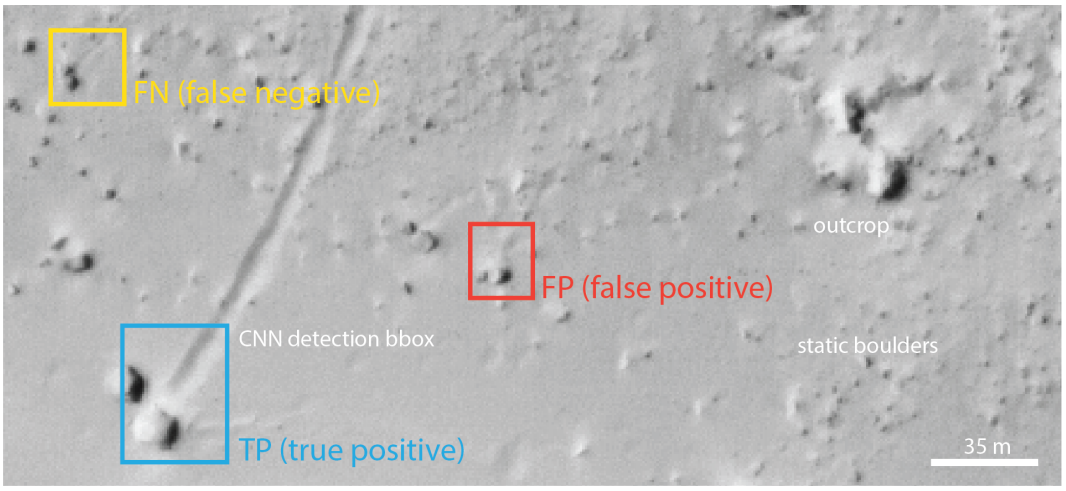


Figure 2.14: Example detections (bounding boxes) made by a CNN on a martian test image. The blue box denotes a True Positive (TP, correct detection), the yellow box denotes a False Negative (FN, missed detection), and the red box denotes a False Positive (FP, false detection). This example also visualizes the challenge of labeling a detection as TP, FN, or FP, particularly for small rockfalls and in the presence of a complex background (static boulders, outcrops, etc.), as discussed in the Dataset section and the discussion.

inform even such applications. For research question (4) we limited the analysis to one single planetary domain, Mars, which effectively eliminates any influence from mixing different planetary geomorphologies and illumination conditions. By only varying the distribution of spatial resolutions in this dataset we tried to understand whether detector performance improvements are caused by multi–domain or multi–scale effects. A summary of the dominant parameters of the four domains is showcased in Table 2.3. The section Sensors and Data features descriptions and details about the instruments and image data used for the different domains, the section Methods describes the various methods applied, and the section Results showcases the results of this study, which are then discussed and summarized.

Sensors and Data

We used data from four different spacecraft instruments, the Lunar Reconnaissance Orbiter's Narrow Angle Camera (NAC), the Mars Reconnaissance Orbiter's High Resolution Imaging Science Experiment (HiRISE), Dawn's Framing Camera (FC), and Rosetta's Optical, Spectroscopic, and Infrared Remote Sensing System (OSIRIS). The following subsections briefly introduce the instruments as well as their data products, as used for this study.

Domain M - Lunar Reconnaissance Orbiter NAC
The LRO NAC consists of two nominally identical line–scan CCD cameras and takes single–channel, optical images in the range between 400 and 750 nm (Robinson et al., 2010). During LRO's mission, NAC has taken more than 2 million images of the lunar surface. The spatial resolution of the NAC imagery used for this study ranges from 0.46 to 2.13 m/pixel. All images are calibrated, 8bit .tif (PTIF) files. NAC images

	M	**Ma**	**67P**	**C**
Body	Moon	Mars	67P	Ceres
Type	moon	planet	comet	dwarf planet
Sensor	NAC	HiRISE	OSIRIS	FC
Res. (m/pix)	0.46-2.13	0.26-0.59	0.17-0.49	2.74-3.17
Sun sync.	no	yes	no	no

Table 2.3: Summary of dominant domain characteristics as used for this study. A spacecraft in a sun-synchronous (polar) orbit always passes over a given geographic location at the same mean local time.

have been downloaded from: http://wms.lroc.asu.edu/lroc/search.

Domain Ma - Mars Reconnaissance Orbiter HiRISE
HiRISE is a pushbroom sensor that is using 14 CCDs to take three–channel images, where only the red channel (550 to 850 nm) covers the full width of each image (McEwen et al., 2007). As of October 2020 HiRISE has taken more than 67,000 images, covering roughly 3.7% of Mars' surface. The spatial resolution of the used HiRISE imagery ranges from 0.26 to 0.59 m/pixel. All images are calibrated, red–channel .jp2 (JPEG2000) files that have been reduced to 8 bit. HiRISE images have been downloaded from: https://www.uahirise.org/.

Domain 67P - Rosetta OSIRIS
The OSIRIS NAC — here called OSIRIS — consists of a single CCD camera that takes images using 11 filters, covering the range from 250 to 1000 nm (Tubiana et al., 2015). During the Rosetta mission, OSIRIS has taken more than 38,000 images covering comet 67P multiple times over and from a variety of distances. The spatial resolution of the used OSIRIS imagery ranges from 0.17 to 0.49 m/pixel. All images are calibrated .IMG files that have been reduced to 8 bit. OSIRIS images have been downloaded from: https://rosetta-osiris.eu/.

Domain C - Dawn FC
Dawn's FC consists of two nominally identical cameras that take images using one clear and seven band–pass filters in the range from 400 to 1050 nm (Sierks et al., 2011). FC has taken more than 70,000 images of Ceres during the Dawn mission, covering some parts of Ceres' surface in great detail. The spatial resolution of the FC imagery used for this study ranges from 2.74 to 3.17 m/pixel. All images are calibrated .IMG files that have been reduced to 8 bit. FC images have been downloaded from: https://sbib.psi.edu/data/PDS-Ceres/pds-ceres.html.

Datasets
The dataset used for this study is publicly available (RMaM–2020) (Bickel et al., 2021c) and consists of a total of 2822 rockfall labels taken from a total of 153 satellite images. RMaM-2020 has been created applying the identical methodology as demonstrated in previous work (Bickel et al., 2018, 2020b), i.e. by labelling the characteristic combination of displaced boulder and the associated track, to guarantee instance uniqueness (e.g. static boulder vs. rockfall). Here, each label describes a localization of a rockfall in a satellite image with a rectangular bounding box. Due to the environmental conditions on Mars and the resulting, complex geomorphological features, such as dunes, sand ripples, etc., the martian data is generally considered to be more complex than the lunar data, both regarding the feature of interest as well as the background. The labels have been tailor–made for a Python, Keras, and TensorFlow implementation of RetinaNet (csv-type input), but can be adapted to work for any object detection architecture. A more detailed description and the dataset itself can be accessed here (Bickel et al., 2021c): https://edmond.mpdl.mpg.de/imeji/collection/DowTY91csU3jv9S2.

Training datasets
RMaM-2020 consists of two equally–sized training datasets, one for the Moon and one for Mars. Both contain 1,000 positive rockfall labels and 300 negative tiles without any rockfalls that can be used to further stimulate detector training (Bickel et al., 2021c). We used the full stack of training labels and kept the total number of labels equal for all experiments.

Testing datasets
RMaM–2020 further contains two testing datasets, a lunar set with 83 positive labels and 17 negative tiles, and a martian set with 91 positive labels and 31 negative tiles. These two testing sets have been complemented with two additional sets that represent unknown domains, one for dwarf–planet Ceres (28 positive labels, 28 negative tiles) and one for comet 67P (2 positive labels, 14 negative tiles), taken from 47 satellite images. Due to the extremely small number of positive testing labels available for comet 67P, we used this domain only for a qualitative analysis of detector performance.

Methods

The object detector (single–stage) architecture used for this work is RetinaNet implemented in Python, Keras, and TensorFlow (Keras RetinaNet by Fizyr: https://github.com/fizyr/keras-retinanet) (Lin

et al., 2018). On the one hand, we choose RetinaNet for this study as it is well–established, fast, achieves high localization and classification accuracies (Lin et al., 2018; Douillard, 2018; Singh, 2019; Weinstein et al., 2019). On the other hand, RetinaNet has been successfully applied to lunar and martian image data before (Bickel et al., 2018, 2020a,b; Nagle-McNaughton et al., 2020), i.e., represents the current state–of–the–art of planetary rockfall detection. In addition, Bickel et al. (2020b) found suggestive evidence that multi–domain training could potentially benefit detector performance using RetinaNet — this means that using RetinaNet for this study also allows for a direct comparison with previously published results. We ran RetinaNet on a desktop computer equipped with a Nvidia GeForce Titan Xp.

Detector training
All detectors have been trained with the identical setup and total number of labels to allow for a direct comparison of their performance (using a focal loss function and an 80–20 training–validation split). Training consisted of 50 epochs where each epoch represents one full loop through the entire training data stack, i.e., 1,000 positive labels and 300 negative tiles. After each epoch, the full data stack has been augmented using image flips, rotation, up- and down–sampling, as well as mild brightness and contrast adaptation operations, resulting in a total of 65,000 augmented labels used for training of each detector. We chose to stop training after 50 epochs as initial observations showed that the regression of the loss stagnated slightly earlier (after multiple reductions of the learning rate). We trained a total of 8 detectors (see Table 2.4), where the initials indicate the mix of domains (Ma and M), the subsequent number indicates the contribution (percentage) of the particular domain on the overall set (100, 90, 50, and 10), and the last number (if applicable) indicates the percentage of labels that have been down–sampled (d). The detectors are: M100, Ma100, Ma90M10, Ma50M50, Ma10M90 (all used for research questions (1-3)), and Ma100_10_{d}, Ma100_50_{d}, and Ma100_90_{d} (used for research question (4)). Table 2.4 showcases a summary of all trained detectors.

The detectors for research question (4) have been trained with partially down–sampled data. Down–sampling has been performed by a factor of 2 using a bilinear interpolation. Including the down–sampled data, the range of spatial resolutions of the modified RMaM–2020 HiRISE training set is 0.26 to 1.18 m/pixel (instead of the original 0.26 to 0.59 m/pixel). We decided to down–sample RMaM-2020 labels instead of replacing RMaM–2020 labels with new, lower–resolution labels in order to isolate the contribution of multiple scales to the overall detector performance — if completely new, low–resolution labels are added, there would be an incalculable contribution from the other dominant domain parameters, such as the illumination and the physical appearance of rockfalls, weakening the insights derived from the experiment.

Detector testing
We count the True Positives (TP, correct detections), True Negatives (TN, missed detections), and False Positives (FP, incorrect detections) derived by a detector in the targeted testset and use them to calculate the detector's recall (sensitivity) and precision (positive predictive value). Recall describes the amount of targets (%) that have been found by the detector in the testset and precision describes the amount (%) of detections that are correct. We then derive the Area–under–the–curve (AUC) of the precision–recall curve for a pre–defined score–threshold range. The AUC is also called Average Precision (AP) and is a common metric in computer vision (Lin et al., 2018, 2017; Ren et al., 2015). A perfect detector would achieve an AP score of 1.0 (100% precision and 100% recall). We consider AP to be the most representative metric as it conveys information about the detectors recall, precision, and confidence distributions in one single

Detector	Question	Domain composition
M100	(1-3)	100% Moon (benchmark)
Ma100	(1-3)	100% Mars (benchmark)
Ma90M10	(1-3)	90% Mars 10% Moon
Ma50M50	(1-3)	50% Mars 50% Moon
Ma10M90	(1-3)	10% Mars 90% Moon
Ma100_10_{d}	(4)	100% Mars 10% down-sampled
Ma100_50_{d}	(4)	100% Mars 50% down-sampled
Ma100_90_{d}	(4)	100% Mars 90% down-sampled

Table 2.4: Summary of all rockfall detectors trained for this study and which research questions addressed by each detector.

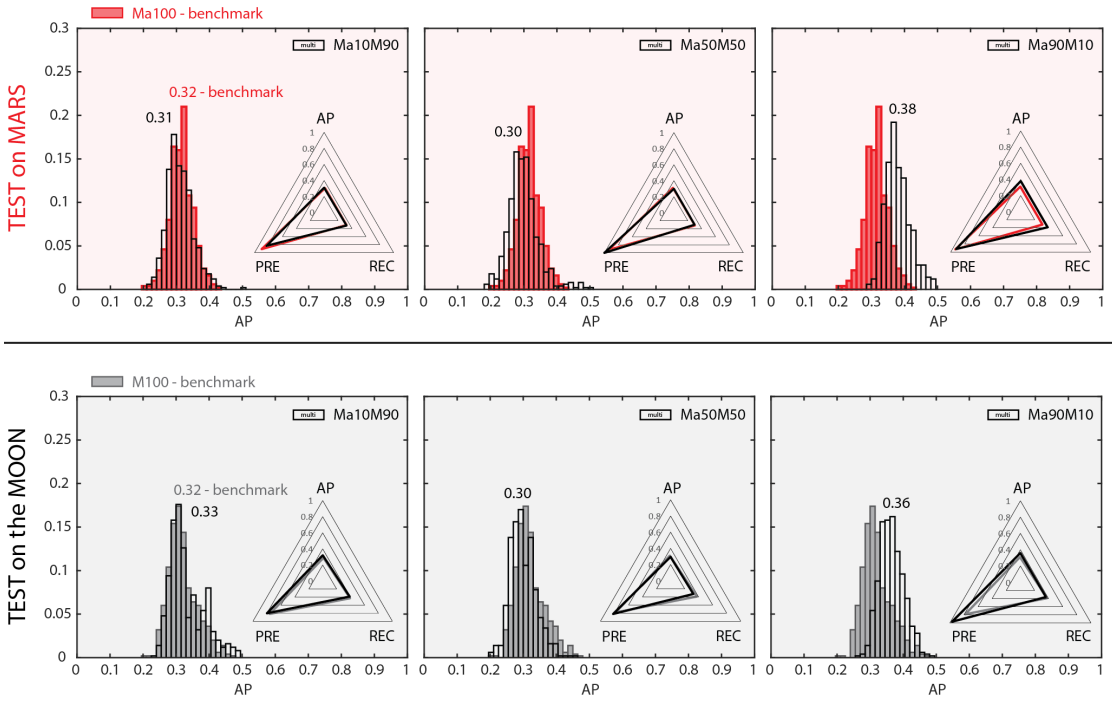


Figure 2.15: Results for research question (1); histograms show the AP score distribution while web plots show the mean AP, recall (REC), and precision (PRE) values. Multi–domain detectors achieve the same or better performance (AP score) than single–domain detectors (benchmarks) on Mars and the Moon. On Mars, the improvement seems to be controlled by a recall boost (Ma90M10) while on the Moon it appears to be controlled by a precision boost (Ma90M10).

number and thus facilitates the evaluation and comparison of the numerous different experiments. Still, we record recall and precision and include both metrics in the analysis as well.

In order to derive an estimate of the AP, recall, and precision score distribution and variance of each detector we apply a bootstrapping approach by randomly drawing 90% of the tiles from the full test set, running the evaluation, storing the respective scores, and then repeating the procedure 500 times. We use RetinaNet's built in evaluation functions with a couple of minor modifications, such as a custom Non–Maximum–Suppression filter (NMS) to remove double–detections (Malisiewicz, 2011). Evaluation uses an Intersection–over–Union (IoU) value of 0.3 and a score–threshold of 0.6. The IoU value describes the spatial overlap of a predicted bounding box with its respective ground truth bounding box: If a predicted box overlaps more than 30% with a ground truth box it is counted as a TP, otherwise it is counted as a FP. The score–threshold denotes the minimum confidence (the posterior probability output of the detector) that a detection must have in order to be used for the evaluation: We only use detections with a confidence score of 60% or higher. The relatively high score–threshold helps to remove detections with low scores that otherwise would have skewed the calculation of the AP: We observe that with decreasing score, the number of detections rapidly increase, overwhelming the fewer high–score detections and negatively affecting the precision–recall curve. Bootstrapping testing has been performed for the Moon, Mars, and Ceres test sets, but not for the comet 67P test set. Due to the extremely low number of positive rockfall labels available for 67P, any systematic testing would not be very expressive. Instead, we use the comet test data to qualitatively test if the different detectors are able to pick up the two cometary rockfalls. One selected example for rockfall detections are shown in Figure 2.14.

First, we investigate whether multi–domain detectors (Ma90M10, Ma50M50, Ma10M90) outperform the martian benchmark (Ma100) in the Mars as well as the lunar benchmark (M100) in the Moon testsets (question (1)). On Mars, we refer to Ma100 as the local martian benchmark; on the Moon, we refer to M100 as the local lunar benchmark. For the second experiment (question (2)) we investigate whether multi–domain detectors trained with a majority of labels (90%) from a foreign domain can achieve the same performance

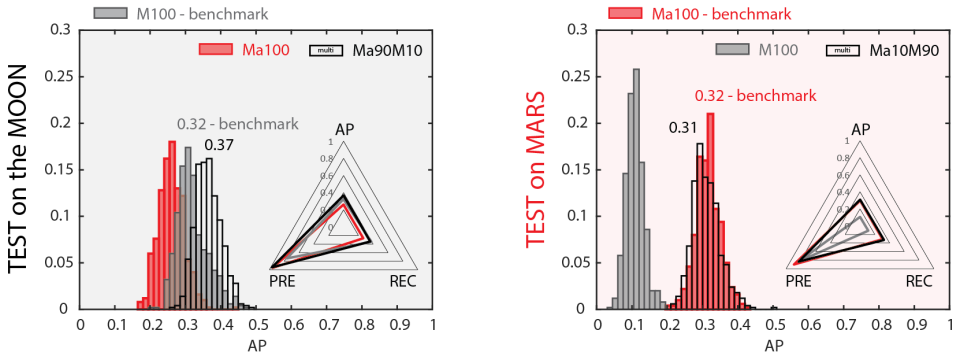


Figure 2.16: Results for research question (2); histograms show the AP score distribution while web plots show the mean AP, recall (REC), and precision (PRE) values. Using mainly foreign domain examples in combination with a small number (10%) of home domain labels can be as powerful or more powerful as exclusively (100%) using home labels in the home domain. The foreign benchmarks are shown in both plots as well (Ma100 on the Moon and M100 on Mars) to illustrate the benefit of domain mixing.

as the local benchmarks (Ma90M10 tested on the Moon and Ma10M90 tested on Mars). Subsequently, we test whether multi–domain detectors (Ma90M10, Ma50M50, Ma10M90) perform better in completely unknown domains, i.e. in the Ceres (quantitatively) and 67P test set (qualitatively)(question (3)). Finally, we investigate the influence of using multiple scales during training on the detector performance by comparing the results of detectors (partially) trained with down–sampled data (Ma100_10_d, Ma100_50_d, Ma100_90_d) and the local benchmark (Ma100) as well as all multi–domain detectors (Ma90M10, Ma50M50, Ma10M90).

Results

All results are reported under their respective research question number.

(1) Multi–domain training improves performance
In order to address research question (1) we compare the performance (AP score variance and mean) of all multi–domain detectors with the performance of the local single–domain benchmarks, i.e., with M100 on the Moon and with Ma100 on Mars. The results of these experiments are summarized in Figure 2.15. We find that the performance of four out of six multi–domain detectors is equal to the performance of the local benchmark. Interestingly, we also find that two of the six multi–domain detectors perform better than the local benchmarks, by approximately 6% AP on Mars and by 4% AP on the Moon. On both Mars and the Moon the most successful detector is Ma90M10, which potentially indicates that rockfall detection on the Moon benefits from many (90%) more complex martian examples while, in contrast, rockfall detection on Mars benefits from a few less complex (10%) lunar examples. On Mars, the performance improvement of Ma90M10 seems to be driven by a recall boost while on the Moon it appears to be controlled by a precision boost.

(2) Transfer learning is possible
We compare the performance of multi–domain detectors that have been trained with a dominant fraction of foreign domain (90% foreign domain) labels with the performance of local benchmark detectors in their respective home domains. The predominantly lunar data–trained multi–domain detector (Ma10M90) produces the equal AP score distribution and mean as the local martian benchmark when applied to the Mars test data, indicating that the knowledge transfer from lunar to martian rockfalls works well, if infused with 10% martian labels. Interestingly, the purely lunar trained detector (M100) achieves a significantly poorer performance in the Mars test set, highlighting the importance of the small amount of martian data involved in the training of Ma10M90. In the Moon test set, the predominantly martian data–trained Ma90M10 exceeds the performance of the local benchmark by 5% AP, indicating that knowledge transfer works both ways. Similar to research question (1), it appears that going from a more complex to a less complex domain helps to boost the performance — or is simply more effective at boosting the performance. The purely martian data–trained detector Ma100 does not match the performance of the local lunar benchmark, but

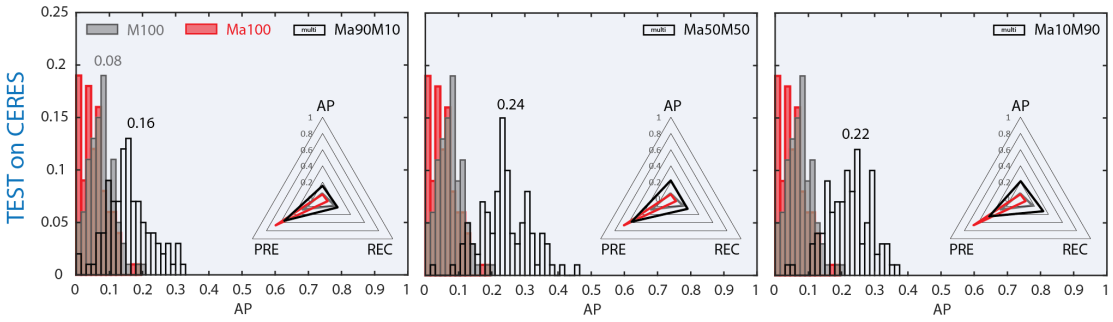


Figure 2.17: Results for research question (3); histograms show the AP score distribution while web plots show the mean AP, recall (REC), and precision (PRE) values. Multi–domain detectors achieve significantly better AP scores in the unknown Ceres domain. The improvements seem to draw mostly from a recall boost.

comes relatively close, supporting the argument about the shift in complexity mentioned above. The test results are shown in Figure 2.16.

(3) Multi–domain detectors work best in terra incognita
We investigate the performance of all single- and multi–domain detectors in two completely unknown domains (Ceres and the comet 67P), directly probing the generalization of the different detectors. Figure 2.17 showcases the results of these experiments. In the Ceres test set, we observe a significantly enhanced detection performance of all three multi–domain detectors, for example, Ma50M50 exceeds both single–domain detectors by up to 16% AP. This observation potentially indicates that the utilization of more diverse training data (from two domains instead of one) helps the detector to generalize, in turn improving its performance in a completely unknown environment. This is supported by the fact that the performance improvements seem to draw mostly from a recall boost. Interestingly, the variance of the multi–domain detector AP score distribution is larger than for the single–domain detectors, which could be indicative of the increased sensitivity of the multi–domain detectors. Figure 2.18 and Figure 2.19 showcase the performance of a few selected detectors in the Ceres and 67P testsets, reflecting the trends observed in the quantitative analysis.

(4) Multi–scale alone does not benefit the performance
We conduct an experiment on a single planetary body (Mars) to test whether the improvement in detector performance is related to the difference in scale (spatial resolution) of the lunar and martian training sets specifically (0.46 to 2.13 vs. 0.26 to 0.59 m/pixel, respectively). The results of this experiment are shown in Figure 2.20, where an increase in the number of downsampled labels used for training directly and consistently decreases the performance of the respective detector. This indicates that, in the Mars testset, a wider range of scales does not only not contribute to a performance increase, but actually is counter–productive. This observation also indicates that the benefits of multi–domain learning instead draw from either variations in the physical appearance of the features of interest or the background, variations in illumination conditions, or both. The degradation of the detector performance seems to be mainly controlled by a reduced recall.

Discussion

The conducted experiments result in four main findings: (1) multi–domain learning appears to improve the performance of rockfall detectors, (2) knowledge transfer across planetary domains is possible and effective for the rockfall case, (3) multi–domain rockfall detectors generalize better and thus perform better in terra incognita, and (4) the scale aspect of multi–domain training by itself appears to not benefit the performance of rockfall detectors. We observe that performance is particularly (or more effectively) improved when labels from the martian domain are applied to the lunar domain (see Figure 2.15 and Figure 2.16). Due to the absence of an atmosphere, the lunar surface environment is presumably less complex than the rather heterogeneous martian surface that is continuously shaped by winds and dust storms. Earlier work experienced that rockfall detection on Mars is generally more challenging (Bickel et al., 2020b), mainly due to the presence of aeolian features, such as sand ripples, that mimic the physical

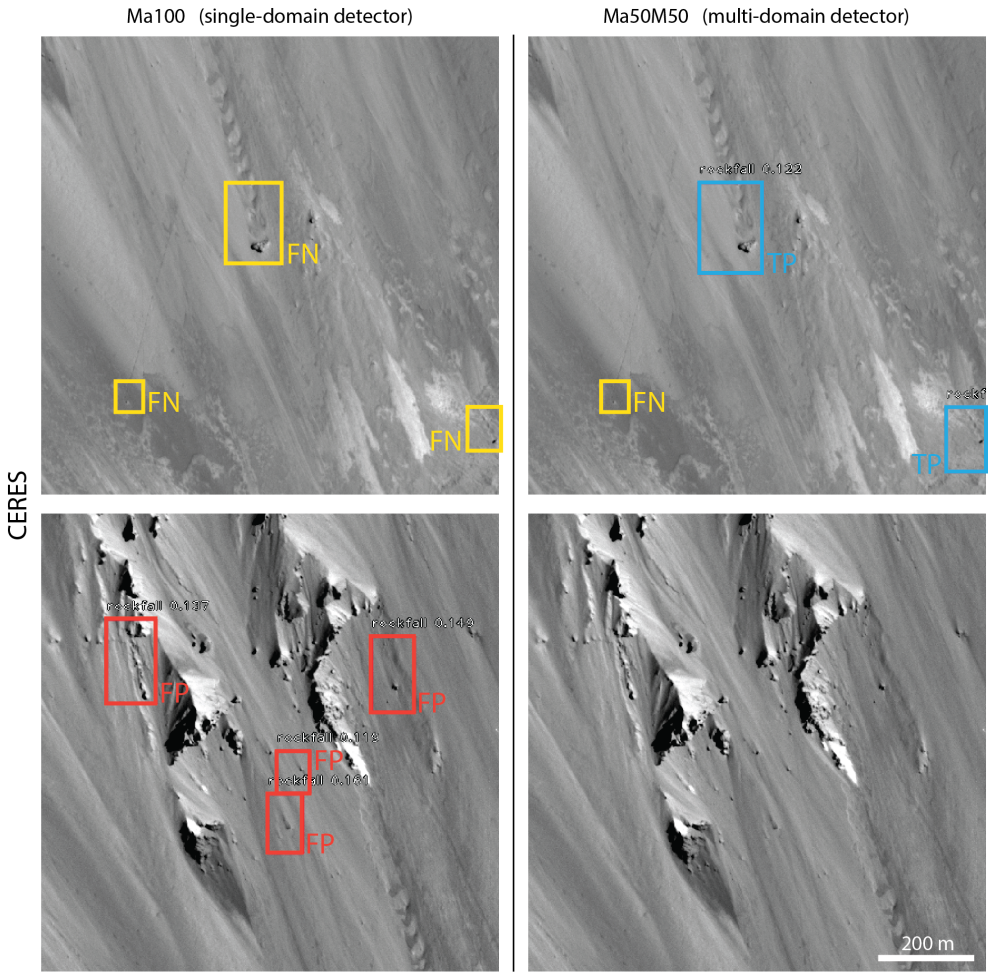


Figure 2.18: Example detections in the Ceres testset, research question (3); all multi–domain detectors (here: Ma50M50) achieve improved recall and precision values (more TPs and fewer FPs).

appearance of rockfall tracks, causing larger numbers of false positives. Here, potentially, the inclusion of the more complex, more challenging martian training data, including negative examples of aeolian features (background), enables a lunar–martian hybrid detector to better generalize and thus to improve its overall mean AP value. Interestingly, the martian–data only detector does not perform so well on the less complex lunar testset; apparently, a few local examples are required (here: 10%) to help the detector get familiar with the local, lunar rockfall features and geomorphology (Figure 2.16).

The domain transfer works in both directions: Our results on Mars show that including a small portion of less complex, lunar labels (here: 10%) helps to boost detector performance on Mars as well (see Figure 2.15). It seems that a certain amount of less complex labels has a positive impact, potentially because it forces the detector to generalize to a wider range of features.

Using a majority (90%) of lunar training data and including only 10% martian data enables a lunar–martian hybrid to achieve benchmark performance on Mars, while a purely lunar trained detector does not (see Figure 2.16). This potentially indicates that a small portion of martian labels (and negatives) are sufficient to inform the hybrid detector about the local challenges on Mars, such as aeolian features, resulting in a significantly improved performance compared to purely lunar–trained detector. In turn, using a majority (90%) of martian labels and adding only 10% lunar labels enables the resulting hybrid detector to outperform the lunar benchmark on the Moon, while the purely martian trained detector cannot compete. This again indicates the benefit of adding more complex (martian) labels, while underlining the need for a small amount of local labels (here: lunar).

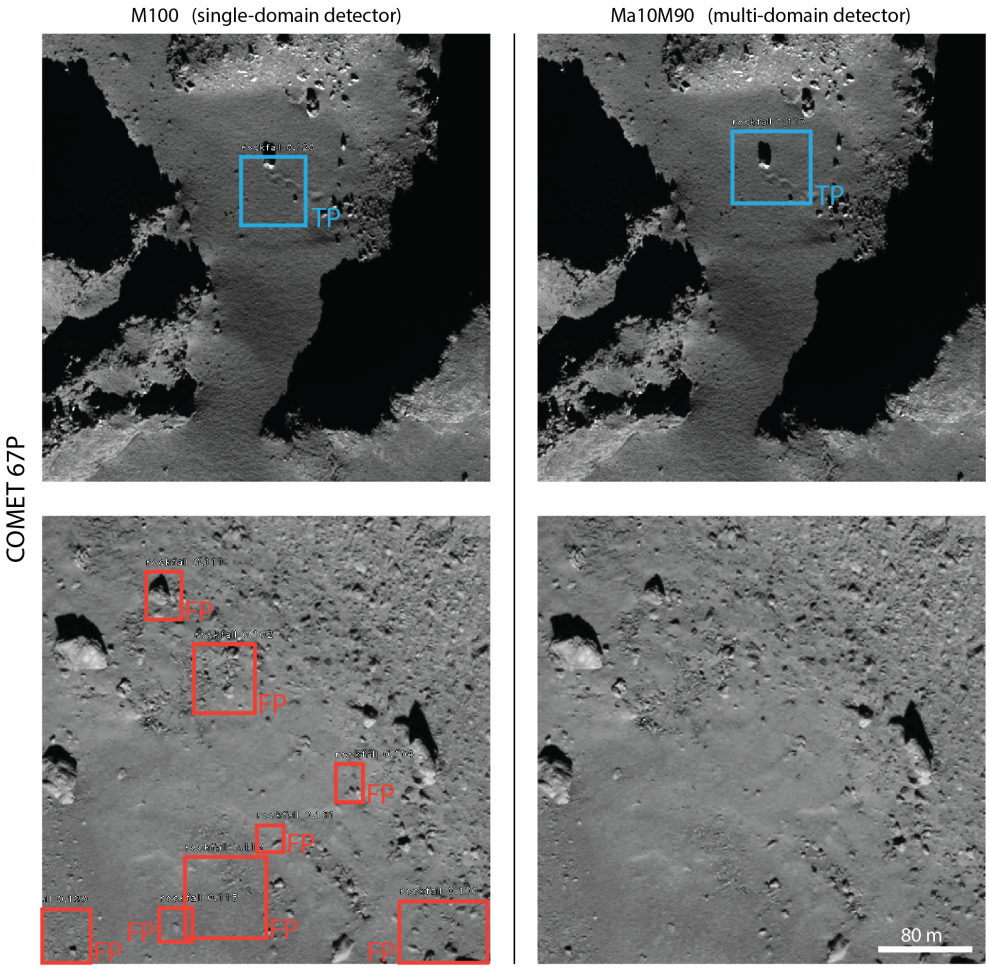


Figure 2.19: Example detections in the comet 67P testset, research question (3); all multi–domain detectors (here: Ma10M90) achieve improved recall and precision values (in this example fewer FPs, specifically).

The experiments with the Ceres testset highlight the superior performance of multi–domain detectors in unknown domains, where every multi–domain detector outperforms all single–domain detectors. Notably, the 50:50 and 10:90 martian–lunar hybrids perform best, potentially indicating that the cererian environment (or background) is less complex than the martian environment, while being slightly more complex than the lunar environment. Ceres has no atmosphere and thus no aeolian features, but does have a very active surface geology, driven by endo- and exogenic processes (Raymond et al., 2020), that causes an abundance of various mass wasting features as well as surface cracks — this might help explain the above observation. Curiously, the AP variance of all multi–domain detectors is larger in the Ceres test set, which could indicate that the detectors are generally more sensitive, i.e., might produce a larger number of true positives (or a smaller number of false negatives), but at the same time a larger number of false positives.

We note that the optimal mixture of domains for a multi–domain detector is likely directly controlled by the environmental conditions and geomorphic complexity of the target body; if known, these conditions could be used to inform the compilation (mixing) of the training data used for detector training. For example, for a terrestrial, airless, rocky planet like Mercury, the predominant fraction of labels could come from the Moon, while for an active, atmospheric moon as Titan, the majority of labels could come from Mars. Figure A.27, Figure A.28, and Figure A.29 in the appendix showcase similarities and differences of the martian, lunar, and cererian domains.

Experiment (4) indicates that the contribution of scale variations to the overall detector performance is

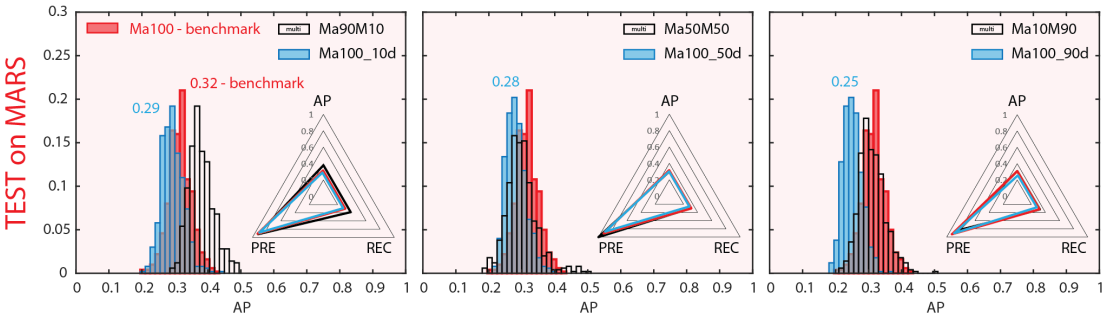


Figure 2.20: Results for research question (4); histograms show the AP score distribution while web plots show the mean AP, recall (REC), and precision (PRE) values. A higher percentage of down–sampled labels decreases detector performance, i.e., a larger range of scales appears to have a negative effect on the detector performance in the Mars test set. The degradation of performance seems to be mainly controlled by a reduced recall. All multi–domain detectors are shown as comparison.

not only insignificant, but also disadvantageous, at least for the rockfall case on Mars. The range of spatial resolutions in the partially downsampled martian training set is 0.26 to 1.18 instead of the original 0.26 to 0.59 m/pixel, while the range of spatial resolutions in the martian testing set is constant at 0.25 to 0.5 m/pixel. In comparison, the range in the lunar training set is 0.46 to 2.13 m/pixel, i.e. it overlaps with the original and the modified martian training set resolution range, while having a larger upper limit. However, the downsampled martian labels have a negative impact on the performance, while the lunar labels have a positive effect (Figure 2.15, Figure 2.16, Figure 2.20), despite the fact that the modified, downsampled martian resolution range is closer to the range of the test set. This observation suggests that scale alone is not the main driver of the performance improvement of multi–domain detectors, but presumably the difference in the physical appearance of the target features (and background), the lighting conditions, or both. Due to the limitations of the available data, it is difficult to further disentangle the contributions of these two different domain aspects to the overall performance improvement, however.

Our four main results have a series of use cases. The finding that training on multiple domains can help to improve the performance of a detector in a planetary science context has impact for several direct applications.

Known Domain Exploration: On the one hand, for the planetary dataset exploration use–case (science discovery), a 6% AP improvement in performance could translate into an improvement of finding ∼6% more science targets (improved recall), making ∼6% fewer false detections (improved precision) requiring a scientist to study fewer candidates, or a combination of both. For example, given 1 to 5 minutes per candidate examination time by an expert, a hypothetical ∼6% increase in precision would result in a total estimated time savings of ∼650 hours for facilitated exploration of the, for example, entire NAC Moon dataset, assuming a dataset would contain 130,000 candidates that need to be examined by an expert (number based on Bickel et al. (2020a) who conducted a global rockfall survey on the Moon).

Unknown Domain Exploration: The observation that we can achieve equal or even superior detector performance in a domain of interest with a detector that has been trained with predominantly foreign domain labels has a variety of use cases. Most importantly, given that creating new labels in the unfamiliar domain can take ∼10–30 minutes per label of expert time (or large numbers of new examples to create labels might simply be non–existent), this achieves a significant time savings of ∼4500 hours (for a dataset with 10,000 labels) before ML assisted exploration of the new dataset can begin. With data labeling being the most time–consuming and tedious aspect of supervised machine learning, a targeted application of this finding could significantly reduce the required effort and time (and resources) to make valuable science discoveries in any (planetary) science datasets.

Real-time Downlink Prioritization: Similarly, the observation of multi–domain trained detectors outperforming single–domain detectors in unknown domains has a variety of useful applications: A multi–domain, pre–trained detector could be deployed on recently downlinked image data or could be part of the downlink pipeline itself, for rapid, on–the–fly science discovery in completely new datasets. This would

also enable the operating science and mission team to identify areas of interest quicker and to make science discovery in the new data much faster. In the context of ever increasing dataset sizes returned by space exploration missions, such an application becomes more and more attractive. Another application of a multi–domain, pre–trained detector would be on an autonomous mission that might encounter an environment it might not be familiar with, but still needs to collect as many scientifically valuable observations as possible.

The findings of research questions (1), (2), and (3) also suggest that adding data from a second (foreign) domain (e.g. Mars) does not necessarily result in sub–optimal performance in the primary domain (e.g. Moon), as suspected by previous work (Ben-David et al., 2010). In turn, domain–mixing appears to benefit the performance, as described by e.g. Wang et al. (2019) for object detection in datasets like KITTI, VOC, and COCO, by Prakash et al. (2021) for terrestrial landslides and EO data, and by Bickel et al. (2020b) for rockfall detection on Mars. Our observation that the improvements in performance cannot be explained by variations in scale has value as well, potentially beyond the planetary science use case. For example, this finding could help to optimize the selection of multi–domain training data for e.g. medical applications, to more effectively and consciously optimize detector performance.

It is important to note that the benefits of multi–domain learning within planetary science are not limited to the application to rockfalls: There are other geomorphic features that are abundant across the solar system that can be mapped to address important science questions, such as impact craters, dunes, boulders, dust devils, ridges, slope streaks, and many others. For example, multi–domain learning could be applied to improve deep–learning–based crater detection and counting routines (like CDAs - crater detection algorithms, e.g. Benedix et al. (2019)), which could greatly enhance the robustness of surface age estimation routines or hazard avoidance routines during spacecraft descent and landing operations on known and unknown planetary bodies.

The findings of this study have a series of limitations. One fundamental uncertainty of the assessment of rockfall detector performance is the training and testing data labeling purity: at times it is challenging for an expert to assign labels to presumable rockfall features, particularly for very small rockfalls (when the boulder diameter approaches the spatial resolution of the image). Consequently, all training and testing data potentially include FPs and FNs, i.e., labels that falsely denote a non–rockfall feature as rockfall and features that are rockfalls but which have not been labeled by an expert. While present, this uncertainty would equally affect all experiments and is not expected to change the findings of this paper in any systematic way. Another uncertainty is introduced by the technical differences of the used cameras. This study combines image data from six different instruments that all feature different spectral ranges, data formats (some data has been reduced to 8 bit), camera specific artifacts or noise, and other factors, which all potentially influence the results of this work in unforeseen or unexpected ways.

Governed by the fact that all previous work with rockfall detectors in a planetary science context has been performed with the same object detection architecture, RetinaNet (Bickel et al., 2018, 2020a,b), we decide to use the identical setup to run these detailed, follow–up experiments. In addition, using RetinaNet is the only way to connect to previous work that found some indication that multi–domain training has a positive impact on performance (Bickel et al., 2020b). RetinaNet is the current state–of–the–art, can be used off–the–shelf, and is well–established, which means that our findings can be directly deployed to support other applications or fields of research that are already familiar with RetinaNet, such as e.g. aeolian feature mapping (Nagle-McNaughton et al., 2020), medical imaging (Jung et al., 2018; Jaeger et al., 2018), and autonomous driving (Hoang et al., 2019).

There is an array of open and new questions that result from this work: What is the dominant driver, if any, of multi–domain learning: a) the variation of the physical appearance of the target feature, b) the nature of the background, c) variations in illumination conditions, or 4) differences in sensor properties? Can we derive and use a quantitative measure for domain complexity and geomorphology to derive the optimal mixture of labels from different domains? Do our findings hold true if object detectors are trained on more than two domains? At what number of domains do we reach an equilibrium for a planetary science use case? How different can the physical appearance of target features from different domains be to still provide multi–domain (transfer learning) benefits? Can our findings help to improve the detection and mapping performance of other geomorphic features, such as dust devils, dunes, craters, and others? Do our findings hold true for more exotic worlds than the rocky planets and moons, such as icy worlds like Europa (icefalls) or metal worlds like Psyche (metalfalls)? Can our findings be applied to data returned

not by space–borne but airborne probes, such as the Dragonfly quadcopter on Titan?

Many of the uncertainties and open questions can be addressed as soon as more high–resolution imagery is returned from known and unknown domains by future missions, such as from Mercury (BepiColombo), Titan (Dragonfly), or Europa (Europa Clipper).

Conclusion

We conduct four experiments to investigate if and how multi–domain training influences the performance of rockfall detectors in a planetary science context. Mixing image data from the Moon and Mars while maintaining a constant total number of training labels, we show that the inclusion of a small amount of rockfall training data from a foreign domain (e.g. Moon) helps to boost the performance of a detector in different domain of interest (e.g. Mars) by up to 6% AP. This finding could be applied to improve the performance of object detectors in existing datasets, effectively maximizing the science discovery output while reducing the time required for candidate review by experts.

We also show that a detector that is trained with a predominant fraction (90%) of foreign domain labels (e.g. Moon) and a small fraction of home labels (e.g. Mars) can still perform as well as or even better than the local (home) benchmark (e.g. a martian detector on Mars). This finding has important applications for science discovery in legacy and new datasets, as only 10% of new labels are required to achieve equal or better detector performance, effectively saving 90% of the expert time required for labeling. Assuming a labeling time of around 30 minutes per label this would result in time savings of about 4500 hours assuming a dataset size of 10,000 labels. We additionally observe that multi–domain detectors outperform single–domain detectors when applied to a completely unknown domain (here: Ceres) by up to 16% AP. This finding has applications for instantaneous science discovery in recently downlinked image datasets, science–informed decision making for on–the–fly mission planning, and autonomous system–based exploration, among others. Varying only the scale (image resolution) of training labels in a single domain (here: Mars) while keeping all other relevant domain parameters constant indicates that the benefits of multi–domain learning draw not from differences in scale but from either the differences in physical appearance of features or the background, differences in lighting conditions, or both. This finding could help to inform future compilation of multi–domain training datasets for object detectors for planetary science applications, as well as for other fields of research.

We conclude that image data–based domain transfer learning has significant, practical potential for the application in a space science and exploration context, not only for rockfalls but potentially for many other abundant geomorphic features as well, such as craters, dunes, slope streaks, dust devils, and others. The findings of this study might hold true for related fields of research, such as astrophysics, terrestrial geoscience, and geophysics.

Acknowledgements

This work has been performed as part of the NASA JPL Visiting Student Research Program (JVSRP). VTB would like to thank the NASA JPL COSMIC team (MLIA 398J) for the welcoming working culture. This work was supported by a fellowship within the IFI programme of the German Academic Exchange Service (DAAD). VTB would like to thank Nvidia for their support with a GPU via the Nvidia GPU Research Grant Program. The workflow is entirely based on open source software. This research was carried out at the Jet Propulsion Laboratory, California Institute of Technology, under a contract with the National Aeronautics and Space Administration. Copyright 2021 California Institute of Technology. U.S. Government sponsorship acknowledged. The labeled dataset of martian and lunar rockfalls including a detailed description is available here: doi:10.3389/frsen.2021.640034

2.4 A Labeled Image Dataset for Deep Learning-driven Rockfall Detection on the Moon and Mars

Published 2021 in Frontiers in Remote Sensing
Bickel, V.T., Mandrake, L., Doran, G., 2021
https://doi.org/10.3389/frsen.2021.640034

Background

The term rockfall describes the rapid displacement of a large, usually meter–sized block of rock down–slope, triggered by, for example, endogenic or exogenic events like impacts, quakes or rainfall (Hungr et al., 2014; Xiao et al., 2013). In a remote sensing context, the term rockfall is also being used to describe the characteristic geomorphic deposit of a rockfall event that can be identified from an air- or space–borne perspective, i.e., the combination of a displaced boulder and the track it carved into the slope substrate while bouncing, rolling, and sliding over the surface (also called 'boulder with track' or 'rolling boulder') (Hovland, Mitchell, 1973; Filice, 1967; Moore, 1970) (see Figure 2.21). In planetary science, the spatial distribution and frequency of rockfalls provide insights into the global erosional state and activity of a planetary body (Bickel et al., 2020a; Tesson et al., 2020) while their tracks act as tools that allow for the remote estimation of the surface strength properties of yet unexplored regions in preparation of future ground exploration missions (Eggleston et al., 1968), such as the lunar pyroclastic (Bickel et al., 2019), polar sunlit (Bickel, Kring, 2020) and permanently shadowed regions of the Moon (Sargeant et al., 2020). Due to their small physical size (meters), the identification and mapping of rockfalls in planetary satellite imagery is challenging and very time–consuming, however. For this reason, Bickel et al. (2018) and Bickel et al. (2020b) trained convolutional neural networks to automate rockfall mapping in lunar and martian satellite imagery.

Parts of the unpublished datasets used for earlier work have now been complemented with newly labeled data to create a well-balanced dataset of 2,822 lunar and martian rockfall labels (which we call 'RMaM–2020' — Rockfall Mars Moon 2020, 416 MB in total, available here: https://edmond.mpdl.mpg.de/imeji/collection/DowTY91csU3jv9S2) that can be used for deep learning and other data science applications. Here, balanced means that the labels have been derived from imagery with a wide and continuous range of properties like spatial resolution, solar illumination, and others. So far, this dataset has been used to analyze the benefits of multi–domain learning on rockfall detector performance (Mars & Moon vs. Moon–only or Mars–only), but there are numerous other (non–planetary science) applications such as for featurization, feature or target recognition (aircraft/spacecraft autonomy), and data augmentation experiments.

Methodology

All labels represent the localization of a rockfall instance in a satellite image, i.e., mark the position of the characteristic combination of boulder and track in an image (see e.g. Bickel et al. (2018)).

Data source
All labels have been either derived with subnadir, calibrated, non map–projected High Resolution Imaging Science Experiment red–channel .jp2 (HiRISE on board the Mars Reconnaissance Orbiter, MRO) (McEwen et al., 2007) or subnadir, calibrated, non map–projected pyramid–tiff .tif (PTIF) Narrow Angle Camera (NAC on board the Lunar Reconnaissance Orbiter, LRO) (Robinson et al., 2010) imagery. HiRISE provides images with spatial resolutions between ∼0.25 and ∼0.75 m/pixel (McEwen et al., 2007) while NAC provides images with spatial resolutions between ∼0.5 and ∼2 m/pixel (Robinson et al., 2010) from their nominal orbits. Image products have been downloaded from either the Arizona State University's LROC (http://wms.lroc.asu.edu/lroc/search) or the University of Arizona's HiRISE (https://www.uahirise.org/) image portals.

Data preprocessing & labelling
The HiRISE images have subsequently been reduced to 8 bit (PTIF NAC images are distributed as 8 bit images already). Using QGIS (https://www.qgis.org/en/site/) a series of approximately 300x300 to 1000x1000 pixel–sized image tiles have been cropped from the full 109 lunar and 44 martian parent images; these tiles either contain rockfalls (positive tiles) or do not (negative tiles). For Mars, there

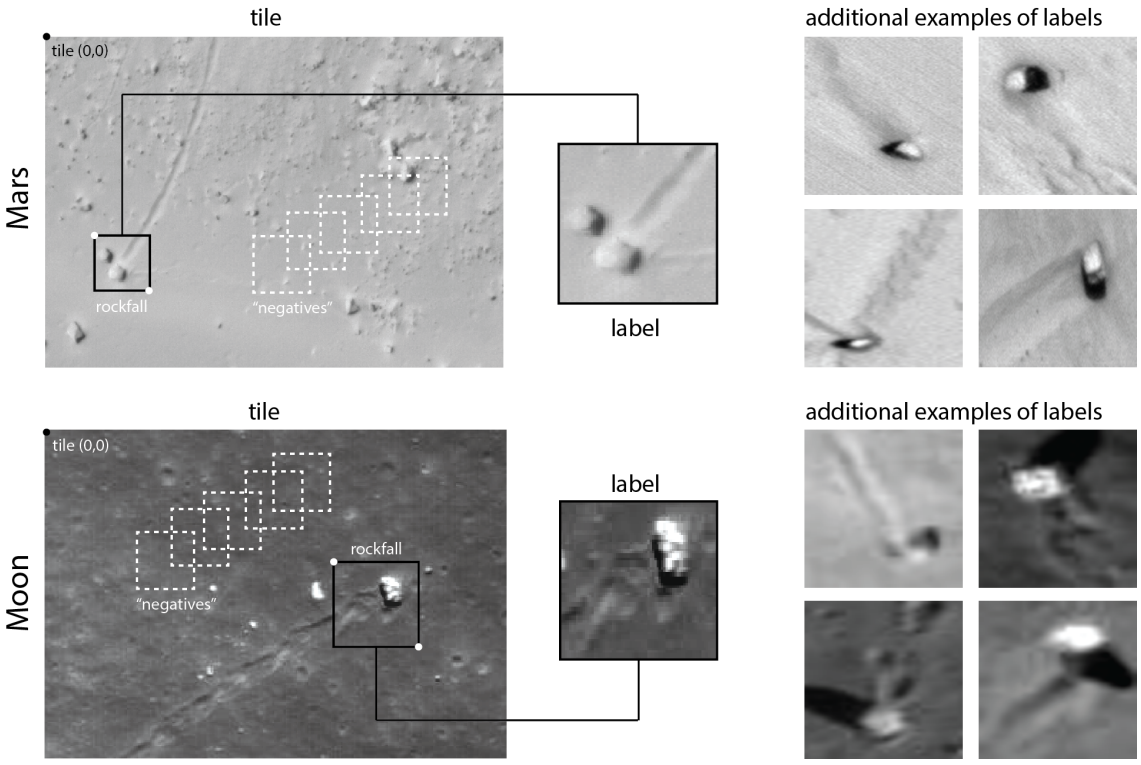


Figure 2.21: Examples of martian HiRISE (top) and lunar NAC (bottom) rockfall labels (bright boulder and elongated track); each example has been cropped from its respective positive tile using its label bounding box coordinates, as indicated in the figure. Tile (0-0) is at the top left (pythonian style). Unlabelled parts of each tile can act as negatives, as indicated in the shown tiles.

are 484 positive tiles and 330 negative tiles, for the Moon there are 377 positive tiles and 317 negative tiles for training and testing. All positive tiles have then been processed in Matlab R2017a, where one experienced (with domain knowledge) human operator manually labeled all rockfalls with rectangular bounding boxes (bboxes) — a particularly time–expensive and tedious process. Some examples of these user–derived labels are showcased in Figure 2.21. A label always contains a boulder and its associated track to guarantee instance uniqueness, i.e., to avoid confusion with static boulders or track sections without boulders (see Figure 2.21). The authors would like to note that, due to the complexity as well as the limited quality and spatial resolution of the available imagery, very small rockfalls could potentially be overlooked or confused with other geomorphic features such as static boulders with a sand tail that got deposited by aeolian processes (on Mars), especially in complex geomorphic contexts like talus cones. While this dataset represents a best effort approach, the potential occurrence of false positives (labels which describe non–rockfall features), false negatives (rockfall features in image tiles which have not been labeled) and duplicates in the dataset cannot be excluded completely. Particular care has been taken to remove all FPs and FNs from the designated testing label sets, to maximize the accuracy of model validation.

Dataset

This dataset has been tailor–made for a Python, Keras, and TensorFlow implementation of RetinaNet (Keras RetinaNet by Fizyr: `https://github.com/fizyr/keras-retinanet`, based on Lin et al. (2018)) and consists of positive and negative image tiles (.jp2 and .tif) as well as labels and classes (.csv). There are a total of 1,000 positive rockfall training labels per planetary domain and an additional 300 negative training tiles without any rockfalls that can be used to further stimulate detector training. The martian testing set contains 91 positive labels and 31 negative tiles, while the lunar testing set contains 83 positive labels and 17 negative tiles, respectively. In total, there are 2174 positive labels and 648 negative tiles for training and testing. All training and testing labels and tiles can be mixed without any limitations, if

required. Each label .csv file consists of 6 column entries (each row represents one label), 1) the path to the image the label belongs to, 2 - 5) the upper left column and row, and the lower right column and row image coordinates of the label bounding box (the pythonian image 0–0 is the top left of the image), and 6) the label class (here: rockfall). After deployment of the dataset, the label paths need to be adapted to point to the correct image tile directory. Each classes .csv file contains 2 column entries, 1) the class (here rockfall) and 2) the class ID (here 0). The class ID can be adapted in case the data are used to train a multi–class detector. The .csv–file structure of RMaM–2020 meets the input criteria for RetinaNet, but can be easily adapted to fit to any other object detection framework. Similarly, all labels can be augmented using geometric operations, as long as the same operations are applied to the labels and the images. The dataset consists of 2 main folders which hold 8 sub–folders and a series of .jp2 (HiRISE), .tif (NAC), .csv files, and one ReadMe file. The dataset structure is shown on the left.

RMaM–2020
- ReadME.txt
- **mars**
  - train_images
    - *.jp2
  - train_labels
    - train_labels_ma.csv
    - train_classes_ma.csv
  - test_images
    - *.jp2
  - test_labels
    - test_labels_ma.csv
    - test_classes_ma.csv
- **moon**
  - train_images
    - *.tif
  - train_labels
    - train_labels_m.csv
    - train_classes_m.csv
  - test_images
    - *.tif
  - test_labels
    - test_labels_m.csv
    - test_classes_m.csv

Analysis

The RMaM–2020 labels cover a large range of spatial resolutions and solar illumination conditions. For Mars, RMaM–2020 contains images with spatial resolutions between 0.25 and 0.5 m/pixel as well as solar incidence and phase angles between 35 and 65 degrees. The solar phase angle describes the angle between the light that comes from the Sun and the light that is reflected into the camera (Sun–Planet–Satellite); the solar incidence angle describes the angle between the incoming light and the surface of a planet, where 0 degree denote vertical and 90 degrees horizontal illumination conditions. For the Moon, RMaM–2020 contains images with a wider range of spatial resolutions (due to the nature of LRO's orbit and NAC's technical setup) between 0.5 and 2.2 m/pixel as well as a wider range of solar incidence and phase angles between 15 and 87 degrees. For both planetary domains, the pairings of differing spatial resolutions and solar incidence angle are relatively well–distributed, i.e., there are low- and high-resolution images for low- and high–incidence angle conditions.

The ratio of label x and y dimensions (the bbox aspect ratio) is consistent for both planetary domains, reflecting the fact that both datasets have been labeled by the same human operator. The shape of each bounding box has been adapted to 1) the orientation of the respective boulder and track and 2) the local geologic background, to avoid that other, non–rockfall objects fall within the label (see Figure 2.21). The good alignment of absolute bbox dimensions across the two planetary domains is surprising, given that the lunar image data have slightly lower spatial resolutions than the martian image data; this could potentially indicate that either 1) martian rockfalls are slightly smaller on average or 2) that the human operator subconsciously increased the size of the bboxes when looking at lower resolution rockfall examples during labeling. The discussed properties of RMaM–2020 are visualized in Figure 2.22 and the IDs of all used HiRISE and NAC images are listed in Table A.5 and Table A.6, respectively.

Future Work

Our goal is to complement RMaM–2020 with more rockfall labels over the next years, not only from the Moon and Mars, but from other planetary bodies such as Ceres (NASA's Dawn Mission), comet 67P (ESA's Rosetta Mission), and from potential future datasets such as from ESA's BepiColombo Mission to Mercury. This way RMaM–2020 (and its successors) would remain a valuable resource for deep learning–driven rockfall detection across the solar system in the future.

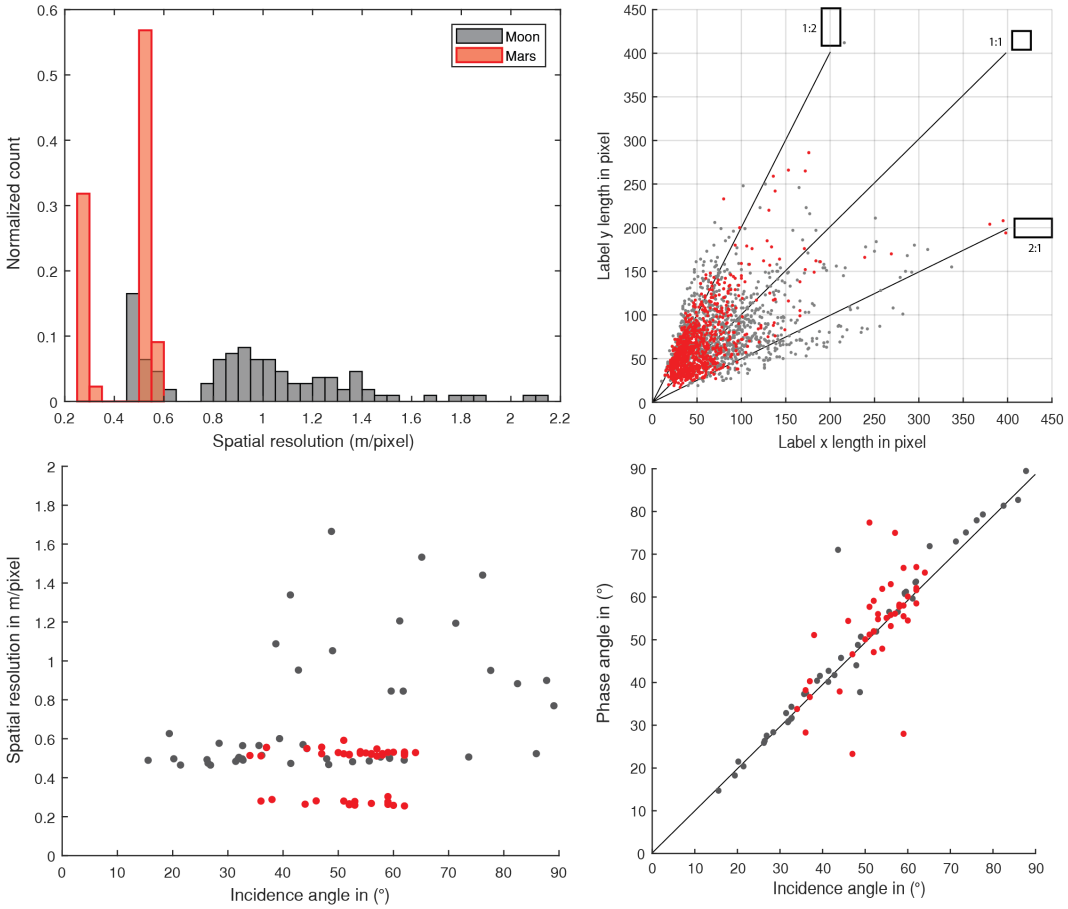


Figure 2.22: Distribution of spatial resolutions of the imagery used for training and testing from Mars (MRO HiRISE, red) and the Moon (LRO NAC, gray) and visualizations of the relations between label dimensions (label aspect ratio), illumination condition (solar incidence and phase), and spatial resolution. The label aspect ratio varies as labels need to adapt to the geomorphic appearance and spatial orientation of rockfalls.

Acknowledgements

This work has been performed as part of the NASA JPL Visiting Student Research Program (JVSRP). VTB would like to thank the NASA JPL COSMIC team (MLIA 398J) for the welcoming working culture. This work was supported by a fellowship within the IFI programme of the German Academic Exchange Service (DAAD). This research was carried out at the Jet Propulsion Laboratory, California Institute of Technology, under a contract with the National Aeronautics and Space Administration. Copyright 2021 California Institute of Technology. U.S. Government sponsorship acknowledged.

Chapter 3

Drivers of Rockfalls

This chapter outlines how we deployed the developed deep learning algorithms to map the global distribution of rockfalls on the Moon. This chapter continues to report the scientific findings and causal relations related to rockfall drivers and transport processes that we made in this global map and a variety of existing - or newly created -, auxiliary datasets.

3.1 Impacts drive Lunar Rockfalls over Billions of Years

Published 2020 in Nature Communications
Bickel, V.T., Aaron, J., Manconi, A., Loew, S., Mall, U., 2020
https://doi.org/10.1038/s41467-020-16653-3

Abstract
Past exploration missions have revealed that the lunar topography is eroded through mass wasting processes such as rockfalls and other types of landslides, similar to Earth. We have analyzed an archive of more than 2 million high-resolution images using an AI and big data-driven approach and created the first global map of 136,610 lunar rockfall events. Using this map, we show that mass wasting is primarily driven by impacts and impact-induced fracture networks. We further identify a large number of currently unknown rockfall clusters, potentially revealing regions of recent seismic activity. Our observations show that the oldest, pre-Nectarian topography still hosts rockfalls, indicating that its erosion has been active throughout the late Copernican age and likely continues today. Our findings have important implications for the estimation of the Moon's erosional state and other airless bodies as well as for the understanding of the topographic evolution of planetary surfaces in general.

Introduction

Over geologic timescales, dynamic erosion processes smooth topography and shape planetary surfaces (Fielder, 1963; Arvidson et al., 1975b). On airless bodies, such as the Moon, erosion has primarily been thought to occur through space weathering (Ryder, 1987). However, recently acquired, high-resolution imagery has revealed a startling feature on lunar slopes: ubiquitous mass-wasting features. These include granular flows (Kumar et al., 2013; Kokelaar et al., 2017), slides, slumps, and creeps (Fielder, 1963; Scaioni et al., 2018), as well as rockfalls (Fielder, 1963; Xiao et al., 2013; Kumar et al., 2019b, 2016), a process where boulders are released or ejected from topographic highs and fall, roll, bounce, and slide to topographic lows. Rockfalls carve tracks into the lunar surface, which provide a record of the dynamic emplacement process. The characteristic combination of a displaced boulder or rock fragment and its track — here called rockfall — enables unambiguous detection from satellite imagery (see inset in Figure 3.1). During the Apollo 17 mission, astronauts Jack Schmitt and Eugene Cernan directly sampled a rockfall at station 6 in Taurus Littrow valley and returned multiple samples to Earth. Using these data in combination with orbital imagery, rockfall track survivability has been estimated to range from ∼1.55 to 35 Ma (Arvidson et al., 1975b; Kumar et al., 2019b, 2016; Arvidson et al., 1975a; Hurwitz, Kring, 2016; Langevin et al., 1982) with an upper limit of ∼150-300 Ma (Basilevsky et al., 2013), meaning that the tracks observed today are the expression of geologically recent (late Copernican) — and potentially current — erosion

processes.

Past studies have mapped lunar rockfall features for selected regions across the lunar equatorial and polar highland, mare, pyroclastic, and permanently shadowed regions (Xiao et al., 2013; Kumar et al., 2019b, 2016; Bickel et al., 2019; Sargeant et al., 2020). These studies have hypothesized that the main drivers of lunar rockfalls are shallow and deep moonquakes, impact-induced shaking, and thermal fatigue caused by the extreme temperature variations on the Moon(Xiao et al., 2013; Watters et al., 2019). Here we use the term rockfall driver to represent both the long-term cause (also called precondition) and short-term trigger, as observations in satellite imagery only allow for an explicit distinction of rockfall triggers and causes in some cases (Kumar et al., 2016, 2019b). Other studies have suggested that major basin-forming impact events can cause intense and global seismic shaking that results in erosion of steep slopes through large-scale mass wasting (Kreslavsky, Head, 2012, 2016). As the latest basin-forming event, the Orientale impact, occurred ∼3.8 Ga ago, all topography older than ∼3.8 Ga would feature shallow slope angles and, thus fewer mass-wasting processes (Kreslavsky, Head, 2016), a finding supported by an apparent absence of mass-wasting features like rockfalls and granular flows on the oldest — (pre-)Nectarian — topography (Xiao et al., 2013). Thus the current assumption is that these ancient, (pre-)Nectarian terranes represent the final evolutionary stage of the lunar surface as they have shallow slopes (Kreslavsky, Head, 2016; Fassett, Thomson, 2014) and may not host mass-wasting features. However, these past studies have focused on small, isolated regions (Kumar et al., 2016, 2019b) and/or applied coarse spatial sampling (Xiao et al., 2013).

A high-resolution, global map of mass-wasting features such as rockfalls is required to identify and better understand their spatial distribution and drivers, as well as the state of lunar erosion activity. We have analyzed an archive of >2 million high-resolution images taken by the National Aeronautics and Space Administration's (NASA's) Lunar Reconnaissance Orbiter (LRO) narrow angle camera (NAC) using a convolutional neural network (CNN) (Bickel et al., 2018) in combination with advanced cloud computing capabilities and created the first global map of the location and size of lunar rockfalls.

Results

Spatial distribution of lunar rockfalls
We identified 136,610 rockfalls across the lunar surface in the latitude range from 80° N to 80° S, with a mean spatial density of ∼2 rockfalls per 1° by 1° quadrangle. The spatial distribution of rockfalls is heterogeneous, with the majority of features located in highland terranes (91%). The distributions over the lunar near side and far side, as well as the northern and southern hemispheres, are relatively well balanced. There are distinct and pronounced clusters of rockfalls across all terranes (Figure 3.1), while the local spatial distribution of rockfalls within selected craters is asymmetric, as is particularly obvious in Tsiolkovsky (Figure 3.2f), Atlas (Figure 3.2c), and Plato craters (Figure 3.2h). The peak rockfall density of 272 rockfalls per 1° by 1° quadrangle has been measured in the Buerg crater on the lunar nearside. Other remarkable, high-spatial density rockfall clusters are located in Mare Orientale basin and the associated Montes Rook and Montes Cordillera, as well as in Tsiolkovsky, Pasteur D, Atlas, Aristoteles, Milne N/L, and Crookes craters. The heterogeneous spatial distribution of rockfall clusters could potentially reveal regions of recent seismic activity. Lunar rockfall (boulder) diameters range from ∼3 to ∼25 m, while the majority of rockfall (boulder) diameters range from ∼7 to ∼10 m (Figure 3.2). The ubiquitous and homogeneous soil on lunar slopes (Carrier et al., 1991) would act in favor of larger deposited boulder diameters, since a large portion of the kinetic energy would be absorbed by the soil and would thus not contribute to boulder fragmentation. On average, older lunar regions appear to host boulders with systematically larger volumes (Supplementary Figure A.30). A potential explanation of this observation could be an increase of the lateral spacing between impact-induced radial fractures as the crater erodes over time, producing larger boulders.

Impacts are the main driver of lunar rockfalls
We found evidence that impact processes directly trigger lunar mass wasting (Figure 3.2e, g) and, given the likely age of rockfall tracks, actively drive the erosion of the lunar topography (Supplementary Figure A.31). One variation of these impact-ejected boulders features tracks that spread radially away from the impact site (Figure 3.2g), where the gradually decreasing distance between individual jumps of each boulder suggests that the boulders were initially airborne and subsequently lost more and more energy along their track. A second variation features an impactor that hits the slope of an existing, larger crater

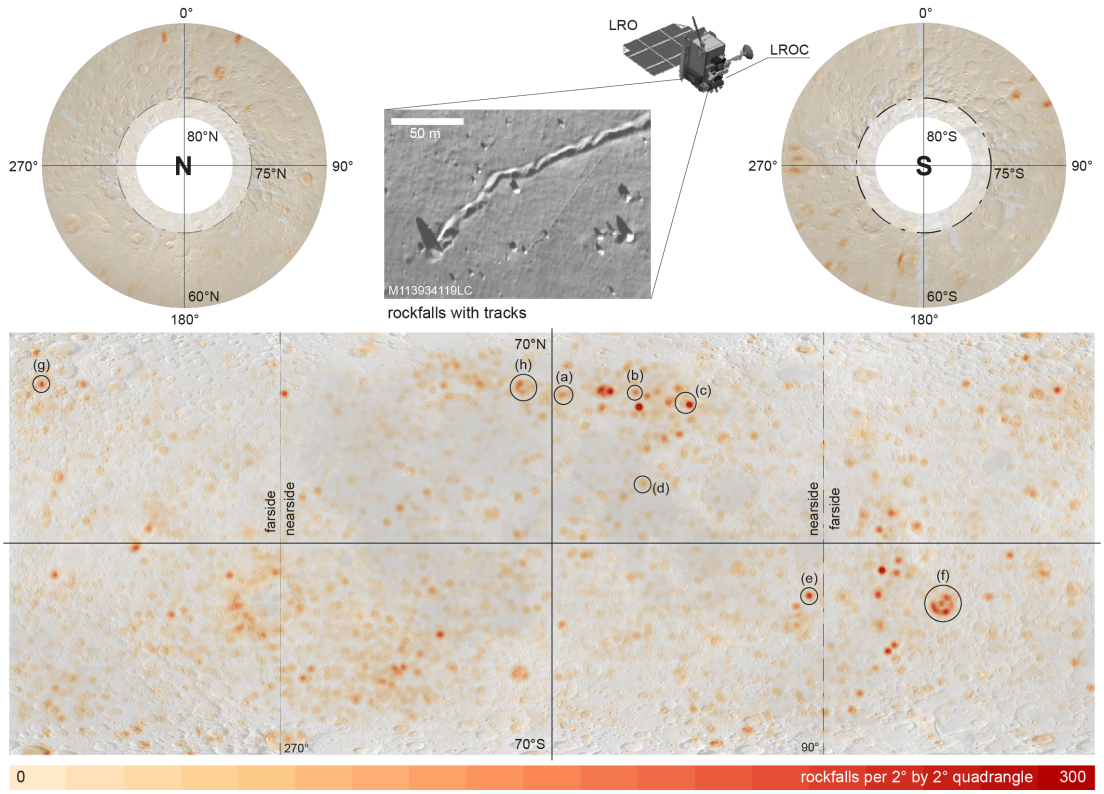


Figure 3.1: Global rockfall distribution heat map. Heat maps of lunar global rockfall distribution in both equirectangular (70° N to 70° S) and polar projection (60° N to 80° N and 60° S to 80° S). Mapping results above 75° N and below 75° S might be less complete due to challenging illumination conditions (indicated by transparent white areas). Rockfall density is given in rockfalls per square degrees, i.e., the number of rockfalls per 2° latitude by 2° longitude quadrangle. The labeled black circles denote details shown in Figure 3.2. Inset shows examples of rockfalls and their tracks with various sizes: detail of LRO NAC (LROC) image M113934119LC. Global WAC mosaic in the background (Wagner et al., 2015). NAC image credits to LROC/ASU/NASA.

(Figure 3.2e), resulting in instant displacement of a number of boulders across the slope of the older host crater. However, the majority of rockfalls occur on crater slopes without the direct influence of a subsequent impactor. This indicates that impacts act not only as a direct trigger but also induce fracture networks that represent the main preconditioning factor for lunar rockfalls. Subsequently, other, more recent geological processes, such as tectonic and/or volcanic activity, can potentially act as alternative or additional triggers of these impact-fractured rock masses.

The majority of rockfalls are located in impact craters or basins (∼84%), while the remaining features are situated in graben or along faults and scarps (∼0.8%), on volcanic edifices or in vents and rilles (∼0.4%), and regular slopes, which include areas with unclassified geomorphic contexts (∼14.8%) (Supplementary Figure A.30). If craters with diameters between 1 and 5 km are neglected (Robbins, 2018), the portion of rockfalls located in craters or basins is ∼72.7% and ∼26.1%, respectively, on regular slopes, including unclassified geomorphic contexts. The percentage of rockfalls in craters is potentially still underestimated (and unclassified overestimated), as craters with diameters <1 km have not yet been mapped on a global scale. Most mapped rockfalls are located in craters with diameters <25 km and the spatial density of rockfalls in these smaller craters is on average three times higher than in the other analyzed geomorphic regions, i.e., $\sim 13E^{-03}$ vs $\sim 4E^{-03}$ rockfalls per square kilometer. We do not observe a general increase in rockfall number or spatial density within or in the direct vicinity of tectonic features, such as graben and faults, which would be expected if recent tectonic activity is a main driver of lunar rockfall. Two potential explanations of this observation are: (1) endogenic seismic activity is a relatively unimportant trigger or (2) there is a lack of impact-induced fracture networks (precondition) for high-frequency rockfall occurrence in tectonic geomorphic contexts. At present, current data cannot distinguish between these

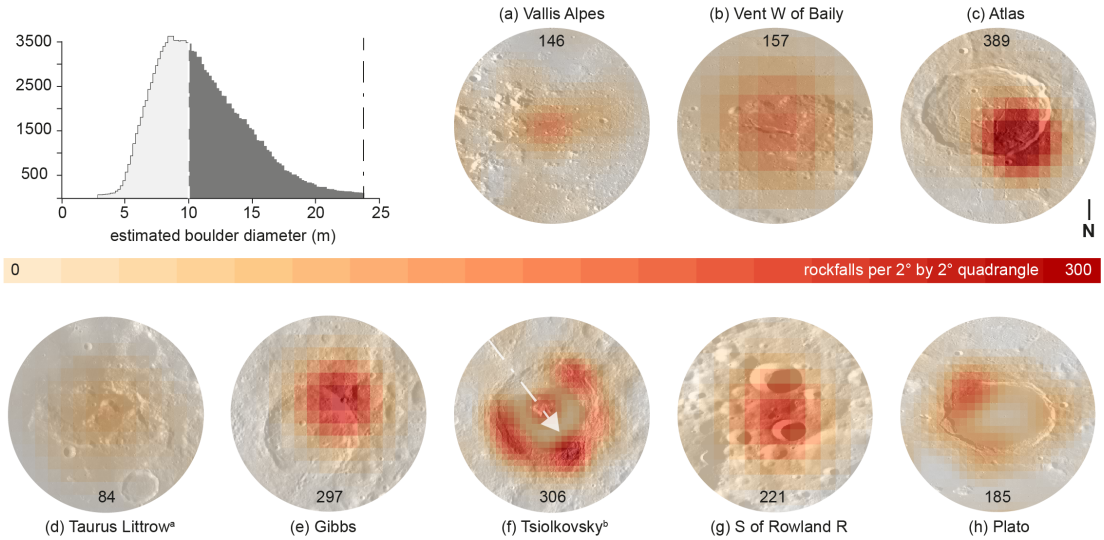


Figure 3.2: General rockfall diameter distribution and details of Figure 3.1. The histogram shows the general distribution of estimated rockfall diameters. Estimated rockfall diameters are based on the output of the neural network and are potentially biased for smaller diameters (section indicated in white), as the CNN's detection accuracy is reduced when detecting small features. Insets a-h are details from Figure 3.1 and represent graben (a), pyroclastic vents (b), craters (c, f, h), regular slopes (d), and recent impacts (e, g). Some craters show a heterogeneous distribution of rockfall abundance, such as c, f, h. The peak count of spatial rockfall density is shown in the insets per 2° by 2° quadrangle. In e, g, we identified a series of rockfalls that are directly induced by small–scale impact events (impact–ejected); for details refer to Supplementary Figure A.31. [a]Apollo 17 landing site, [b] Morse et al. (2018) proposed an impact trajectory for (f) based on the distribution of the ejecta blanket (axis NW-SE), which agrees with the rockfall distribution (white arrow). Global WAC mosaic in the background (Wagner et al., 2015).

two hypotheses. There are limited exceptions to this observation, such as the rockfall clusters in Vallis Alpes (a graben, Figure 3.2a and Supplementary Figure A.32c), Aristarchus plateau (a volcanic region, Supplementary Figure A.32a), and a pyroclastic vent west of the Baily crater (Figure 3.2b). Thus, while rockfall frequency and density peak in impact craters, particularly in young and steep (Kreslavsky, Head, 2016) craters (e.g. Figure 3.3), i.e., lunar rockfalls appear to be predominantly driven by impacts, our results show that recent tectonic and potentially volcanic activity contribute as well. This means that our global map of rockfalls could also be applied to better understand, localize, and constrain the current tectonic — and potentially volcanic — activity of the Moon.

Rockfalls and the erosional state of the lunar surface

The majority of rockfalls occurs in Imbrian terranes (∼46%; Figure 3.3), but a substantial number of rockfalls (∼25%) are located in ancient Nectarian and pre-Nectarian terranes and craters with estimated ages of >3.8 Ga (Figure 3.3; Supplementary Figure A.33). This is a remarkable observation, as the current assumption is that these ancient terranes only feature shallow slopes (Kreslavsky, Head, 2016) and would not host any mass-wasting features other than slope creep (Xiao et al., 2013). The mean spatial density of rockfalls as a function of geologic epoch peaks in very young (Copernican) craters and declines over time (Figure 3.3). This peak is expected, as fresh topography is usually sharp and erosion rates are high. As erosion proceeds, the topography becomes smoother (Kreslavsky, Head, 2016; Fassett, Thomson, 2014) and the rockfall density declines. We find that after ∼1.5 Ga the density of rockfalls is reduced by roughly 50% compared to the (initial) Copernican density (see Figure 3.3). This observation implies that the spatial density of rockfalls could be used to complement the analysis of the age of lunar topography (see Equation 3.1 in the "Methods" section) as derived from diffusive erosional processes (Fassett, Thomson, 2014). We note that inaccuracies in the geologic map may influence these counts (Supplementary Figure A.34); however, given the global coverage of our rockfall map (Figure 3.1) and manual checking of detections (Supplementary Figure A.33), we think that mapping inaccuracies cannot entirely account for the presence of rockfall in ancient terranes.

In contrast to the counting of rockfalls in terranes of specific ages, the estimate of the time of occurrence of

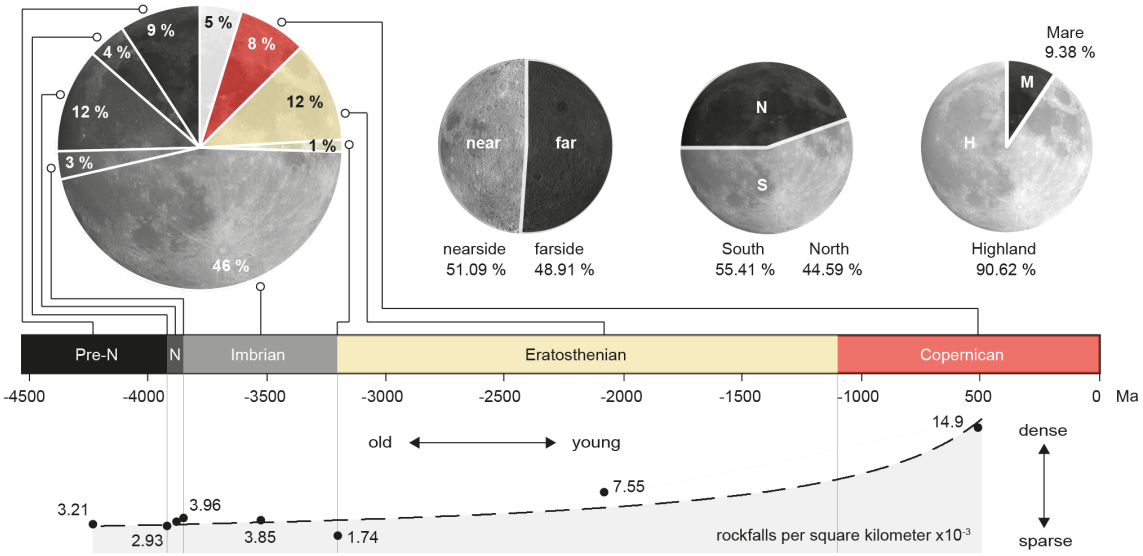


Figure 3.3: Statistics about rockfall distribution in space and time. Statistics highlight the spatial distribution of rockfalls and its implications. More rockfalls occur in highland terranes and the majority of rockfalls occur in Imbrian terranes, while Nectarian (N) and even pre-Nectarian sites (pre-N) feature a substantial number of recent rockfalls (∼25%). Owing to inaccuracies in the underlying geologic map, the number of rockfalls in ancient terranes is potentially reduced in favor of the Copernican and Eratosthenian bins (see Supplementary Figure A.34). The normalization of the CNN-derived rockfall counts over area in the regions provides a first-order estimate (power law fit, black dashed line) of the advective erosion rate of the lunar topography and its evolution over time (Equation 3.1 in the "Methods" section). Geologic lunar timescale based on Hawke et al. (2004) and Neukum et al. (2001).

rockfall events is controlled by the survival time of the tracks carved by the displaced boulders. If boulder tracks erode quickly, the mapped rockfall features would indicate very recent erosional activity; if tracks survive for a long time, the occurrence of rockfalls is more difficult to constrain. Survival times of boulder tracks have been estimated to lie between ∼1.55 and 35 Ma using observations made by astronauts, dating of in situ samples, and satellite imagery (Arvidson et al., 1975b; Kumar et al., 2019b, 2016; Arvidson et al., 1975a; Hurwitz, Kring, 2016; Langevin et al., 1982). However, track survival times might vary at different locations due to variations in impactor influx and local topographic differences (Arvidson et al., 1975a). A maximum survival time of tracks between ∼150 and 300 Ma can be established by using the mean survival time of lunar boulders >2 m (Basilevsky et al., 2013), assuming that boulders would outlast their tracks. Thus our observations of rockfalls in (pre-)Nectarian terranes (>3.8 Ga old) imply that these ancient terranes have been actively eroded in the past 300-∼1.55 Ma and likely are subject to erosion today. One direct consequence of this observation is that ∼3.8 Ga are not sufficient to completely erode the relief of an airless and dry body, even if slopes underwent instantaneous, global, impact-induced large-scale mass wasting such as hypothesized through, e.g., the Orientale impact ∼3.8 Ga ago (Kreslavsky, Head, 2012, 2016). This observation also indicates that the oldest surfaces of other bodies in the solar system with similar properties and impact histories as the Moon might still be subject to (small-scale) erosion as well, such as the pre-Calorian inter-crater plains on planet Mercury (Gault et al., 1975; Trask, John, 1975) or the pre-Veneneia crust on asteroid 4Vesta (Williams et al., 2014).

Discussion

The results presented here substantiate that impacts are the primary driver of lunar rockfalls. A substantial proportion of the observed lunar rockfalls occur in craters >3.8 Ga, suggesting that the legacy of impacts as a driver of rockfall activity lasts for geologic timescales. Previous work has shown that impacts cause substantial fracturing of the target bedrock, including sets of radial, concentric, spall, and shear discontinuities (Shoemaker et al., 1963; Polanskey, Ahrens, 1990; Kumar, 2005). On Earth, discontinuities are the main preconditioning factor for rockfalls (Kumar, 2005; Collins, Stock, 2016) and our results indicate that the same is true for the Moon (Figure 3.4). Additional evidence for impact-induced fracture systems

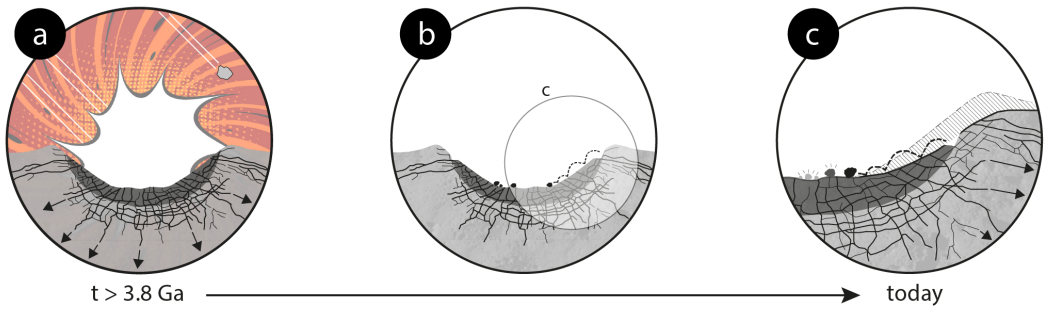


Figure 3.4: Conceptual model of lunar mass wasting. (a) Impacting bodies batter the lunar surface, creating topography (craters and associated terrain) as well as intense fracturing of the bedrock. (b) Impact craters feature radial, concentric, shear, and spalling fractures that cause the release of boulders-rockfalls- over time. (c) The extent of fracture networks is sufficient to drive rockfalls over billions of years. Fracture distribution pattern taken from Polanskey, Ahrens (1990)

governing rockfall occurrence is provided by the spatially asymmetric occurrence of rockfalls in craters such as Tsiolkovsky on the lunar far side, which agrees with the inferred impact direction(-axis) along a NW-SE trajectory (Morse et al., 2018) (Figure 3.2f and Supplementary Figure A.32d). An oblique impact angle would cause a denser and more consistent fracture network on the far side of the crater that predisposes the production of an increased number of rockfalls over time. In addition, the morphology and density of the impact-induced fracture systems controls the magnitude of lunar rockfalls that are considerably larger than on Earth, on average (Corominas et al., 2018).

The unexpected and long-lasting effect of pre-Nectarian impactors on the — potentially ongoing — erosion of ancient terranes could be favored by an increased impactor influx during the early days of the Earth-Moon system. It has been hypothesized that there was a systematically higher flux of impactors during the (pre-)Nectarian period — sometimes referred to as the Late Heavy Bombardment — that transitioned to an impactor population with lower impact ratios roughly 3.5-3.8 Ga ago (Tera et al., 1974; Head et al., 2010) or potentially even earlier in the Moon's history (Mojzsis et al., 2019). A significantly increased number of impacts could potentially result in a more pronounced fracture network and loss of rock bridges in (pre-)Nectarian rock masses that drive mass wasting over a period of >4 billion years.

Methods

Deep learning-driven rockfall detection and mapping
We applied a CNN to automatically search for lunar rockfalls in the image archive of NASA's LRO NAC, which contains >2 million entries. The used CNN is the fifth and most recent generation (M5) of a series of networks that have been trained, validated, and tested in a previous step (Bickel et al., 2018). M5 has been trained with 809,550 augmented rockfall images using an implementation of a state-of-the-art single-stage dense object detector (RetinaNet Lin et al. (2017), Fizyr (2018)) in combination with a ResNet101 backbone (He et al., 2015) and using open-source-only software (Python, Keras, TensorFlow). In the testing set, M5 achieved an average precision score of 0.89, a recall of 0.44-0.69, and a precision of 0.98-1.00 for confidence levels of 50% and 60%, respectively (Bickel et al., 2018). A confidence level of 60% was selected for the analysis as it provides the optimal compromise between recall and precision, based on the testing set; it has to be noted that M5's performance on the global dataset might deviate from the performance in the testing set. M5 was applied to optical, single-band, high-resolution satellite imagery that is acquired by NASA's LRO, a lunar spacecraft that has been in polar orbit around the Moon since 2009 (Robinson et al., 2010). The spatial coverage by LRO NAC is excellent and almost global, with limitations of coverage in the proximity of the lunar poles, due to the challenging illumination conditions and shadows.

We used pre-calibrated and compressed NAC pyramid image files as they have the maximal spatial resolution but a reduced bit depth (8 bit) and file size, allowing for optimized processing speeds. We accessed these data through a customized NASA JPL Moon Trek api (application programming interface) using an image selection algorithm that selected NAC images based on three criteria: (1) spatial resolution,

(2) solar incidence angle, and (3) overlap with surrounding images. This routine uses the Klee algorithm (Klee, 1977) to first calculate the overlap of neighboring NAC images and then find the best combination of images that cover the area of interest with maximum underlap and minimum overlap. Overlap needs to be minimized in order to avoid processing of redundant imagery and to avoid detections of physically identical rockfalls in different images. Underlap needs to be minimized to avoid gaps in the coverage and to achieve a seamless scanning of the lunar surface. The algorithm prioritizes images with the highest spatial resolution and with incidence angles between 30 and 60°, wherever possible. After identification of the NAC images, the data are tiled and input into the CNN. Subsequently, all detections are extracted and their positions reconstructed in real-world coordinates using the associated meta data from the LROC image archive (see Supplementary Figure A.35). In addition, the size of each detection's bounding box (predicted by the CNN) has been used to estimate the size of the rockfall (Bickel et al., 2018). We used a total of 2 local computers and 9 Google Cloud instances (AI Notebooks) to process the data, with a total of 30 central processing units and 15 graphics processing units (NVIDIA Titan Xp, NVIDIA GTX 1080Ti, NVIDIA Tesla K80, NVIDIA Tesla V100). The access to the cloud instances was provided by the NASA Frontier Development Lab, its numerous sponsors, and a Google Cloud Academic Research Grant. We processed a total of 240,401 NAC images to achieve global coverage, totaling to ∼64 Tpixels and ∼7.5 TB of data.

Limitations of the deep learning-driven approach

The limitations of CNN-driven rockfall detection and mapping have been extensively discussed in previous work (Bickel et al., 2018). The main limitations are: (1) spatial gaps between NAC images due to incomplete coverage or poor image selection, (2) unfavorable lighting conditions (shadows), (3) bad images (noise-only), and (4) poor performance of the CNN (mis-classifications or missed detections). All possible steps were taken to minimize the influence of these limitations, such as the implementation of a routine that discards bad NAC images and the minimization of mis-classifications (false positives) by selecting a CNN confidence level that achieves high detection precisions while maximizing recall. With the selected 60% confidence level, M5 achieves an expected recall between 0.44 and 0.69 and a precision of around 0.98, meaning that a portion of rockfalls is not detected (false negatives) and that there is a limited potential for false detections to occur (false positives) (Bickel et al., 2018).

Global analysis of rockfall distribution

The results from the global CNN-driven rockfall mapping were analyzed in combination with other relevant data and maps in an open-source Geographic Information System (QGIS). Auxiliary data included a global LRO wide angle camera mosaic (Wagner et al., 2015), a Digital Terrain Model (Scholten et al., 2012), and a geologic map by the United States Geologic Survey (USGS, 2013; Fortezzo, Hare, 2013) - version May 2019. Other data were retrieved from the LROC vector data archive, such as shape file data for highland-mare boundaries (Nelson et al., 2014), craters between 5 and 20 km in diameter (Povilaitis et al., 2017), the locations of Copernican craters (Ravi et al., 2016), and lobate scarps (Nelson et al., 2014). Additional data was added to QGIS, specifically information about graben and other tectonic features (French et al., 2015; Nahm, 2016; Nahm et al., 2018), volcanic edifices and features (Spudis et al., 2013b), craters between 1 and 5 km (Robbins, 2018), and craters >20 km in diameter (Kadish et al., 2011). Volcanic edifices on the Moon are predominantly regional topographic swells called shield volcanoes (Spudis et al., 2013b). These edifices have diameters of tens to hundreds of kilometers and elevations of several thousand meters, while their slopes are gentle with average angles of about 1°(Spudis et al., 2013b). Volcanic domes are similar in size to shield volcanoes but feature steeper slopes of up to 20°(Guest, Murray, 1976). Other volcanic features, such as sinuous rilles and pyroclastic vents, can feature even steeper slopes of up to ∼25°, with depths and widths of hundreds of meters (Howard et al., 1972). Tectonic features on the Moon with a topographic expression are, e.g., graben, wrinkle ridges, scarps, and faults with slope angles around ≤ 15° (Golombek, 1979) and lengths between hundreds to several thousands of meters (Nahm et al., 2018). Craters are the dominant topographic feature on the lunar surface, where the steepest slopes of >45° are usually associated with the youngest craters. Over time, the slopes of craters erode and degrade, resulting in slope angles <∼35° for pre-Imbrian craters, >3.8 Ga (Kreslavsky, Head, 2016).

Some of the auxiliary data used were not directly available as vector data and had to be digitized first (e.g., information from refs. Nahm (2016); Nahm et al. (2018); Spudis et al. (2013b)). In addition, some of the auxiliary data are incomplete or scarce, as they were not intended to provide information on a global scale. However, no other data are currently available, which means that the results of the geomorphic rockfall distribution analysis are controlled and potentially affected by the amount and quality of the available auxiliary data. Wherever possible and feasible, the imported information was updated and optimized. It

should be noted that some of the used auxiliary data have associated uncertainties and, potentially, errors, such as, for example, the crater map with diameters between 1 and 5 km (diameter)(Robbins, 2018). The mapping of other features, such as craters <1 km, is beyond the scope of this work and has not been performed. As more accurate, consistent, and global auxiliary data become available, the results of this study can be updated and improved. We worked with the Moon2000 reference system in a (1) equi–rectangular, (2) north polar–stereographic, or (3) south polar–stereographic projection system, depending on the type of analysis and the type and properties of the used auxiliary data. As geomorphic features tend to overlap, e.g., small craters tend to be located in larger craters, all feature polygons were dissolved, i.e., all overlapping polygons were merged, in order to avoid double counts in overlapping polygons. The geologic map (USGS, 2013; Fortezzo, Hare, 2013) was refined by removing a number of overlapping polygons in the region around 50° W and 50° E (50° N to 50° S) and merging the six individual maps to create a seamless, consistent, and global map. For the analysis, the global geologic map (USGS, 2013; Fortezzo, Hare, 2013) was used in (1) an equirectangular (45° N to 45° S, maps I-0703, I-0948, I-1034, and I-1047), (2) a north polar-stereographic (45° N to 80° N, map I-1062), or (3) a south polar-stereographic projection (45° S to 80° S, map I-1162). Owing to the challenging polar illumination conditions, we expect a reduced number of detections in the region poleward from ∼75° N to ∼75° S, but we included latitudes up to 80° N and 80° S in the analysis to preserve its completeness. Rockfalls were counted in eight temporal classes (epochs): Copernican, Eratosthenian, Eratosthenian-Imbrian, Imbrian, Imbrian-Nectarian, Nectarian, Nectarian-pre-Nectarian, and pre-Nectarian. Owing to inconsistencies in the geologic map, a small number of classes needed to be discarded, e.g., a null class as well as the pre-Imbrian class, as it could not be classified as Imbrian-Nectarian, Nectarian, Nectarian-pre-Nectarian, or pre-Nectarian. The spatial density of the mapped rockfall features has been calculated in two different ways: (1) per 1° by 1° or 2° by 2° quadrangle and (2) per square kilometer. Metric 1 has been applied for the global spatial density analysis and visualization, as the counts per quadrangle (ranging from 0 to >300 rockfalls) are easier to comprehend than the counts per square kilometer ($\sim 4.0E^{-03} - 12.9E^{-03}$ rockfalls/km^2). In addition, a spatial resolution of one square kilometer would result in a small spatial representation of rockfall clusters in the global map. Metric 2 has been applied to express the normalization of the rockfall counts over their host area (geomorphic or geologic), as these are usually provided in square kilometer. In either case, the spatial densities are calculated considering the projection system of the GIS.

Estimation of rockfall diameter

The used CNN predicts a rectangular bounding box for each detected rockfall (see Supplementary Figure A.35). Based on the diameter of a box and the spatial resolution of the used image, we reconstructed an approximation of the boulder's diameter (Bickel et al., 2018). The used transformation function has been calibrated using several landmark boulders in combination with detections of these landmark boulders in different images with a large variety of spatial resolutions, ranging from ∼0.4 to ∼1.5 m/pixel.

Estimation of rockfall driven erosion rates

We use the rockfall counts per geologic epoch (eight bins, as described above) to qualitatively assess their erosional state, where more rockfalls indicate a higher advective erosion rate and fewer rockfalls indicate a lower advective erosion rate. The count for each epoch has been plotted in the temporal center of its respective epoch as well as at the borders between epochs (see Figure 3.3). We applied a power law fit to the plotted data and found a quantitative description of the approximated age and erosional state of lunar topography based on the spatial density of rockfalls, described with:

$$\gamma_{rockfall} = 2.636a^{0.813} \tag{3.1}$$

with a as the age in Ma and $\gamma_{rockfall}$ as rockfalls per square kilometer (the spatial rockfall density) (Figure 3.4). It has to be noted that Equation 3.1 represents a first-order approximation, as the fit will change if the underlying timescale changes and as it depends on the quality of the used geologic map (for the rockfall counts, see Supplementary Figure A.34). The fit also depends on the performance of the used CNN, i.e., its recall and precision: Equation 3.1 should only be applied in combination with rockfall counts made by CNN M5 (used for this study) — a human will perform differently, potentially biasing an age estimate derived with Equation 3.1. The normalization of Equation 3.1 with the Copernican spatial rockfall density results in a model-independent equation:

$$\%\ rockfall\ relative\ to\ Copernican = \frac{2.636a^{0.813}}{14.9E^{-3}} \tag{3.2}$$

where at an age of 500 Ma the relative density is ∼1, at 1.5 Ga ∼0.5, and at 3.2 Ga ∼0.25. Interestingly, our quantitative best fit agrees with the qualitative conclusion of an Apollo-era study which suggested that lunar mass wasting tempers off over time and that this trend could be described with a logarithmic fit, based on the assessment of Apollo 10 imagery (Pike, 1971). The measure of spatial rockfall density could be combined with other methods to estimate crater age, such as topography diffusion (Fassett, Thomson, 2014).

Acknowledgements

The authors would like to thank Emily Law, Natalie Gallegos, and the rest of the Solar System Treks team for providing access to LRO's NAC image archive via JPL's Moon Trek api and for their general support. The authors gratefully acknowledge the support by the NASA Frontier Development Lab — and its numerous sponsors — with computational resources on the Google Cloud Platform. This work has been supported with a Google Cloud Academic Research grant and an NVIDIA Academic GPU grant. One of the authors (V.T.B.) further acknowledges the financial support by the Engineering Geology group, Department of Earth Sciences, ETH Zurich, and the International Max Planck Research School (IMPRS) at the Max Planck Institute for Solar System Research (MPS). Parts of the NAC image selection algorithm have been developed as part of the SpaceHack Vol.1 in Goettingen that has been held in partnership with MPS, NASA JPL, SerNet, and GWG in May 2019.

3.2 Global Drivers and Transport Mechanisms of Lunar Rockfalls

Submitted to the Journal of Geophysical Research: Planets
Bickel, V.T., Aaron, J., Manconi, A., Loew, S., in review - might be subject to change

Abstract
The long- and short-term drivers and transport mechanisms of lunar rockfalls are currently not well understood, but could provide valuable information about the geologic processes that still shape the surface of the Moon today. Here we compare the global distribution of rockfalls with relevant geophysical data, such as seismic, topographic, thermal, gravity anomaly, and tidal displacement datasets. We show that rockfalls predominantly occur 1) on equator-facing slopes and thus in regions with large thermal amplitudes, 2) on slope angles well above-average (Δ $\sim$8°), and 3) in regions with above-average surface roughness. We do not observe a qualitatively or statistically relevant relation between rockfall abundance, monitored Apollo-era shallow seismic activity, and the distribution of visible tectogenetic features. Informed by our global analysis, we conduct a targeted, in-depth study of 687 rockfall boulders and trajectories in 13 sites across the Moon, including seven craters, two volcanic vents, two tectonic structures, and two unclassified geomorphic regions. We identify 4 different source regions types and note that rockfall occurrence is controlled by the source region type which in turn is controlled by surface age rather than geomorphic context. We find that rockfall trajectories are mainly controlled by the trigger energy and the geometry of the slope. Our results suggest that erratic small-scale impacts (mainly in old, Imbrian-Nectarian, shallow terranes), aided by solar-induced thermal fatigue of fractured bedrock (mainly in young, Copernican-Eratosthenian steep terranes), were the dominant, global-scale long- and short-term drivers of rockfalls in the Moon's recent geologic past.

Introduction

Lunar rockfalls are ubiquitous mass wasting features that were first observed in Lunar Orbiter high-resolution photographs in the late 1960s (Filice, 1967; Eggleston et al., 1968; Moore, 1970). Rockfall events, which have been previously referred to as block falls or rolling boulders, involve the detachment of a boulder or rock mass from an elevated source region, which then slides, bounces and rolls down the local topographic gradient, ultimately depositing downslope. Despite the fact that these features were recognized in the late 1960's, all early studies have only examined rockfalls in relatively small geographic areas on the lunar surface, because of a lack of available high resolution imagery (Eggleston et al., 1968; Hovland, Mitchell, 1973). Due to this, the characteristics of source regions, as well as the mechanisms that govern the failure and runout of lunar rockfall remain largely unknown. After a $\sim$40 year high-resolution imagery hiatus, the NASA Lunar Reconnaissance Orbiter's (LRO) Narrow Angle Camera (NAC) started to downlink high-resolution, optical imagery with a nominal spatial resolution of 0.5 m/pixel in 2009 (Robinson et al., 2010). The extensive NAC image archive enabled new studies of lunar surface processes such as rockfalls (Figure 3.5 shows an exemplary boulder with track from Taurus Littrow valley; Figure 3.14 features additional examples). Displaced boulders can feature distinct, largely uneroded tracks, which indicate that they have been displaced in the recent geologic past, i.e., less than $\sim$1.55 to $\sim$35 Ma ago (Arvidson et al., 1975b; Hurwitz, Kring, 2016; Kumar et al., 2019b).

In the Apollo-era (1960s and 1970s) there were many potential mechanisms hypothesized as the drivers of lunar rockfall detachment, including erosion through micro-impacts, thermal breakdown, moonquakes, and impact events (Hovland, Mitchell, 1973; Titley, 1966). More recently, Xiao et al. (2013) used LRO NAC imagery to map $\sim$50 rockfalls across the surface of the Moon, and argue that seismic activity and meteoritic impacts are the main long- and short-term causal drivers of mass wasting features, including rockfalls. Here, a 'long-term driver/causal factor' or 'preparatory causal factor' describes ground conditions and processes that reduce (slowly or rapidly) the stability of potentially unstable rock compartments until failure occurs (weathering), while a 'short-term driver/causal factor' or 'trigger' describes a process that ultimately initiates the release of a boulder (erosion) (Popescu, 1994). The usage of the terms 'long- and short-term driver' is required, as the available data cannot be used to distinguish clear triggers for the vast majority of cases. Kumar et al. (2013, 2016) identified a number of rockfalls in Schrödinger Basin and suggested that these events have likely been triggered by seismicity and meteoritic impacts, due to their proximity to thrust faults and small impact craters, respectively. More recently, Kumar et al. (2019b) and

Mohanty et al. (2020) looked at rockfalls in Laue crater and in the proximity of Mare Orientale which are located next to two extrapolated Apollo-era shallow moonquake epicenters from January 3rd, 1975 and December 9th, 1972, respectively. They argue that the presence of rockfalls in these regions is connected to seismicity along lobate scarps, wrinkle ridges, and ring faults in the area, i.e., are predominantly seismically triggered. Similarly, Watters et al. (2010) and Watters et al. (2019) use the abundance of rockfalls on or close to tectogenetic features such as lobate scarps as indicators for present-day seismic activity in the respective regions. In contrast, Valantinas, Schultz (2020) do not observe any rockfalls on or in the direct vicinity of presumably seismically active wrinkle ridges (extensional faults), adding that the slope angles of these tectonic features might be too low for boulders to start moving, even when experiencing ground motion.

Rockfalls have been studied on other planetary bodies as well, such as Mars. Roberts et al. (2012) noticed that rockfall and boulder abundance and size vary across the Cerberus Fossae fault system, leading them to suggest that these events have been triggered by local seismic shaking. Due to an apparent lack of uniformly distributed boulder sizes, they specifically exclude temperature- and climate-related triggers for rockfalls in the Cerberus Fossae fault system. In strong contrast, Tesson et al. (2020) analyzed the spatial distribution of a series of rockfalls as a function of latitude and found that events mainly occur on N- and S-facing, as well as equator-facing slopes, indicating that solar-induced thermal breakdown of bedrock plays a crucial role in rockfall occurrence on Mars. Martian and lunar rockfalls could potentially share their physical drivers, as in contrast to Earth, both planetary bodies lack precipitation events in their most recent geologic past, and feature substantial evidence of impact-related processes as well as strong temperature amplitudes. Previous studies observed that solar-induced thermal breakdown can drive rockfall occurrence on Earth as well (Collins, Stock, 2016; Collins et al., 2018).

Once detachment has occurred, lunar rockfalls rapidly move downslope, leaving distinctive tracks across the lunar surface. On Earth, rockfall transport generally initiates with a period of free fall, followed by bouncing, rolling and sliding, depending on boulder shape and topographic gradients (Evans, Hungr, 1993). On the Moon, energetic triggering (through meteorite impacts) and generally low topographic gradients may influence rockfall transport mechanisms, although little is known about this at present. The tracks of displaced boulders were used to estimate some of the geomechanical properties of the lunar regolith in preparation of the Apollo missions (Moore, 1970; Hovland, Mitchell, 1973). More recently, lunar rockfall tracks mapped in NAC imagery have been used to estimate geomechanical properties of regions of increased exploration interest, such as large pyroclastic deposits (Bickel et al., 2019), sunlit south polar regions (Bickel, Kring, 2020), and south polar permanently shadowed regions (Sargeant et al., 2020). It is important to note that all conclusions concerning rockfall drivers, on the Moon as well as on other celestial bodies, are based on observations and datasets with significant spatial limitations, and thus suffer from a strong observational bias. In particular, the majority of studies do not distinguish between long- and short-term rockfall initiation processes, and do not present detailed analyses of the characteristics of rockfall source regions. Additionally, studies of lunar rockfall transport mechanisms have mostly focused on specific geographic regions, and an understanding of the prevalence of the various kinematic modes, typical runout lengths, boulder shapes and slope angles at deposition across the surface of the Moon is largely missing.

Recently, Bickel et al. (2018, 2020b) developed a method to automate rockfall mapping in satellite imagery using a convolutional neural network, and used that tool to map the global distribution of lunar rockfalls in more than 250,000 NAC images. For the first time, a global study of lunar rockfalls and their drivers was possible (Bickel et al., 2020a). Based on the observation that the total number of rockfalls as well as the spatial density of rockfalls is significantly increased in impact craters, Bickel et al. (2020a) argue that impact processes are the main driver of lunar rockfall occurrence. However, the majority of lunar rockfalls did not have an obvious trigger, and other preparatory factors (long-term drivers) may contribute to the occurrence of rockfalls.

This work aims at analyzing the 136,610 rockfalls mapped by Bickel et al. (2020a), in order to better understand the boulder source regions, the short- and long-term initiation, and the transport mechanisms that govern lunar rockfall occurrence on a global scale. This is achieved through combining the rockfall catalog from Bickel et al. (2020a) with global information about the geologic, seismic, thermophysical, topographic, gravitational, and tidal properties of the Moon. Moreover, we perform a detailed local analysis of 687 rockfalls across 13 selected focus regions to study details of rockfall source regions and transport processes which are not resolvable on large spatial scales. The results of this work have important impli-

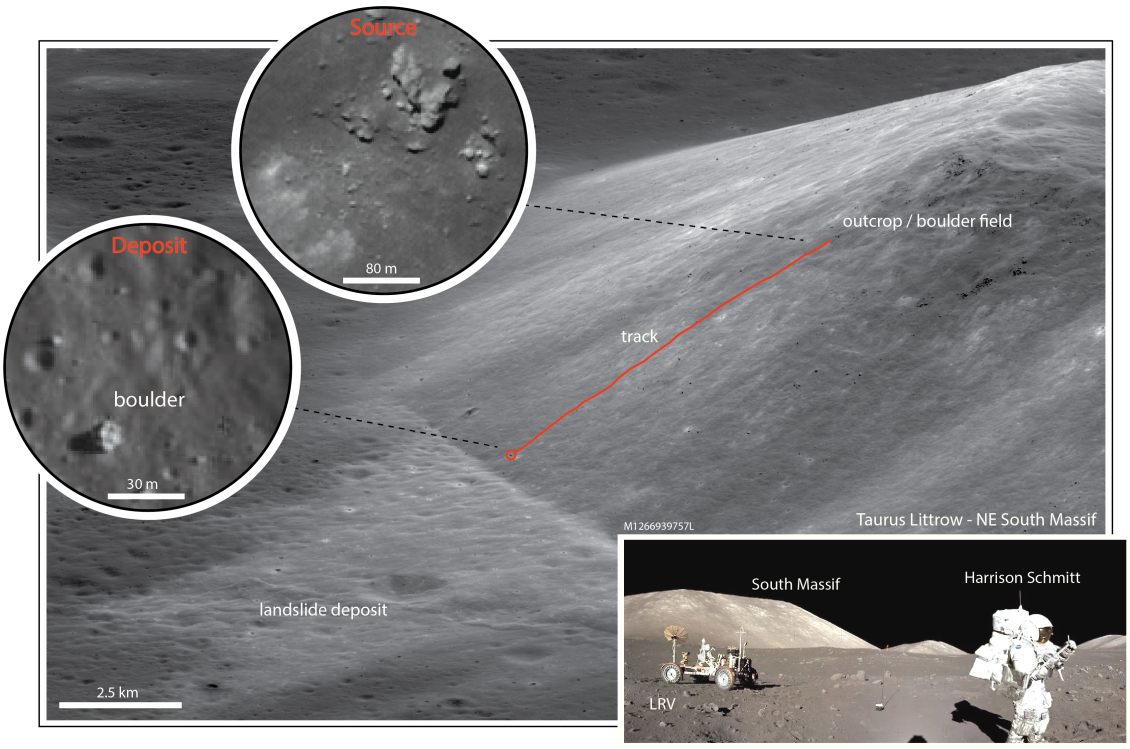


Figure 3.5: LRO NAC oblique image of an example rolling boulder/rockfall on the slope of the South Massif in Taurus Littrow valley (mean slope angle of ∼25°), the Apollo 17 landing site (image taken towards the southeast). A bright landslide deposit is visible as well. The high emission angle illustrates the dramatic topography (oblique photograph): the South Massif is ∼2300 m tall, i.e., is ∼500 m higher than the Grand Canyon is deep. An Apollo 17 Hasselblad image further illustrates the local topography (see inset, image taken towards the west). The marked rolling boulder/rockfall event occurred after the landslide. Boulder and track are marked in red; the circular insets show (sub)nadir LRO NAC close-ups of the source and deposition regions. Due to the viewing geometry the scale bar only represents an approximation. Image credits: LROC/ASU/GSFC and NASA.

cations for understanding erosion processes on the Moon and other airless planetary bodies.

The paper is structured as follows. Section "Datasets" introduces the datasets that have been used for the global and local scale analyses, section "Methods" describes the applied methodology and the selected focus regions, and section "Results" reports the results, which are discussed in section "Discussion" and concluded in section "Conclusion".

Datasets

We use a variety of existing, global geophysical datasets for this study. Some of these datasets are only used for the global analysis, some only for the local analysis, some for both. In order to avoid feature distortion issues at very high latitudes (e.g. affecting slope aspect determination), all direction-sensitive, non-latitude dependent datasets, are re-projected to a conformal Mercator projection before they were used for the global analysis. All other datasets used for the global analysis are in a default equirectangular projection (Moon2000). All datasets used for the local study are either in a regular equirectangular projection (Moon2000) or a polar stereographic projection (Moon2000), depending on the geographic location of the area of interest, as further discussed in the following chapters.

Primary rockfall dataset
Bickel et al. (2020a) created a global catalog of lunar rockfalls using a convolutional neural network (CNN), which mapped 136,610 rockfalls. This dataset consists of point locations of each mapped rockfall, scattered across the surface of the Moon from 70°N to 70°S, as well as CNN-derived meta annotations, such

as estimated boulder diameter.

Auxiliary datasets
We used subnadir and oblique high-resolution imagery from LRO's NAC (Robinson et al., 2010) for the detailed local geologic site analyses. Subnadir images were processed and map-projected using ISIS3, either to an equirectangular or a polar stereographic projection, depending on the location of the area of interest. Processing steps included the default steps: lronac2isis, spiceinit, lronaccal, lronacecho, maptemplate, cam2map, gdal_translate. The spatial resolution of the projected subnadir images range from 0.49 to 1.53 m/pixel. Oblique images were downloaded as PTIF versions and manually stitched to form NAC left-right mosaics. The spatial resolution of the oblique images is difficult to define due to the high emission angle (ground sampling distance changes significantly across the image), but is lower than the resolution of the sub-nadir NAC imagery due to the increased distance between spacecraft and lunar surface.

Further, we use the 118 m/pixel LOLA DEM (Lunar Orbiter Laser Altimeter Digital Elevation Model) ('Moon LRO LOLA DEM 118m') (LOLA, n.d.) for the global and local analyses related to topography. For all analyses related to lunar surface temperature, we made use of global thermal maps created by Moseley et al. (2020a) from LRO DIVINER data, specifically maps of daily minimum temperature, daily maximum temperature, and the daily temperature amplitude. Here, the daily temperature amplitude describes the difference between the daily minimum (midnight) and maximum (noon) temperature value at each point on the lunar surface. We also include three thermophysical (anomaly) maps generated by a Variational AutoEncoder (Lord VAEder) (Moseley et al., 2020a). These maps entangle (and thus represent) different physical processes: a) solar thermal onset, b) thermal conductivity, and c) solar effective albedo. Solar thermal onset describes the time of local sunrise, i.e., this map visualizes how east-facing slopes are illuminated first, and west-facing slopes are illuminated last during a lunar day. We point out that this dataset is not sensitive to N- and S-facing slopes. The thermal conductivity map describes how the surface maintains its temperature over the course of a lunar night, i.e., it describes the thermal inertia (and thermal conductivity) of the surface, where young, rocky regions usually have high thermal conductivity. The solar effective albedo map describes how hot the surface becomes during lunar noon, which is a function of the albedo of the surface and the influence of local topography, which affects the amount of received solar illumination. All six temperature-related maps have been constructed from ∼425 billion level 1 DIVINER measurements taken over 9 years that have been resampled to ∼250 m/pixel (modified from Moseley et al. (2020a). We further use a DIVINER-derived rock abundance map retrieved from the PDS with a spatial resolution of ∼250 m/pixel (Bandfield et al., 2011).

We include maps of the free-air (unprocessed gravity anomalies) and Bouguer gravity (gravity anomalies with topography removed) disturbances created using the GRGM1200A gravity model (Lemoine et al., 2014). These two maps have a spatial resolution of ∼2000 m/pixel. Additionally, we utilize maps of estimated lunar radial tidal displacements generated by Thor et al. (2020), which is based on LOLA altimetry data that has been processed to retrieve vertical surface displacements (tides), and of nightside surface albedo (Lyman-alpha wavelength bands), which is based on LAMP (Lyman Alpha Mapping Project) far-ultraviolet data (Gladstone et al., 2012). The latter has a spatial resolution of ∼1000 m/pixel. We further use Nakamura et al. (1979)'s and Watters et al. (2019)'s databases of extrapolated shallow moonquake epicenters as well as Thompson et al. (2017)'s wrinkle ridge database, and digitized the global locations of young lobate thrust fault scarps from Watters et al. (2019). All used global auxiliary maps are showcased in the supplementary information, Figs. A.36 through A.40, and are summarized in Table A.7.

Methods

Global analysis
In order to understand potential long- as well as short-term rockfall drivers across the surface of the Moon, we first imported all above-listed global, auxiliary datasets into QGIS (https://qgis.org/de/site/). Using the LOLA DEM (LOLA, n.d.), we created two additional datasets for the analysis, specifically a global slope aspect and slope angle map, using QGIS' built-in functions "Raster/Analysis/DEM/Slope" and "Raster/Analysis/DEM/Aspect". We subdivide each global map into five individual geographic regions (latitude bands): 1) equatorial (15°N to 15°S), 2) northern sub-equatorial (15°N to 40°N), 3) northern sub-polar (40°N to 70°N), 4) southern sub-equatorial (15°S to 40°S), and 5) southern sub-polar (40°S to 70°S).

To analyze global drivers of lunar rockfall, we compare the distribution of the attributes of a given geophysical dataset at the locations of deposited rockfalls with the distribution of attributes of the entire dataset, per latitude band (as defined above). If both distributions match, then the attributes derived at the rockfall locations are sampled randomly, meaning that this particular geophysical property does not influence the distribution of rockfalls in a given latitude band (with the spatial resolution and quality available). In contrast, a mismatch of both distributions could indicate that this particular geophysical property does have an influence on the rockfall distribution. To do so, we used the rockfall catalog derived by Bickel et al. (2020a) to extract the values (attributes) of each global map at each rockfall location. We refer to the distributions of these extracted attributes (values derived at all rockfall locations) as "distribution of dataset <type> at-target", or short "at-target". Similarly, we refer to the attributes derived from the entire dataset as "background distribution of dataset <type>", or short "background".

Next, we investigated the potential role of lunar seismicity as a short- and long-term driver. To do this, we analyzed our global database of lunar rockfall using similar methodologies that previous researchers have used to argue that seismicity is an important driver locally (Kumar et al., 2019b; Mohanty et al., 2020). As summarized in the introduction, this previous work has been partly based on spatial correlations between the distribution of rockfall and known tectonic features and shallow moonquake epicenters (based on Apollo-era seismic data). In the present work, we perform two separate spatial correlations: (1) a visual, qualitative comparison of the locations of rockfall hotspots with vector data that describes the geographic position and extent of visible lobate scarps (digitized from Watters et al. (2019)), wrinkle ridges (Thompson et al., 2017; Valantinas, Schultz, 2020), graben (Nahm et al., 2018), multi-ring basins larger than 200 km in diameter (Kadish et al., 2011), and the extrapolated Apollo-era shallow moonquake epicenters (Nakamura et al., 1979; Watters et al., 2019); (2) a statistical, quantitative analysis of the relation of spatial rockfall frequency and seismic event magnitude or stress drop.

For (2), we first derived the distances between the 28 original Apollo shallow moonquake epicenter locations (Nakamura et al., 1979), the 12 recently confirmed, re-located Apollo-era epicenter locations (Watters et al., 2019) and all rockfalls mapped by Bickel et al. (2020a). We then used three different spatial buffers (0.5°, 1°, and 5°radius around each epicenter, i.e., ∼15, ∼30, and ∼150 km at the equator, respectively), and determined the number of rockfalls within each buffer. We specifically highlighted the strongest recorded shallow moonquake (magnitude 3.2) from January 3rd, 1975, as well as the December 9th, 1972 event close to Mare Orientale (magnitude 1.2). We then assessed whether the rockfall density around epicenter locations is anomalously high, by comparing rockfall densities at epicenter locations to rockfall density at 1,000 randomly selected locations, using the same three spatial buffers. Finally, we compare the relation between seismic event magnitude and the number of rockfalls around each epicenter, within the three spatial buffers. Due to the nature of the available datasets, distance has been measured in degrees (°).

Local geologic and geomorphic analysis

In order to further study the characteristics of rockfalls on a local scale we selected and performed measurements in 13 areas of interest (AoIs) across the Moon (Bickel, 2021). These specific locations have been selected because they are rockfall hotspots and belong to one of the four relevant lunar geomorphic (sub)classes as outlined by Bickel et al. (2020a): crater (impact-caused, -induced, -ejected), volcanic vent, tectonic structure, or other, unclassified geomorphic context. We included an increased number of impact-related AoIs because the vast majority of rockfalls are located in impact craters (Bickel et al., 2020a). We manually mapped 687 rockfalls in these AoIs, where we expect that an estimated ∼60 to 70% of these manually mapped features are also present in the global rockfall catalog derived by Bickel et al. (2020a) used for the global study, based on the recall (percentage of rockfalls found in a testset) of the deployed CNN (Bickel et al., 2018). All AoIs are characterized in more detail in Table 3.1 and their locations are shown in Figure 3.6. Local overview maps of all AoIs are showcased in the Supplementary Information, Figure A.41.

The local geologic analysis consists of a series of detailed observations and measurements made in high-resolution, subnadir NAC imagery. Where available, oblique NAC imagery has been used to gain a qualitative understanding of the overall topography of an area of interest as well as of the structure and geology of the source and deposition regions of rockfalls, thus, complementing the main analysis. Using subnadir NAC imagery, we measured a large number of rockfall and track characteristics, specifically: boulder short axis, boulder long axis, boulder shadow length, track length, slope angle at source and at deposition, and the elevation drop from source to deposition (using the LOLA DEM).

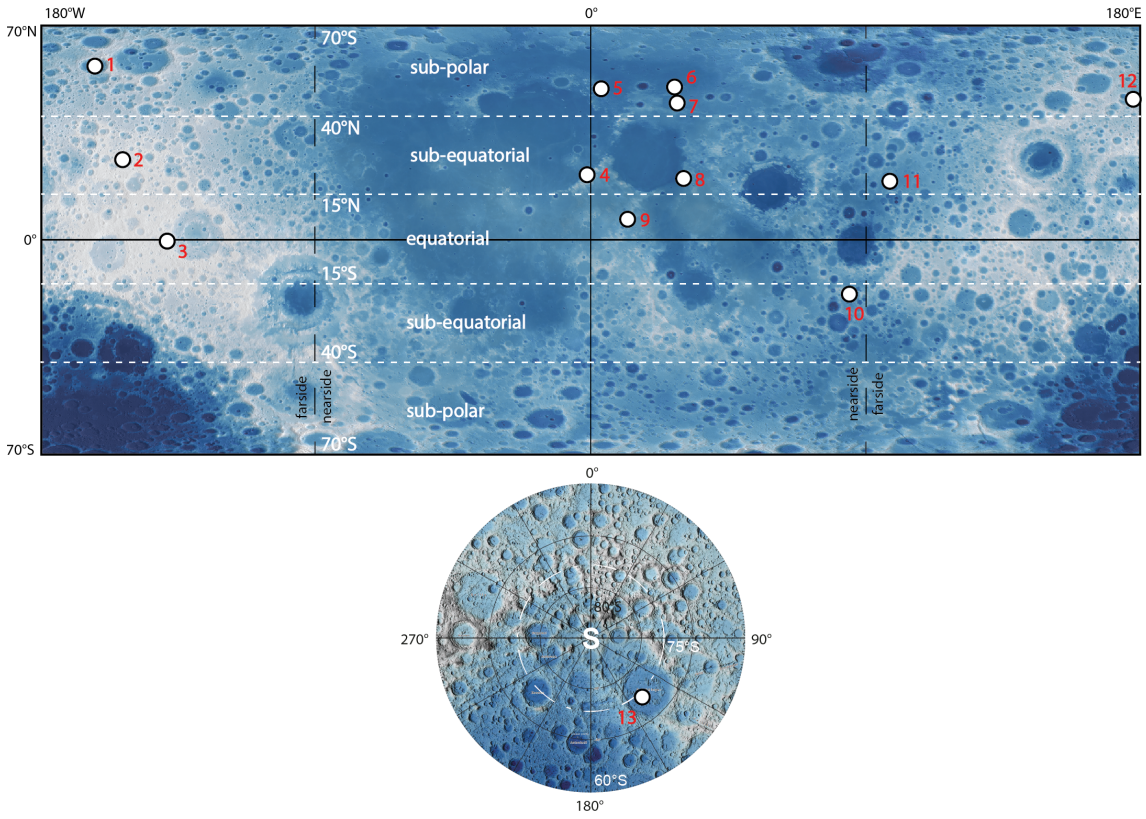


Figure 3.6: Overview map of all 13 local AoIs (white dots), in equirectangular and south polar stereographic projections (bottom): 1-Rowland R crater, 2-Ingalls crater, 3-Vavilov crater, 4-Montes Apenninus, 5-Vallis Alpes, 6-Baily vent, 7-Buerk crater, 8-Taurus Littrow, 9-Rima Ariadaeus, 10-Gibbs crater, 11-Giordano Bruno crater, 12-Duner crater, 13-Schrödinger basin vent. The white dashed lines visualize the geographic classification as used for this study: equatorial, sub-equatorial, and sub-polar regions (additionally indicated with white labels). Topographic background map modified from Hare et al. (n.d.), showing low elevations in blue and high elevations in white.

We also recorded several qualitative aspects of the AoIs and rockfalls, such as the texture and roughness of the slope substrate along each rockfall trajectory (regolith, debris), the rockfall kinematic (bouncing, rolling, sliding), the geologic characteristics of the source region (cliff, outcrop, boulder field, plain slope), if a rockfall deviated off the steepest descent path during its displacement (yes, no), the geologic unit, and the geologic age of the host surface (Pre-Nectarian, Nectarian, Imbrian, Eratosthenian, Copernican). Using these observations, we calculated a number of additional values, specifically: boulder height (using the shadow length and solar incidence angle), boulder volume (assuming an ellipsoidal shape), approximated boulder (macro-) sphericity (assuming an ellipsoidal shape, using the three orthogonal boulder axes), and the reach angle or Fahrböschung (the relation of vertical drop height and horizontal runout) (Heim, 1932) of each rockfall. We also derived accurate trajectories of two individual rockfalls, one in an impact-caused and one in an impact-ejected setting. For these two events, we created map- and longitudinal-views of their trajectories, which describe the spatial variation of jump heights, widths and kinematics.

We observe that the vast majority of rockfalls begin their displacement by sliding or rolling. In order to understand at what slope angle boulder movement initiation can occur without additional external forces (assuming exclusively gravitational acceleration) we apply a simplified limit-equilibrium planar slope failure analysis with:

$$F = \frac{\tan(\phi)}{\tan(\beta)} \tag{3.3}$$

assuming that sliding occurs when F $<$ 1, i.e., the driving forces (governed by the local slope angle β) are larger than the resisting forces (governed by the regolith's angle of internal friction ϕ), neglecting sinkage

Name	Geomorphic Context	Impact-driven class	N	Location	Rockfall Density rockfall/2x2° quadrangle	Geologic age
Buerk	Crater	Impact-caused	56	28.7°E, 45.0°N	499	Copernican
Giordano	Crater	Impact-caused	44	102.9°E, 35.9°N	94	Copernican
Duner	Crater	Impact-caused	15	178.9°E, 44.5°N	19	Nectarian
Ingalls	Crater	Impact-induced	62	-149.9°E, 24.1°N	58	Pre-Nectarian/ Nectarian
Gibbs	Crater	Impact-induced	66	85.0°E, -17.6°N	297	Nectarian
Rowland	Crater	Impact-ejected	71	-169.4°E, 52.5°N	221	Pre-Nectarian
Vavilov	Crater	Impact-ejected	77	-135.4°E, -6.1°N	60	Nectarian
Baily Vent	Volcanic	-	47	27.1°E, 49.5°N	156	Imbrian
Schrödinger Basin Vent	Volcanic	-	40	139.3°E,-75.3°N	19	Imbrian
Rima Ariadeous	Tectonic	-	31	12.0°E, 6.9°N	19	Imbrian
Alpes Vallis	Tectonic	-	71	3.2°E, 49.1°N	146	Imbrian
Taurus Littrow	Other	-	83	30.7°E, 20.1°N	75	Nectarian
Montes Appeninus	Other	-	25	1.4°E, 23.7°N	15	Nectarian

Table 3.1: Overview of the 13 areas of interest used for local geomorphic mapping, using 4 distinct geomorphic classes: 1) impact structures, 2) volcanic features, 3) tectonic features, and 4) unclassified geomorphic regions, per Bickel et al. (2020a). This study follows the typology for impact-driven rockfalls as recently suggested by Bickel et al. (2020a), i.e., impact-caused - a rockfall occurs in a crater as consequence of substantial, impact-caused fracturing of the upper crater rim but without obvious trigger -, impact-induced - a rockfall is triggered by a close, small- or large-scale impact event -, and impact-ejected - a rockfall is directly ejected from an impacting, small-scale meteoritic body. Rockfall density per Bickel et al. (2020a).

of the boulder. The literature reports a wide range of mare and highland regolith friction angles, ranging from 13 to 50°(Carrier et al., 1991). We use an estimate of ϕ=29°as derived by Bickel et al. (2019) who estimated the average angle of repose of lunar regolith by measuring the slope angle of inclines that are partially covered by deposits of regolith that flowed downslope, using high-resolution, LRO NAC-based elevation models. Boulders located on slopes that are steeper than the critical slope angle for sliding will start to move unless restrained by other factors, such as cohesion, micro-topography, or other obstacles, which may degrade through time.

Results

Global analysis

The global, GIS-based analysis provides a series of important findings, summarized in Figures 3.7 through 3.11. The geomorphic appearance of the Moon is dominated by (circular) impact craters, which means that the background distribution of slope aspect is uniform, i.e., equally distributed over north, east, south, and west. In contrast, the overall at-target (rockfall) slope aspect distribution is not uniform: around the equator more rockfalls appear to be located on N- and S-facing slopes. Further, rockfalls in the sub-equatorial regions are more abundant on equator-facing slopes, i.e., on slopes that receive more solar insolation and thus experience larger thermal amplitudes. Interestingly, E- and W-facing slopes appear to host more rockfalls in the sub-polar regions (Figure 3.7). The slope angle at-target distribution reveals that more rockfalls are located on steeper-than-average slopes, over all studied latitudes. Interestingly, the majority of rockfalls are located on slopes with angles less than ∼20°. It is important to note that all

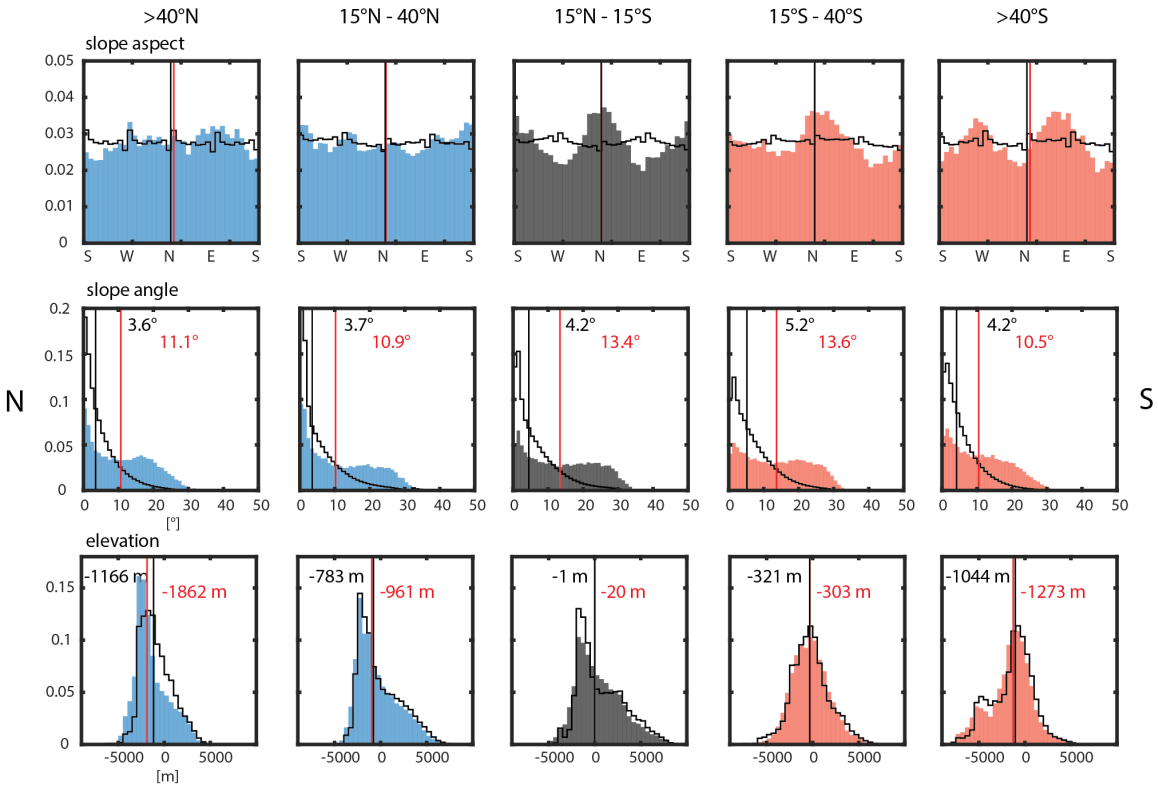


Figure 3.7: Comparison of at-target (colored) and background (black line) normalized (per dataset, i.e., row) distributions for absolute elevation, slope angle, and slope aspect as function of latitude (5 bins): equatorial (15°N to 15°S, black, center), northern sub-equatorial (15°N to 40°N, blue, center-left), southern sub-equatorial (15°S to 40°S, yellow, center-right), northern sub-polar (40°N to 70°N, blue, outer left), and southern sub-polar (40°S to 70°S, yellow, outer right). The red vertical line represents the at-target median, the black vertical line the background median, the respective numerical values are indicated, where applicable. All counts are normalized to facilitate a direct comparison.

at-target values are derived at rockfall deposition locations, i.e., these slope angles do not represent the global source region slope angle distribution. This will be addressed further when we present the results of the local analysis of the areas of interest. The absolute topographic elevation background and at-target distributions match relatively well, indicating that the absolute elevation does not significantly influence the abundance of rockfalls. We note that there is a lack of rockfalls in equatorial regions at elevations of ∼-500 to ∼2000 m; these elevations are predominantly occupied by the nearside maria. In the northern sub-polar regions we observe an over-abundance of rockfalls at elevations from ∼-1800 to ∼-5000 m; we attribute this to the presence of a large number of young, intra-mare impact craters which are among the locations with the highest spatial density of rockfalls on the lunar surface (e.g. craters Buerg, Hercules, Atlas, and Aristoteles)(Bickel et al., 2020a)(Figure 3.7).

The free-air and Bouguer gravity anomaly distributions generally match well, suggesting that gravity anomalies do not significantly influence rockfall abundance. We note a slight overabundance of rockfalls in southern sub-equatorial regions with Bouguer gravity values between ∼-500 and ∼-50 mGal, which could be caused by the two distinct rockfall hotspots located in Mare Orientale and Tsiolkovsky crater. There is a lack of rockfalls in the southern sub-polar regions at Bouguer gravity values between ∼-350 and ∼0 mGal, but we do not recognize a distinct physical reason for that observation (Figure 3.8). We further observe a slight difference between the tidal radial displacement background and the at-target distributions at various latitudes (Figure 3.8). The at-target distributions derived with the surface minimum and maximum temperature as well as the temperature amplitude generally match well, across all studied latitudes (Figure 3.9). We point out that we are only able to sample rockfall deposition locations, not their source regions, meaning that the extracted values are not entirely descriptive of the acting of thermal

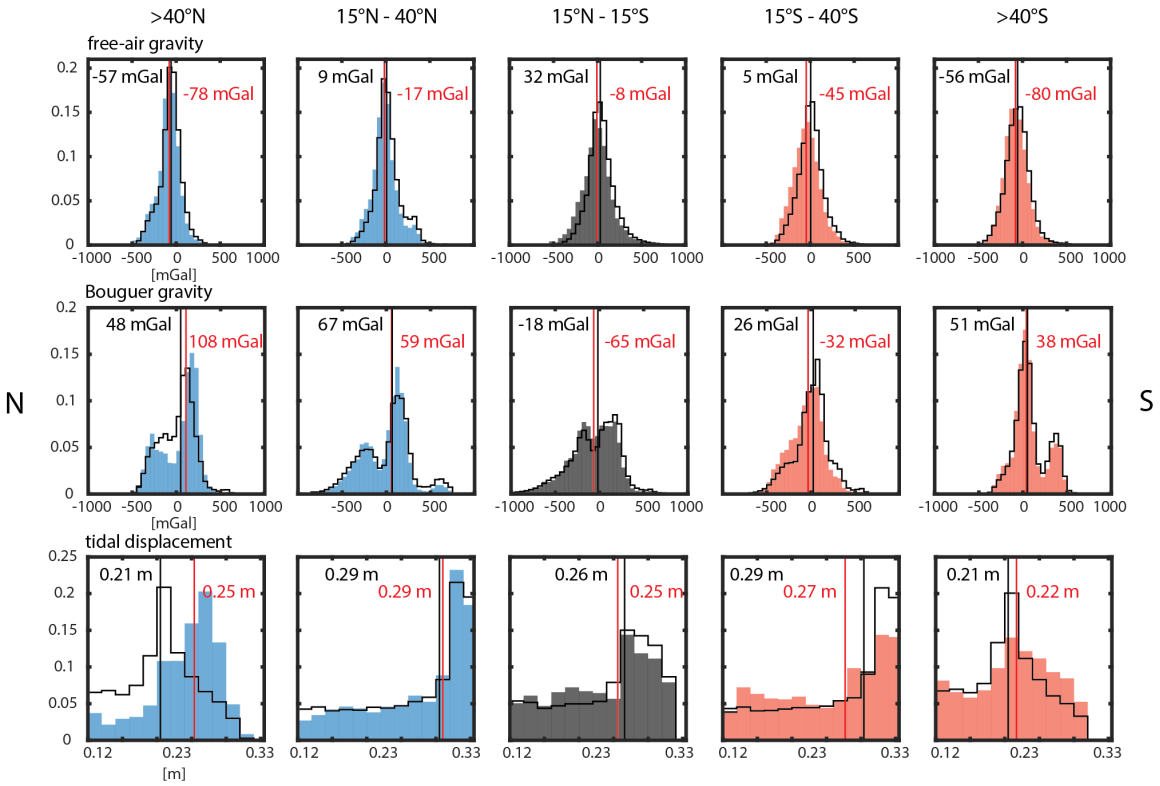


Figure 3.8: Comparison of at-target (colored) and background (black line) normalized (per dataset, i.e., row) distributions for free-air gravity, Bouguer gravity, and tidal displacement as function of latitude (5 bins): equatorial (15°N to 15°S, black, center), northern sub-equatorial (15°N to 40°N, blue, center-left), southern sub-equatorial (15°S to 40°S, yellow, center-right), northern sub-polar (40°N to 70°N, blue, outer left), and southern sub-polar (40°S to 70°S, yellow, outer right). The red vertical line represents the at-target median, the black vertical line the background median, the respective numerical values are indicated, where applicable. All counts are normalized to facilitate a direct comparison.

fluctuations at and around source regions. Figure 3.9 additionally shows that rockfalls occur in regions with thermal amplitudes ranging between ∼110 and ∼250 K or more, to a maximum of ∼290 K. The at-target distribution of the solar thermal onset is slightly shifted from the background distribution over all studied latitudes, indicating that more rockfalls occur on slopes which are illuminated in the morning and afternoon of a lunar day vs. during noon. In other words, more rockfalls are located on inclined, E- and W-facing slopes than in flat regions. We note that the solar onset map is not sensitive to illumination on N- and S-facing slopes (Moseley et al., 2020a). The surface thermal conductivity at-target distribution suggests that more rockfalls tend to be located in regions with lower thermal inertia and higher thermal conductivity, i.e., usually young and/or rocky regions (Figure 3.10). The subtle, absolute shift of the effective albedo at-target from the background distribution to lower values in equatorial and sub-equatorial regions suggests that 1) more rockfalls tend to be located in highland regions, which feature slightly lower effective albedo values as the mare regions in the used dataset (Moseley et al., 2020a) (see Figure 3.8), and 2) more rockfalls are located on equator-facing slopes. This supports observations in other auxiliary datasets, such as slope aspect (Figure 3.10).

The at-target rock abundance distribution shows that more rockfalls tend to occur in regions with increased rock abundance, i.e., in generally rougher terranes. This observation agrees with the observations made in the thermal conductivity dataset, mentioned earlier (Figure 3.10). The at-target and background distributions of nightside surface albedo generally agree well, while there is a shift in the equatorial region (Figure 3.11), indicating that around the equator more rockfalls are located in regions with high surface (UV) albedo, i.e., in rocky and/or young terranes, which usually are UV-bright. This observation further supports our findings in the rock abundance and thermal conductivity datasets (Figure 3.10). All auxiliary

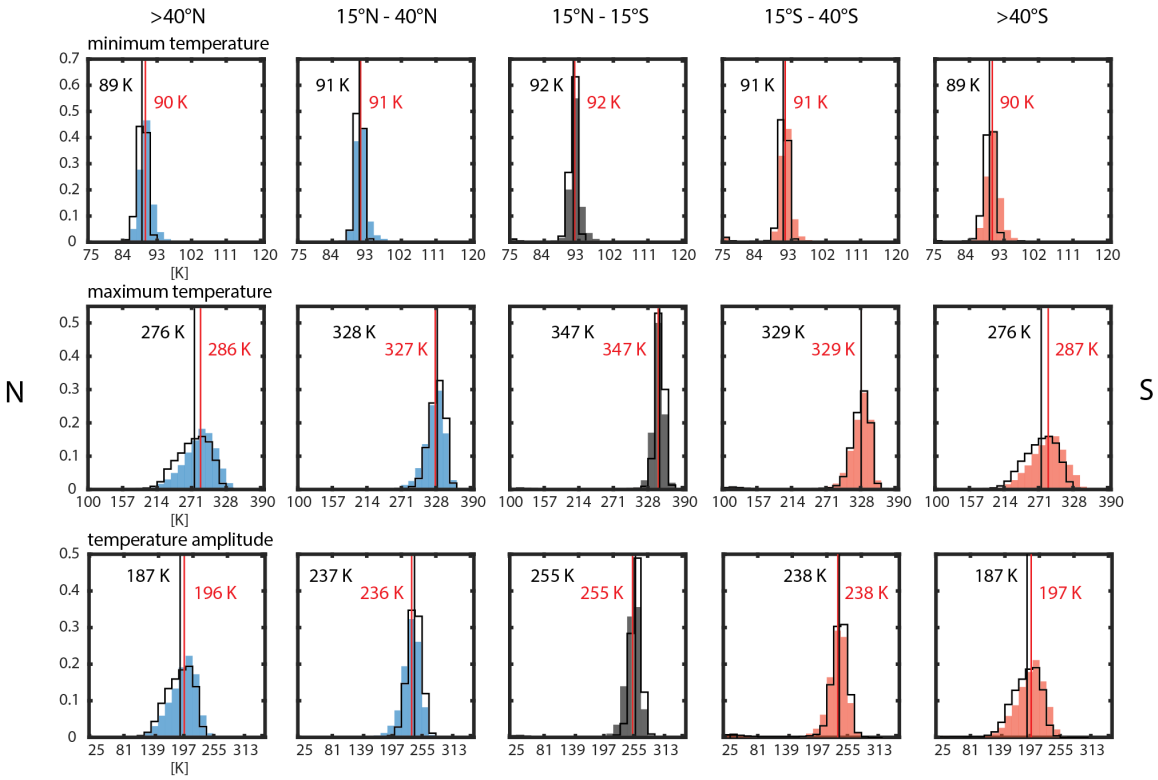


Figure 3.9: Comparison of at-target (colored) and background (black line) normalized (per dataset, i.e., row) distributions for minimum & maximum temperature and temperature amplitude as function of latitude (5 bins): equatorial (15°N to 15°S, black, center), northern sub-equatorial (15°N to 40°N, blue, center-left), southern sub-equatorial (15°S to 40°S, yellow, center-right), northern sub-polar (40°N to 70°N, blue, outer left), and southern sub-polar (40°S to 70°S, yellow, outer right). The red vertical line represents the at-target median, the black vertical line the background median, the respective numerical values are indicated, where applicable. All counts are normalized to facilitate a direct comparison.

maps used for the global analysis are shown in the supplementary information, Figures A.36 through A.40.

We further investigate how surface roughness and age influence rockfall size. Here, a young surface is defined by steeper slope angles, increased rock abundance (roughness), and increased thermal conductivity values. These parameters serve as a proxy for age as continuous micrometeorite bombardment and space weathering degrade exposed rocks, which decreases rock abundance, thermal conductivity, and slope angle values (Hoerz et al., 2020). The relations of estimated rockfall diameter and these three parameters at-target are shown in Figure A.42 in the supplementary information. We observe that rockfall diameters increase with decreasing thermal conductivity, decreasing rock abundance, and slope angle. In other words, estimated rockfall diameters are smaller in younger terranes and larger in older terranes, consistent with the findings of Bickel et al. (2020a).

In order to better understand the role of tectonic activity and moonquakes we visually analyzed the distribution of rockfall hotspots and visible tectonic structures, including lobate scarps, wrinkle ridges, graben, and basins >200 km, as well as Apollo-era shallow moonquake epicenters (Figure 3.12). This qualitative analysis shows that the geographic locations of rockfall hotspots, quake epicenters, and visible tectonic structures only partially overlap. For example, the accumulation of rockfall hotspots in the Lacus Mortis and Mare Frigoris regions are relatively well aligned with 5 Apollo-era epicenters as well as a number of lobate scarps and presumably active wrinkle ridges. However, a significant number of epicenter and tectonic feature locations do not overlap with rockfall hotspots. Notably, the moonquake with the highest magnitude (3.2) in the Laue crater region does not correlate with a rockfall hotspot.

We performed a statistical test to further improve our understanding of the influence of lunar seismicity

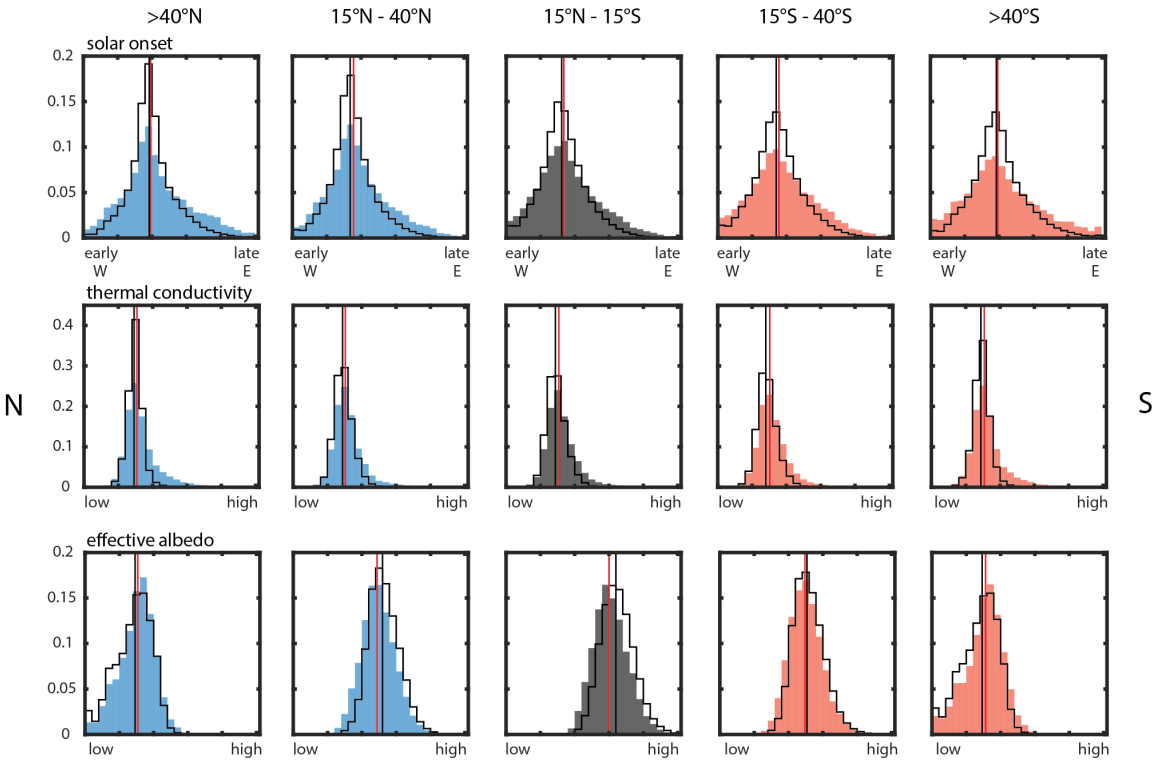


Figure 3.10: Comparison of at-target (colored) and background (black line) normalized (per dataset, i.e., row) distributions for solar onset, thermal conductivity, and effective albedo as function of latitude (5 bins): equatorial (15°N to 15°S, black, center), northern sub-equatorial (15°N to 40°N, blue, center-left), southern sub-equatorial (15°S to 40°S, yellow, center-right), northern sub-polar (40°N to 70°N, blue, outer left), and southern sub-polar (40°S to 70°S, yellow, outer right). The red vertical line represents the at-target median, the black vertical line the background median, the respective numerical values are indicated, where applicable. All counts are normalized to facilitate a direct comparison.

on rockfall occurrence, analyzing the number and distance distributions of rockfalls from Apollo-era quake epicenters as well as randomly selected locations. The results, showcased in Figure 3.13, reveal that the average number of rockfalls and distance average mean, standard deviation, and variance for all events, real quakes and random locations, and all spatial buffers are almost identical. Similarly, the test performed using only the Laue crater epicenter data (the Apollo event with the highest magnitude value, 3.2, Jan. 3rd 1975) does not show any statistical relation, just as the test with the Mare Orientale event (1.2, Dec. 9th 1972). The rockfall frequency and seismic event magnitude relation for all original and re-located Apollo-era events (Figure 3.12) does not reveal any clear trend either.

Local analysis

To overcome some of the limitations of the global analysis, such as the lack of information about source region types and slope angles, as well as boulder track trajectories, we further study 687 individual rockfalls that originate from 4 different types of source regions in the 13 AoIs considered, using subnadir and oblique NAC imagery. We label these source regions as: 1) cliffs, i.e., large-scale, continuous (intact), inclined to (near)vertical bedrock outcrops that extent over tens of meters, 2) outcrops, i.e., fractured bedrock outcrops with spatially limited extent, intermixed with closely spaced boulders, 3) boulder fields, i.e., accumulations of individual blocks that are not as closely spaced (that are e.g. part of ejecta blankets), and 4) plain slopes, i.e., smooth slopes without signs of bedrock outcrops or larger boulder fields and only a few scattered boulders. We note that there is a certain overlap between classes, as this classification is only based on qualitative geologic observations made in satellite images with limited spatial resolution. Figure 3.14 shows examples of the different source region types; in addition, Figure A.43 in the supplementary information shows an Apollo 17 ground-based photograph of a boulder field-type source region on the Taurus Littrow South Massif summit. It is important to note that all source region types occur

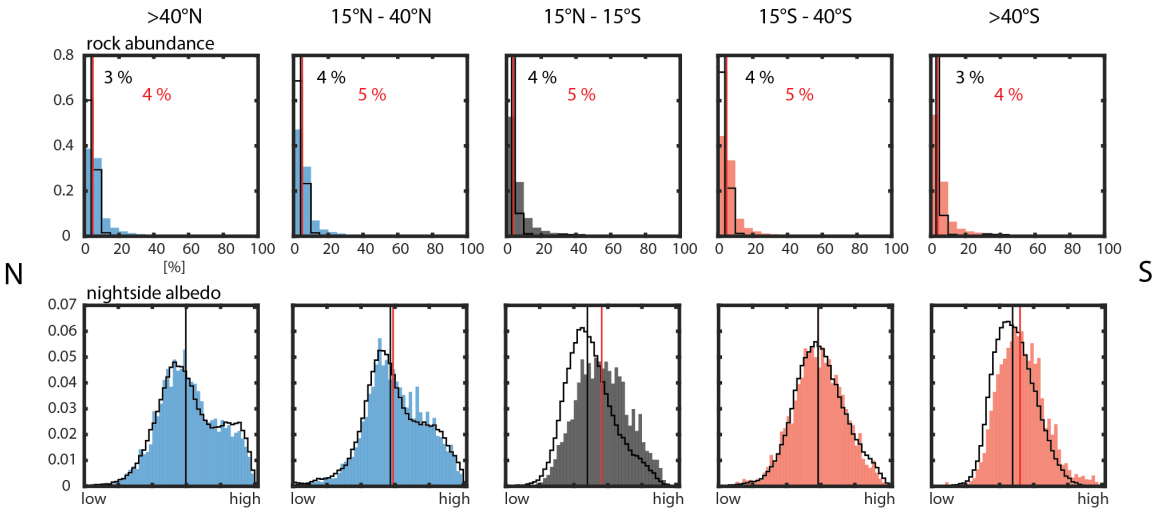


Figure 3.11: Comparison of at-target (colored) and background (black line) normalized (per dataset, i.e., row) distributions for rock abundance and nightside albedo as function of latitude (5 bins): equatorial (15°N to 15°S, black, center), northern sub-equatorial (15°N to 40°N, blue, center-left), southern sub-equatorial (15°S to 40°S, yellow, center-right), northern sub-polar (40°N to 70°N, blue, outer left), and southern sub-polar (40°S to 70°S, yellow, outer right). The red vertical line represents the at-target median, the black vertical line the background median, the respective numerical values are indicated, where applicable. All counts are normalized to facilitate a direct comparison.

in all geomorphic contexts, but cliff and outcrop source types predominantly occur in geologically young terranes (Copernican).

The analysis of the collected measurements across the AoIs (Figure 3.15) shows that source region slope angles are very similar across all analyzed geomorphic contexts, ranging between ∼15 and ∼35°with a mean of ∼24.9°across all regions (excluding impact-ejected rockfalls), which is close to the approximated angle of repose of regolith on lunar slopes (29°) as estimated by Bickel et al. (2019), among others. Only impact-ejected rockfalls feature a wider range of source region slope angles, from ∼0 to ∼35°, as they occur wherever an impactor strikes - they do not require a topographic gradient (mean source region slope angles are shown in Figure 3.15). A comparison with the globally-derived slope angle values is shown in Figure A.44. Using these measurements, we evaluated Eqn. 3.3 using the average source slope angle for each geomorphic context (and an internal friction angle of 29°), which resulted in F values of between 1.11 and 1.29. This basic, numerical experiment indicates that mean source region slope angles in all geomorphic AoIs are close to or slightly below the angle of repose (∼29°). We note that there are source regions with $F > 1$ across our AoIs, i.e., some source regions are steep enough for boulders to start moving without external force applied, considering the assumptions made.

Displaced boulders across all geomorphic regions feature similar shapes (sphericity between 0.8 and 1 assuming an ellipsoidal shape) and volumes (up to ∼1000 m^3 assuming an ellipsoidal shape) except for volcanic regions, which feature slightly more angular (sphericity between 0.6 and 1) and smaller boulders («1000 m^3) (average shape values are displayed in Figure 3.15). This could point to differences in the fracture networks (extent and spacing) that produce the boulders that ultimately get displaced. Boulders have very similar average dimensions across the AoIs as well, ranging from 5.95 x 3.5 x 3.0 m (volcanic-related) to 8.56 x 5.82 x 6.36 m (impact-related) (see Figure 3.15), agreeing with the global distribution of boulder diameters (∼7 to 10 m) as derived by Bickel et al. (2020a). The vast majority of rockfalls across the thirteen AoIs do not have an obvious trigger, independent of the geomorphic context. Only rockfalls that belong to the impact-induced and impact-ejected class feature distinct triggers, specifically small-scale, meter to hundreds of meter-sized, meteoritic impactors that either eject rockfalls directly or cause strong ground motion which in turn activates boulder detachment and/or displacement downslope (see Figure A.45).

The track length of rockfalls varies across geomorphic regions: in impact craters and unclassified geomor-

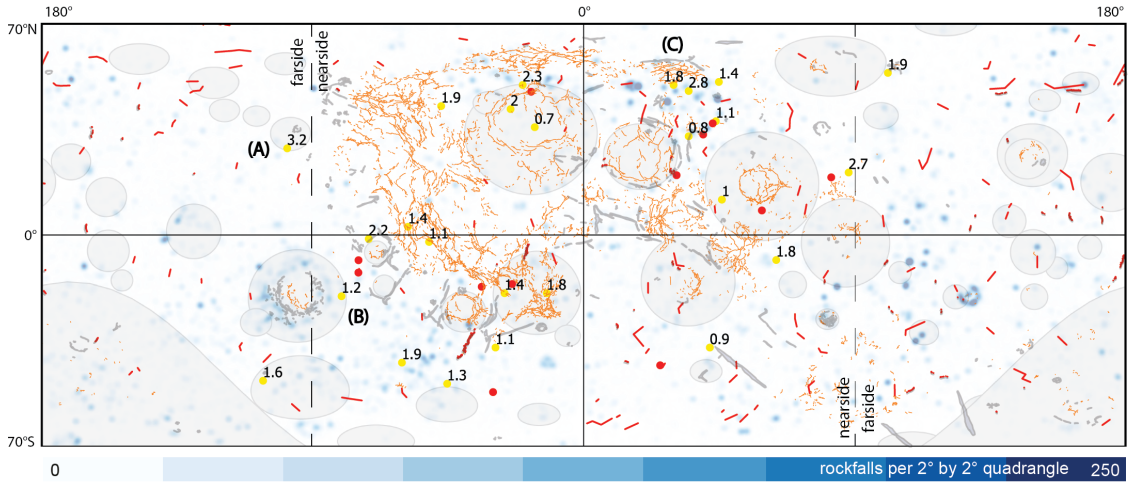
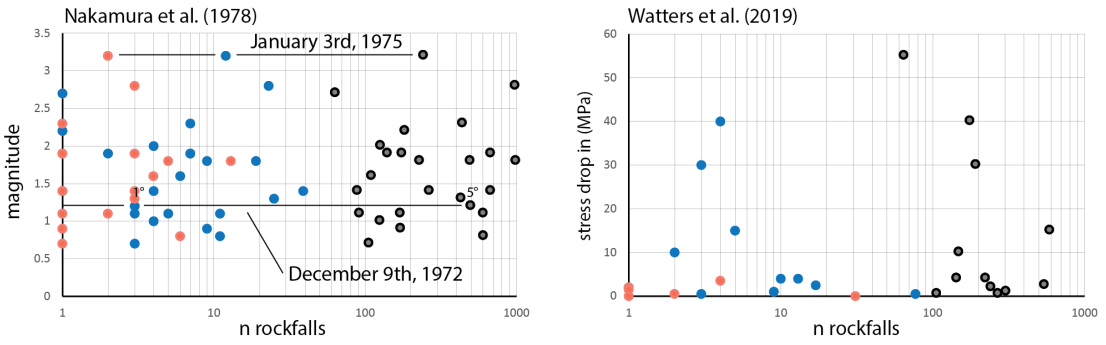


Figure 3.12: Global map of rockfall hotspot distribution (modified from Bickel et al. (2020a)), lobate scarps (digitized from Watters et al. (2019), red lines), wrinkle ridges (Thompson et al. (2017), orange lines), graben (Nahm et al. (2018), gray linear areas), large (multi-ring) impact basins (Kadish et al. (2011), gray circular areas), Apollo-era shallow moonquake epicenters (Nakamura et al. (1979), yellow dots, event magnitudes shown), and 12 confirmed, relocated Apollo-era moonquake epicenters (Watters et al. (2019), red dots). (A) denotes the Laue crater event (January 3rd, 1975), (B) denotes the Mare Orientale event (December 9th, 1972), and (C) denotes the Mare Frigoris/ Lacus Mortis region. Three epicenter locations beyond the shown latitude range are omitted for graphical reasons. Equirectangular projection (Moon2000), north is up.

phic contexts runout can reach up to ∼4,000 m and more (average is ∼1,070 m); impact-ejected rockfall runout can reach up to ∼2,000 m (average is ∼430 m); in tectonic regions runout does not exceed ∼2,000 m (average is ∼670 m), and in volcanic regions runout does not exceed ∼1,000 m (average is ∼270 m) (summarized in Figure 3.15). It is important to note that runout lengths could be influenced by differences in topographic scale across the different regions, as volcanic and tectonic regions do not feature as drastic topographic gradients and absolute elevation differences as impact craters and unclassified regions (e.g. valleys). The longest track lengths are achieved by boulders that either have high sphericity values, predominantly bounce, and/or originate from steep source regions. Interestingly, boulders with larger volumes do not appear to travel further than boulders with smaller volumes (see Figure A.46).

We observe that boulders only bounce on slopes steeper than ∼20°and move by rolling or sliding as soon as the slope gradient declines (Figure A.47). Across our AoIs we note that rolling is the most common kinematic mode, where 79.6 % of all mapped rockfalls predominantly roll, 20.1 % bounce, and 0.3 % slide. Most rockfalls across the AoIs feature similar movement types at the beginning of their trajectories: We observe that usually boulders start to roll, gain speed, potentially start bouncing, eventually slow down due to a slope angle decline, and then roll or slide until they finally stop moving. There is no indication that the approximated boulder (macro-) sphericity (as derived using only the long and short boulder diameters as well as the height) influences the displacement mode. The only exception to the usual sequence of movement types as described above are impact-ejected rockfalls: usually, impact-ejected boulders are initially airborne, then bounce over the surface in slowly declining rebounds, eventually slow down and finally roll or slide to a halt. Figure A.47 showcases the trajectories of one impact-ejected and one impact-caused rockfall, visualizing the described observations and differences.

We observe that the majority of rockfall trajectories follow the path of steepest descent along their complete trajectory. However, we note a series of rockfalls that deviate off steepest descent, specifically in the Rowland, Ingalls, and Vavilov crater AoIs. The rockfalls in these AoIs either belong to the impact-induced or impact-ejected class, i.e., these rockfalls have evident, highly energetic triggers that could influence their trajectories: in the Rowland crater AoI, the trigger impact ejected boulders in all directions, irrespective of the local topography and topographic gradient; in the Ingalls and Vavilov crater AoIs the trigger impact appears strong enough to not only have initiated the observed rockfalls, but to have given the respective



	distances in (°)	Nakamura et al., 1978	Watters et al., 2019	Jan. 3rd, 1975 quake	Dec. 9th, 1972 quake	1000 randomly selected locations
0.5°	Ø mean distance	0.34	0.34	0.32	-	0.34
	Ø std	0.04	0.06	0.04	-	0.04
	Ø variance	0.003	0.008	0.002	-	0.004
	Ø n	~2	~3	~2	0	~2
1°	Ø mean distance	0.68	0.67	0.70	0.92	0.68
	Ø std	0.16	0.15	0.19	0.03	0.14
	Ø variance	0.03	0.03	0.04	0.0008	0.03
	Ø n	~9	~12	~12	~3	~8
5°	Ø mean distance	3.49	3.27	3.23	3.55	3.36
	Ø std	1.10	1.09	1.13	0.94	1.11
	Ø variance	1.23	1.23	1.29	0.88	1.26
	Ø n	~344	~247	~241	~495	~200

Figure 3.13: Statistical analysis of moonquake epicenters and randomly selected locations vs. the global rockfall distribution as derived by Bickel et al. (2020a). Scatter plots show number of rockfalls as a function of event magnitude for the three spatial buffers (0.5°red, 1°blue, 5°black), the Laue crater and Mare Orientale events are marked; the table shows statistical descriptors for distance distributions (epicenter - rockfall) for the three spatial buffers.

boulders a lateral "push", enough to influence their initial descent path (see Figure A.45).

The rockfalls in the different geomorphic contexts show minor differences in the relation between boulder drop height (vertical displacement component) and boulder track length (horizontal displacement component), i.e., the reach angle or Fahrböschung. The overall mean Fahrböschung angle is 18.4°, while rockfalls in volcanic and tectonic regions feature angles of 17.41°and 15.08°, respectively, below the overall mean Fahrböschung angle. The rockfalls in the other geomorphic contexts feature mean Fahrböschung angles slightly above the overall mean value.

Discussion

Long- and short-term drivers of lunar rockfall

The combination of a global rockfall catalog, detailed mapping of select areas of interest, and a large number of geophysical auxiliary datasets has revealed a number of interesting findings regarding the long- and short-term factors that control lunar rockfall occurrence. Firstly, detailed mapping of the areas of interest has revealed that rockfalls originate from 4 main source region types, 1) cliff-type, 2) outcrop-type, 3) boulder field-type, and 4) plain slope type, where all source region types are present in all different geomorphic contexts. We note that the occurrence of source region types is controlled by the age of the host terrane rather than the geomorphic class: cliffs and outcrops are common on the steep slopes of e.g. fresh (Copernican) terranes, while boulder fields and plain slopes are common on the shallower inclines of e.g. old (Imbrian and pre-Imbrian) terranes. Here, regolith-dominated source regions (type 3 and 4) can either be the result of continuous weathering of cliff- and outcrop-type source regions, or can be created through impact processes that exhume and deposit boulders on the surface of the Moon (ejecta blankets). We observe that cliff- and outcrop-type source regions (young source regions) are more productive, i.e., they appear to release more rockfalls per given source region area. This agrees with observations made in

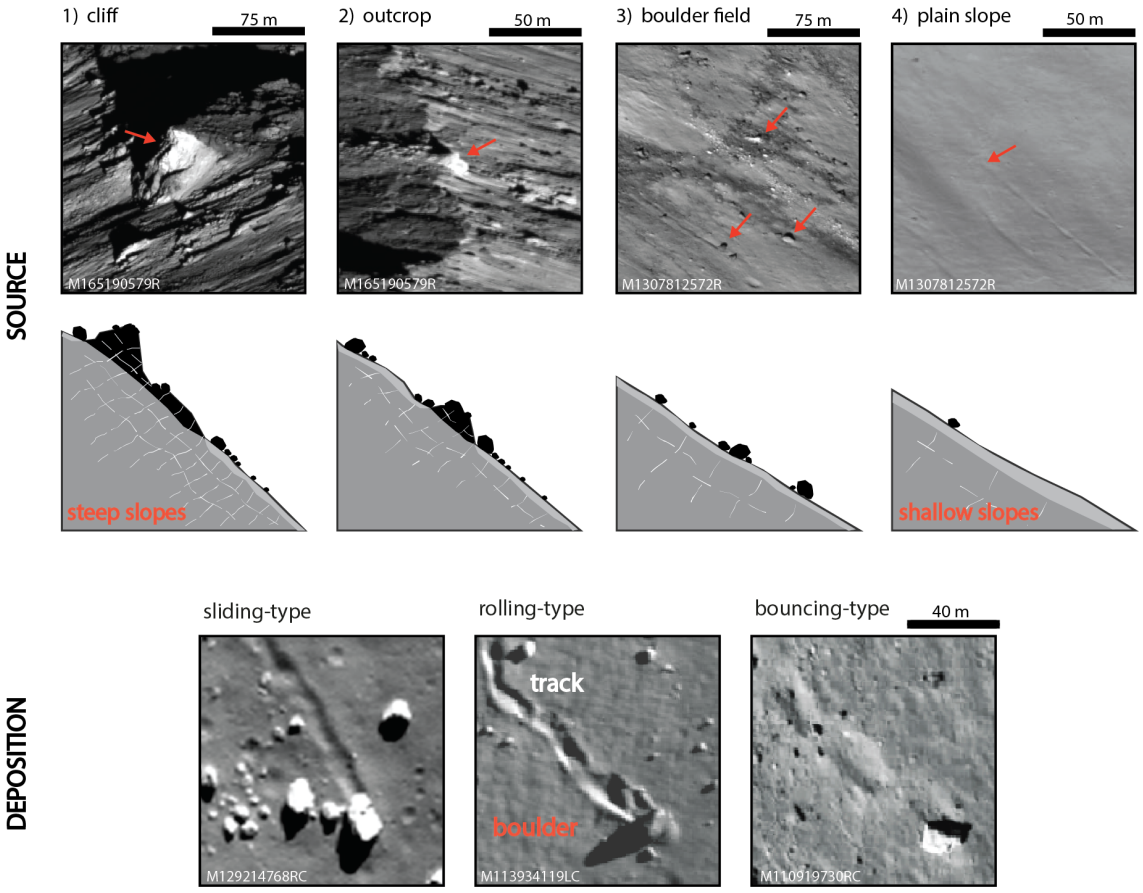


Figure 3.14: Typical lunar rockfall source regions in oblique NAC imagery (top) and as cross-sectional sketches (center), from left to right: 1) cliff, 2) outcrop (images of a Copernican-aged crater, Giordano Bruno, 36°N, 102.8°E), 3) boulder field, and 4) plain slope (images of a pre-Imbrian-aged crater, Gibbs, 18.4°S, 84.3°E) source region type. Sketches feature bedrock (dark gray), exposed bedrock and boulders (black), surface regolith (gray), and subsurface fracture networks (light gray). Relevant features are indicated by red arrows. Typical rockfall deposition regions in sub-nadir NAC imagery (bottom), from left to right: sliding-type (Rima Ariadaeus, 7.2°N, 11.1°E), rolling-type (Archytas, 58.9°N, 4.2°E), and bouncing-type (Giordano Bruno, 36°N, 102.8°E); rockfall-deposited boulders highlighted in red. Image credits: LROC/ASU/GSFC.

previous work that younger terranes feature higher spatial concentrations of rockfalls (Bickel et al., 2020a).

The global analysis shows that rockfalls are generally located in rougher than average terranes and on steeper than average slopes. The measured mean source region slope angles are very similar for all analyzed geomorphic contexts and source region types and range from ∼24 to ∼27°across all regions. These angles are close to the slope angle needed (∼29°) to initiate passive shearing and sliding in the more regolith-supported source region types 3) and 4), based on the limit equilibrium analysis presented above. Across all AoIs, ∼10 % of source region slope angles exceed ∼29°. We note that impact-ejected rockfalls are an exception, as these occur regardless of local topography - these rockfalls have been excluded from the planar sliding analysis. The simplified limit equilibrium analysis indicates that a limited number of the analyzed source regions features conditions favorable for passive rockfall initiation, in the absence of any cohesion. In rockier source regions, such as type 1) and 2), cohesion could be provided by rock bridges, and degraded through time by mechanisms such as (micrometeorite) impacts, thermal breakdown, tidal displacements and local seismic shaking (Hoerz et al., 2020). We note that all source region slope angles have been derived using a DEM with a spatial resolution of ∼118 m/pixel, whereas the average boulder has a diameter of about ∼7 to ∼8 m; the local, small-scale source region slopes angles could therefore be even steeper than reported here, facilitating rockfall initiation in all source region types.

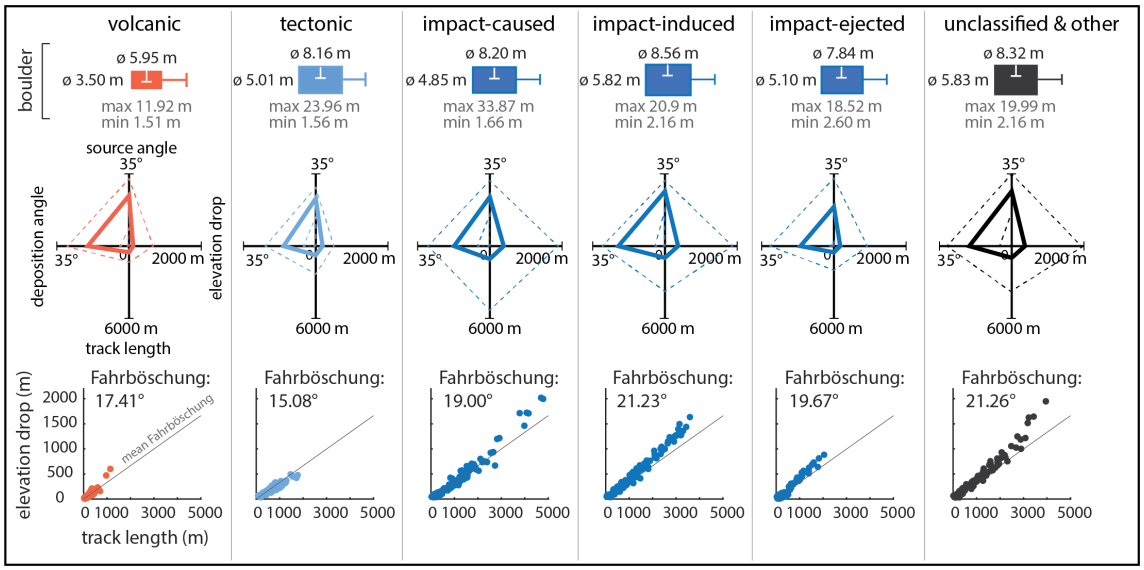


Figure 3.15: AoI rockfall fact sheet for all geomorphic contexts: mean boulder long (top) and short (bottom) diameters, spider plots of mean source and deposition region slope angle, mean elevation difference source - deposition, mean track length (max and min values are indicated by dashed lines), and scatter plot of the relation of track length and elevation drop, i.e., the Fahrböschung (mean Fahrböschung angle of each context is shown; the gray line represents the overall mean angle of 18.4°). The axis labels in the spider plots represent the minimum (always = 0) and maximum values of a given property.

The distinct and globally-visible relation between rockfall occurrence and slope aspect suggests that solar-driven thermal fatigue may be an important global-scale long-term driver of lunar erosion and rockfall. In equatorial and sub-equatorial regions, Figure 3.7 shows there are more rockfalls located on equator-facing slopes. These regions are expected to have higher noon temperatures and larger thermal amplitudes than the global average, however we donât observe this (Figure 3.9), potentially due to the limited spatial resolution of the available thermal datasets and sampling these distributions at deposition locations, rather than source locations. We additionally derive the temperature amplitude distribution for all source regions as listed in the local rockfall catalog (687 measurements) and compare it to the at-target (deposition) distribution, but are not able to observe any significant difference either, likely caused by the same limitations of the data as discussed above, assuming that the spatial scale of source regions (<50 m) is much smaller than the spatial resolution of the used datasets (»∼250 m/pixel).

Figure 3.9 further shows that rockfall sites at higher latitudes feature smaller thermal amplitudes than equatorial sites. The same figure indicates that, 1) a daily temperature amplitude of ∼110 K might be sufficient to drive fracture growth and rockfall occurrence, and 2) larger temperature amplitudes might generate a larger rockfall population (in the equatorial regions). Solar-induced thermal fatigue might also act as short-term causal factor and true trigger of lunar rockfalls in steep (>∼29°), young and exposed type 1) and 2) source regions, where thermal fatigue has been shown to be most effective (Molaro et al., 2017). Past work has shown that damage accumulation rates appear to decrease in older, more fractured rocks, meaning that thermal fatigue would become a less important driver in older terranes (Molaro et al., 2017).

The reason for the rockfall at-target slope aspect rotation from N-S to E-W (Figure 3.8) at high latitudes is currently unknown; on Mars, a similar, weaker trend has been observed by Tesson et al. (2020) for rockfalls and by Dundas et al. (2015) for gullies, but has not been specifically recognized or addressed yet. Dundas et al. (2015) mention that martian slope aspect analyses could generally be affected by the sun-synchronous, mid-afternoon orbit of the Mars Reconnaissance Orbiter (mapping bias), but this observation cannot be directly translated to the Moon, as the LRO does not follow a sun-synchronous orbit. Still, the more complicated illumination situation at higher latitudes could potentially impact the CNN-driven rockfall detection and the slope aspect analysis. Potentially, the rockfall E-W orientation at higher latitudes is controlled by the peak interior and surface thermal stresses that have been shown to occur in the

local morning and afternoon, i.e., on E- and W-facing boulder faces and slopes (Molaro et al., 2017). The important role of directional insolation in driving mechanical weathering of boulders has been observed on Earth (McFadden et al., 2005; Eppes et al., 2010) and Mars (Eppes et al., 2015) and has additionally been used to explain asteroid activity (Molaro et al., 2019). The decreased influence of the effective albedo with increasing latitude could result in a more pronounced effect of the sunrise/sunset-related thermal effects. Another potential explanation for the observed E-W rotation could be that existing impact-generated fracture networks are reworked by the global, near-surface stress field of the Moon as proposed by e.g. Watters et al. (2019) and Matsuyama et al. (2021), which features an extensive E-W trend at latitudes beyond ∼50°N and S. High resolution, outcrop-scale data returned from future missions, such as Lunar Trailblazer (Ehlmann et al., 2021), will help to further address the potential relation between the thermophysical properties of the lunar surface and the weathering/erosion of the Moon.

In contrast to thermal fatigue, the importance of impact events in driving lunar rockfalls is more evident. Earlier work found that rockfalls predominantly cluster in impact features, indicating that the impact process itself facilitates or initiates topographic erosion through rockfalls, among other mass wasting processes (Bickel et al., 2020a). Across all geomorphic contexts, small-scale impacts trigger rockfalls, either directly, i.e., by ejecting boulders in all directions (impact-ejected type), or indirectly, i.e., by inducing the displacement of pre-existing boulders or by triggering the failure of slope compartments on topographic inclines (impact-induced type). Similar processes have been observed by Kumar et al. (2016), Xiao et al. (2013), and Hovland, Mitchell (1973). We note that the vast majority of rockfalls in old terranes (Imbrian and pre-Imbrian) as well as in polar regions appear to be triggered by impact processes (impact-induced and impact-ejected), indicating that terrane age and thus source region type influence rockfall occurrence and triggers. Additionally, we observe that rockfalls in more rocky (and likely younger) regions tend to be smaller than elsewhere, on average: One explanation for this observation might be that young impact craters feature particularly closely spaced fractures that result from the catastrophic damage introduced by the impact event itself, leading to smaller block sizes during the early stages of crater wall erosion. Another potential explanation could be the spatial divergence of impact-generated, radial fractures that steadily increases as the erosion of the crater wall progresses outwards (see Figure 3.16). Generally, rocky and/or rough terranes host an increased number of rockfalls, as indicated by the relation of rockfall distribution and rock abundance, thermal conductivity, nightside surface albedo, and slope angle (Figure A.42).

Past work extensively highlighted the seemingly decisive role of lunar tectonic activity in contributing to or controlling mass wasting and rockfall occurrence (Titley, 1966; Xiao et al., 2013; Kumar et al., 2019b; Mohanty et al., 2020). This assumption is mainly based on the apparent spatial proximity of rockfalls to visible topographic expressions of tectonic activity (Watters et al., 2019; Kumar et al., 2016) and/or to the epicenters of Apollo-era shallow moonquakes (Kumar et al., 2019b; Mohanty et al., 2020). However, all past work is based on locally constrained data, thus, is not representative of larger regions or the entire lunar surface. In order to test whether endogenic activity has been an important, global-scale driver of rockfall, we use the first consistent and global map of lunar rockfalls (Bickel et al., 2020a) in combination with relevant auxiliary data and find that a large fraction of Apollo-era shallow moonquake epicenters and geomorphically visible lobate scarp, wrinkle ridge, graben, and basin-associated ring fault features do not spatially align with rockfall hotspots (Figure 3.12). Some regions show some level of overlap, such as Mare Frigoris and the Lacus Mortis region, but those regions appear to be rare. We further observe that a number of rockfall hotspots are associated with impact basins, but subsequent, detailed observations suggest this to be a consequence of 1) the large size of impact basins, meaning that they have a larger chance to contain basin-unrelated rockfall hotspots, such as small Copernican/Eratosthenian impact craters that are located within the basin, 2) the impact process itself, i.e., they feature impact-generated, subsurface fracture networks that likely drive boulder production and displacement over long timescales (Bickel et al., 2020a), rather than seismic activity along potential faults.

Similar to these qualitative observations, our quantitative analysis shows no statistically significant difference between the spatial distributions of rockfalls around known moonquake epicenters and randomly selected locations on the lunar surface. Further, there seems to be no global relation between moonquake magnitude or stress drop and spatial rockfall frequency. This is also the case for the January 3rd, 1975 and December 9th 1972 events, i.e. the moonquake with the largest recorded magnitude as discussed by Kumar et al. (2019b) and a quake close to Mare Orientale as discussed by Mohanty et al. (2020). On Earth, the minimal, local earthquake magnitude expected to trigger rockfall is 4 (Keefer, 1984), which suggests that none of the globally mapped rockfalls occurred during the Apollo-era. However, we note that magnitude is not a good measure for local rockfall susceptibility, as the key factors controlling seismicity-driven rock-

fall are local peak-ground acceleration, earthquake duration, local topography, and local geology, such as degree of fracturing and weathering (Newmark, 1965; Keefer, 1993; Massey et al., 2014) meaning that the correlation of quake epicenters location and magnitude with rockfall hotspots is not ultimately conclusive. It is important to note that the majority of observable rockfalls and tracks (which likely survive erosion over millions of years) (Hurwitz, Kring, 2016) have likely been produced outside of the small Apollo-era seismic monitoring time window (∼9 years), meaning that a comparison of rockfall and moonquake locations is not particularly conclusive. In addition, the recorded shallow seismic activity probably does not represent the true lunar endogenic activity as it occurred over the past few millions of years, which likely features events with return periods much larger than 9 years, i.e., events with potentially significantly increased magnitudes. In addition, endogenic activity might originate from blind thrust faults that do not have a geomorphic expression on the surface.

Acknowledging the limitations of this analysis, mostly governed by the available data, our results indicate that lunar tectonic activity as recorded during the Apollo era has not been a main, global-scale driver of rockfalls in the Moon's recent geologic past. Our findings are reflected in the observation that the number and spatial concentration of rockfalls in the proximity of geomorphically visible tectonic features is very low: only 0.8 % of all mapped lunar rockfalls are close to tectonic features such as graben (Bickel et al., 2020a). Thus, while we cannot definitively exclude the possibility that lunar seismic activity was a dominant, global driver of rockfalls in the lunar geologic past and that lunar seismicity still triggers rockfalls on local or even regional scales (Bickel et al., 2020a; Mohanty et al., 2020), this possibility is not supported by the analysis presented here. Future, ground-based, long-term geologic investigations and global geophysical monitoring networks, such as e.g. promoted by e.g. Jawin et al. (2018) and Nunn et al. (2021), will help to address many of the remaining questions. Our results suggest that observations of mass wasting features, such as rockfalls, on planetary surfaces may not always be a direct proxy for recent seismic activity or even seismic hazard, but can have other, potentially more likely drivers.

We observe that regions with large radial tidal displacement values can feature an increased number of rockfalls (Figure 3.8). Currently, tidal forces can only be mapped on large spatial scales (Thor et al., 2020) and we are not able to observe the same trend in all studied geographic regions, meaning that our observations are not entirely conclusive. Tidally-driven, cyclic, vertical displacements of the lunar crust on the order of tens of centimeters could, in theory, favor fracture growth, weathering, and erosion in general, resulting in more rockfall events on average. On Earth, tides have been observed to trigger shallow thrust fault earthquakes (Metivier et al., 2009; Cochran et al., 2004). Tidal displacement could also interact with the near-surface stress state of the Moon (Watters et al., 2019), potentially helping to explain the observed at-target rockfall slope aspect rotation from N-S to E-W at higher latitudes (Figure 3.7).

All observations combined indicate that short-term meteoritic impacts, aided by long-term temperature cycles, have been the dominant drivers of rockfall occurrence in the Moon's recent geologic past. The distinct daily temperature cycle - predominantly controlled by the Sun - likely interacts with impact-generated fracture networks to drive fracture growth over long timescales (Molaro et al., 2017), which could eventually lead to kinematically free boulders and their subsequent detachment and failure in rocky and steep source regions (types 1 and 2), as hypothesized by Hovland, Mitchell (1973) in the Apollo-era. This means that thermal fatigue is likely a major long-term, global-scale causal driver of lunar erosion and rockfall. Short-term thermomechanical triggering of rockfalls, as observed on Earth during extremely hot days (Collins, Stock, 2016), is less probable on the Moon, however, but might occur in steep, exposed type 1) and 2) source regions. Our observations further indicate that in more regolith-supported, debris-type source regions (granular soil slopes, types 3 and 4) with shallower slopes angles, predominantly present in older terranes, meteoritic impacts act as the dominant short-term causal drivers. Small-scale impacts also appear to be the dominant short-term driver of rockfalls in the polar regions (>85°N and S), as previously observed by e.g. Bickel, Kring (2020). Rockmass degradation and boulder initiation in all source regions could potentially be facilitated by continuous, abrasive meteoritic micro-bombardment. We summarize our observations in a conceptual model, depicted in Figure 3.16, illustrating how a new impact crater is formed, how thermal fatigue drives wall erosion on equator-facing slopes in the time period after the impact, how impact-induced and -ejected rockfalls become the dominant short-term drivers of rockfall as crater age increases, and how long-term seismicity might contribute both to long-term damage and short-term rockfall triggering in the vicinity of visible or invisible tectonic features.

On Mars, an atmospheric body unlike the Moon, Tesson et al. (2020) also observed that rockfall occurrence is likely connected to thermal stress induced by solar insolation, as the rockfalls in their study

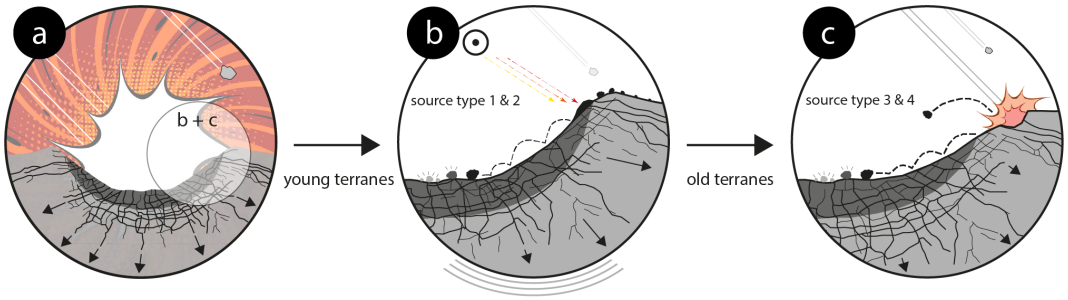


Figure 3.16: Conceptual model of long- and short term lunar rockfall drivers, modified from Bickel et al. (2020a). In young terranes with cliff- and outcrop-type source regions (type 1 & 2), thermal fatigue can act as dominant long- and possibly short-term driver of rockfall, in addition to impacts and potentially moonquakes. In old terranes with boulder field- and plain slope-type source regions (type 3 & 4) thermal fatigue appears to become a less important driver, while small-scale impacts appear to play an increasingly important role in driving rockfall occurrence. We note that in reality all drivers can be active in young and old terranes, but we only show the dominant drivers per panel to maintain clarity.

area tend to cluster on equator-facing slopes as well. Using their observations, Tesson et al. (2020) argue that thermal fatigue plays an important role in causing rockfall events on Mars. Studies by Eppes et al. (2015) provide additional evidence that sun-induced thermal stress is a dominant driver of fracture propagation in martian boulders. Similarly, Molaro et al. (2017, 2019) observe that directional insulation controls rock breakdown on airless planetary bodies such as asteroid Bennu. Despite the geologic and environmental differences between the Moon, Mars, and other (airless) planetary bodies, the agreement between the different and independent sets of observations increases our confidence in the presented results.

We note that the CNN used by Bickel et al. (2020a) to map the global population of lunar rockfalls has specific limitations, e.g. related to the detection performance (limited recall and precision, i.e., potential for missed or mis-classified features) and the Klee-based (Klee, 1977) image selection algorithm (Bickel et al., 2020a) that might select poorly-lit imagery (solar incidence and phase angles are not appropriate for a given terrain). However, we expect that any negative impact of the image selection algorithm would equally and evenly affect the detection performance, i.e., should not bias the analysis as presented in this paper. We point out that the detection of rockfalls at higher latitudes is more likely to be biased by the illumination conditions, as the solar incidence steadily increases and thus the portion of shadowed regions.

Another limitation of our global analysis is that the used CNN only detects deposited rockfalls. Thus, the globally derived at-target distributions represent the physical properties of the rockfall deposition regions, not necessarily the source regions. Considering that the measured (across 13 AoIs), average track length of a lunar rockfall is ∼600 m, the effect of this on the comparison with low-resolution datasets (>2 km/pix, e.g. GRAIL gravity data) is probably minor, but could affect the comparison with high-resolution datasets (∼250 m/pix), specifically the temperature-related datasets. Datasets like slope aspect are more robust versus that source-deposition uncertainty, as very low slope angles (<10°) still produce the same aspect value as high slope angles (>30°), meaning that the attributes derived from rockfall source and deposition regions are more likely to be very similar or identical. In some cases the separation of deposition and source region properties is desired, however, for example when calculating the elevation difference or Fahrböschung; here, the relatively low spatial resolution of some auxiliary datasets can also introduce uncertainties, e.g. in cases where the rockfall track length is shorter than one pixel of an auxiliary map (note that the spatial resolution of the used DEM is ∼118 m/pixel). We point out that the generally low spatial resolution of all available auxiliary datasets complicates the interpretation of our global-scale results: rockfall-deposited boulders and their source regions are meters in size, not hundreds of meters or kilometers (see e.g. Figure 3.14) - the current set of observations and interpretations will significantly benefit from future, high resolution datasets.

Finally, the qualitative and quantitative assessment of the relation between rockfall abundance and seismic activity is potentially biased, too, as the epicenters of all Apollo-era moonquakes are only spatial approximations due to the small spatial extent of the Apollo-era geophysical network, meaning that Nakamura et al. (1979)'s and Watters et al. (2019)'s catalogs of events contain a localization error that could bias

our analysis in unforeseen ways. Our analysis is additionally impacted by the short Apollo-era monitoring period that likely introduces a spatial, temporal, and event scale-related bias. As for the rest of the analysis, future data will help to address these uncertainties and limitations.

Transport mechanisms of lunar rockfall

After detachment, boulders usually start to roll and speed up, before they potentially start to bounce. Once they reach the toe of the slope, they slow down and stop. Our (locally constrained) measurements show that rockfalls originate from source regions with average angles of ∼25°(in our AoIs) and are deposited on slopes of around ∼13°(globally, Bickel et al. (2020a)), on average, across all geomorphic contexts (see Figure A.44). Rockfalls that originate on steeper slopes achieve longer runout lengths, as one would expect. Interestingly, there are rockfalls in all AoIs that stop on inclines as steep as ∼30°. These boulders are not anomalous with regard to their shape or trigger; apparently, a very small reduction of the local slope angle and/or collisions with micro-topography or obstacles which are not resolved by the NAC camera are sufficient to force the respective boulders to a halt. In comparison, on Earth rockfall trajectories are strongly influenced by the roughness of the slope and the size and character of obstacles present (Dorran, 2015). Again, impact-ejected rockfalls are excluded from this comparison, as they occur on the full range of slope angles present on the lunar surface. Impact-ejected rockfalls are initially airborne and keep bouncing until they lose enough energy to enter a rolling or sliding displacement mode. Most impact-ejected rockfall trajectories have a distinct first bounce mark, usually a particularly deep and wide circular depression that likely is the result of an initial impact from high altitudes (impact ejecta).

We additionally observe that a) bouncing boulders with b) higher approximated sphericity values achieve the longest runout distances. As non-impact-ejected boulders only bounce on slopes steeper than ∼20°, the slope geometry, combined with a higher likelihood of rolling kinematics (indicated by higher sphericity values), could be the dominant factor influencing lunar rockfall transport kinematics. Interestingly, and in contrast to Earth, we are not able to identify any relation between boulder volume and runout length. We note that we use a simplified characterization of boulder shape and volume, based on only three orthogonal axes (length, width, height) that assumes an ellipsoidal shape, which may omit potential relations between runout and boulder properties. On Earth, boulder micro-topography has been identified as one of the main aspects that control rockfall trajectories (Dorran, 2015); unfortunately, the data available for the Moon (space-borne sensors) does not match the quality and amount of data available for Earth (ground-based and air-borne sensors) which means that a more detailed reconstruction of lunar boulder shapes will only become possible in the future.

We observe a number of rockfalls that do not follow a steepest descent path, specifically during the first tens of meters of their displacement: these boulders start off following the direction of steepest descent, and then deviate from this direction before eventually returning to a steepest descent path further down the slope (see Figure A.42). This means that these boulders have been triggered by a (highly) energetic trigger which provided a lateral push. The observations in our AoIs indicate that rockfalls that deviate from the steepest decent direction are exclusively associated with small-scale impact features, suggesting that these boulders either are impact-induced but with a lateral component, or impact-ejected but with very low ejection velocities (given their spatial proximity to the impact itself). Other than impact-ejected rockfalls, we do not observe any boulders that start bouncing directly after being triggered, indicating that neither impact processes (impact-induced type) or seismic shaking appear to have a sufficient amount of energy to get lunar boulders off the ground directly.

We note that rockfalls with longer runouts tend to have relatively more vertical drop than rockfalls with shorter runouts, apparently independent of the geomorphic context (see Figure 3.15). In contrast, the rockfalls in AoIs with a tectonic geomorphic context, Vallis Alpes and Rima Ariadaeus, feature a very constant, quasi-linear distribution of Fahrböschung angles (Figure 3.15 and highlighted in Figure A.48). In other words, rockfalls in tectonic regions travel farther per meter dropped when compared to the other geomorphic regions. This is surprising, as source region slope angles, approximated boulder sphericity, and boulder volumes are very similar across all AoIs. The anomalous mean Fahrböschung angles could be the result of a sampling bias (too few AoIs per context were studied) or could represent differences in the absolute relief across the AoIs, where tectonic features would feature smaller absolute elevation differences than, for example, impact craters. The difference in mean Fahrböschung could also be related to regional or local variations of slope characteristics (e.g. roughness and restitution coefficients) that are not obvious in the available imagery. Additional mapping efforts in various AoIs are required in order to exclude observational bias and to substantiate these initial observations, however.

Ultimately, many of the open questions could be addressed by closely monitoring a presumably active lunar slope with a ground-based geophysical monitoring system which not only includes seismometers but also optical and thermal instruments that allow for the cross-correlation of rockfall occurrence, visual changes, and thermal fluctuations with high spatial and temporal resolution.

Conclusion

We performed the first comprehensive and global study of lunar rockfall long- and short-term causal drivers and transport mechanisms using data about more than 130,000 rockfalls in combination with highly detailed local data about 687 rockfalls in 13 focus regions, covering volcanic, tectonic, and impact geomorphic contexts. Lunar rockfalls appear to predominantly occur on the slopes of equator-facing, rocky/rough impact structures that experience large thermal amplitudes over the course of the lunar day. We do not observe a qualitatively or statistically relevant relation between rockfall abundance, recorded Apollo-era shallow moonquake activity, and the distribution of visible tectogenetic features, indicating that moonquakes have not been a main, global driver of lunar rockfalls in the Moon's recent geologic past.

Our observations suggest that rockfalls originate from 4 source region types, specifically: cliff-, outcrop-(rock-supported), boulder field-, and plain slope-type (regolith-supported) source regions, where cliff and outcrop type source regions are more common in young, Copernican terranes and produce larger numbers of rockfalls. The transportation length of boulders appears to depend on their sphericity and the source region slope angle, but not on their volume. We note that the displacement kinematic of regular lunar rockfalls appears to be controlled by the inclination of the slope, specifically, where boulders potentially start to bounce above $\sim 20^{\circ}$.

Our results suggest that, in addition to impacts, continuous, solar-induced fracture propagation (thermal fatigue) is an important and global long-term driver of lunar rockfall mainly in young terranes with steep, exposed bedrock, potentially supported by continuous and abrasive micrometeorite bombardment and long-term tectonic and seismic activity. Erratic, small-scale impacts appear to be an important and global short-term driver of lunar rockfall (more pronounced in old terranes with shallow slopes and fewer bedrock outcrops). We note that shallow, seismic events could act as short-term drivers as well, particularly in the vicinity of tectonic features such as grabens, lobate scarps, and wrinkle ridges. We find that the trajectories of lunar rockfalls are mainly controlled by the trigger energy and the geometry of the slope.

Our findings can be applied to study the endo- and exogenic activity of the Moon, while complementing existing and ongoing studies of the weathering and erosion of atmospheric and airless planetary bodies in general, including Earth, Mars, and small bodies such as asteroid Bennu. Our findings can further inform and support the planning of future, geophysical surface exploration missions to the Moon.

Acknowledgements

We thank Kerry Leith for contributing his ideas regarding the relation of slope aspect and rockfall distribution. We further thank Urs Mall for interesting discussions regarding the image selection algorithms and geophysical datasets. One of the authors (V.T.B.) gratefully acknowledges the financial support by the Engineering Geology group, Department of Earth Sciences, ETH Zurich, and the International Max Planck Research School (IMPRS) at the Max Planck Institute for Solar System Research (MPS). This research has made use of the USGS Integrated Software for Imagers and Spectrometers (ISIS). We thank Deanne Rogers, Jamie Molaro and an anonymous reviewer for their contributions to refine and improve this work.

Chapter 4

Exploration Applications of Rockfalls

This chapter describes how we developed and applied a purely remote sensing-based method to derive a first order estimate of the surface strength of yet unexplored lunar regions such as pyroclastic deposits and the sunlit south polar regolith. Further, we applied the method to derive surface strength estimates of permanently shadowed regions; please refer to the supplementary information A.1 for more details.

4.1 Analysis of Lunar Boulder Tracks: Implications for Trafficability of Pyroclastic Deposits

Published 2019 in the Journal of Geophysical Research: Planets
Bickel, V.T., Honniball, C.I., Martinez, S.N., Rogaski, A., Sargeant, H.M., Bell, S.K., Czaplinski, E.C., Farrant, B.E., Harrington, E.M., Tolometti, G.D., Kring, D.A., 2019
https://doi.org/10.1029/2018JE005876

Abstract
In a new era of lunar exploration, pyroclastic deposits have been identified as valuable targets for resource utilization and scientific inquiry. Little is understood about the geomechanical properties and the trafficability of the surface material in these areas, which is essential for successful mission planning and execution. Past incidents with rovers highlight the importance of reliable information about surface properties for future, particularly robotic, lunar mission concepts. Characteristics of 149 boulder tracks are measured in Lunar Reconnaissance Orbiter Narrow Angle Camera images and used to derive the bearing capacity of pyroclastic deposits and, for comparison, mare and highland regions from the surface down to ∼5 m depth, as a measure of trafficability. Results are compared and complemented with bearing capacity values calculated from physical property data collected in situ during Apollo, Surveyor, and Lunokhod missions. Qualitative observations of tracks show no region dependent differences, further suggesting similar geomechanical properties in the regions. Generally, bearing capacity increases with depth and decreases with higher slope gradients, independent of the type of region. At depths of 0.19 to 5 m, pyroclastic materials have bearing capacities equal or higher than those of mare and highland material and, thus, may be equally trafficable at surface level. Calculated bearing capacities based on orbital observations are consistent with values derived using in situ data. Bearing capacity values are used to estimate wheel sinkage of rover concepts in pyroclastic deposits. This study's findings can be used in the context of traverse planning, rover design, and in situ extraction of lunar resources.

Introduction

As a new era of lunar exploration begins, attention has turned to lunar pyroclastic deposits (LPDs) as high priority targets for scientific research and in situ resource utilization (ISRU). These unique locations may be important sources of volatiles such as OH and/or H_2O (referred to in this work as water) that can be utilized for long term human exploration. A pyroclastic vent in the Schrödinger basin may be, for example, the largest indigenous source of water in the south polar region (Kring et al., 2014). In addition to being a source of water, the surfaces of glassy material in these types of deposits can be enriched by factors of 3 to 400 in Ag, Br, Cd, Cu, S, and Zn relative to their interiors (Baedecker et al., 1974; Cho

et al., 2007; Wasson et al., 1976). Modest chemical etching or abrasion may remove the elements for ISRU. More importantly, pyroclastic deposits with significant FeO and/or the mineral ilmenite can be reduced to produce oxygen needed for consumption by crew and as propellant (Allen et al., 1996). The pyroclastic material is also a suitable building material. Aside from the economic potential of LPDs, they provide a wealth of geologic information about the thermal and magmatic evolution of the Moon, as specified in a report of the National Research Council about The Scientific Context for Exploration of the Moon (NRC, 2007). Pyroclastic deposits can be used to determine the origin and variability of lunar basalts, determine the compositional range of LPDs, and determine the flux of lunar volcanism and its evolution through space and time. In general, pyroclastic deposits provide a window into the lunar mantle, the magmas generated there, and the igneous evolution of the Moon.

Several newly proposed landing sites and traverses exist in the proximity of LPDs (Allender et al., 2019; Kring, Durda, 2012; Potts et al., 2015; Steenstra et al., 2016). In particular, an immense ∼400 m tall pyroclastic vent in the Schrödinger basin on the lunar farside was among the Tiers I and II targets during the Exploration Systems Mission Directorate phase of the Lunar Reconnaissance Orbiter (LRO) mission because of its ISRU potential for future human missions. Thus far, three landing site and traverse studies have explored the feasibility of crew working in the vicinity of that pyroclastic vent (Allender et al., 2019; Bunte et al., 2011; O'Sullivan et al., 2011). Moreover, several human assisted robotic sample return missions to the same pyroclastic vent have also been explored (Potts et al., 2015; Steenstra et al., 2016). In all cases, it was assumed trafficability would be possible along the periphery of the deposit, but it remains uncertain if a rover can operate in proximity of the vent center. To further assess missions to the pyroclastic deposit in the Schrödinger basin and LPDs elsewhere on the Moon, additional information about the geomechanical properties is needed to optimize rover design and reduce operational risk of trafficability.

Lunar exploration has historically been plagued with uncertain assessments of trafficability. Despite a first successful soft landing of the Soviet Union's Luna 9 probe in 1966, concerns remained that the lunar surface would not be traversable; that is, the regolith would not be able to bear any kind of load (Carrier et al., 1991). Those concerns were addressed by several NASA Surveyor missions that provided opportunities to analyze the mechanical properties of the lunar regolith in situ (NSSDC, 2006). In addition, NASA's Lunar Orbiter missions from 1966 to 1967 (USRA, n.d.) returned photographs of the surface, which led to the discovery of boulder tracks carved by rockfalls. These boulder tracks were studied (Eggleston et al., 1968; Filice, 1967; Hovland, Mitchell, 1971, 1973; Moore, 1970; Moore et al., 1972; Pike, 1971) to derive geomechanical properties of the lunar regolith in regions not been directly sampled by landers. Results suggested crew and rovers would be able to traverse the surface safely.

Mobility was first demonstrated in 1969 by astronauts Armstrong and Aldrin walking over distances of ∼100 m around the Apollo 11 landing site (NASA, 2017). The use of rovers began in 1970 with the Soviet Union's Lunokhod 1 (Carrier et al., 1991; Spectrum, 2010). This rover was followed by the Modular Equipment Transporter (MET) (1971), the Lunar Roving Vehicle (LRV) (1971-1972), the Union of Soviet Socialist Republic's USSR's Lunokhod 2 rover (1973), and the Chinese Yutu rover (2013)(Carrier et al., 1991; NSSDC, 2006; ESA, n.d.a). On 3 January 2019, the Chinese Chang'e 4 probe delivered a second Yutu rover to the lunar surface that is currently exploring a part of the South Pole Aitken basin on the farside of the Moon (ESA, n.d.b). In addition, the Indian Space Research Organization is planning to deploy a rover as part of the upcoming Chandrayaan 2 mission, in early 2019 (ISRO, n.d.). The tracks created by astronauts, rovers, and landers provided additional information about the geomechanical properties and trafficability of the lunar regolith (Costes et al., 1970; Carrier et al., 1991; Mitchell et al., 1974; Scott et al., 1971; Slyuta, 2014). Despite a general level of success, operational limitations were also noted. During its first use around the Apollo 15 landing site, the LRV entered an area of soft soil and experienced 100% wheel slip (Costes et al., 1972). To resolve the issue, the astronauts manually moved the vehicle out of the trench to continue the traverse (Carrier et al., 1991; Costes et al., 1972). Lunokhod 2 encountered soft soils on the inside walls of craters and at the base of slopes. While its wheel sinkage was normally 2 cm, it increased to >20 cm near some impact craters (Carrier et al., 1991; Florensky et al., 1978). Incidences such as these are of concern when planning robotic missions that will not be able to be corrected manually.

The previous missions occurred in highland and mare terrains. LPDs have only been traversed along their periphery (e.g., Apollo 17), and availability of in situ data for them is limited. Thus, if they are to be explored successfully in the future, a geomechanical assessment must be performed. Recent spacecraft missions, such as NASA's LRO, have produced high resolution imagery of boulder tracks that are suitable for that assessment. Here those boulder tracks are used to determine the ultimate bearing capacity of

LPDs from the near surface to a depth of ~5 m and compared with similar analyses of lunar highland and mare regions.

Ultimate bearing capacity is one measure of the trafficability of a surface material, which is a term that describes the ability of a soil to bear a load, to provide sufficient traction for propulsion, and other locomotion related properties (Bekker, 1956; Carrier et al., 1991). The derived bearing capacity has been used to estimate the sinkage of current and future rover concepts in the investigated regions. In addition, we explore how bearing capacity can be used to adjust important rover specifications such as total allowable vehicle mass as a function of wheel or footpad dimensions. The results of this work can be used to reduce the risk of robotic and human traverses, while also providing a baseline needed to design infrastructure used for ISRU and large scientific instrumentation such as telescopes.

The available data and the selection of LPDs for this study are described in section 2, followed by a mathematical description of bearing capacity theory. Section 3 describes the measurements made in high resolution orbital images. Section 4 presents and discusses the results. Finally, in section 5, the implications of those results are provided along with an outlook for application in future missions.

Methods

This work compares the ultimate bearing capacity of lunar regolith in LPDs, mare, and highland regions as a potential measure for their trafficability. Using the Terzaghi (1951) (Terzaghi, 1951) bearing capacity equation (used during the Apollo era for site assessments) (Moore, 1970) and Hansen's (1970) (Hansen, 1970) updated equation for shallow foundations, bearing capacity is calculated using values derived from measurements of boulder tracks. Orbital imagery is used to identify and measure these boulders and their associated tracks. In addition, track appearances and shapes in all regions of interest are compared in a qualitative manner as an additional measure for regolith behavior and strength. Soil mechanical values used in the two equations are retrieved from literature pertaining to the Apollo soils. Data measured in photographs taken during the Apollo and Surveyor missions, as well as data measured in situ during the Lunokhod missions, are used to derive bearing capacity values for comparison with the remotely measured data.

2.1 Site Selection and Orbital Imagery

High resolution orbital imagery allows for the assessment of trafficability in LPDs by measurements of boulder tracks from rockfalls. LPDs range in size from less than 1,000 to 49,013 km^2 or more (Gaddis et al., 2003). This study focused on large deposits (i.e., those with 600 km^2 or more) that contain rockfalls with boulder tracks. Large deposits have been chosen, because they provide the most opportunity for selection of potential landing and traverse sites. A total of eight LPDs are investigated (Table A.8 in the supporting information, generally denoted S). Additionally, the selected LPDs have been evaluated for their TiO_2 and FeO content, plus theoretical and experimental water content (Table A.8). Figure A.49 displays the locations of all boulder tracks used for this study.

In order to achieve sufficient measurement accuracy, image data with the highest possible spatial resolution and quality are required. Seventy nine LRO Narrow Angle Camera (NAC) images that contain boulder tracks have been processed from experimental data record level 0 to reduced data record level 2, with spatial resolution ranging from 0.38 to 1.68 m/pixel. Subsequently, all images have been adjusted to the appropriate projection in ArcGIS 10.1 using Isis3. The LRO Wide Angle Camera (WAC) DTM GLD 2013 100 m (Scholten et al., 2012) was used for measurements relating to slope and elevation. See Figure A.50 for a detailed image processing workflow.

2.2 Bearing Capacity Equations and Calculations

Analysis of boulder tracks on the surface of the Moon has been used to estimate the bearing capacity of regolith since the Lunar Orbiter program began imaging the lunar surface in 1966 (Eggleston et al., 1968; Filice, 1967; Moore, 1970). The ultimate bearing capacity is the maximum load the ground can sustain before failure (Meyerhof, 1951). It is a potential measure for a soil's trafficability, a term that not only describes the ability of a soil to bear a load (i.e., the sinkage of a load into the surface) but also whether a soil is able to provide traction as well as propulsion (Bekker, 1956; Carrier et al., 1991). Other aspects of trafficability describe terrain, energy consumption of a vehicle due to surface roughness, and rolling resistance (Bekker, 1956; Carrier et al., 1991). Because ultimate bearing capacity denotes the at failure

state of the soil, the driving forces (boulder weight) and the resisting forces (shear strength of the soil) are equal and cancel out. This means that the weight of the boulders can be neglected (i.e., no density measurements of the boulders are required) while only intrinsic soil properties are used.

Amongst the available bearing capacity equations (Terzaghi, 1951), Equation 4.1 has traditionally and widely been used by geotechnical engineers. In addition, Equation 4.6 (Hansen, 1970) incorporates various adaptations and expansions to Terzaghi's approach, to better address the contact interface between an imposing object (whether it be a boulder or mechanical system) and a geologic surface. For these reasons, both approaches are explored in this work.

2.2.1 Terzaghi

Terzaghi's (Terzaghi, 1951) ultimate bearing capacity (q_f) formula for shallow circular footings (Equation 4.1) consists of three terms that represent the total shear strength of the soil, that is, the cohesion, the soil surcharge, and the soil friction along the footing:

$$q_f = 1.3cN_c + q_0N_q + 0.3\gamma_s B_{av} N_\gamma \tag{4.1}$$

where c is the cohesion of the soil, q_0 is the vertical stress within the soil, and γ_s is the unit weight of a homogeneous isotropic soil. B_{av} is the diameter of the circular footing, which is the average of the two effective horizontal footing dimensions B_T and L_T as derived using Figure A.51. The surcharge q_0 is the product of the depth of track (i.e., depth of footing, D) and the soil unit weight (γ_s), which is derived from the density of soil (ρ) and gravity on the Moon (g_M). Depth of track is calculated using the shadow length (S) that is cast within the track and the incidence angle (i) of the Sun:

$$D = \frac{S}{\tan(i)} \tag{4.2}$$

Lastly, the bearing capacity factors (N_c, N_q, N_γ) are derived from Terzaghi (Terzaghi, 1951), Equation 4.3 and Equation 4.4 and Coduto et al. (2011)'s, Equation 4.5:

$$N_q = \frac{\exp^{(\frac{3\pi}{4} - \frac{\phi}{2})} * \tan(\phi)}{2\cos^2(45° + \frac{\phi}{2})} \tag{4.3}$$

$$N_c = (N_q - 1) - \cot(\phi) \tag{4.4}$$

$$N_\gamma = \frac{2(N_q + 1) * \tan\phi}{1 + 0.4\sin(4\phi)} \tag{4.5}$$

where ϕ is the internal friction angle, which is the angle between the shear stress and the normal effective stress where shear failure in a dry granular material occurs (Melosh, 2011).

Terzaghi's equation assumes that lunar boulders are spheroids and, thus, have a circular footprint. A circular footing is not entirely representative of the observed shapes of lunar boulders and the pressure acting onto the surface through a sphere but has been used in the past and is used as one possible approximation for this study because a realistic reproduction of the exact boulder surfaces is beyond the scope of this work. Terzaghi's bearing capacity equation (Equation 4.1) also assumes that the base of the footing is rough and requires that the depth of track is less than the width of footing, that is, either the respective boulder diameter or the track width, depending on the observed displacement method (Figure A.51). In general, Terzaghi's equation does not consider inclined terrain and, thus, overestimates the bearing capacity for sites located on slopes (Castelli, Lentini, 2012; Meyerhof, 1957). Boulder tracks produced at the source of the track and at the terminus are measured. At these locations, it is assumed that the boulder has minimal kinetic energy and can be approximated as a static load. While the soil reacts with inertial resistance upon dynamic impacts, the assumption of a static load will result in conservative bearing capacity values (Carrier et al., 1991; Hovland, Mitchell, 1973; Moore et al., 1972). The static assumption is also useful to generalize the otherwise complex lunar boulder displacement methods that have been observed,

that is, jumping, rolling, sliding, and their influence on bearing capacity (Figure 4.1).

2.2.2 Hansen

It has been shown (Shill, Hoque, 2015) that bearing capacity estimations using Terzaghi's formula tend to deviate from results using other equations, particularly at higher friction angles. In addition, Terzaghi's approach does not consider a number of variables such as the local slope. For those reasons, an additional approach is considered in this work. Hansen's (Hansen, 1970) equation for shallow foundations (Equation 4.6) utilizes a different weighting to the bearing capacity factors (Equation 4.7 to Equation 4.9) and considers depth factor d(c,q,γ) (Equation A.6 to Equation A.14), shape factor s(c,q,γ) (Equation A.15 to Equation A.17), and local slope inclination factor g(c,q,γ) (Equation A.18 and Equation A.19; all in the supporting information). The formula also considers load inclination i(c,q,γ) and foundation (boulder) inclination b(c,q,γ) factors. Hansen's additional factors are valid if (1) the local slope angle is smaller than the material's internal friction angle and (2) the local slope angle plus footing inclination angle is smaller than 90° (Hansen, 1970). As the dynamic displacement component is being neglected and as observations indicate that rockfalls carve into the slope substrate, this study assumes that the curved surface underneath a boulder on a slope can geometrically be described as a horizontal plane at each point x in time and, thus, there is no footing and load inclination to account for. Consequently, all i and b factors have been set to 1. This general assumption is equally valid for boulders of various sizes, including rover wheels and boots, and has been used by previous studies, such as that by Hovland, Mitchell (1971), in a similar manner.

In contrast to the selected equation from Terzaghi for circular foundations, the Hansen formulae approximate rectangular footings and are given by Hansen (Hansen, 1970) and Bowles (Bowles, 1997) as:

$$q_f = cN_c s_c d_c i_c b_c g_c + q_0 N_q s_q d_q i_q b_q g_q + 0.5\gamma B_H N_\gamma s_\gamma d_\gamma i_\gamma b_\gamma g_\gamma \tag{4.6}$$

$$N_q = \exp^{(\pi \tan(\phi))} \tan^2(45^\circ + \frac{\phi}{2}) \tag{4.7}$$

$$N_c = (N_q - 1)\cot(\phi) \tag{4.8}$$

$$N_\gamma = 1.5(N_q - 1)\tan(\phi) \tag{4.9}$$

The depth and shape factors are dependent on the orientation of the boulder during its displacement, which means that the input parameters for foundation width (B_H, short boulder diameter) and length (L_H, long boulder diameter) have to be determined based on observations using the schematic in Figure A.51. The measurements can then be applied in Equation A.6 through Equation A.17, listed in the supporting Information. The slope inclination factor can be derived by using Equation A.18 and Equation A.19 in the supporting information. Other methods and modified approaches to calculate bearing capacity of soils such as Hovland, Mitchell (1971), Vesic (1973), Durgonuglu, Mitchell (1975), Kusakabe et al. (1981), Saran et al. (1989), and EuroCode7 (1996) have been developed. However, besides minor mathematical and methodical differences between Hansen (Hansen, 1970) and these approaches, previous studies such as Shill, Hoque (2015) have shown that most methods produce similar bearing capacity results. Due to that finding and a realization that some of these approaches rely on outdated assumptions due to the data quality at that time, only the bearing capacities calculated with the original Terzaghi (Terzaghi, 1951), Equation 4.1 and Hansen (Hansen, 1970), Equation 4.6 equations will be analyzed and compared in this work, using improved assumptions that are based on new high resolution image data from LRO.

2.3 Trafficability

The ultimate bearing capacity of regolith can be used as a measure for its trafficability, that is, if the soil is able to support a vehicle or astronaut, which is a fundamentally important question that has to be answered prior to the deployment of human or robotic assets in unknown regions, to avoid loss of mobile assets due to stalling. A load will cause the regolith to fail in shear until a layer that is able to bear it is reached and is therefore an indirect measure for the sinkage of a load into the soil, for example, a rover

wheel or a robot's footpad, also referred to as flotation. Since failure and therefore sinkage stops as soon as load pressure and bearing capacity are equal, the basic relation

$$q_f = \frac{mg_M}{A_{eff}} \tag{4.10}$$

can be used to estimate sinkage, with m as the mass of the object under consideration and A_{eff} as the effective area of contact with the surface. For lander footings, rover legs with plane footpads, or astronaut boots, the effective area A_{eff} will be always equal, regardless of the sinkage into the soil. For round rover wheels however, the effective contact area will increase as the wheel begins to sink into the soil, until the point where it has sunk into the soil up to its center, that is, its radius. The same is valid for curved footpads of leg wheel rover hybrids, such as RHex and SpaceBok type rovers (Boston-Dynamics, 2019; SpaceBok, 2017), Figure A.52 and Figure A.53); however, the calculation of their contact area is slightly more complex. Bekker (1956) and Bekker (1960) stress that usage of soil shear strength as a measure for trafficability is precarious and always dependent on the shape of the wheel/pad ground contact area. Therefore, Bekker (1960) recommends to conduct shear strength based sinkage estimations only for vehicles with strip like contact areas, that is, with wheel/pad width to diameter ratios of less than ∼0.5 (class II or higher). This criterion is being met by all assessed wheeled rover and all hybrid rover designs (Table A.9). For this work, the footpads of legged rovers, such as Spot type robots (Boston-Dynamics, 2019), have been approximated as wheels, due to their shape. In this study, Equation 4.10 is used to provide an estimate of sinkage using ultimate bearing capacity but does not consider soil compaction, dilatancy, or effects caused by elastic wheel deformation and across profile wheel or footpad curvature. In addition, the sinkage is estimated assuming a static load scenario, that is, no movement of the rovers is considered. The estimations based on Equation 4.10 also assume that the wheel or pad has a closed and solid surface. This study estimated wheel or leg sinkage of current and future wheel based rover designs such as the Lunar Electric Rover (LER, also known as Space Exploration Vehicle), Resource Prospector, and Yutu (Figure A.53a-Figure A.53c), as well as of leg based or hybrid robots such as SpaceBok, Spot, and RHex type rovers (Figure A.53d-Figure A.53f).

2.4 Soil Mechanical Properties

Lunar soil mechanical properties such as density, cohesion, and internal friction angle have been estimated throughout literature, often resulting in a wide range of results (Carrier et al., 1991). Therefore, a range of values have been used when calculating bearing capacity of the lunar surface and the associated friction angle, making the results difficult to compare (Hovland, Mitchell, 1969a, 1973; Moore, 1970). Generally, the soil property values used in the literature represent bulk lunar soil. In order to calculate bearing capacities at different locations on the lunar surface, specific soil property values have been obtained for each LPD, highland, and mare regions. Soil density values have been selected from Apollo core tube analyses that best represent LPD, highland, and mare material (Table A.10). For each location, density values for the top 30 cm and lower than 30 cm of regolith are available. The top 30 cm represents the soil that will be considered for calculations in the shallow depth domain (rover tracks and shallow boulder tracks), while the density below 30 cm will be used for calculations of boulder tracks that run deeper than the indicated shallow domain. Cohesion values have been calculated in previous studies based on measurements taken on the lunar surface and produce a range of values of 0.1 to 4.9 kN/m^2 (Carrier et al., 1991). Boreholes drilled during the Apollo 16 and 17 missions remained open after the drill stem has been withdrawn, demonstrating the significant cohesion of the lunar regolith (Carrier et al., 1991). For the bearing capacity calculations in this work, an estimate of 1 kN/m^2 is used for cohesion (Hovland, Mitchell, 1971; Houston et al., 1972).

The angle of internal friction is dependent on the local context and conditions of the soil, including porosity, density of stratification, and the shape of particles (e.g., sphericity, smoothness, and roundness) (Melosh, 2011; Cho et al., 2007). Authors such as Melosh (2011), Houston et al. (1972), and Mitchell et al. (1974) provide values ranging from around 13 to 50° for lunar soils and terrestrial analogs, based on in situ and remote measurements. Despite this wide range, the use of isolated friction angle parameters out of their original spatial context might add uncertainties to the bearing capacity calculations, particularly as this parameter is decisive for the accuracy of the calculations (the N factors in particular). In lieu of the absence of site specific literature values, the angle of repose of shallow granular flows is measured in six high resolution NAC based digital elevation models (DEMs). The DEMs have been processed for mare, highland, and LPDs using the Ames Stereo Pipeline (Shean et al., 2016); details about the DEMs are displayed in Table A.11. The internal friction angle of a dry granular mass expresses itself as the so called

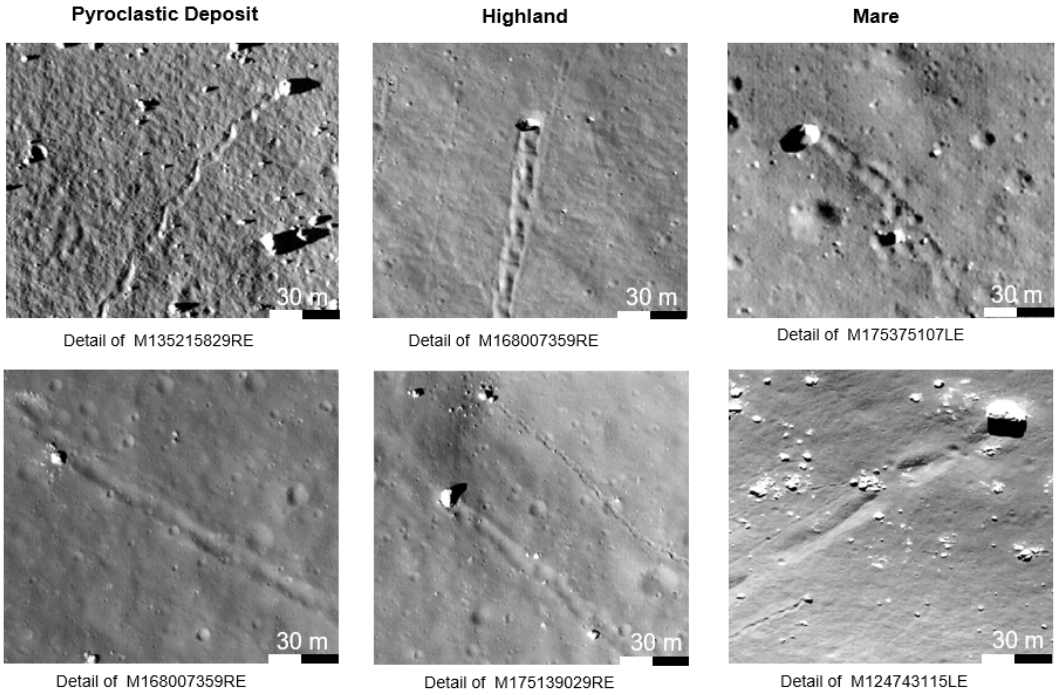


Figure 4.1: Qualitative comparison of boulder track shape and appearance in mare, highland, and LPDs; no differences in appearance suggest similar geomechanical properties of material. Tracks with potential inertial soil responses and rounded edges are displayed in the second row. North is up. LPDs = lunar pyroclastic deposits.

angle of repose, that is, the maximum angle at which a loose pile of material still stands stable (Melosh, 2011). By measuring the local slope angle of flow features at their toe, the internal friction angle can be closely approximated, assuming that the material of the flow is the same as the substrate. The respective measurements are performed across several shallow granular flow like features to derive a representative average. The resulting friction angle values are 28° for mare material, 30° for highland material, and 31° for LPD material, which is a significant refinement of literature values.

Measurements

A total of 149 boulder tracks are used to make eight unique measurements for the bearing capacity calculations. Measurements include long (L) and short diameters (B) of the boulder, track width (W), shadow length within the boulder track (S), and local slope (β), according to Figure A.51 and Figure A.52. All measurements are taken near the boulder's terminus and near its origin (static assumption). The width and shadow length measurements are conducted 3 times for each of the individual tracks whenever possible. One source of variability in boulder track measurements results from irregular tracks where the track width changes due to wobbling along the track. Such effects have been minimized through average measurements where data were obtained at maximum, minimum, and intermediate width. Further, tracks that show signs of a strong inertial response, such as rounded edges, have been measured in a conservative way, that is, using the distance between the inner rim of the two exterior track bulges.

Measurements of shadow length are performed on the same segment of track as the corresponding width measurements. Track shadow length near the boulder as well as the source are both measured by determining the location of the Sun and then measuring shadow length parallel to direction of illumination. Images in which the shadow length is perpendicular to the track provide the most accurate measurements. Inaccuracies occur when the shadow is not perpendicular to the track, in which case a shadow length measurement should be taken parallel to the Sun direction (Figure A.54). This should result in an equivalent shadow length measurement if the boulder track has spherical track elements. However, if the boulder

track does not contain spherical boulder footprints and the Sun orientation is not parallel to the track, then a potentially misleading shadow length will be measured. Data that do not meet the criteria for a correct shadow length will not be considered in this work. As the derivable track depth depends on the measurable shadow length (Equation 4.2), the spatial resolution of LRO's NAC of ∼0.5 m/pixel is limiting the ability of the technique to calculate bearing capacities at very shallow depths, that is, between surface level and ∼0.35 m. However, using imagery with very high solar incidence angles that cause long shadows even for very shallow tracks, the available horizontal resolution is sufficient to sample shadow length and, thus, track depth as small as ∼0.19 m.

Slope for the boulder and source locations is determined from the 100 m resolution, global LRO WAC stereo derived DEM (Scholten et al., 2012). As the spatial resolution of this DEM is coarse in comparison to the size of boulders, three high resolution DEMs (2 to 10 m/pixel) for highland, mare, and LPD sites have been produced with the Ames Stereo Pipeline (Shean et al., 2016); details about the DEMs are displayed in Table A.11. These NAC DEMs are compared to the global DEM of Scholten et al. (2012) to assess potential uncertainties, which could have been introduced by the use of the lower spatial resolution DEM. The direct comparison suggests that the lower spatial resolution of the used WAC DEM is sufficient and does not influence the accuracy of the slope measurements. All measured data are presented with histograms in Figure A.55 with respect to their respective region on the Moon.

In addition to boulder tracks, this study uses measurements performed in photographs taken during the Apollo and Surveyor missions, as well as in situ during the Lunokhod missions. Besides astronauts and rovers (LRV, Lunokhod), the MET and the boulder tracks measured on the ground during Apollo 17 are used for this analysis. The use of in situ data allows for a comparison of the remote sensing based results and for a calculation of bearing capacity results for shallow depths.

Results

Differences in the shape of boulder tracks in mare, highland, and LPDs may indicate differences in geomechanical properties. However, no differences of that type are observed among the regions, implying LPDs have similar geomechanical properties as those in mare and highland regions. Difference in track appearances appears to be influenced instead by boulder shape and displacement method, that is, rolling, sliding, or bouncing, than by region. Figure 4.1 displays a comparison between boulder tracks in all areas of interest. In this work, bearing capacity is investigated as a function of depth, slope, and equation used. In addition, the results have been classified by the region and the geomorphological context at which their corresponding measurements have been made. This allows for the comparison of pyroclastic soils with mare and highland material, as well as for the comparison of material on regular slopes, crater slopes, rilles, and pyroclastic vents. In order to evaluate the deviation in results between the Hansen and Terzaghi equations, the bearing capacity values calculated for all boulders are compared (Figure A.56). Both equations provide similar results for lower bearing capacity values. As bearing capacity values begin to increase the correlation between Terzaghi and Hansen weakens. Further, there is a trend in which the Terzaghi method provides generally higher bearing capacity values than Hansen. For both approaches, the N factors are decisive for the calculation of the bearing capacity. To put them into perspective and context, the derived factors for N_c, N_q, N_γ have been plotted in Figure A.57. The difference in the N factors is one reason why Hansen produces lower bearing capacity values. Lower values are also a result of the application of correction factors for Hansen (Equation A.6 to Equation A.19) that reduces the bearing capacity, based on the physical conditions and the geometry of the investigated site. As Hansen (Hansen, 1970) partially addresses these uncertainties (e.g., regarding boulder shape and slope inclination), it is considered the more representative approach for this study, as it provides a better restricted and realistic lower boundary for the ultimate bearing capacity.

The bearing capacity values at each location type (LPDs, highland, and mare) and in varying geomorphological context are plotted with respect to the local slope angle where the measurements have been taken (Figure 4.2 and Figure A.56). The data are further subdivided by the depth of track. The boulders that are believed to have fully penetrated the surface regolith likely interacted with more consolidated material below. For this reason, these points have been plotted as hollow shapes to indicate that their values may not be representative of the upper regolith that this study is investigating. The estimate for the local average regolith thickness has been taken from several sources, using the shallowest estimate (see Table A.12 and Figure A.58). Results are shown for both Terzaghi and Hansen calculated values. A least squares fit

has been applied with a shaded error bar derived from an estimate of the standard deviation of the error. As seen in Figure 4.2 and Figure A.56, bearing capacity values increase with increasing depth. The values calculated using Hansen have a greater dependence on slope angle where the bearing capacity decreases with increasing slope angle. Bearing capacity values in mare and highland areas are similar, while LPDs show slightly higher values. An analysis of bearing capacity in relation to slope and geomorphological context shows no significant dependency and, thus, does not indicate a direct potential influence of local context (Figure A.59).

Bearing capacity as a function of track depth is presented in Figure 4.3a and Figure A.57 for LPDs, highland, and mare material for both the Terzaghi and Hansen equations. Due to the limitation in spatial resolution of NAC images at around 0.5 m/pixel, no boulders smaller than ∼1.5 m in diameter can be observed; that is, no shallow boulder tracks can be measured, causing a gap of remote sensing derived bearing capacity values from 0 to a depth of ∼0.19 m in all regions. A least squares fit has been applied, and a shaded error bar derived from an estimate of the standard deviation of the error. Generally, the bearing capacity for each location increases with depth, which is to be expected as the material at depth becomes increasingly compact and less porous (Carrier et al., 1991; Houston et al., 1972; Mitchell et al., 1972b) and because a larger soil column causes a higher surcharge load (Equation 4.1 and Equation 4.6). As in Figure 4.2 and Figure A.54 the Terzaghi equation provides consistently higher estimates for bearing capacity. Hollow data points represent depth measurements that exceed the estimated regolith thickness at the measured location, based on Table A.12 and Figure A.58. Bearing capacity as a function of depth and geomorphological context does not indicate a significant influence of local context (Figure A.60).

To compare the bearing capacity values generated in this work, a two sample t test assuming unequal variances (two tail) was run between each of the three regions for four depth subdivisions (0.19 to 1, 1 to 2, 2 to 6, 6 + m), which provided twelve p values based on a 95% confidence interval (detailed statistics and results can be found in Table A.13). Results indicate that LPDs have equal or significantly higher bearing capacity values for the four investigated depth ranges than mare and highland areas. Mare and highland regions show statistically equal bearing capacities over the entire depth range from 0.19 to 6 + m.
Based on the statistical similarity and degree of correlation of bearing capacity over depth between mare and highland regions, the calculated mare and highland bearing capacity values are plotted together and combined with the bearing capacity values calculated using boulder tracks measured in photographs taken during the Apollo 17 mission (Figure 4.3b). The results from both the in situ and the remotely measured values can be directly compared in the depth range from 0.19 to ∼5 m and show a high degree of correlation. Based on this correlation and in order to close the gap between surface level and 0.19 m depth, lines of best fit have been interpolated to link the results based on boulder tracks (remote and in situ) to bearing capacity results calculated with the identical method (Hansen, 1970; Terzaghi, 1951) but using shallower measurements taken from Apollo MET and LRV track photographs in mare and highland regions. These fits consist of three segments in the previously selected depth ranges of 0 to 1, 1 to 2, and 2 to 6 m, cut at 5 m. The derived fit for 0 to 1 m is based on values calculated from the in situ measurements as well as on values derived from boulder track measurements. For the depth range from 1 to 2 and 2 to 6 m only the bearing capacity values calculated based on in situ measurements (Apollo 17 observations of boulder tracks) have been used, because they represent a conservative lower limit for the soils' strength in mare and highland regions at that depth (Figure 4.3b). The derived equations for the line fits with q_f in kN/m^2 and D in meters are

$$0 - 1m : q_f = \frac{D + 0.14}{0.026} \tag{4.11}$$

$$1 - 6m : q_f = \frac{D + 0.596}{0.0.037} \tag{4.12}$$

As shown by the statistical analysis, the bearing capacity of LPDs based on boulder tracks appears to be equal or significantly higher than in mare and highland areas along the entire investigated depth range from 0.19 to 5 m. It may, thus, be possible that the derived interpolated linear fit for mare and highland regions represents a conservative lower limit of bearing capacity in LPDs. Based on the assumption that the mechanical behavior of LPDs is only governed by the factors considered by the used equations, the derived lower limit has been extrapolated to close the sampling gap between the surface and 0.19 m depth. This extrapolation is based on the assumption (discussed further below) that soil strengthening processes such as sintering are absent or do not significantly contribute to the mechanical behavior of LPD regolith

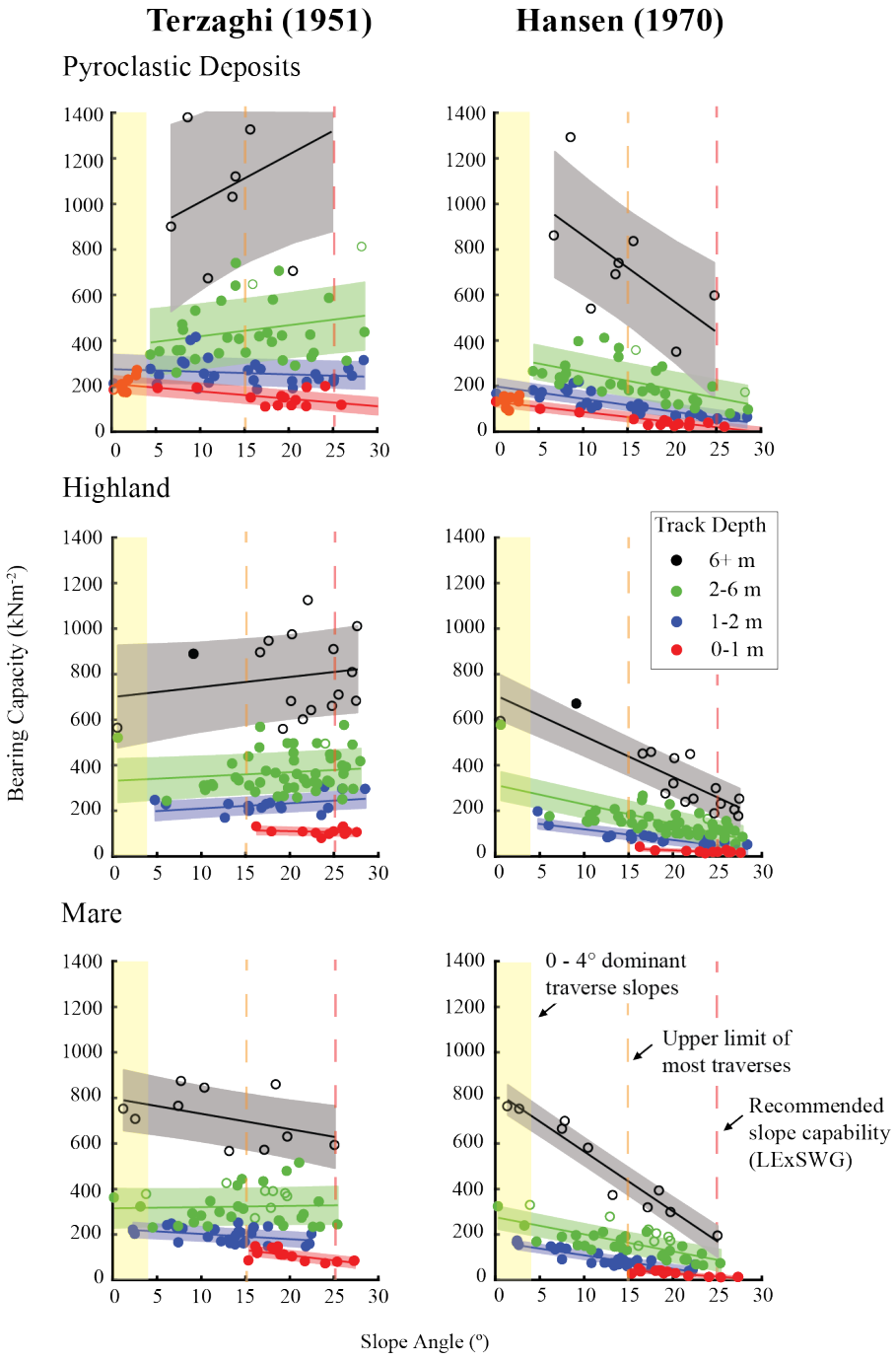


Figure 4.2: Bearing capacity values are shown here as a function of slope angle. Values are provided from both the Terzaghi and Hansen calculations. Colors correspond to the depth of track from which the values are derived. Hollow circles indicate track depths that exceed local regolith thickness estimates. Slope traverse values are taken from the final report of the Lunar Exploration Science Working Group (LExSWG, 1995).

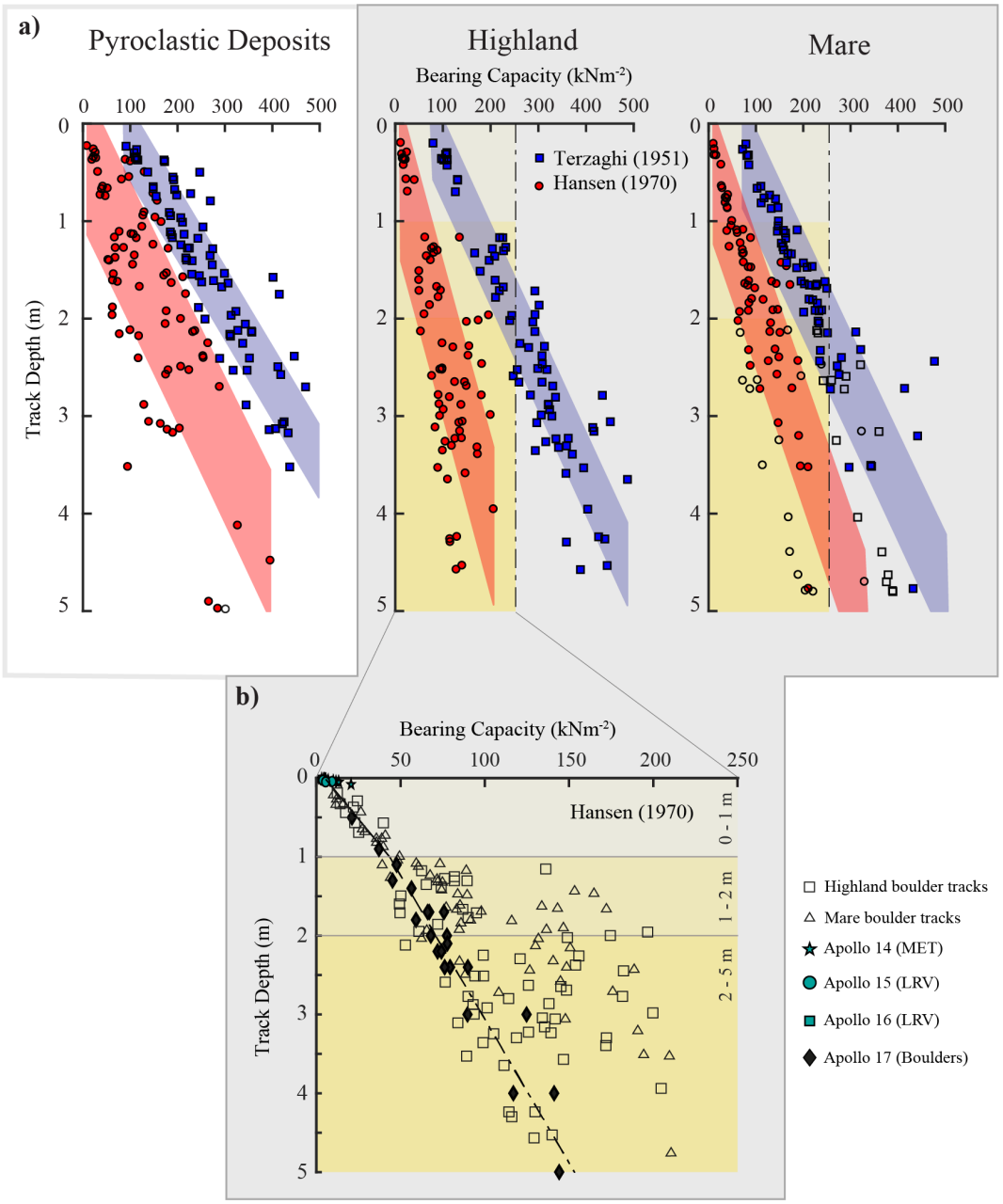


Figure 4.3: (a) The bearing capacity values for each boulder site are presented as a function of track depth. The vertical line indicates the adapted x axis limit for Figure 4.3b, while the vertical color gradient indicates depth ranges used in Figure 4.3b. Hollow shapes indicate boulders that are believed to have cut through the regolith at their location based on estimates taken from sources listed in Table A.12/Figure A.58. (b) Combination of bearing capacity values (mare and highland) calculated Hansen (Hansen, 1970) based on remotely measured data and in situ measured data.

in the investigated depth range. The extrapolated linear bearing capacity envelope has been used for the subsequent trafficability analysis. Numerical results of calculated ultimate bearing capacity including associated error for each investigated location type at the specified depth ranges and for varying slope values are displayed in Table A.14.

Discussion

This study uses observations of tracks carved by rockfalls to derive qualitative and quantitative properties of the regolith in LPDs in comparison to that in mare and highland areas. Hovland, Mitchell (1971) note that boulder track width appears to be sensitive to changes in regolith conditions. However, observations of boulder track shapes and appearances in the regions of interest did not show any significant differences. Slight differences in track sharpness, clarity, and apparent width equally occur in all investigated regions and could be indicative of an inertial response of the shearing soil that is pronounced due to the lower gravitational acceleration on the Moon, initially caused by very dynamic boulder displacements. Rounded track edges could also express an ongoing erosion over time, for example, driven by microimpacts.

Besides the described Apollo 15 LRV incident, the Soviet Union's Lunokhod 2 rover experienced increased wheel sinkage as it approached the toe of a slope in Le Monnier Crater (Carrier et al., 1991; Florensky et al., 1978). This sinkage indicates a reduction of bearing capacity that could be connected to the geomorphological environment or the genesis of this specific site. Melosh (2011) suggests that slow downslope movement of regolith occurs on lunar slopes, resulting in characteristic slope lobes and textures. Material transport is caused by thermal variations, micrometeorite impacts, seismic shaking, and electrostatic levitation. Downslope movement of regolith implies it accumulates at the bottom of slopes, potentially resulting in an increased regolith thickness and lower bearing capacity values, possibly influenced by a higher porosity of the regolith present (Houston et al., 1972). However, the results derived here do not directly imply reduced bearing capacities at the bottom of slopes. In contrast, soil strength appears to increase with lower slope gradients; that is, it is observed to be higher at the toes of slopes, as it has previously been described by Carrier et al. (1991) based on in situ sampling. On slopes, however, as illustrated by Figure 4.2 and Figure A.57, bearing capacity of lunar regolith generally varies, where higher slope gradients reflect lower bearing capacities. Based on Hansen's (Hansen, 1970) equation, this is caused by the fact that an inclination of the surface results in a reduced soil volume that is bearing the boulder. This reduces the surcharge and friction terms, as well as the bearing capacity (Castelli, Lentini, 2012; Meyerhof, 1957). Results derived with Terzaghi (Terzaghi, 1951) also show a slight but noticeable decreasing bearing capacity trend with increasing slope angles for very shallow track depths, independent on region or geomorphological context, although the equations do not consider slope inclination (Figure 4.2 and Figure A.56). This could indicate that there is another reason or predisposition that reduces the bearing capacity of lunar regolith on slopes in the depth range from 0 to 1 m, such as potential surficial mass movements as previously suggested by Melosh (2011) or Houston et al. (1972) that form a shallow regolith colluvium with altered mechanical properties.

Cone penetrometer data from human and robotic lunar surface missions indicate a similar behavior of the soil, as regolith has been found to be weaker on slopes than in flat areas, at least down to a depth of 70 cm (Carrier et al., 1991). A direct comparison of different geomorphological settings suggests that bearing capacity of impact crater slopes, regular slopes, slopes in pyroclastic vents, and lopes in rilles is similar over the entire slope angle and depth range (Figure A.56 and Figure A.57). Therefore, the influence of geomorphology and genesis on regolith bearing capacity in the investigated depth range might be limited or at least less significant than the observed influence of slope angle and location along the slope. However, the technique used in this study to derive bearing capacity has a limited capability to investigate distribution of bearing capacity at very shallow depths ~0.19 m and less, due to the limitations in spatial resolution of the used sensor (NAC). Therefore, geomorphology dependent heterogeneities and variations of bearing capacity at shallow centimeter scale depths on lunar slopes and their toes cannot be ultimately excluded and remain to be tested in situ.

Some clues about the potential properties of pyroclastic material at shallower depths can be gleaned from Apollo 15 and 17 observations of pyroclastic glass deposits. At Apollo 15, where green pyroclastic glass was mixed with other soil constituents, no significant increase in the sinkage of astronauts or the LRV was noted as a function of increasing green color of the soil. At Apollo 17, where a unit of wholly orange and black pyroclastic glass was exposed at the surface, no increase in sinkage was observed (e.g., NASA images

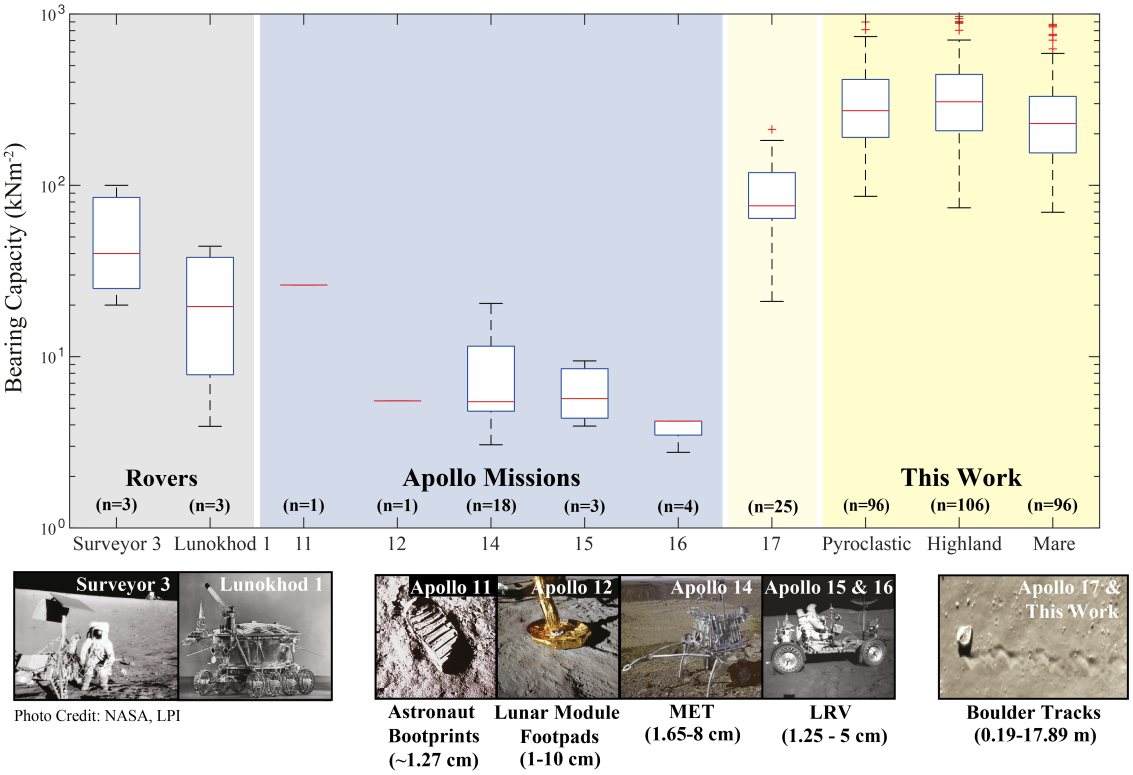


Figure 4.4: Comparison of bearing capacity values in this work and those calculated from literature values, including from different vehicles and objects, that is, astronaut bootprints, rover wheels, lander footpads, and rockfalls (Jaffe, 1971). Values used in calculations are taken from Apollo preliminary science reports 11-17 (Mitchell et al., 1972a, 1973, 1974). Lunokhod 1 bearing capacity values have not been calculated with the method presented in this paper but have been transferred from kg/cm^2 to kN/m^2 (Basilevsky et al., 2015). Bearing capacity values are dependent on depth; that is, small bearing capacity values reflect shallow penetration depths of the respective vehicle (e.g., landing pads). Black lines in box plots indicate the median of the respective data set, and red crosses indicate outliers. Highland and mare data are taken from widespread locations, and the average regolith thicknesses within those materials, from the literature, are used to constrain estimated regolith thickness. This explains overlap in sample numbers.

A17-137-20986 and A17-137-20990) (Muehlberger et al., 1973). Near Shorty Crater, where a deposit of pyroclastic glass is exposed at the surface (0 cm) and extends to a depth of at least 70 cm, the bearing capacity is similar to, if not greater than, that of nearby pyroclastic poor soils. It is so remarkable that Mitchell et al. (1973) reported the orange pyroclastic soil is unusually compact and exhibits high cohesion. The material was affected by the Shorty Crater impact event but that would have had a tendency to reduce cohesion, not increase it. Moreover, no degradation of that cohesion seems to have occurred over the past 19 Ma (Eugster et al., 1977) after being re-exposed by the Shorty Crater impact event. Rover traverse planning draws on extensive use of slope maps to determine whether rovers are able to access specific regions of interest, as wheels tend to be susceptible to slip as slope gradients increase. However, the results of this study imply that trafficability analyses should also consider variations, and potentially heterogeneities, of bearing capacity along slopes to prevent rovers from unfavorable wheel sinkage. In addition, knowledge about variations of wheel sinkage along slopes based on bearing capacity might help optimize rover wheel design to trade off sinkage and traction for on slope propulsion.

The observed increase of bearing capacity with increasing depth (Figure 4.3 and Figure A.57) is expected and is caused by the decrease of soil porosity and an increase of the soil surcharge shear strength term that contains the depth of footing, representing the fact that the volume of soil that resists a load increases with depth. Interestingly, the increase of bearing capacity over depth is more significant for LPDs than for mare and highland areas, although reasons for this observation are unknown. The bearing capacity envelope of the three investigated regions down to a depth of ~5 m might support the design and construction of

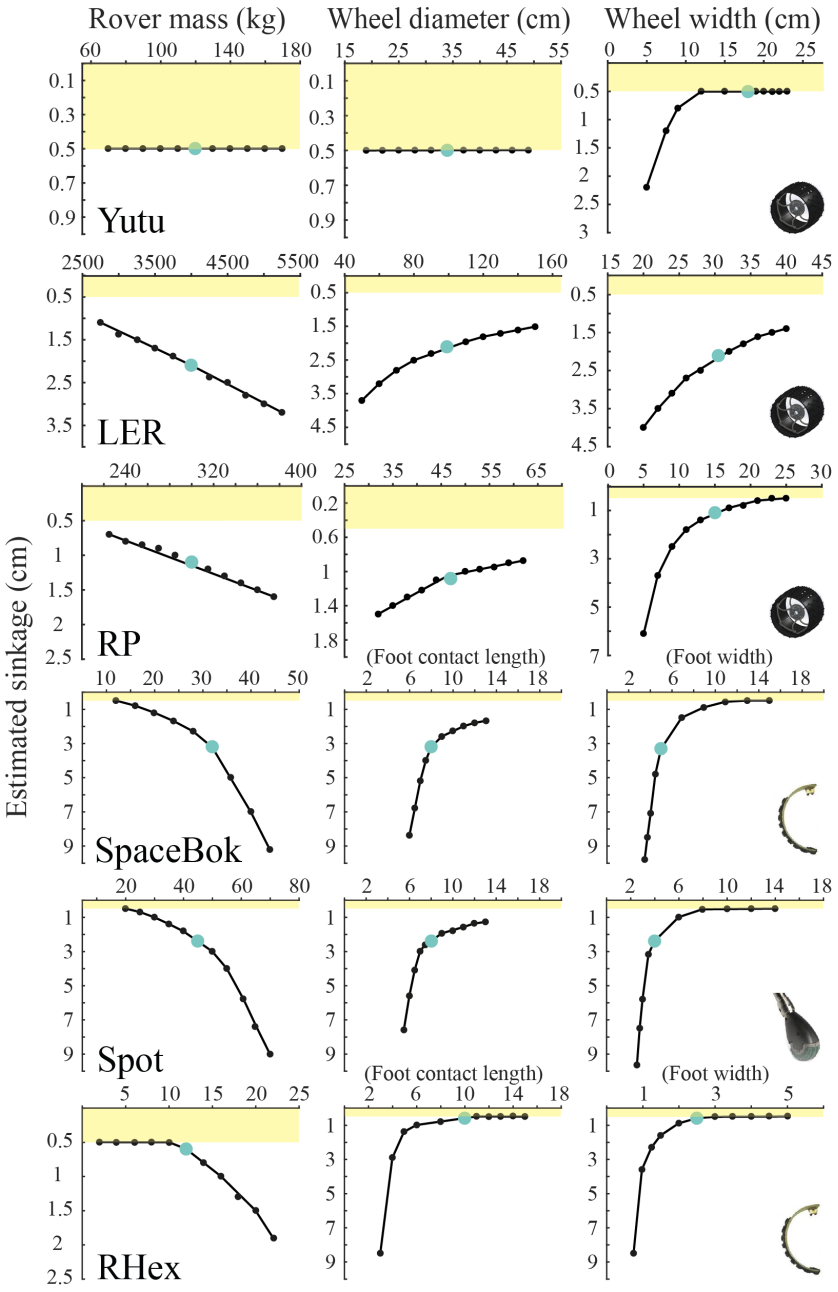


Figure 4.5: Yutu, LER, RP, SpaceBok, Spot, RHex type rover estimated sinkage as function of difference in mass, wheel diameter/foot contact length, and wheel/foot width, based on derived bearing capacity values. All wheels/legs touch the ground. Cyan point denotes the sinkage using the default vehicle design specifications. Shaded area marks depth range from 0 to 0.5 cm, where sinkage has not been calculated. Vehicle specifications have been taken or inferred from Carrier et al. (1991), Asnani et al. (2009), ESA (n.d.a), ESA (n.d.b), W. J. Bluethmann (pers. comm., 2018), NASA (2010), Boston-Dynamics (2019), SpaceBok (2017), and photographs/blueprints (where information was not directly accessible). Vehicle details are available in Table A.9. SEV = Space Exploration Vehicle; RP = Resource Prospector; LER = Lunar Electric Rover.

shallow foundations for future infrastructure elements used for long term exploration (Sanders, Larson, 2013) or ISRU purposes such as habitats, radiation shields, storage units, or scientific instruments such as large telescopes. Figure 4.2, Figure 4.3, and Figure A.57 also include measurements that appear to reflect a consolidated type of regolith at depth. We note that the thickness of the regolith has been shown to vary greatly from as little as 2 m in some regions to as much as 15 m in others (Bart et al., 2011; McKay et al., 1991). This variation in regolith thickness is important when interpreting bearing capacities derived from boulder track measurements at larger depths since large rockfalls can potentially penetrate below the unconsolidated regolith. The bearing capacity derived from deep penetrating boulder tracks would then reflect the bearing capacity of the deep, consolidated layers and thus would be much higher, as displayed in Figure 4.2, Figure 4.3, Figure A.56, and Figure A.57 with bearing capacity values reaching up to ∼800 kPa and beyond. Using the shallowest unconsolidated regolith thickness estimates, potential tracks that carved into consolidated material have been identified and marked (Table A.12 and Figure A.58).

To further illuminate the results derived here based on orbital observations of boulder tracks, we compare them with results derived from previous Apollo era missions. First, using the identical equations, the bearing capacities derived from measurements of boulder tracks in photographs taken during the Apollo 17 mission are calculated (Figure 4.3b and Figure 4.4). Second, bearing capacities for shallower depths based on measurements in photographs taken from Surveyor 3 footpads, Apollo 11 bootprints, Apollo 12 LM footpads, Apollo 14 MET tracks, and Apollo 15/16 LRV tracks are calculated (Figure 4.3b and Figure 4.4). In addition, bearing capacity results from Lunokhod 1 tracks are included in the comparison (Figure 4.4). Bearing capacities derived with different measurement methods correlate well and provide a similar lower limit for bearing capacity in mare highland and LPD regions. As additional support, photographs of LRV tracks in the three investigated regions have been analyzed in a qualitative manner (Figure A.61). The LRV tracks show no region dependent differences, potentially supporting the assumption of a linear type bearing capacity envelope as described by Equation 4.11 and Equation 4.12. Here the regolith at Shorty Crater, Apollo 17 station 4, is assumed to approximate LPD regolith. However, the surface material next to station 4 might not be entirely representative for the regolith encountered in large scale pyroclastic deposits. Bearing capacities calculated based on boulder tracks measured in Apollo ground imagery tend to fall on the lower side of the point cloud in Figure 4.3b, while staying within the results derived using NAC imagery. Potential explanations of this tendency could be that the regolith in the Apollo 17 area actually has a slightly lower bearing capacity or that there is a slight bias in the observations and measurements of track properties in the Apollo imagery. For example, a bias could be introduced by the different viewing geometry or spatial resolution of the Apollo era images.

The extrapolated bearing capacity envelope (Figure 4.3b) has been used to assess the trafficability of LPDs, mare, and highland regions, using the relation between vehicle mass and effective contact area between vehicle and soil (Equation 4.10). To do so, current rover design specifications for LER, Resource Prospector, Yutu, SpaceBok , Spot , and RHex type rovers have been modified to explore the parameter space and simulate potential surcharge load due to additional crew or collected specimens during a science or resource extraction mission (Figure 4.5). Results indicate that Yutu's sinkage is limited within the applied parameter space, with sinkage only significantly increasing with narrow wheels. A modification of wheel width appears to be an effective way to ensure that a rover, in particular the LER, is capable of traversing LPDs and other lunar regions. Figure 4.5 also illustrates that legged walking and jumping rovers like Spot and SpaceBok type robots, as well as hybrids like RHex, are able to traverse LPDs, using the extrapolated bearing capacity envelope. Like for wheeled rovers, sinkage of legged robots could be effectively limited by adapting the footpad width. For wheeled rovers, extra mass due to collected samples, as well as wheel diameter appear to have smaller influence on the estimated sinkage. In contrast to wheeled rovers, the investigated legged robots appear to be more susceptible to sinkage as a function of increasing weight. These deliberations do not consider detailed effects of modified wheel diameter width ratio or footpad size on other trafficability aspects such as propulsion and energy consumption, however.

The assessment of LPD trafficability has implications for the design of future missions. A high priority target for robotic and crewed missions is the pyroclastic vent in the Schrödinger basin, but it has been unclear whether wheeled or legged assets are able to traverse its periphery and to access its center (Allender et al., 2019; Bunte et al., 2011; O'Sullivan et al., 2011; Potts et al., 2015; Steenstra et al., 2016). The results of this study provide no evidence that the previous assumption of a traversable surface around the vent is invalid, thus, surface missions in this and similar locations may be possible using existing and proposed rover designs. Besides optimizing wheel or footpad width to avoid sinkage, a safe alternative could be to adapt the diameter of the wheels. Because bearing capacity values appear to be remarkably high at

depths larger than 0.19 m, wheels with diameters >38 cm should not encounter flotation issues, based on the results of this study. However, such an increase in wheel diameter would require sufficient rover ground clearance and could result in an increased rolling resistance — among others — and, thus, would demand motors that can produce higher torque — depending on the effective sinkage. Based on the results of this study, the interior of Schrödinger basin's vent may be traversable as well, concerning near surface bearing capacity. The bearing capacity envelope developed here as a function of slope angle could be used to produce a map of the vent and its surrounding that illustrates the spatial distribution of bearing capacity and identifies no go areas for specific vehicles, similar to a maximum traversable slope angle map used for mission planning. Further, the findings of this work could support the assessment and adjustment of vehicle properties in order to optimize the locomotion performance of rovers like the LER within and outside of the vent. Thus, the results of this study help to reduce and better anticipate risk related to future exploration and ISRU missions to the pyroclastic vent in the Schrödinger basin as well as similar sites on the Moon. It has to be noted that this study investigated LPD trafficability in terms of bearing capacity (wheel sinkage) only. In steep terrain, such as pyroclastic vents, other trafficability parameters become important for a successful traverse, for example, wheel slip and traction.

Conclusions

This work uses measurements of boulder tracks in NAC imagery to derive the bearing capacity of LPD, mare, and highland regions to assess their trafficability. A statistical analysis of the results suggests that all investigated regions have similar bearing capacity values from 0.19 to a depth of ∼5 m and along varying slope gradients, where bearing capacity increases with depth and decreases with higher local slope gradients. In addition, LPDs exhibit statistically equal or significantly higher bearing capacities than mare and highland regions in all investigated depth ranges. Results indicate that the influence of geomorphological context and genesis on bearing capacity is limited over the observed depth and slope range. Qualitative observations of boulder tracks in all regions of interest show no region based differences and, thus, support the quantitative analysis. Results derived with the implemented equations using remote measurements correlate well with results derived using data collected in photographs taken during the past Surveyor and Apollo missions, as well as in situ during the past Lunokhod lunar surface missions. The high degree of statistical correlation between mare and highland areas, as well as the in situ based values, is used to establish a general bearing capacity distribution trend from the surface down to a depth of ∼5 m. As LPDs generally display equal or significantly higher bearing capacity values based on the statistical analysis along the observable depth range, this general trend is anticipated to be representative for LPDs as well, assuming that mechanical strength of LPD regolith is only caused by the considered parameters. A comparison of LRV tracks in the three investigated regions potentially supports this hypothesis.

Based on this assumption, the derived general bearing capacity distribution enables an analysis of the estimated sinkage of current and potential future rover designs as a measure for surface trafficability. The analysis shows no evidence that LPDs are not able to generally bear even heavy vehicles such as the LER. Therefore, this study promotes the feasibility of previously proposed traverses into untraversed lunar regions, including high priority targets such as the surrounding and potentially the center of the pyroclastic vent in Schrödinger basin (Allender et al., 2019; Bunte et al., 2011; O'Sullivan et al., 2011; Steenstra et al., 2016). In addition, this study investigates changes in rover specifications such as wheel/footpad width, pad contact length, and wheel diameter and simulates extra mass caused by sample collection and finds that vehicle sinkage could be effectively limited by an optimization of wheel and pad width. Wheel diameters larger than 38 cm could be an alternative to assure trafficability of vehicles in LPDs, to the potential cost of higher rolling resistance, requiring larger driving torque. For example, the radii of the wheels on the prototype LER (34.3 cm) (Harrison et al., 2008) and on the anticipated flight version of it (49 cm) (NASA, 2010) exceed 19 cm. Thus, that vehicle should be able to traverse pyroclastic deposits. Other applications of this study's findings potentially include the design of foundations for exploration and ISRU infrastructure, as well as heavy instrumentation.

Acknowledgments

The authors would like to acknowledge the support of the Lunar and Planetary Institute (LPI) in Houston, TX, and the Universities Space Research Association. Funding was provided by the NASA Solar System Exploration Research Virtual Institute (NNXA14AB07A, PI David A. Kring). The research was performed

as part of the Exploration Science Summer Intern Program hosted by the LPI and the NASA Johnson Space Center in Houston, TX. The authors thank William J. Bluethmann of NASA's Human Robotic Systems Project and Julie D. Stopar of the LPI for their willingness to provide insights about the LER and LROC systems, respectively. In addition, the authors would like to acknowledge the ideas of Christian Venturino presented during a previous LPI Exploration Science Summer Internship boulder track related project. Moreover, one of us (V. T. B.) gratefully acknowledges financial support from the International Max Planck Research School at the Max Planck Institute for Solar System Research (IMPRS) and the Engineering Geology Group, Department of Earth Sciences, Swiss Federal Institute of Technology Zurich (ETHZ). This research has made use of the USGS Integrated Software for Imagers and Spectrometers (ISIS) and the Ames Stereo Pipeline (ASP). Due to online storage limitations, data can only be made available upon request to the authors. Alternatively, used data can be retrieved from the cited references or from the LROC image archive: http://wms.lroc.asu.edu/lroc/search. All used NAC image IDs can be found in the supporting information (Table A.15). This is LPI contribution 2166. The study was conceived by D. A. K and implemented by V. T. B., C. I. H., S. N. M., A. R., and H. M. S. with D. A. K. ISRU issues were addressed by C. I. H., A. R., and H. M. S., while V. T. B., C. I. H., S. N. M., A. R., and H. M. S. selected sites of interest. V. T. B. processed imagery and DEMs; V. T. B. and H. M. S. conceived the implementation of bearing capacity equations; S. N. M. and A. R. built the GIS and performed measurements; and V. T. B. performed the trafficability analysis. V. T. B., C. I. H., S. N. M., A. R., and H. M. S. analyzed the results and wrote the first draft of the paper. All authors contributed to a discussion of findings, their implications for future missions, and editing the paper. The authors thank Ralph Lorenz, an anonymous reviewer, and Associate Editor Elizabeth Turtle for their constructive comments.

4.2 Lunar South Pole Boulders and Boulder Tracks: Implications for Crew and Rover Traverses

Published 2020 in Icarus
Bickel, V.T., Kring, D.A., 2020
https://doi.org/10.1016/j.icarus.2020.113850

Abstract
Knowledge about the geomechanical properties of the southern circumpolar regolith and its spatial variability is essential for effective and diligent planning of future crew and rover traverses. At this time, the trafficability of the lunar south pole remains untested and could potentially be different from low-latitude regions that have been traversed in the past. Geomechanical properties of those untraversed regions can be estimated using observations of boulder tracks captured from orbit. Eighty-four boulders with tracks in the region poleward from 85° S have been mapped in Lunar Reconnaissance Orbiter's NAC imagery using a deep learning-driven and operator-complemented approach. An additional 13 boulder tracks have been mapped that enter and disappear in Shackleton Crater's permanently shadowed region. A recently developed methodology has been adapted for extreme lighting conditions and used to estimate the bearing capacity of regolith crossed by 16 boulders in sunlit regions in the vicinity of the south pole. Estimated bearing capacity values are similar to those derived for equatorial highland regions of the Moon that were successfully traversed in the past. A qualitative and semi-quantitative comparison of track morphologies across the regions does not show any major differences. Measurements of boulder tracks have then been used to establish a conservative quantitative relation between track depth, local slope angle, and circumpolar bearing capacity. This relation has been used to map the approximate surface strength of the sunlit lunar south polar region as function of topography. The resulting product has been applied to study the estimated sinkage of exploration rovers on slopes, indicating that sinkage-related issues might only start to occur on inclines steeper than 25° while the potential for local, slope independent mechanical strength anomalies remains. The results of this study show no evidence that future south polar surface operations would be affected by insufficient sunlit regolith bearing capacities.

Introduction

The Moon is an airless body completely exposed to colliding planetary debris. Any time astronauts or robots navigate its surface, they must contend with a regolith that has been shaped and modified by impact cratering processes on scales ranging from micrometeorites to full-size asteroids in excess of a hundred kilometers in diameter. Those processes produced a regolith and unconsolidated soil profile that were successfully traversed during the Apollo and Luna programs, albeit with some caveats. Apollo's Lunar Roving Vehicle (LRV) became stuck during the Apollo 15 mission (Costes et al., 1972) and Luna's Lunokhod 2 rover (Carrier et al., 1991; Florensky et al., 1978) encountered soft soils on the inside walls of craters and the base of slopes in crater Le Monnier. Both those missions involved terrains dominated by volcanic basalt plains (mare). Other wheeled assets successfully traversed highland terrains that are typically older and composed of more feldspathic material. Apollo and Luna data, when combined with that of landed Surveyor spacecraft, provided insights to the lunar surface at 17 landing sites in equatorial to low latitude sites on the lunar nearside. Most recently, Chang'e missions provided additional data for a lunar nearside landing site and the first near-equatorial farside location.

Regolith conditions probably differ elsewhere on the Moon, particularly in polar and pyroclastic regions. Usually, mobility considerations are either based on analogue materials (Atkinson et al., 2019; Jayalekshmi, Kumar, 2019) or based on values derived during the Apollo and Lunokhod missions (Basilevsky et al., 2019; Khademian et al., 2019; Speyerer et al., 2016) and might, therefore, not be entirely representative. For that reason, we initiated a systematic assessment of trafficability of potential science and exploration targets using local boulders and boulder tracks produced by rockfalls. A study of boulder tracks on large pyroclastic deposits, targets for both scientific objectives (NRC, 2007) and in situ resource utilization (ISRU) (Allen et al., 1996), indicated they have average bearing capacities no less than that experienced in highland and mare terrains (Bickel et al., 2019). More recently, a study of tracks in permanently shadowed regions (PSRs) suggests that they, too, can be traversed (Sargeant et al., 2020). PSRs are of interest because they may host large quantities of ices, which may hold clues about the volatile evolution of the Moon (NRC, 2007) and significant quantities of ISRU material, too. That study was limited to latitudes of 70 to 76° S,

however, so it remains unclear what type of trafficability may exist closer to the poles and in the coldest PSRs. With the advent of the Artemis program and its planned landing of astronauts at the south pole in 2024, it is necessary to take a closer look at circumpolar sunlit regolith properties that may affect landers, crew and robotic traverses, as well as infrastructure. Thus, here we extend our series of studies with an examination of sunlit regolith bearing capacities in the immediate vicinity of the lunar south pole and other sites poleward of 85° S.

First, the materials and methods are described, including descriptions of the deep learning-based rockfall and boulder track mapping, the applied bearing capacity methodology, its adaptation to the polar environment, and the used soil mechanical input parameters. Subsequently, results are presented and discussed, including an assessment of estimated sinkage behavior of two proposed rover concepts, a VIPER-class rover (Volatiles Investigating Polar Exploration Rover, former Resource Prospector) and LER (Lunar Electric Rover), followed by a conclusion of the work done.

Materials and Methods

This study is based on images taken by NASA's Lunar Reconnaissance Orbiter (LRO) Narrow Angle Camera (NAC) that has been in orbit around the Moon since 2009. NAC acquires single-band images with spatial resolutions of ∼0.5 m/pixel from LRO's nominal science orbit (Robinson et al., 2010) that allow for the mapping of small-scale geomorphological processes (rockfalls) and features (boulders with tracks). All NAC images used for analysis and measurements have been processed from level 0 (EDR, experimental data record) to georeferenced, projected, and GIS-ready products using ISIS3, following the same workflow as it has been used for previous studies of lunar bearing capacity (Bickel et al., 2019; Sargeant et al., 2020). The complete image list is shown in Table A.24 in the appendix. Other used data include a Digital Elevation Model of the south pole (30 m/pix) that is based on LRO laser altimeter measurements (LRO-L-LOLA-4-GDR-V1.0 from the Planetary Data System), selected boulder track data from Bickel et al. (2019), as well as a map of south polar PSRs (McGovern et al., 2013).

2.1. Polar rockfall and boulder track mapping

Detection and mapping of boulders with tracks in the latitude range from 85° S to 90° S was performed with a combination of two approaches: (1) fully automated mapping with a convolutional neural network (Bickel et al., 2018) and (2) a subsequent operator-based verification phase. The application of a Convolutional Neural Network (CNN) reduces the required time to scan through the >1300 NAC images that cover the region of interest from weeks to hours, being orders of magnitude faster than a human operator. A list of NAC images (1293 NACs) taken from Wagner et al. (2015) has been scanned, in combination with additional, more recent imagery taken over the region of interest. All CNN detections were checked and verified by a human operator and were complemented, if required, using map-projected NAC imagery.

The mapping of small features in the polar regions of the Moon is challenging due to the extreme lighting conditions. Based on the experiences of the authors, the ability of a CNN to detect rockfalls in polar NAC imagery is limited to a similar extent as the ability of a human operator: successful detections are impeded by the presence of shadows, a lack of spatial resolution, and by boulder diameters below the NAC ground sampling distance (usually boulders smaller than ∼2 m), respectively (Bickel et al., 2018). Previous studies have shown that boulders with tracks can be identified in NAC images within regions of permanent shadow (PSRs), but not farther south than ∼76° S, due to high solar incidence angles and a lack of backscattered light from the surrounding topography (Sargeant et al., 2020). This means that rockfalls within PSRs in the region of interest (90° S to 85° S) have not been mapped and are, thus, excluded from this study. Boulder tracks that enter PSRs have been mapped, however, to inform potential follow up studies.

2.2. Qualitative, semi-quantitative, and quantitative regolith bearing capacity estimation

A previous study implemented a method to estimate the bearing capacity of regolith based on measurements of boulders and their tracks in satellite imagery (Bickel et al., 2019), customizing theory about shallow foundations from Terzaghi (Terzaghi, 1951) and Hansen (Hansen, 1970). Bearing capacity is a fundamental geomechanical and trafficability property that can be used to approximate the static sinkage or flotation of landers, rovers, and crew on previously untraversed surfaces, based on the weight of an object and the effective contact area with the ground. An elegant method to estimate sinkage has been described by Mitchell et al. (1974) and Carrier et al. (1991) that is based on the modulus of subgrade reaction derived from Apollo astronaut bootprints, using a linear Winkler model (Winkler, 1867). However,

the applicability of this method in unexplored regions is currently limited, as it is unclear whether the fundamental surface properties of the circumpolar regolith are similar to the equatorial landing sites of past missions. We choose to apply Hansen (Hansen, 1970) in combination with circumpolar boulder track data to be as independent as possible of site-specific (equatorial) information like bootprint or other data. Knowledge about the sinkage of surface assets is not only important to ensure their mobility, but also helps to understand and minimize their energy consumption. In general, static sinkage in a dry granular medium continues until the bearing pressure q_p of the object is equal to the bearing capacity q of the soil (limit equilibrium principle):

$$q = q_p = \frac{mg_M}{A_{eff}} \tag{4.13}$$

with m as the mass of the object, g_M as the gravitational acceleration of the Moon, and A_{eff} as the effective contact area. Depending on the relative density of the soil, failure of a shallow foundation can be in general (high relative density), local, or punching shear (low relative density) (Vesic, 1973), where general shear activates a larger portion of soil underneath and around the object, resulting in an increased (ultimate) bearing capacity (Costes et al., 1970). General shear can also occur in soils with intermediate relative densities, but high internal friction angles $>36°$ (Vesic, 1973). In contrast to general shear, punching shear occurs in soils with very low relative densities and friction angles, acting only vertically underneath the object, resulting in a significantly decreased bearing capacity (Vesic, 1973). The intermediate shear mode is called local shear and occurs for intermediate relative densities and friction angles around or $<29°$ (Vesic, 1973). As the density of the lunar regolith increases rapidly over depth (see Figure A.67 and e.g. Carrier et al. (1991)), the mode of shear could be expected to be punching and local in the very first centimeters of soil (described by the allowable bearing capacity), while quickly transitioning to a general shear mode at larger depth (described by the ultimate bearing capacity). Costes et al. (1970) performed laboratory tests with returned lunar soil to study this transition and found that a difference in density by 0.41 g/cm^3 results in completely different shear modes (punching vs general).

Terzaghi (Terzaghi, 1951) performed fundamental work by establishing equations to calculate the ultimate bearing capacity for shallow foundations, assuming general shear. Based on Terzaghi's work, Hansen provided an improved equation that allows for a better adaptation of the bearing capacity calculations to the local situation of a foundation. Hansen (Hansen, 1970) defined q_f with

$$q_f = cN_c s_c d_c i_c b_c g_c + q_0 N_q s_q d_q i_q b_q g_q + 0.5\gamma B_H N_\gamma s_\gamma d_\gamma i_\gamma b_\gamma g_\gamma \tag{4.14}$$

with c as the soil's cohesion, q_0 as the vertical stress, γ as the soil's unit weight, B_H as the shorter width of a rectangular footing, and $N_{c,q,\gamma}$ as the bearing capacity factors that are only dependent on the soil's internal friction angle. Hansen further added a series of correction factors to improve the accuracy of the calculations, called depth- d(c,q,γ), shape- s(c,q,γ), local slope inclination- g(c,q,γ), load inclination- i(c,q,γ) and foundation (boulder) inclination factor b(c,q,γ).

The deployed method (Bickel et al., 2019) attempts to predict the mechanical properties of regolith using only remote sensing data. There are several limitations to this methodology, which - not exclusively - include uncertainties in the estimation of boulder track depth, potentially non-representative assumptions of input geomechanical properties such as bulk density or internal friction angle, and general inaccuracies of the measurements in satellite images due to a lack of spatial resolution. All limitations are extensively discussed either in the Discussion or in Bickel et al. (2019). While being unknown, the required geomechanical input parameters of the circumpolar regolith, i.e., bulk soil density, internal friction angle, and cohesion, affect the accuracy of the performed bearing capacity estimations. These input parameters have been adopted from various sources based on the observation that the south pole is a highland-type terrane with a feldspathic regolith composition: Values adopted from (1) (Bickel et al., 2019) represent conservative assumptions derived from sources across the literature, while values taken from (2) (Linke et al., 2018) and (3) (Carrier et al., 1991) represent less conservative, but potentially more realistic assumptions that are only based on measurements taken in equatorial regions, however. Based on the collective knowledge derived during the Apollo program, (3) (Carrier et al., 1991), incorporating work by Mitchell et al. (1972a) and Mitchell et al. (1974), provide a general relation between depth, bulk soil density, and relative density based on measurements performed in situ during the Apollo missions and with regolith samples in

terrestrial laboratories, where bulk density as function of depth z is described as

$$\rho = 1.89 * \frac{z + 1.69}{z + 2.9} \tag{4.15}$$

Carrier et al. (1991) further provide values for cohesion and internal friction angle based on the relative soil density, derived from basaltic regolith simulant on Earth. The relation of depth and density is asymptotic, meaning that the values for bulk density increase rapidly with increasing depth (see Figure A.67). The conservative geomechanical values adopted from (1) bickel2019 can be divided in two bins, above and below 30 cm depth: it was found that this separation is able to represent the majority of the variations of regolith bulk density as reported by Carrier et al. (1991), Hovland, Mitchell (1969b), Hovland, Mitchell (1973), and Moore (1970). The reported range of values for the angle of internal friction has been constrained by Bickel et al. (2019) using the angle of repose of dry granular flow features. As the main goal of this study is to estimate the strength of the circumpolar surface and the first centimeters underneath it, which both are likely to fail in local shear (see Figure A.67), the adaptation of conservative soil input values also helps to satisfy (Terzaghi, 1951)'s and (Vesic, 1973)'s criteria, where bearing capacity equations like Hansen (Hansen, 1970) can be adapted to provide strength estimates for local shear modes by reducing the effective friction angle and cohesion by one third. The usage of these conservative input values can be further justified with an additional argument: their adoption allows for a direct comparison of south pole bearing capacities with previous work that derived soil strength estimates in highland, mare, pyroclastic (Bickel et al., 2019) and PSR regions (Sargeant et al., 2020) using the identical input values. It is important to note that the adaptation to a local shear mode will result in an underestimation of the bearing capacity at larger depths and in an overestimation at extremely shallow depths (see Figure A.67). In order to link this study to other ongoing analogue studies of lunar trafficability, the geomechanical input parameters of a specific lunar regolith simulant (TUBS) (Linke et al., 2018) have been included in the analysis as well (2). This specific simulant has been designed to represent the mechanical properties of the lunar regolith as observed during the Apollo missions and its mechanical properties are provided as one set of values. The geomechanical input values as recommended by Carrier et al. (1991) and as applied by Linke et al. (2018) for the TUBS simulant have been used to put the calculated bearing capacities into context and to highlight the effect of the input parameters' variability on the surface strength estimation. All used soil parameters are displayed in Figure A.67 and listed in Table A.25 in the appendix.

The lunar polar environment poses additional challenges for the estimation of bearing capacity, particularly the high solar incidence angles >85°. A result of high incidence angles (i) is long shadows, where even small objects will cast substantial shadows. This has one advantage and one disadvantage for this study: (1) longer shadows allow for the measurement of the depth of very shallow boulder tracks, as longer shadows facilitate the measurement of shadow length in NAC images; the shadow length is then used to estimate the depth of the track, in combination with the solar incidence angle (Bickel et al., 2019). The measurement of very shallow tracks helps to derive bearing capacity values close to the lunar surface (<20 cm depth), where these values are most valuable for the assessment of rover and crew traverses. Still, this remote sensing based methodology is limited by the available spatial resolution of the used NAC instrument: very shallow tracks will cast very short shadows, which cannot be measured with the available spatial resolution, effectively limiting the depth of track that can be identified (roughly 0.1 m based on the experience of the authors). Besides resolution-dependent issues; (2) high solar incidence angles can cause a "shadow overflow" of tracks, particularly for tracks with cone-shaped morphologies and distinct edges. In such an overflow scenario, the rim of the track casts a shadow that covers >50% of the interior of the track, potentially even up to 100% of the track width (i = 90°); this ultimately results in a wrong estimation of the track's depth, as tracks appear to be shallower than they actually are (see Figure 4.6). In this work, the ratio r between the track width and the measured shadow length has been used to estimate the degree of shadow overflow; i.e., the ratio of track width to shadow length. Ratios close to 2 are optimal (usually the case for solar incidence angles of 45°), while ratios of 1 indicate completely overflown tracks (no depth signal), assuming that the deepest point of a track is at its center. Using the apparent depth D_{app} the effective track depth D_{eff} can be triangulated, using the track width W, the shadow length S, the track aperture angle α, and the solar incidence angle i. This correction assumes that the shape of tracks is triangular. The correction for r larger or smaller 2 can be described as:
if $W - S < \frac{W}{2}$ and $r < 2$:

$$D_{eff} = \frac{D_{app}}{W - S} * \frac{W}{2} \tag{4.16}$$

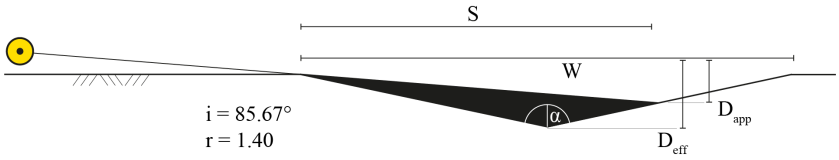


Figure 4.6: Correction of apparent depth for an exemplary track cross–section at the south pole, using track width W, shadow length S, solar incidence angle i, track aperture angle α , and ratio r. The illumination direction is always orthogonal to the track direction; i is to scale.

if $W - S > \frac{W}{2}$ and $r > 2$:

$$D_{eff} = \frac{D_{app}}{S} * \frac{W}{2} \tag{4.17}$$

It has to be noted that estimated polar track depths are generally less reliable than those derived in equatorial regions and, furthermore, that they are potentially being underestimated.

The above described methodology has first been used to derive and locate south polar bearing capacities in the context of existing work. It has to be kept in mind that the performed analysis is representing an estimation of south polar surface strength, not an accurate measure. The main value of the quantitative analysis lies in the direct comparison of strength estimates derived with the same method and data in traversed and un-traversed regions of the Moon: if strength estimates for un-traversed and traversed terranes are similar, the un-traversed region might be trafficable as well (index test). In addition to the quantitative analysis, the appearances and shapes of tracks have been compared in a qualitative and semi-quantitative manner, including the range of boulder diameters, as well as measurements of track width, track depth, and track aperture angle (track width to depth ratio). Subsequently, a conservative quantitative relation between slope angle, track depth, and bearing capacity has been established by binning strength estimates in three slope angle bins, 5 to 15°, 15 to 25°, and 25 to 35°. The bins need to be wide as the available south polar boulder track samples (16) are scarce. In order to increase the available data, bearing capacity values shallower than 3 m derived by a previous study in highland regions (32 samples) (Bickel et al., 2019) have been included. A least squares linear fit has been used to estimate the bearing capacity of each bin at surface level and at shallow depths (from the surface down to 3 m depth). All estimates have finally been used to study the variation of the estimated surface bearing capacity values as function of the south polar topography. The resulting maps are products for first-order analyses within the context of future circumpolar exploration. For first-order analyses it is assumed that the spatial resolution of the used laser altimeter-derived Digital Elevation Model (DEM) (30 m/pix) is sufficient to describe the small-scale variability of the south polar terrain as encountered by a rover wheel.

Results

The results of the combined deep learning-driven and operator-complemented rockfall mapping are shown in Figure 4.7, with one example of a south polar boulder with track shown in Figure 4.8. A total of 84 boulders with tracks were found on the flanks of Mons Malapert, as well as on the upper walls and rims of Shackleton, Amundsen, Nobile, Haworth, and Ibn Bajja, including some other, smaller craters (Figure 4.7a and b). Inspection of the mapping results shows that south polar rockfalls feature smaller diameter boulders, appear to be rounder, occur on steeper slopes, have shallow tracks, and shorter runouts than rockfalls in other, more equatorial regions of the Moon (Bickel et al., 2019) (Figure A.68 in the appendix). However, these observations could be misleading, as shadowed regions at the bottom of slopes and craters cannot be directly observed in polar regions — only rockfall features on the rims and upper flanks of topographic heights can be investigated, which might not represent the entire rockfall population of the lunar south pole. A total of 13 tracks were mapped that enter Shackleton crater's PSR (Figure 4.7a), but which cannot be traced in their entirety; this indicates that there is an unknown and potentially large rockfall population that lies hidden in PSRs (Sargeant et al., 2020). Observations further show that all south polar rockfalls are associated with impact features of varying scales and ages (Figure 4.7a and b). The ages of rockfalls, particularly those with visible tracks, are not likely to exceed a few tens of millions

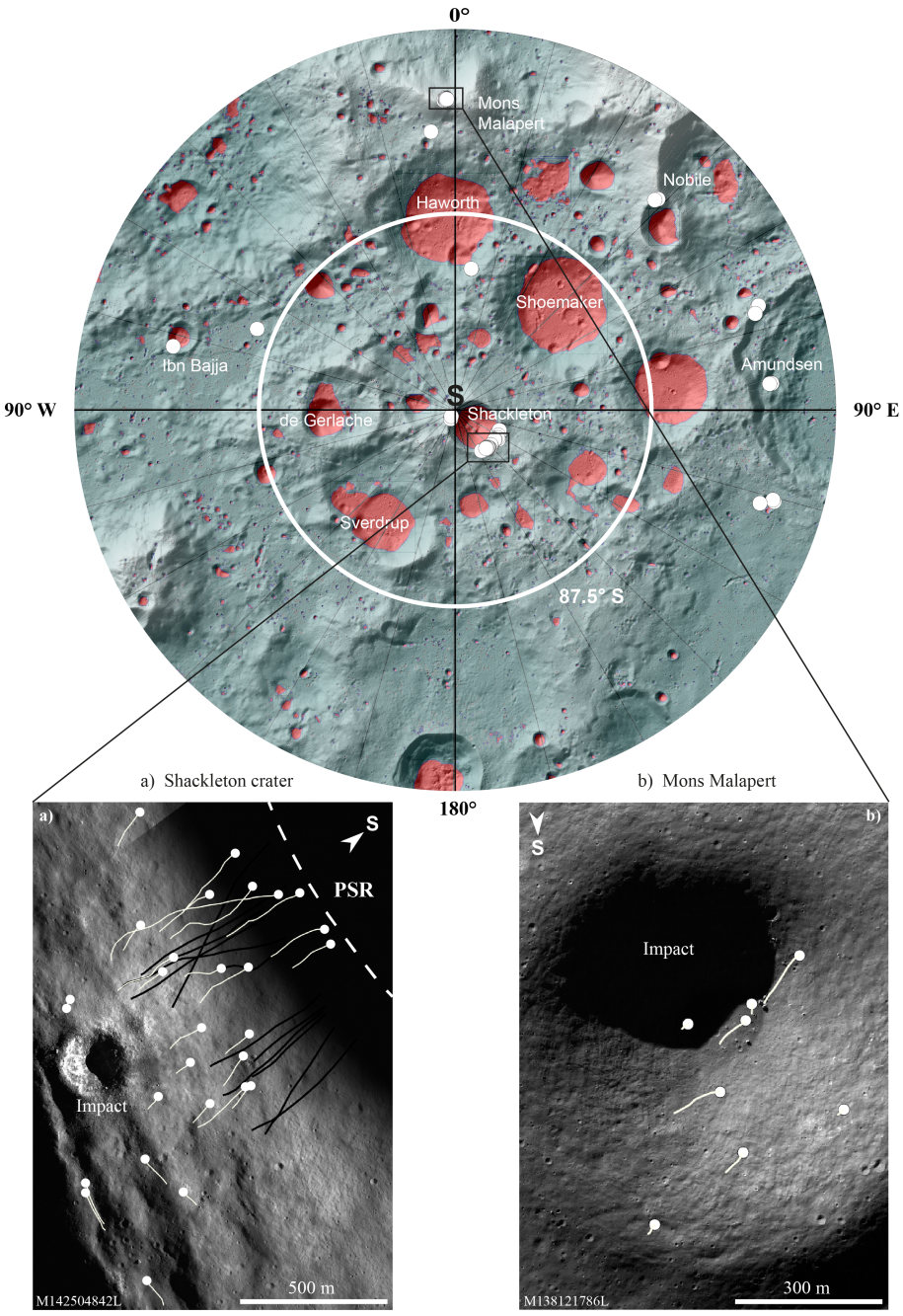


Figure 4.7: Map of all detected rockfalls (84, white shapes) in the study area (>85° S) created using a convolutional neural network that has been trained for this purpose (Bickel et al., 2018). Examples of the boulders and boulder tracks in close-up views appear in Figure 4.8. The study region has a radius of 150 km, similar to the 100-km exploration zone distances of being examined in Mars-forward mission architectures. Red areas indicate permanently shadowed regions (PSRs, modified from McGovern et al. (2013)). Hillshade as background. Details of a) the northern upper wall of Shackleton crater and b) the northern flank of Mons Malapert are displayed: white lines and spheres indicate boulder tracks and boulders, respectively, and black lines indicate boulders whose tracks enter a PSR (boulder is not visible). The captured illumination conditions or SNR (when contrast and brightness optimized) of the available NAC images is not sufficient to trace these tracks into the shadowed region, i.e., runout length and boulder location / shape is unknown. Interestingly, some of the mapped boulder tracks run parallel to Shackleton's crater rim, following local minor topography gradients. If recent, those 'irregularly' rolling boulders on the rim could potentially affect operations in the area. Details of NACs M142504842L and M138121786L.

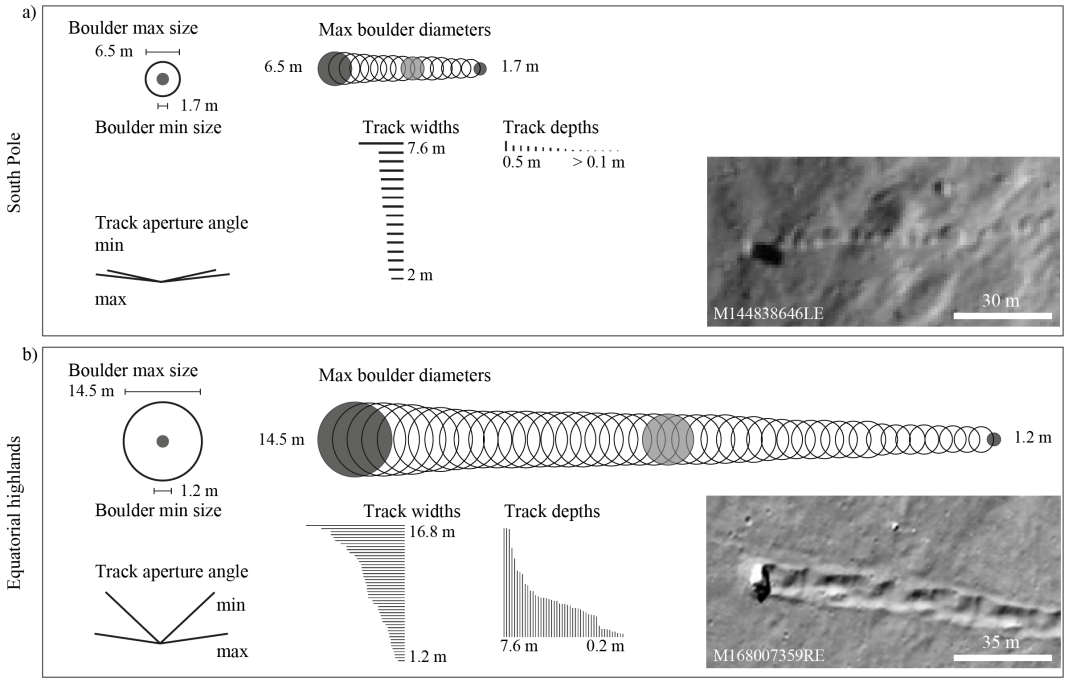


Figure 4.8: Qualitative and semi-quantitative comparison of polar a) and equatorial highland b) boulder track cross-sections. A qualitative comparison [NAC insets in a) and b)] of highland and polar boulders and tracks does not show any significant differences, suggesting similar mechanical properties of the slope substrate in both terranes. Semi-quantitative comparison features max and min boulder sizes, the overall boulder size distribution (grey circle indicates the mean size), track widths and depths, as well as track aperture angles (width to depth relation). South polar tracks appear to be shallower, while the associated boulders are smaller as well. Corresponding plots in a) and b) are to scale. Details of NACs M168007359RE and M144838646LE.

of years (Arvidson et al., 1975b; Hurwitz, Kring, 2016). Thus, while the rockfalls are associated with older and younger craters, all of the features are geologically young. Besides dynamically displaced boulders with tracks, manual inspection of NAC imagery also showed that there are thousands of static boulders with diameters larger than 2 m present along the rims and walls of south polar craters and topography in general that could represent science-rich targets for future exploration.

Sixteen of the mapped rockfalls and tracks were distinct enough to be used to estimate the apparent south pole bearing capacity distribution as function of depth (∼10 to ∼52 cm) using the methods described earlier. The mean shadow overflow ratio was 1.57, highlighting the necessity of the applied depth correction. The derived values were used to compare the south polar surface strength with equatorial highland regions (Bickel et al., 2019) that have been successfully traversed in the past. In the observed depth range, south pole bearing capacity compares well with previous quantitative estimations (Figure 4.9), where circumpolar values appear to be either similar or slightly higher than in equatorial highland regions (using the identical conservative input values as Bickel et al. (2019). In support of that, a qualitative comparison of boulder tracks in both regions shows no significant differences in track appearance and morphology, suggesting similar geomechanical properties of the regolith in both regions as well (Figure 4.8). A semi-quantitative comparison of the observed track shapes indicates that the lunar south pole features tracks that are as shallow, but less deep as equatorial tracks (Figure 4.8). The absence of deep tracks might be caused by the generally smaller boulder dimensions found in the vicinity of the pole (Figure 4.8). All above observations combined indicate that the south polar sunlit regolith should be capable of providing a sufficient level of (sinkage-related) trafficability, as demonstrated in equatorial highland regions in the past (e.g. Apollo 16).

As trafficability information is most interesting on or very close to the surface, 16 south polar and 32 equatorial highland boulders and tracks have been used to establish a relation between track depth and bearing capacity (applying Hansen's method) for three slope angle bins (Figure 4.10), using the conservative input parameters as applied by Bickel et al. (2019)). Using one linear least squares fit per bin, the bearing

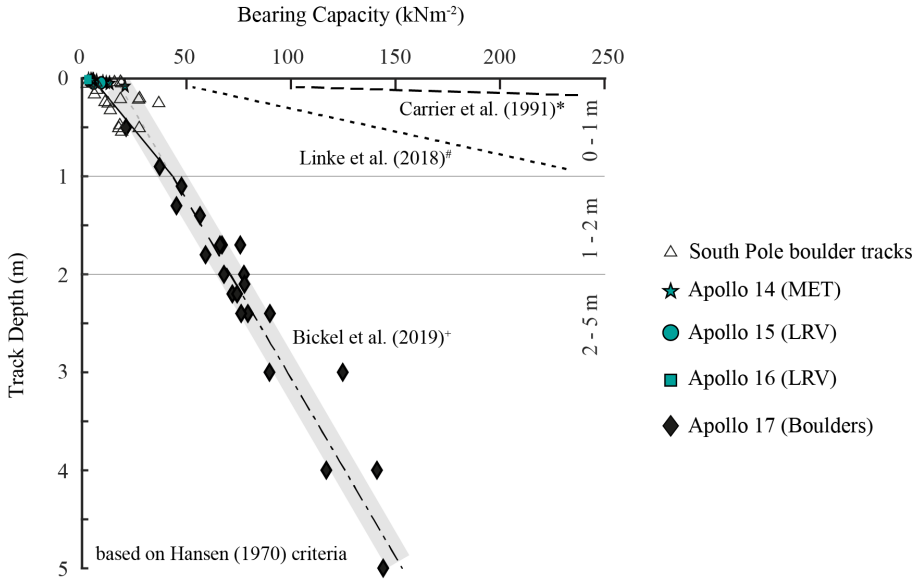


Figure 4.9: Estimated bearing capacity at the location of 16 south pole boulders in comparison to the general bearing capacity envelope estimated by Bickel et al. (2019) (solid and dashed black line on the left), based on Hansen (Hansen, 1970) using conservative input values. It has to be noted that this envelope represents a lower limit of bearing capacity derived using a local shear mode, i.e., the strength of the regolith is likely to increase more rapidly over depth. Approximated bearing capacity envelopes as derived with alternative input parameters (Linke et al., 2018; Carrier et al., 1991) are indicated as well. Estimated south pole values are mainly shallow, but compare well to equatorial strength values and the previously derived strength envelope. South pole points that plot on the right side of the envelope represent measurements on low slope angles: Figure 4.10 displays the bearing capacity as function of both, slope angle and depth. +,#,*outline of general bearing capacity envelope using input parameters as recommended by Bickel et al. (2019), Linke et al. (2018), and Carrier et al. (1991).

capacity at surface level has been estimated for the three used bins. These fits can be described as

$$5 - 15^\circ : q_f = 62.8z + 13.2 \tag{4.18}$$

$$15 - 25^\circ : q_f = 40.1z + 6.4 \tag{4.19}$$

$$25 - 35^\circ : q_f = 31.5z + 1.9 \tag{4.20}$$

with z in meters and q_f in kN/m^2. Due to the assumptions made, these fits are expected to be representative in the depth range from ∼1 to ∼5 cm. The conservative fits based on input parameters adopted from Bickel et al. (2019) have been used to produce a map that approximates the spatial distribution of bearing capacity as function of the topography based on all assumptions made, shown in Figure 4.11. This product in combination with two maps that highlight potentially challenging terrain (Figure 4.12, Figure 4.13) indicates regions with potentially insufficient bearing capacity that could cause sinkage-related issues for landers, vehicles, as well as infrastructure.

Discussion

This study implemented a hybrid mapping approach to detect south polar boulders with tracks, using a combination of automated deep learning-driven and user-complemented mapping. The most recent 5th generation network that has been trained by Bickel et al. (2018) has been used with a "maximum recall"

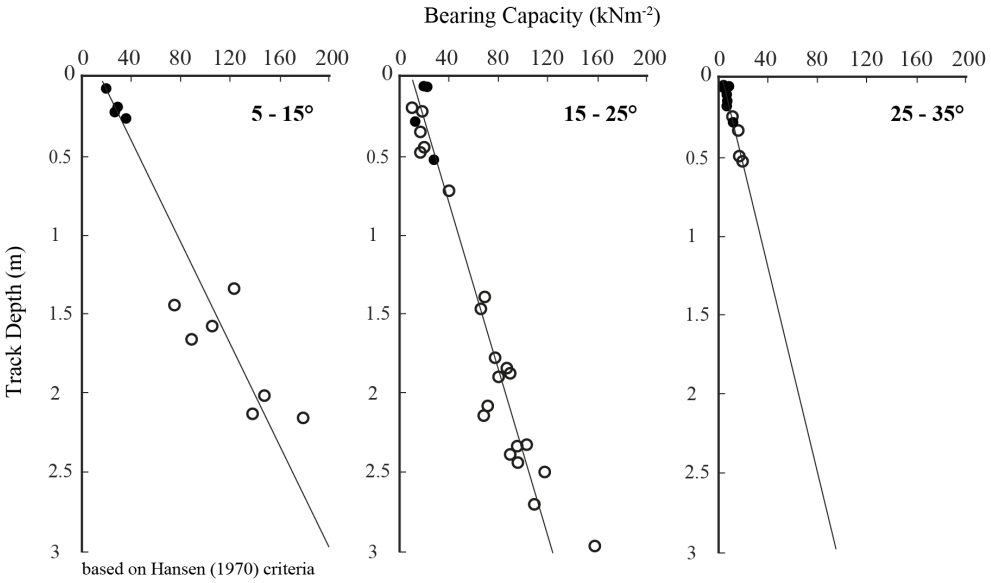


Figure 4.10: Bearing capacity as function of depth, sorted in 3 slope angle bins (5 to 15°, 15 to 25° and 25 to 35° for input parameters taken from Bickel et al. (2019). Least square fits through polar (solid shapes) and equatorial highland points (hollow shapes) (Bickel et al., 2019) are used to estimate bearing capacity at shallow depths <15 cm for each slope angle bin. It has to be noted that a linear fit might oversimplify the actual bearing capacity envelope, particularly at extremely shallow depths. However, the scarcity of available boulders with tracks impedes more sophisticated fits.

approach. In max-recall, the focus lies on extracting as many targets from a dataset as possible; i.e., on finding as many boulders with tracks in the existing NAC images taken over the lunar south pole as possible. The purpose of such a max-recall-focused approach is to (1) process a large amount of data in a very short time, and (2) to inform a supervisor or user about the general distribution of the detections and about particularly interesting and promising sites (e.g. spatial clusters of detections). These sites can then be mapped by an operator in greater detail as well as with higher accuracy and precision. The CNN also reduces the involved bias, as the neural network does not inherit any preferences on where to look for rockfalls, as a human operator would. After completion of the CNN-driven mapping, a human operator reviewed the CNN-derived map and complemented it, where required, to ensure the accuracy and precision of the final map (Figure 4.7).

More boulders with tracks are located in either Shackleton crater or on the northern flank of Mons Malapert, but targets were found on the slopes of other craters as well, such as in Amundsen and Haworth craters. Although the data suggest (Figure A.68) that rockfalls at the lunar south pole generally feature smaller diameters, this might be a direct consequence of the limited observability of the bottom of slopes due to shadowing. This limitation results in a potential bias, as only rockfalls on higher portions of slopes and on the rims of craters can be observed. Future work could compare these south polar 'on rim/on upper slope' rockfalls with more equatorial counterparts to identify a potential bias, caused by the high solar incidence angles at the south pole.

Interestingly, on Mons Malapert the occurrence of (detected) rockfalls is limited to a single, smooth impact crater on the flank of the massif. These boulders cannot be traced back to a distinctive source region, as illustrated by Figure 4.7b and Figure A.69. In Shackleton crater, the bulk of the identified rockfalls is caused (and potentially triggered) by a recent small-scale impact (Figure 4.7a). In addition five boulders carved tracks that run along the rim of the crater (bottom of Figure 4.7a). These tracks run along the contour lines of Shackleton while neglecting the dominant slope gradient, following a local minor topography gradient instead. This observation is further illustrated in Figure A.70. As these boulders run towards the mentioned recent impact, it is unlikely that they have been ejected by the same impact event. If the displacement of these five boulders is more recent, there is potential for the (re)mobilization of these or other boulders in this specific region, which could potentially impact the safety of future exploration

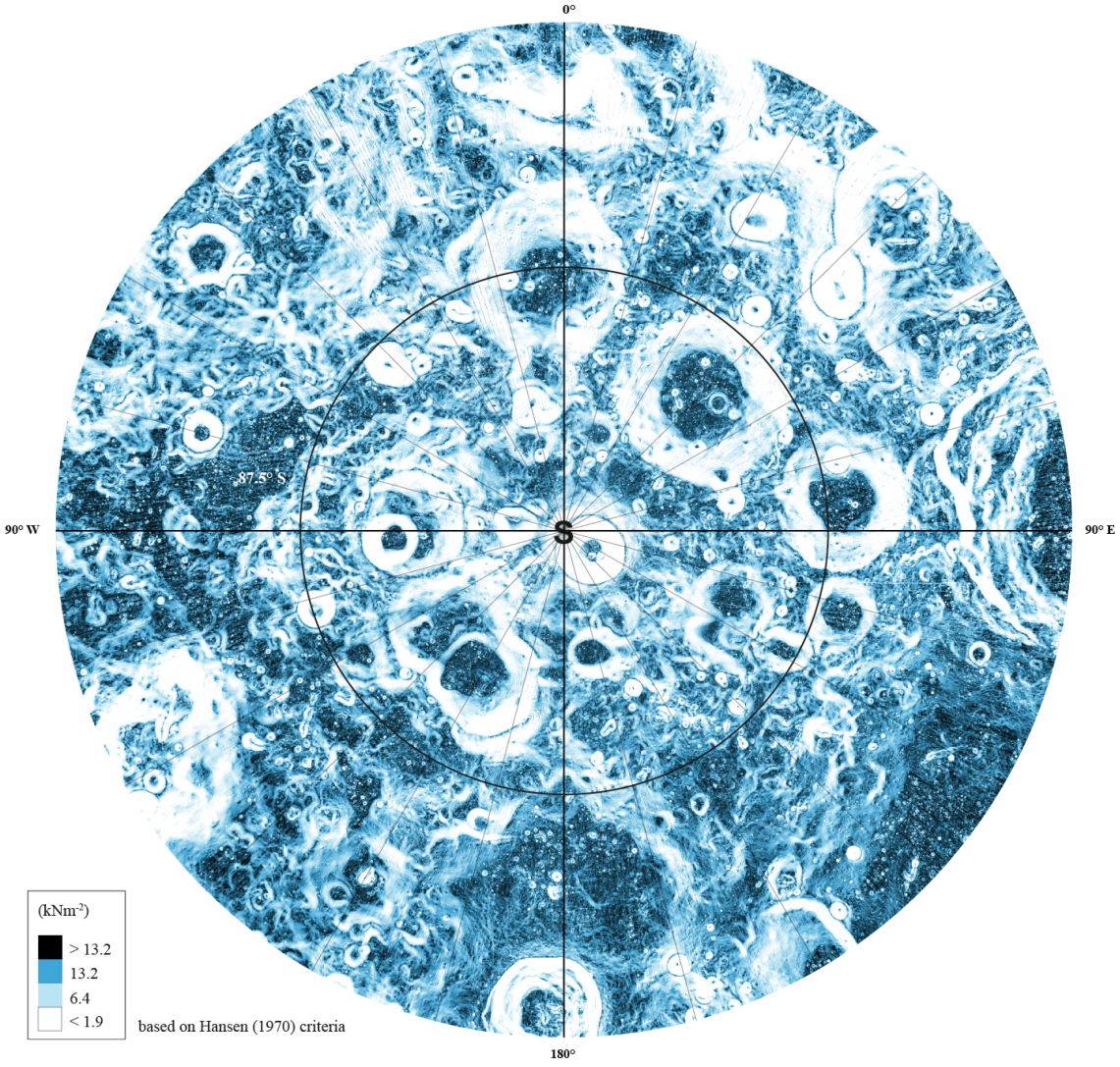


Figure 4.11: Estimated south pole surface bearing capacity as function of topography based on analyses of sunlit regolith, applying conservative input values taken from Bickel et al. (2019). The bearing capacity within PSRs (not outlined here) will deviate from the values shown here due to the potential influence of ice - see dedicated work about PSR trafficability (Sargeant et al., 2020). Local linear artefacts are caused by artefacts in the used DEM. The spatial resolution of this map is directly connected to the resolution of the available topography data; in this case 30 m/pix. The study region has a radius of 150 km, similar to the 100-km exploration zone distances of being examined in Mars-forward mission architectures.

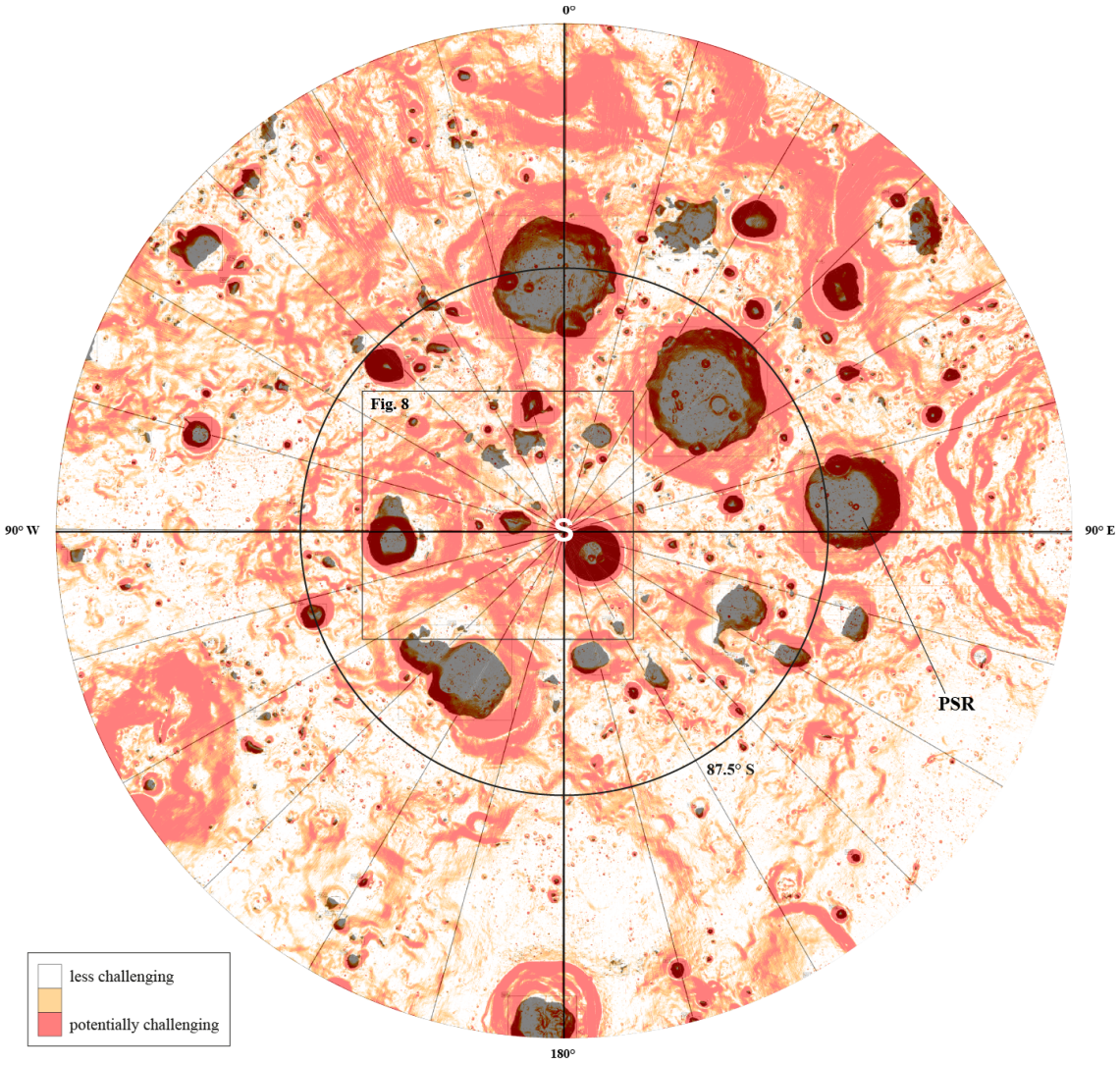


Figure 4.12: Map of potentially challenging terrain (sinkage) for VIPER and LER, using conservative input parameters (see Figure 4.11). Areas that might feature increased sinkage (orange and red) correspond to slopes steeper than 15° and 25° respectively. On inclines >25° VIPER would sink (static) an estimated ∼4 cm and LER an estimated ∼6 cm, respectively, on average. While sinkage might not fundamentally affect the mobility, it might affect other important aspects of a surface mission, such as energy consumption. Data scatter and historical experience suggest variable sinkage around those average values are likely. PSRs are indicated in black (PSR map modified from McGovern et al. (2013)). The spatial resolution of this map is directly connected to the resolution of the available topography data; in this case 30 m/pix. The study region has a radius of 150 km, similar to the 100-km exploration zone distances of being examined in Mars-forward mission architectures. The extent of a detailed map (Figure 4.13) is indicated with a black rectangle.

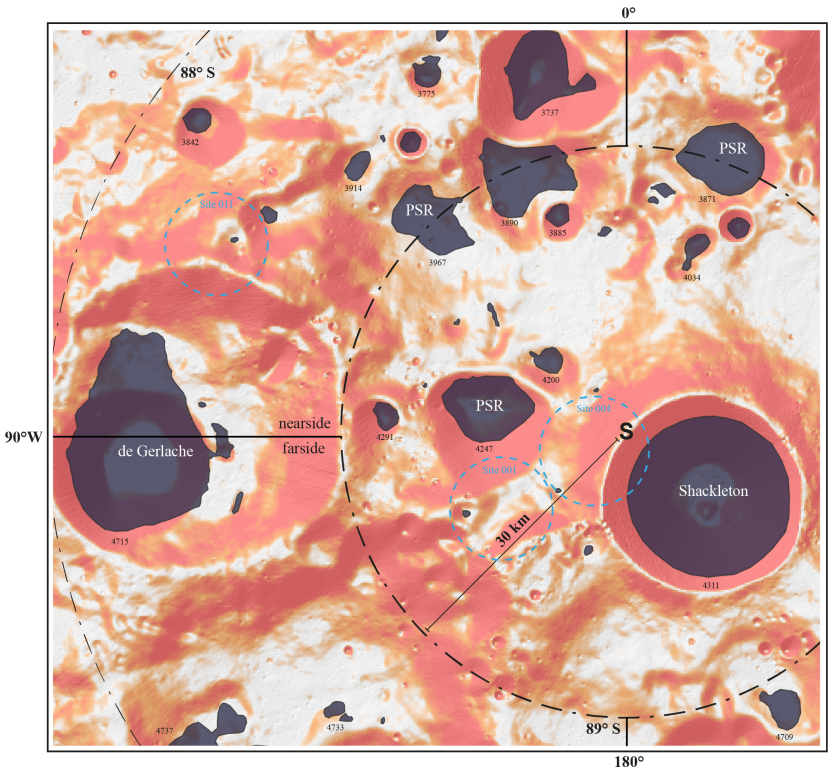


Figure 4.13: Detailed map (see Figure 4.12) of potentially challenging terrain (sinkage) west of the lunar south pole for VIPER and LER, using conservative input parameters (see Figure 4.11). Areas that might feature increased sinkage (orange and red) correspond to slopes steeper than 15° and 25°, respectively. On inclines of around 15° (orange), VIPER's and LER's estimated static sinkage would not exceed ∼1 cm and ∼2 cm, respectively, on average. On inclines ∼25° (red), sinkage of up to ∼4 cm (VIPER) and ∼6 cm (LER) could occur, on average. Data scatter and historical experience suggest variable sinkage around those average values are likely. PSRs are indicated in black (including IDs) (PSR map modified from McGovern et al. (2013)). This type of sinkage estimation map could be combined with other trafficability data such as (small–scale) surface roughness maps (e.g. boulder and crater density) to support path and mission planning efforts. The spatial resolution of this map is directly connected to the resolution of the available topography data; in this case 30 m/pix. The blue dashed circles approximate the locations of potential sites of interest for the upcoming Artemis program (NASA, 2020).

campaigns, e.g., landers or static infrastructure. While this risk is minimal, any potential negative impact of boulder displacements on exploration efforts could be considered.

Thirteen tracks were found on the south-pole facing flank of Shackleton crater that enter and disappear in a PSR. There is some evidence for a significantly larger number of tracks and rockfalls in the same region that enter the PSR, but the available image resolution does not allow for explicit detection and mapping. This is not a restriction that is caused by the south polar environment, but is a general limitation for mapping in all lunar regions: as boulder diameters decrease, their abundance increases (see Figure A.68 and Bickel et al. (2019)). When boulder diameters approach the spatial resolution (ground sampling distance) of the used sensor, the number of possible detections decreases and eventually a cut-off value is reached (∼<2 m boulder diameter or less).

A recent study by Sargeant et al. (2020) investigated the bearing capacity of the regolith in PSRs using boulder tracks, but in PSRs situated at 70° to 76° latitude only, where shadowed regions are scarcely and indirectly illuminated at times. At higher latitudes, such as directly at the south pole, not enough signal can be retrieved from the available NAC imagery in shadowed regions — without sacrificing the required high spatial resolution for increased CCD exposure times — as indirect illumination is insufficient. This means that rockfalls, although present in south polar PSRs, cannot be used to estimate their surface strength and trafficability. For the time being, such an investigation is limited to the sunlit portions of the

southern circumpolar region.

A total of 16 boulders and tracks were measured and combined with a variety of soil mechanical input parameters to estimate the bearing capacity of the sunlit regolith at the south pole as function of depth and slope. Many of the limitations of the here applied methodology have been mentioned in the Methods or have been extensively discussed in Bickel et al. (2019) and in Sargeant et al. (2020). For example, the estimation of bearing capacity is dependent on the shear mode occurring underneath a wheel or boulder. In addition, Hansen's (Hansen, 1970) equation (Equation 4.14) assumes that the local slope angle at the foundation is smaller than the internal friction angle of the substrate (here between ∼30° and ∼57°). Therefore, the expressivity of bearing capacities derived for local slope angles larger than ∼30° (5 out of 16 samples) might be reduced. In addition, it has to be noted that all estimates of bearing capacity are highly dependent on the quality of the available images and on the used soil mechanical input parameters. For example, Figure 4.9 highlights the influence of slightly enhanced geomechanical input parameters on the estimated bearing capacity. The most valuable observation of this study is that boulder track-based strength estimates derived with the identical method and data produce similar bearing capacity values for un-traversed and traversed regions, implying that the south pole might be trafficable as well. It is important to note that the performed analysis is providing an estimation of south polar bearing capacity, not an accurate measure; all results remain to be confirmed in situ.

While accurate absolute quantitative estimations of surface strength are difficult to achieve based on remote sensing data alone, a comparison of the geomorphological appearance of tracks across the regions can provide additional confidence in the results. In general, south polar tracks appear to be as shallow as equatorial tracks, while having similar minimum boulder diameters (Figure 4.8), suggesting that the mechanical properties are indeed similar, as suggested by the quantitative analysis (Figure 4.9, Figure 4.10). In combination with the qualitative comparison of boulder track morphologies across south polar and equatorial highland sites, there is no indication that geomechanical properties would not be sufficient to support ground-based exploration.

Although trafficability in the depth range from the surface down to ∼5 cm is most relevant for lunar exploration, it is not possible to directly estimate the bearing capacity in this depth range due to the limitations of the existing data and uncertainties of the performed measurements. Therefore, the strength of the shallow subsurface has been approximated by extrapolating from all available local data (16 tracks) that have been augmented with data derived at more equatorial highland sites (32 tracks). The utilization of distal data can be justified by the observation that south polar bearing capacities compare well to values derived in equatorial regions (Figure 4.9), i.e., distal data are expected to not introduce a significant error. The high solar incidence angles at the south pole complicate the observation and measurement of boulder tracks, but also allow for the measurement of very shallow tracks. A number of these shallow south polar tracks are included in the used dataset and assure that all least square fits intercept the surface layer at as realistic (local) bearing capacity values as possible. The applied distal values have been derived at greater depth (Figure 4.10), which increases the ability of the local shallow data to control the fit at the most important shallow depth. It should be noted that a linear fit might oversimplify (overestimate) the actual bearing capacity envelope, particularly at extremely shallow depths. However, the scarcity of the available boulders with tracks and their measurements impedes more sophisticated fits.

Carrier et al. (1991) report an allowable surface bearing capacity (not considering slope) of about 7 to 8 kPa for the Apollo landing sites based on in situ data, while Bickel et al. (2019) estimated 5.4 ± 4.5 kPa using the described remote sensing method. This study estimates a surface strength of about 13.2 kPa for inclines <15° at the lunar south pole. The slightly higher south polar estimates could be caused by a variety of reasons: (1) this study extrapolates estimates derived for depths >10 cm, where uncertainties could be introduced, for example, by the forced linear fit. Other reasons for the slightly increased surface strength estimate could be (2) a generally higher strength of the regolith at the lunar south pole and (3) inaccuracies in the measured track widths and depths, caused by the limitations of the available imagery. Until ground truth becomes available, lander and rover design should rather be based on conservative surface strength values.

All above observations combined suggest that the highland-style regolith at the lunar south pole has a similar mechanical strength as regolith in other regions of the Moon and that future exploration will likely not be affected by general and excessive flotation issues. Due to the extreme lighting conditions, all track measurements have been performed on crater rims or crater slopes; potentially, the properties of



Figure 4.14: The Apollo 15 LRV and astronaut David Scott on a 18°-slope at station 6a. The white arrows indicate unusually deep LRV tracks that could be the result of a non–static interaction of the wheel with a weaker slope colluvium (e.g. through excessive wheel spin). David Scott had to stabilize the LRV in order to prevent it from sliding downhill (Costes et al., 1972). Apollo photograph AS15-86-11659.

the regolith in intra-crater regions might differ from the estimated values. It has to be kept in mind that displaced boulders and their tracks provide discrete point measurements only and that the derived surface strength estimates and maps might not be representative for the entire surface of the south pole. The potential for local regolith heterogeneities and mechanical strength anomalies, as reported by Florensky et al. (1978) and Carrier et al. (1991) during the Lunokhod and Apollo missions, remains and cannot be excluded. In fact, targeted observations of these local heterogeneities would be interesting and relevant secondary scientific objectives for future ground-based exploration.

In contrast to the equations customized from Hansen (Hansen, 1970), Terzaghi's approach does not specifically consider the local slope angle; i.e., the equation always assumes that a foundation rests on horizontal ground. Interestingly, the results derived with Terzaghi (Terzaghi, 1951), following Bickel et al. (2019), still appear to express a physical relation between slope angle and bearing capacity, where steeper slopes feature lower bearing capacity values, as highlighted by Figure A.71. Bickel et al. (2019) observed a similar behavior of the uppermost meter of regolith in other regions of the Moon. This observation also agrees with findings made in situ during the Apollo missions where astronauts found that the substrate on slopes is weaker than on flat terrain (Carrier et al., 1991). One potential reason for the decreased soil strength on slopes could be surficial (long-term) mass movements (Houston et al., 1972; Carrier et al., 1991) that result in a regolith colluvium with reduced density and mechanical strength. On steep slopes, this colluvium could cause trafficability issues that are not exclusively related to increased sinkage through punching shear, but also to wheel slip and traction. During the Apollo 15 mission, astronauts observed that the LRV slid downslope as soon as both crewmen left the vehicle (Figure 4.14) (Costes et al., 1972). This observation could be an expression of such a shallow regolith colluvium with altered mechanical properties. If existent, the mechanical behavior of such a layer and its impact on astronaut and vehicle mobility would need to be further investigated in situ to better understand the capabilities and limitations of wheeled vehicles on steep slopes. As an alternative for locomotion on steep lunar inclines the utilization of legged or wheeled-legged robots could be considered (such as SpaceBok, see Figure A.72 or Arm et al. (2019)): these assets are able to adapt their center of mass to minimize the influence of challenging topography and geomechanical properties.

In order to assess the sinkage-related performance of the VIPER and LER rovers in the southern circum-

polar environment, the relevant vehicle specifics, i.e., wheel dimensions (width and diameter) and the rover weight, have been compared to bearing capacity as function of the local slope angle (derived with conservative input parameters, Figure 4.11, Figure 4.12, Figure 4.13). All used vehicle specifics are reported in Table A.26 in the appendix. As the weight of the rovers is fixed (current assumption), the bearing pressure is only controlled by the effective contact area between the regolith and the wheels, which in turn is controlled by the sinkage. When applying the conservative bearing capacity envelope on flat terrain as reported by previous work (Bickel et al., 2019) the static sinkage of both, VIPER and LER, would not exceed ∼1 or ∼2 cm, respectively (Bickel et al., 2019). Applying the local, extrapolated surface strength values, VIPER and LER would sink even less, as the estimated bearing capacity of the south polar regolith could be slightly higher — or as the previous estimation of equatorial surface strength was too conservative. However, on slopes, the bearing capacity of the regolith is generally decreased due to (1) a reduction of the soil volume that carries a load (Shields et al., 1990) (see Figure A.73) and (2) an apparent drop of physical strength, as discussed above. Increased sinkage of the LRV on slopes was first observed during the Apollo 15 mission (Costes et al., 1972), but has not been quantified (see Figure 4.14).

This has important implications for the planning of future landings and traverses. The mechanical surface strength of the sunlit and flat (<∼15°) circumpolar regions appears to be unproblematic in regard to sinkage. However, the calculated bearing pressures of VIPER and LER would result in increased sinkage on inclined terrain. Figure 4.10, Figure 4.11 suggest that surface soil strength is reduced by a factor of ∼2 on slopes between 15° and 25° (similar to Shields et al. (1990)), and by a factor of ∼7 on slopes steeper than 25°, resulting in an estimated static sinkage of ∼4 and ∼6 cm, respectively, on slopes steeper than 25°. Using the identical estimated surface strength values, the manned LRV would sink, on average, between ∼1 to ∼2 cm and about ∼5 cm on slopes between 15° to 25° and on slopes steeper 25°, respectively. The reported average depth of actual LRV tracks is 1.25 cm, but depths of up to 5 cm were recorded as well (Carrier et al., 1991), comparing well to the estimated values. Reports show that sinkage can exceed 5 cm occasionally (Figure 4.14); in these cases, the sinkage is non-static and is controlled by excessive wheel spin or other traction-related issues, for example on slopes.

Figure 4.12, Figure 4.13 highlight the abundance of steep slopes at the south pole and, thus, challenging terrain that might cause increased wheel sinkage. Figure 4.13 in particular shows that access to large PSRs is usually only possible with a traverse across inclined slopes and underlines the importance of considering the effects of reduced bearing capacities on slopes on the mobility and energy consumption of rovers. Any static sinkage could potentially be worsened in case grousers are installed on the wheels of an (actively forward moving) rover (Jayalekshmi, Kumar, 2019). However, Jayalekshmi, Kumar (2019) found that the negative impact of grousers on the dynamic sinkage can be minimized by increasing the number of lugs, while reducing the height of each individual lug.

When applying extra mass on the VIPER and LER rovers, as caused by retrieved geologic samples or during a potential emergency extraction of crew, bearing pressure would be slightly increased. When applying an additional 250 kg to LER (additional crew and samples) as well as an additional load of 15 kg (samples) to VIPER, estimated sinkage only increases slightly (sub-cm range), however. In general, the mass of a vehicle has a smaller impact on sinkage than the effective contact area of the wheels (Bickel et al., 2019). Therefore, the wheel dimensions of VIPER and LER could be adapted to reduce the estimated static sinkage, even on slopes steeper than 25°. An additional option would be the application of wire-mesh wheels, which achieve larger effective contact areas due to the deformation of the wheel under load. Such wired-mesh wheels have been applied on the Apollo-era LRV and have proven to provide excellent trafficability and maneuverability performance (Costes et al., 1972; Carrier et al., 1991). The deliberations above are based on approximated bearing capacity values and should only be considered in the context of the applied methodology's limitations and uncertainties, as discussed above.

In summary, no evidence has been found that the regolith in the sunlit southern circumpolar region would be less trafficable than in the equatorial regions that have been successfully traversed in the past. The results of this study suggest that the mobility of landers and vehicles at the lunar south pole is not limited in any other way than it was for the Apollo and Lunokhod missions. While sinkage might not fundamentally affect the mobility of surface assets, the increased sinkage on inclines will result in an increased energy consumption. The insights summarized above can be directly applied to benefit the Artemis program and other exploration efforts.

Conclusions

Information about south polar surface properties may affect ongoing hardware design, mission, and potentially infrastructure planning. This study applied a hybrid deep learning-driven and user-complemented approach to identify and map 84 boulders with tracks in NAC images in the vicinity of the lunar south pole (>85° S). Thirteen tracks were identified that traverse into Shackleton crater's PSR, along with indications that there are 10s to 100 s of additional regular and cross-PSR tracks in the region, but right at or below NAC's spatial resolution. Rockfalls have been found to mainly cluster around impact features of varying scales and ages; e.g. on Mons Malapert's flanks or in Shackleton crater.

The identified boulder tracks have been used to estimate the bearing capacity of the sunlit south polar regolith, using an established methodology that was modified to suit the circumpolar illumination environment. The estimated strength values compare well with values derived for equatorial highland regions that have been successfully traversed during the Apollo and Lunokhod missions. A direct comparison of the tracks' appearance, morphology, track width to depth ratios, and associated boulder diameters reveals that south polar rockfalls tend to feature shallow depths and small boulders, where the minimum track depth and boulder size are similar for the circumpolar and equatorial environments observed. None of the observations above indicates that the sunlit regolith at the lunar south pole would be less trafficable than in other regions of the Moon.

Based on a combination of local and distal measurements, the variability of the sunlit south polar bearing capacity as function of slope and depth has been approximated for 5° to 15°, 15° to 25°, and >25° slope inclination bins. This relation has been used to map the estimated spatial variability of the surface strength as function of the circumpolar topography. The derived products suggest that exploration-relevant static sinkage issues might only occur on slopes steeper than 25°, while the potential for local, slope independent mechanical strength anomalies remains. Within their limitations and uncertainties, the results of this study can be used to inform and support the current efforts to send manned and unmanned exploration assets to the lunar south pole.

Acknowledgments

One of the authors (VTB) would like to thank Dr. David Carrier for the inspiring and rewarding discussions about lunar soil mechanics as well as Dr. Jordan Aaron for the discussions about general soil mechanics. The authors thank Dr. William Bluethmann for discussions of lunar mobility using flight versions of assets derived from the Lunar Electric Rover (LER) and Resource Prospector (RP) rover. VTB would also like to thank Dr. Mark Shirley for providing recent technical specifications for the VIPER rover. VTB gratefully acknowledges the financial support by the International Max Planck Research School at the Max Planck Institute for Solar System Research at the University of Goettingen (IMPRS) and the Engineering Geology group, Department of Earth Sciences, Swiss Federal Institute of Technology Zurich (ETHZ). This work was supported by Solar System Exploration Research Virtual Institute contract NNA14AB07A. This is LPI contribution No. 2365.

Chapter 5

Conclusion

In the Apollo-era, the hypothesized drivers of lunar rockfall were erratic events, such as meteoritic impacts and moonquakes, and continuous processes, such as micro-meteoritic abrasion and solar-induced thermal breakdown (Hovland, Mitchell, 1973). In recent years, the focus shifted onto lunar endogenic activity, i.e., moonquakes, which still are widely promoted as the main driver of lunar rockfalls (Kumar et al., 2019b; Mohanty et al., 2020). However, all previous studies, co- and post-Apollo, only considered a limited number of observations made in small, spatially limited geographic regions. Even the most recent studies of lunar rockfall did not attempt to deal with the massive LRO image archive of more than 2.6 million images to increase the number of observations available for scientific conclusions. Therefore, the under-exploited LRO archive represents a unique opportunity to lift the study of rockfalls from a local to a global level, and to reduce or remove spatial, selective and other observational biases, helping to either confirm or reject existing hypotheses concerning rockfall occurrence and drivers.

In this dissertation we developed and presented a way to extract valuable knowledge from the challenging LRO image archive by adopting cutting–edge, deep learning algorithms (CNNs) from the fields of computer vision and robotics, opening a novel opportunity for geomorphology-focused planetary science (Bickel et al., 2018). The developed CNNs are capable of processing LRO images in a fraction of the time required by a human expert, while maintaining a near–expert–level of detection performance, effectively unlocking LRO's big data archive. We additionally showed how these algorithms can be customized to be effectively applied for rapid rockfall mapping on different planetary bodies, such as Mars (Bickel et al., 2020b). We further showed that the combination of training data from the Moon and Mars helps to train rockfall detectors which outperform single–domain detectors — with regard to recall, precision, and robustness — on all tested planetary bodies, including completely unknown bodies (to the detector) such as dwarf planet Ceres and comet 67P (Bickel et al., 2021b). Moreover, we demonstrated that we can use existing labels from previously studied planetary bodies (e.g. the Moon) to train detectors for new, unknown bodies (e.g. Mars) which are just as effective as locally-trained detectors, meaning that one can save around 90% of the time required for image labeling on that new, unknown body, by applying domain transfer learning principles (Bickel et al., 2021b). All training and testing labels created in the course of this dissertation — a key resource for deep learning — were shared (open access) with the scientific community to support future developments and studies (Bickel et al., 2021c). In addition, NASA JPL's Moon Trek website is hosting our latest rockfall detector for utilization by the scientific community and the general public, here: `https://trek.nasa.gov/moon/`[1]. Our work could inspire the development of algorithms which could be used map other features of scientific interest on large spatial scales, such as other types of mass wasting features, dust devils, impact craters, and dunes. In addition, our findings related to the application of transfer learning and multi–domain–trained detectors could be deployed to enhance rapid science discovery in new datasets returned by future missions, such as ESA's BepiColombo mission to Mercury — and could even be applied in fields other than planetary science, such as medical imaging, where high-quality labels are similarly scarce.

Using the developed CNNs in combination with substantial cloud computation resources, we created the first global map of lunar rockfalls with more than 130,000 detections (Bickel et al., 2020a). We embedded this new map on a stack of a large number of existing, geophysical datasets, including seismic, topographic,

[1] (registration required)

thermal, gravitational, and tidal data. We further selected a number of focus regions and mapped a few hundred rockfalls as well as their source regions manually and in great detail to enhance the global rockfall dataset with local, small-scale information inaccessible by global-scale data and efforts (Bickel et al., 2021a; Bickel, 2021). Using these data we discover that 1) more than 80% of all rockfalls occur in impact craters, 2) the spatial density of rockfall is highest in Copernican (young) craters, 3) rockfalls still occur in pre-Nectarian terranes, i.e., in regions billions of years old, and 4) we can use the spatial density of rockfall to estimate the age of a specific terrane. We further observe that rockfalls predominantly occur on 5) equator-facing slopes, i.e. in regions with large thermal amplitudes, 6) on slope angles well above-average, 7) in regions with large tidal displacements, and 8) and in regions with high surface roughness (rock abundance).

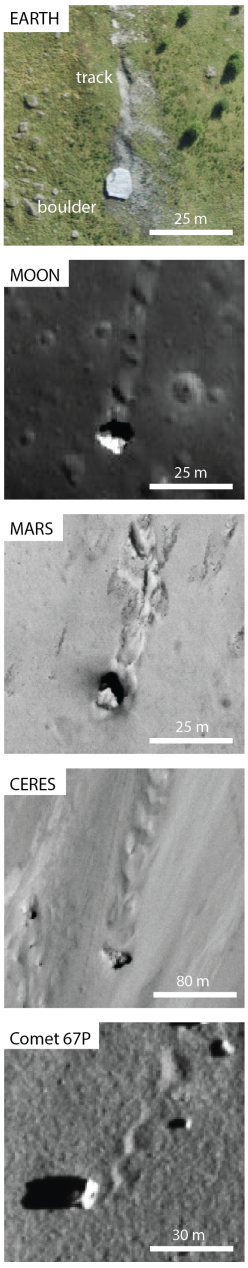


Figure 5.1: Rockfalls across the Solar System.

We note that rockfalls originate from 4 different source regions: cliff-, outcrop- (rock-supported, mainly in young terranes), boulder field-, and plain slope-type (soil-supported, mainly in old terranes) regions. The transport mechanism of lunar rockfalls appears to be controlled by the energy of the driver as well as the properties and geometry of the slope and source region, such as terrane age and steepness, rather than the boulder volume and shape. In summary, we argue that lunar rockfalls predominantly occur on the steep, equator-facing slopes of young impact craters, where long-term, continuous solar-induced thermal fatigue drives fracture growth, in addition to micro-meteoritic impacts. With increasing terrane age, erratic small-scale meteoritic impacts become increasingly important in driving rockfall occurrence, either by ejecting boulders or by inducing boulders through seismic shock waves that would have been stable otherwise. We find that less than 1% of all rockfalls are located in the vicinity of tectogenetic features such as graben and lobate scarps and do not observe any qualitative or statistical relation between Apollo-era seismic activity and rockfall abundance, which suggests that endogenic activity has not been a main, global driver of lunar rockfalls in the Apollo era and the Moon's recent geologic past. We note that seismicity might play an important role in the vicinity of tectogenetic features, however. Inspired by work of several Apollo era scientists, we developed a method to derive a first–order estimate of the surface strength of an untraversed lunar region, using only observations of rockfall boulder tracks made in LRO imagery as well as bearing capacity theory. We deployed this method to estimate the bearing capacity of high priority exploration regions such as pyroclastic and sunlit polar regions (Bickel et al., 2019; Bickel, Kring, 2020), as well as the permanently shadowed regions (Sargeant et al., 2020). The application of the methodology in PSRs required the development of an effective noise filter to minimize the negative effects of the low-light environment on the image quality — a tool we are still continuing to develop, currently using physical noise model-based, environment-informed neural networks (Moseley et al., 2020b, 2021); the most recent version of the tool is called "HORUS", Hyper-effective nOise Removal U-net Software. Using these tools, we derived (point) estimates of surface strength within PSRs which indicate that future robotic and human explorers should not face any sinkage–related difficulties in these regions, keeping in mind the limitations of the method. The developed method could be directly applied to other planetary bodies, such as Mars, Mercury and Ceres, as well as asteroids and comets.

We are left with a significantly improved understanding of the erosional activity, the geological evolution and the physical surface properties of our celestial neighbor. Using deep learning and big data, this work lifted the analysis of lunar rockfall from a local to a global level and revealed that the Sun has a significant influence on rockmass degradation and rockfall occurrence on the Moon, similar to meteoritic impact events. This means that the results of this thesis strongly suggest a shift from endogenic to predominantly exogenic rockfall drivers, i.e., a shift back to the hypotheses established during the Apollo-era by e.g. Hovland, Mitchell (1973) — a hypothesis to be tested with future data. Having a global and consistent perspective on lunar rockfall also allowed us to develop our understanding of the associated hazard for future

crewed and robotic exploration: on Earth, catastrophic landslides - rockfalls among them - account for ∼1000 fatalities (Clague, Roberts, 2012; EM-DAT, 2018) and billions of US Dollar worth of economic loss per year (DeBlasio, 2011; Sidle, Ochiai, 2006), representing a significant threat to human life. On the Moon, however, rockfalls (and mass wasting in general) do not appear to be a significant threat - as of today, no event has been observed directly. Our studies show that the occurrence of lunar rockfalls is controlled by the physical properties of the surface and a few long- and short-term drivers, meaning that regions of hypothetical, increased risk could be avoided - and further studied. It is important to note that the currently available data is not sufficient to investigate the temporal frequency of rockfall events, nor magnitude-frequency relationships, nor the (probably significant) rockfall population $<\sim$2 m. This means that we are currently not able to determine a reliable estimate of rockfall risk on the Moon. Despite that, we would like to point out that future mission planning efforts - particularly concerning permanent lunar structures and monitoring systems - could still consider the potential threat posed by rockfalls in 1) the proximity of known rockfall hotspots and 2) at the toes of slopes in general, regardless of their age and degree of inclination. Here, it is worth noting that rockfalls not always follow the local topographic gradient: we identified a series of likely impact-triggered rockfalls that got displaced parallel to the rim of Shackleton crater, in direct proximity to the south pole (Chapter 4.2, e.g. Figure 4.7) (Bickel, Kring, 2020), — an area that is currently targeted by NASA's crewed Artemis program.

From time to time we have been gazing beyond the Moon, too, and identified rockfalls on a very diverse set of bodies across the Solar System, including terrestrial planets (Bickel et al., 2020b), dwarf planets (Bickel et al., 2021b), moons (Bickel et al., 2018), asteroids, and comets (Bickel et al., 2021b), see Figure 5.1. These bodies share specific physical characteristics, but also feature distinct differences: For example, Mars hosts a (thin) atmosphere, while the Moon and Ceres are airless, resulting in disparate surface temperature fluctuation regimes; the gravitational acceleration on Ceres is a factor 14 lower than on Mars and a factor 36 lower than on Earth; comet 67P consists of very different material than the Earth, Moon and Mars. Yet, they all host rockfall with some stunning similarities. We observed the largest rockfall on Ceres with a block size of about 40 m in diameter (Bickel et al., 2021b), while the largest identified rockfalls on the Moon and Mars are about 30 and 20 m in diameter, respectively (Bickel et al., 2020a, 2019; Kumar et al., 2012; Tesson et al., 2020). In comparison, the largest rockfalls on Earth are about 10 m in diameter (Corominas et al., 2018; Kumar et al., 2012), i.e., substantially smaller than observed across the Solar System. Interestingly, lunar rockfalls feature lower Fahrböschung angles ($\sim$18°) (Bickel et al., 2021a) than e.g. terrestrial rockfalls ($\gg\sim$25°) (Corominas et al., 2018, 2003), indicating that boulders travel farther per meter dropped on the Moon than on Earth. This might be explained by the different gravity regimes, but could also be influenced by different slope geometry and substrate characteristics. Regardless of the body, all rockfalls in our Solar System appear to share a similar physical appearance and originate from distinct source regions such as bedrock outcrops and boulder fields. Therefore, one could hypothesize that the global drivers of rockfall as identified on the Moon are active throughout the entire solar system, with local differences as governed by, for example, atmospheres (denser atmosphere = fewer meteoritic impacts), orbital dynamics (larger obliquity = more pronounced seasons), and gravity (changes in gravity = modification of the displacement parabola). However, the complex mechanisms that control rockfall occurrence on Earth - including weather and climate - urge us to acknowledge the importance of the environmental conditions on each individual planetary body: comprehensive and detailed studies of rockfalls on each of these bodies are required before such a universal hypothesis could be adopted. Further, it is important to note that our current findings and hypotheses are influenced by the quality, coverage, and spatial resolution of the image data available today and might change once more data becomes available.

Currently, the Moon is in the focus of space agencies and private companies all around the globe. The coming years will see a multitude of robotic and potentially crewed exploration missions to the Moon, with a significant potential to further broaden our knowledge about lunar erosion and rockfall, and to provide ground truth for our current, almost exclusively remote sensing-based findings. For example, the proposed

Lunar Geophysical Network (Jawin et al., 2018; Nunn et al., 2021), consisting of a well-distributed, long-lived network of seismic monitoring stations, could revolutionize our understanding of the lunar endogenic activity and would enable a far more accurate comparison of rockfall abundance and seismic activity. NASA's Trailblazer smallsat mission (Ehlmann et al., 2021) and related cubesat missions will provide thermal and optical imagery with unprecedented temporal and spatial resolution, potentially enabling a more detailed study of rockfall occurrence in relevant sites of interest.

The study of extraterrestrial rockfalls is not limited to the Moon, however: The coming decades will see space probes visiting numerous places throughout the solar system which could potentially, or likely, host mass wasting features similar to rockfalls as observed on the Earth, Moon, and Mars: ESA's BepiColombo probe will return high-resolution imagery of Mercury, the planet closest to the Sun, that features extremely prominent thermal gradients, a distinct, impact-battered, and extraordinary rough surface, as well as a potentially active (subsurface) volatile cycle. NASA's DragonFly quadcopter mission will visit Saturn's moon Titan, a world with a unique nitrogen-based volatile cycle and geomorphic features like mountains, valleys, and lakes. NASA's Europa Clipper and ESA's JUICE (Jupiter Icy Moons Explorer) missions are going to explore the Jovian system, specifically Jupiter's icy moons Europa, Ganymede, and Callisto, which all are believed to host subsurface oceans and thus active geologic (sub)surface processes. NASA's Psyche mission will visit the metallic asteroid 16 Psyche, a world radically different from what we are used to.

How does mass wasting on these worlds look like? Are rockfalls on these worlds controlled by similar long- and short-term drivers as on the Moon? Is precipitation of methane and ethane driving rockfall occurrence on Titan? Is solar illumination triggering icefalls on Europa? Do metalfalls occur on Psyche? We are on a quest to find the answers to these intriguing questions - and to find new questions as we keep exploring our solar system and the worlds beyond.

Bibliography

Aharonson O., Schorghofer N., Gerstell M.F. Slope Streak Formation and Dust Deposition Rates on Mars // Journal of Geophysical Research: Planets. 2003. 108.

Alexe B., Deselaers T., Ferrari V. Measuring the Objectness of Image Windows // IEEE Trans. Pattern Anal. Mach. Intell. 2012. 11.

Allen C.C., Morris R.V., McKay D.S. Oxygen Extraction from lunar Soils and pyroclastic Glass // Journal of Geophysical Research. 1996. 101.

Allender E.J., Orgel C., Almeida N.V., Cook J., Ende J.J., Kamps O., Kring D.A. Traverses for the ISECG-GER Design Reference Mission for Humans on the lunar Surface // Advances in Space Research. 2019. 63.

Arm P., Zenkl R., Barton P., Beglinger L., Dietsche A., Ferrazzini L., Hampp E., Huber J., Schaufelberger D., Schmitt F., Sun B., Stolz B., Kolvenbach H., Hutter M. SpaceBok: A dynamic legged Robot for Space Exploration // IEEE Int. Conf. on Robot. and Automat. 2019.

Arvidson R., Crozaz G., Drozd R.J., Hohenberg C.M., Morgan C.J. Cosmic Ray Exposure Ages of Features and Events at the Apollo Landing Site // The Moon. 1975a. 13.

Arvidson R., Drozd R.J., Hohenberg C.M., Morgan C.J., Poupeau G. Horizontal Transport of the Regolith, Modification of Features, and Erosion Rates on the lunar Surface // The Moon. 1975b. 13.

Asnani V., Delap D., Creager C. The Development of Wheels for the lunar Roving Vehicle // Journal of Terramechanics. 2009. 46.

Atkinson J., Durham W.B., Saeger S. The Strength of ice-saturated extraterrestrial Rock Analogs // Icarus. 2018. 315.

Atkinson J., Prasad M., Abbud-Madrid A., Dreyer C.B. Penetration and Relaxation Behavior of dry lunar Regolith Simulants // Icarus. 2019. 328.

Baedecker P., Chou C.-L., Sundberg L., Wasson J. Volatile and siderophilic Trace Elements in the Soils and Rocks of Taurus Littrow // Lunar and Planetary Science Conference. 1974.

Balme M., Greeley R. Dust Devils on Earth and Mars // Rev. Geophys. 2006. 44.

Bandfield J.L., Ghent R.R., Vasavada A.R., Paige D.A., Lawrence S.J., Robinson M.S. Lunar Surface Rock Abundance and Regolith Fines Temperatures derived from LRO Diviner Radiometer Data // Journal of Geophysical Research: Planets. 2011. 116.

Bart G.D., Nickerson R.D., Lawder M.T., Melosh H. Global Survey of lunar Regolith Depths from LROC images // Icarus. 2011. 215.

Basilevsky A.T., Abdrakhimov A.M., Head J.W., Pieters C.M., Wu Y., Xiao L. Geologic Characteristics of the Luna 17/Lunokhod 1 and Chang'E-3/Yutu Landing Sites, northwest Mare Imbrium of the Moon // Planetary and Space Science. 2015. 117.

Basilevsky A.T., Head J.W., Hortz F. Survival Times of meter-sized Boulders on the Surface of the Moon // Planet. Space Sci. 2013. 89.

Basilevsky A.T., Krasilnikov S.S., Ivanov M.A., Malenkov M.I., Michael G.G., Liu T., Head J.W., Scott D.R., Lark L. Potential lunar Base on Mons Malapert: topographic, geologic, and Trafficability Considerations // Solar System Research. 2019. 53.

Bekker M.G. Theory of Land Locomotion: The Mechanics of Vehicle Mobility // University of Michigan Press. 1956.

Bekker M.G. Off-the-road Locomotion: Research and Development in Terramechanics // University of Michigan Press. 1960.

Ben-David S., Blitzer J., Crammer K., Kulesza A., Pereira F., Wortman-Vaughan J. A theory of learning from different domains // Machine Learning. 2010. 79, 151â175.

Benedix G.K., Lagain A., Chai K., Meka S., Anderson S., Norman C., Bland P. A., Paxman J., Towner M. C., Tan T. Deriving Surface Ages on Mars Using Automated Crater Counting // Earth and Space Science. 2019. 7.

Bickel V.T. A Catalog of 687 Lunar Rockfalls // MPDL Edmond. 2021.

Bickel V.T., Aaron J., Manconi A., Loew S., Mall U. Impacts drive lunar rockfalls over billions of years // Nature Communications. 2020a. 11, 2862.

Bickel V.T., Aaron J., Manconi A., Loew S., Mall U. Global Drivers and Transport Mechanisms of Lunar Rockfalls // Journal of Geophysical Research: Planets. 2021a. In review.

Bickel V.T., Conway S.J., Tesson P.-A., Manconi A., Loew S., Mall U. Deep Learning-Driven Detection and Mapping of Rockfalls on Mars // IEEE JSTARS. 2020b. 13.

Bickel V.T., Honniball C.I., Martinez S.N., Sargeant H.M., Rogaski A., Bell S.K., Czaplinski E.C., Farrant B.E., Harrington E.M., Tolometti G.D., Kring D.A. Analysis of Lunar Boulder Tracks: Implications for Trafficability of Pyroclastic Deposits // JGR: Planets. 2019. 124.

Bickel V.T., Kring D.A. Lunar south pole boulders and boulder tracks: Implications for crew and rover traverses // Icarus. 2020. 348.

Bickel V.T., Lanaras C., Manconi A., Loew S., Mall U. Automated Detection of Lunar Rockfalls Using a Convolutional Neural Network // IEEE TGRS. 2018. 57, 6.

Bickel V.T., Mandrake L., Doran G. Transfer Learning for Enhanced Rockfall Mapping in known and unknown planetary domains // ISPRS. 2021b. In review.

Bickel V.T., Mandrake L., Doran G. A labeled image dataset for deep learning-driven rockfall detection on the Moon and Mars // Frontiers in Remote Sensing. 2021c.

Boston-Dynamics . Robots: Changing your Idea of what Robots can do // Boston Dynamics. 2019.

Bourke M.C., Edgett K.S., Cantor B.A. Recent aeolian Dune Change on Mars // Geomorphology. 2008. 94.

Bowles L. Foundation Analysis and Design // McGraw Hill International Book Company. 1997.

Bridges N.T., Ayoub F., Avouac J.-P., Leprince S., Lucas A., Mattson S. Earth-like Sand Fluxes on Mars // Nature. 2012. 485.

Brusnikin E.S., Kreslavsky M.A., Zubarev A.E., V.D.Patratiy , Krasilnikov S.S., J.W.Head , I.P.Karachevtseva . Topographic Measurements of Slope Streaks on Mars // Icarus. 2016. 278.

Bunte M.K., Porter S., Robinson M.S. A Sortie Mission to Schroedinger Basin as Reconnaissance for Future Exploration // Geol. Soc. of America. 2011. 483.

CG Society. Next-Gen lunar Rover by NASA // CGS. 2014.

Carrier W.D., Oelhoeft G.R., Mendell W. Physical Properties of the Lunar Surface // Lunar Sourcebook. 1991.

Castelli F., Lentini V. Evaluation of the Bearing Capacity of Footings on Slopes // Int. Jour. of Phys. Model. and Geotech. 2012. 12.

Cho G.C., Dodds J., Santamarina J.C. Closure to Particle Shape Effects on Packing Density, Stiffness, and Strength: Natural and in crushed sands // ASCE. 2007.

Christensen P.R., Engle E., Anwar S., Dickenshied S., Noss D., Gorelick N., Weiss-Malik M. JMARS - A planetary GIS // ASU. 2009.

Cisneros E., Awumah A., Brown H., Martin A., Paris K., Povilaitis R., Robinson M.S. LROC Permanently Shadowed Region Imaging - Atlas and Controlled Mosaics // Lunar and Planetary Science Conference. 2017.

Clague J.J., Roberts N.J. Landslide Hazard and Risk // Cambridge University Press. 2012.

Cochran E.S., Vidale J.E., Tanaka S. Earth Tides can trigger shallow Thrust Fault Earthquakes // Science Reports. 2004. 306.

Coduto D.P., Yeung M.C., Kitch W.A. Geotechnical Engineering: Principles and Practices // Pearson. 2011.

Colaprete A. Resource Prospector: evaluating the ISRU Potential of the lunar Poles // LEAG Report. 2016. 9.

Colaprete A., Schultz P., Heldmann J., Wooden D., Shirley M., Ennico K. Detection of Water in the LCROSS Ejecta Plume // Science. 2010. 330.

Collins B.D., Stock G.M. Rockfall Triggering by cyclic thermal Stressing of Exfoliation Fractures // Nature Geoscience. 2016. 9.

Collins B.D., Stock G.M., Eppes M.-C., Lewis S.w., Corbett S.C., Smith J.B. Thermal influences on spontaneous rock dome exfoliation // Nature Communications. 2018. 9, 762.

Corominas J., Copons R., Vilaplana J.M., Altimir J., Amigo J. Integrated Landslide Susceptibility Analysis and Hazard Assessment in the Principality of Andorra // Natural Hazards. 2003. 30.

Corominas J., Mavrouli O., Ruiz-Carulla R. Magnitude and Frequency Relations: Are there Geological Constraints to the Rockfall Size? // Landslides. 2018. 15.

Costes N., Carrier W., Mitchell J., Scott R. Apollo 11 Soil Mechanics Investigation // Science. 1970. 167.

Costes N.C, Farmer J.E., George E.B. Mobility Performance of the lunar Roving Vehicle: Terrestrial Studies // Apollo 15 Results. 1972.

Crawford I.A. Lunar Resources: A Review // Prog. in Phys. Geography. 2015. 39.

DeBlasio F.V. Introduction to the Physics of Landslides // Springer Dordrecht. 2011.

Dorran L.K.A. A Review of Rockfall Mechanics and Modelling Approaches // Prog. in Phys. Geography: Earth and Environment. 2015. 27.

Douillard A. Object detection with deep learning on aerial imagery // Medium. 2018.

Duarte K.D., Schmidt B.E., Chilton H.T., Hughson K.H.G. Landslides on Ceres: Diversity and Geologic Context // JGR: Planets. 2019. 124.

Dundas C.M., Diniega S., McEwen A.S. Long-term monitoring of martian gully formation and evolution with MRO/HiRISE // Icarus. 2015. 251.

Dundas C.M., McEwen A.S., Chojnacki M., Milazzo M.P., Byrne S., McElwaine J.M., Urso A. Granular flows at recurring slope lineae on Mars indicate a limited role for liquid water // Nature Geoscience. 2017. 10.

Durgonuglu H.T., Mitchell J.K. Static Penetration Resistance of Soils: I Analysis // Proc. Spec. Conf. on In Situ Measurement of Soil Prop. 1975.

EDU OSP. Bearing Capacity and Stability of Foundations // OSP EDU. n.d.

EM-DAT . The International Disasters Database // IDD. 2018.

ESA . Chang'E-3 Moon-landing Mission // ESA. n.d.a.

ESA . Chang'E-4 far side Mission of China // ESA. n.d.b.

Eggleston J.M., Patterson A.W., Throop J.E., Arant W.H., Spooner D.L. Lunar Rolling Stone // Photogrammetric Engineering. 1968. 34.

Ehlmann B.L., Klima R.L., Bennett C.L., Blaney D., Bowles N., Calcutt S., Dickson J., Hanna K. Donaldson, Edwards C.S., Green R., House M.A., Klesh A., Pieters C., Seybold C., Thompson D., Williamson W., Wood J. Lunar Trailbazer: A Pioneering Smallsat for Lunar Water and Lunar Geology // Lunar and Planetary Science Conference. 2021.

Eigen D., Rolfe J., Fergus R., LeCun Y. Understanding Deep Architectures using a Recursive Convolutional Network // ArXiv. 2014.

Endres I., Hoiem D. Category Independent Object Proposals // Proc. Eur. Conf. Comput. Vision. 2010.

Eppes M.C., Fadden L.D., Wegmann K.W., Scuderi L.A. Cracks in desert pavement rocks: Further insights into mechanical weathering by directional insolation // Geomorphology. 2010. 123.

Eppes M.C., Willis A., Molaro J., Abernathy S., Zhou B. Cracks in Martian boulders exhibit preferred orientations that point to solar-induced thermal stress // Nature Communications. 2015. 6, 6712.

Eugster O., Eberhardt P., Geiss J., Groegler N., Jungck M., Moergeli M. The cosmic-ray Exposure History of Shorty Crater Samples: The Age of Shorty Crater // Lunar and Planetary Science Conference. 1977. 8.

EuroCode7 . Eurocode 7: Geotechnical Design // BS EN 1997-1:2004. 1996.

Evans S.G., Hungr O. The Assessment of Rockfall Hazard at the Base of Talus Slopes // Canadian Geotech. Journal. 1993. 30.

Fa W., Jin Y. A primary Analysis of microwave Brightness Temperature of lunar Surface from Chang'E-1 multi-channel Radiometer Observation and Inversion of Regolith Layer Thickness // Icarus. 2010. 207.

Fanara L., Gwinner K., Hauber E., Oberst J. Automated Detection of Block Falls in the North Polar Regions of Mars // Planet. Space Sci. 2020. 180.

Fassett C.I., Thomson B.J. Crater Degradation on the lunar Maria: topographic Diffusion and the Rate of Erosion on the Moon // Journal of Geophysical Research: Planets. 2014.

Fergason R.L., Hare T.M., Laura J. HRSC and MOLA blended Digital Elevation Model at 200m v2 // PDS Annex USGS. 2017.

Fielder G. Erosion and Deposition on the Moon // Planet. Space Sci. 1963. 11.

Filice A. L. Lunar Surface Strength Estimate from Lunar Orbiter II Photograph // Science. 1967. 156.

Fizyr . Keras RetinaNet // GitHub. 2018.

Florensky C.P., Basilevsky A.T., Bobina N.N., Burba G.A., Grebennik N.N., Kuzmin R.O. The Floor of Crater Le Monier: A Study of Lunokhod 2 Data // Lunar and Planetary Science Conference. 1978.

Fortezzo C.M, Hare T.M. Completed digital Renovation of the 1:5,000,000 lunar geologic Map Series // Lunar and Planetary Science Conference. 2013. 44.

French R.A., Bina C.R., Robinson M.S., Watters T.R. Small-scale lunar Graben: Distribution, Dimensions, and Formation Processes // Icarus. 2015. 252.

Gaddis L.R., Staid M.I., Tyburczy J.A., Hawke B.R., Petro N.E. Compositional Analyses of lunar pyroclastic Deposits // Icarus. 2003. 161.

Gardin E., Allemand P., Quantin C., Thollot P. Defrosting, dark Flow Features, and Dune Activity on Mars: Example in Russell Crater // Journal of Geophysical Research: Planets. 2010. 115.

Gault D.E., John E., John B. Guest, Michael C., Malin M. Some Comparisons of Impact Craters on Mercury and the Moon // Journal of Geophysical Research: Planets. 1975. 80.

Gertsch L., Gustafson R., Gertsch R. Effect of Water Ice Content on Excavatability of lunar Regolith // Int. Forum on Space Tech. and App. 2006.

Giguere T.A., Taylor G.J., Hapke B.R., Lucey P.G. The Titanium Contents of lunar Mare Basalts // Science. 2010. 35.

Girshick R., Donahue J., Darrell T., Malik J. Region-Based Convolutional Neural Networks for Accurate Object Detection and Segmentation // IEEE Trans. Pattern Anal. Mach. Intell. 2016. 38.

Gladstone G.R., Retherford K.D., Egan A.F., Kaufmann D.E., Miles P.F., Parker J.W. Far-ultraviolet Reflectance Properties of the Moon's permanently shadowed Regions // Journal of Geophysical Research. 2012. 117.

Golombek M.P. Structural Analysis of lunar Grabens and the shallow crustal Structure of the Moon // Journal of Geophysical Research. 1979. 84.

Goodfellow I., Bengio Y., Courville A. Deep Learning. 2016.

Guest J.E., Murray J.B. Volcanic Features of the Nearside equatorial Maria // Jour. Geol. Sci. 1976. 132.

Haas T. de, Conway S.J., Krautblatter M. Recent (Late Amazonian) enhanced Backweathering Rates on Mars // Journal of Geophysical Research: Planets. 2015. 120.

Hansen J.B. A revised and extended Formula for Bearing Capacity // Bulletin. 1970. 11.

Hare T.M., Hayward R.K., Blue J.S., Archinal B.A. Image Mosaics and topographic Map of the Moon // PDS Annex USGS. n.d.

Harrison D.A., Ambrose R., Bluethmann B., Junkin L. Next Generation Rover for lunar Exploration // JSC-released IEEE AC. 2008. 1196.

Haruyama J., Ohtake M., Matsunaga T., Morota T., Honda C., Yakota Y. Lack of exposed Ice inside lunar south Pole Shackleton Crater // Science. 2008. 322.

Hawke B.R., Blewett D.T., Lucey P.G., Smith G.A., Bell J.F., Campbell B.A., Robinson M.S. The Origin of lunar Crater Rays // Icarus. 2004. 170.

Hayne P., Hendrix A., Sefton-Nash E., Siegler M., Lucey P.G., Retherford K.D. Evidence for exposed Water Ice in the Moon's south polar Regions from LRO ultraviolet Albedo and Temperature Measurements // Icarus. 2015. 255.

Hayne P., Siegler M., Paige D., Lucey P., Fisher E. Carbon Dioxide Frost at the Poles of the Moon: Thermal Stability and observational Evidence from the LRO // Lunar and Planetary Science Conference. 2019.

He K., Zhang X., Ren S., Sun J. Deep Residual Learning for Image Recognition // ArXiv. 2015.

Head J.W., Fassett C.I., Kadish S.J., Smith D.E., Zuber M.T., Neumann G.A., Mazarico E. Global Distribution of large lunar Craters: Implications for resurfacing and Impactor Populations // Science. 2010. 329.

Heim A. Bergsturz und Menschenleben // Fretz und Wasmuth, Zurich. 1932.

Hoang T.M., Nguyen P.H., Truong N.Q., Lee Y.W., Park K.R. Deep RetinaNet-Based Detection and Classification of Road Markings by Visible Light Camera Sensors // Sensors. 2019. 19.

Hoerz F., Basilevsky A.T., Head J.W., Cintala M.J. Erosion of Lunar Surface Rocks by Impact Processes: A Synthesis // Planetary and Space Science. 2020. 194.

Hough P.V. America Patent No. 3069654 // AP. 1962.

Houston W.N., Hovland H.J., Mitchell J.K., Namiq L.I. Lunar Soil Porosity and its Variation as estimated from Footprints and Boulder Tracks // Lunar Science Conference. 1972. 3.

Hovland H.J., Mitchell J.K. Friction Angle of lunar Surface Soils estimated from Boulder Tracks // Space Sciences Lab. Lunar Surface Eng. Prop. Exp. Def. 1969a. 2.

Hovland H.J., Mitchell J.K. Lunar Surface Engineering Properties Experiment Definition // University of California. 1969b. 2.

Hovland H.J., Mitchell J.K. Lunar Surface Engineering Properties Experiment Definition: Volume 2 - Mechanics of rolling Sphere-Soil Slope Interaction // University of California Final Report. 1971.

Hovland H.J., Mitchell J.K. Boulder tracks and nature of lunar soil // The Moon. 1973. 6.

Howard K.A., Head J.W., Swann G. Geology of the Hadley Rille: Preliminary Report // USGS Interagency Report. 1972. 41.

Hungr O., Leroueil S., Picarelli L. The Varnes classification of landslide types, an update // Landslides. 2014. 11. 167–194.

Hurley D.M., Lawrence D.J., Bussey D.B., Vondrak R.R., Elphic R., Gladstone G.R. Two-dimensional Distribution of Volatiles in the lunar Regolith from Space Weathering Simulations // Geophysical Research Letters. 2012. 39.

Hurwitz D., Kring D.A. Identifying the geologic Context of Apollo 17 Impact Melt Breccias // Earth and Planetary Science Letters. 2016. 436.

IFFI . ISPRA // IFFI. 2018.

ISRO . GLSF-F10/Chandrayaan 2 Mission // ISRO. n.d.

Jackson T.L., Farrell W.M., Killen R.M., Delory G.T., Halekas J.S., Stubbs T.J. Discharging of roving Objects in the lunar polar Regions // Jour. of Spacecraft and Rockets. 2011. 48.

Jaeger P.F., Kohl S.A.A., Bickelhaupt S., Isensee F., Kuder T.A., Schlemmer H.P., Maier-Hein K.H. Retina U-Net: Embarrassingly Simple Exploitation of Segmentation Supervision for Medical Object Detection // arXiv. 2018.

Jaffe L.D. Bearing Strength of lunar Soil // The Moon. 1971. 3.

Jawin E.R., Valencia S.N., Watkins R.N., Crowell J.M., Neal C.R., Schmidt G. Lunar Science for landed Missions Workshop Findings Report // Earth and Space Science. 2018. 6.

Jayalekshmi S., Kumar P.G. Studies of the Sinkage of rigid plain Wheels and lugged Wheels on TRI-1 lunar Soil Simulant // Journal of Terramechanics. 2019. 82.

Jung H., Kim B., Lee I., Yoo M., Lee J., Ham S., Woo O., Kang J. Detection of masses in mammograms using a one-stage object detector based on a deep convolutional neural network // PLOS ONE. 2018.

Kadish S.J., Fassett C.I., Head J.W., Smith D.E., Zuber M.T., Neumann G.A., Mazarico E. A global Catalog of large lunar craters (>20 km) from the Lunar Orbiter Laser Altimeter // Lunar and Planetary Science Conference. 2011. 42.

Keefer D.K. Landslides caused by Earthquakes // Geol. Soc. of America Bull. 1984. 95.

Keefer D.K. The Susceptibility of Rock Slopes to Earthquake-induced Failure // Bull. Assoc. Eng. Geol. 1993. 30.

Khademian Z., Kim E., Nakagawa M. Simulation of lunar Soil with irregularly shaped, crushed Grains: Effects of Grain Shapes on the mechanical Behaviors // Journal of Geophysical Research: Planets. 2019. 124.

Klee V. Can the Measure of S (ai,bi) be computed in less than O(nlogn) steps? // Am. Math. Monthly. 1977. 84.

Kloos J.L., Moores J.E., Sangha J., Nguyen T.G., Schorghofer N. The temporal and geographic Extent of seasonal cold trapping on the Moon // Journal of Geophysical Research: Planets. 2019. 124.

Koeber S., Robinson M.S. LROC Observations of permanently shadowed Regions // Lunar and Planetary Science Conference. 2013.

Koeber S., Robinson M.S., Speyerer E. LROC Observations of permanently shadowed Regions on the Moon // Lunar and Planetary Science Conference. 2014.

Kokelaar B.P., Bahia R., Joy K.H., Viroulet S., Gray J.M. Granular Avalanches on the Moon: Mass-wasting Conditions, Processes, and Features // Journal of Geophysical Research: Planets. 2017. 122.

Kreslavsky M., Head J.W. New observational Evidence of global seismic Effects on basin-forming Impacts on the Moon from Lunar Reconnaissance Orbiter Lunar Orbiter Laser Altimeter Data // Journal of Geophysical Research. 2012. 117.

Kreslavsky M., Head J.W. The steepest Slopes on the Moon from Lunar Orbiter Laser Altimeter (LOLA) Data: spatial Distribution and correlation with geologic Features // Icarus. 2016. 273.

Kring D.A., Durda D.D. A global lunar Landing Site Study to provide the scientific Context for Exploration of the Moon // Lunar and Planetary Institute Contribution. 2012. 1694.

Kring D.A., Kramer G.Y., Bussey D.B.J., Hurley D.M. Prominent volcanic Source of Volatiles in the south polar region of the Moon // LEAG contribution. 2014. 1820.

Krishna N., Kumar P.S. Impact Spallation Processes on the Moon: a Case Study from the Size and Shape Analysis of Ejecta Boulders and Secondary Craters of Censorinus Crater // Icarus. 2016. 264.

Kumar P.S. Structural Effects of Meteorite Impact on Basalt: Evidence from Lonar Crater, India // Journal of Geophysical Research. 2005. 110.

Kumar P.S., Keerthi V., Kumar A.S., Mustard J., Krishna B. Gopala, Ostrach L.R., Kring D.A., Kumar A.S. Kiran, Goswami J.N. Gullies and landslides on the Moon: Evidence for dry-granular flows // Journal of Geophysical Research: Planets. 2013. 118.

Kumar P.S., Keerthi V., Kumar A.S., Mustard J., Krishna B. Gopala, Ostrach L.R., Kumar A.S. Kiran, Goswami J.N. Recent Seismicity in Valles Marineris, Mars: Insights from young Faults, Landslides, Boulder Falls and possible Mud Volcanoes // Earth Planet. Sci. Letters. 2012. 505.

Kumar P.S., Krishna N., Lakshmi K.J. Prasanna, Dhabu A., Platz T. Recent seismicity in Valles Marineris, Mars: Insights from young faults, landslides, boulder falls and possible mud volcanoes // Earth and Planetary Science Letters. 2019a. 505.

Kumar P.S., Mohanty R., Lakshmi K.J.P., Raghukanth S.T.G., Dabhu A.C., Rajasekhar R.P., Menon R. The Seismically Active Lobate Scarps and Coseismic LunarBoulder Avalanches Triggered by 3 January 1975(MW4.1) Shallow Moonquake // JGR: Planets. 2019b. 46.

Kumar P.S., Sruthi U., Krishna N., Lakshmi K.J.P., Menon R., Krishna B.G, Kring D.A., Head J.W., Goswami J.N., Kumar A.S. Siran. Recent shallow moonquake and impact-triggered boulder falls on the Moon: New insights from the Schroedinger basin // Journal of Geophysical Research: Planets. 2016. 121.

Kusakabe O., Kimura T., Yamaguchi H. Bearing Capacity of Slopes under Strip Loads on the top Surfaces // Soils and Foundations. 1981. 21.

LExSWG . Lunar Surface Exploration Strategy // LEAG Final Advisory Group Report. 1995.

LOLA LRO. LRO LOLA // NASA. n.d.

Langevin Y., Arnold J.R., Nishiizumi K. Transport Processes on the lunar Surface: Comparison of Model Calculations and Radionuclides Data // Journal of Geophysical Research. 1982. 87.

Lawrence D.J., Feldman W.C., Elphic R.C., Little R.C., Prettyman T.H., Maurice S. Iron Abundances on the lunar Surface as measured by the Lunar Prospector gamma-ray and neutron Spectrometers // Journal of Geophysical Research: Planets. 2002. 107.

Lemoine F.G., Goossens S., Sabaka T.J., Nicholas J.B., Mazarico E., Rowlands D.D., Loomis B.D., Chinn D.S., Neumann G.A., Smith D.E., Zuber M.T. GRGM900C: A degree 900 lunar gravity model from GRAIL primary and extended Mission Data // Geophys. Research Letters. 2014. 41.

Li S., Lucey P.G., Milliken R.E., Hayne P.O., Fisher E., Williams J.P. Direct Evidence of Surface exposed Water ice in the lunar polar Regions // Proc. of the Nat. Acad. of Sciences. 2018. 115.

Lin T. Y., Dollar P., Girshick R., He K., Hariharan B., Belongie S. Feature Pyramid Networks for Object Detection // IEEE Conference on Computer Vision and Pattern Recognition. 2017.

Lin T.Y., Goyal P., Girshick R., He K., Dollar P. Focal Loss for Dense Object Detection // arXiv. 2018.

Linke S., Windisch L., Kueter N., Voss A., Przwara P., Grasshoff M., Stoll E., Schilde C., Kwade A. TUBS-M and TUBS-T - new lunar Regolith Simulants adaptable to local Surface Characteristics // IAC Bremen. 2018. 69.

Lorenz R. D., Reiss D. Solar Panel Clearing Events, Dust Devil Tracks, and in-situ Vortex Detections on Mars // Icarus. 2005. 248.

Lucchetti A., Penasa L., Pajola M., Massironi M., Brunetti M.T., Cremonese G., Oklay N. The Rocky-Like Behavior of Cometary Landslides on 67P/Churyumov-Gerasimenko // Geophysical Research Letters. 2019. 46.

Lucey P.G. Mineral Maps of the Moon // Geophys. Research Letters. 2004. 31.

Lucey P.G., Blewett D.T., Jolliff B.L. Lunar Iron and Titanium Abundance Algorithms based on final Processing of Clementine ultraviolet-visible Images // Journal of Geophysical Research. 2000. 105.

Lyndon B. Apollo 17 Mission Report // NASA Tech. Rep. 1973.

MOLA Team. Mars MGS MOLA DEM 463m v2 // PDS Annex USGS. 2014.

Malin M.C. Mass movements on Venus: Preliminary results from Magellan cycle 1 observations // JGR: Planets. 1992. 97.

Malisiewicz T. Blazing fast NMS // Computer Vision Blog. 2011.

Massey C.I., McSaveney M.J., Taig T. Determining Rockfall Risk in Christchurch using Rockfalls triggered by the 2010-2011 Canterbury Earthquake Sequence // Earthquake Spectra. 2014. 30.

Matsuyama I., Keane J.T., Trinh A., Beuthe M., Watters T.R. Global tectonic patterns of the Moon // Icarus. 2021.

McEwen A.S., Eliason E.M., Bergstrom J.W., Bridges N.T., HiRISE team the. Mars Reconnaissance Orbiter's High Resolution Imaging Science Experiment (HiRISE) // JGR: Planets. 2007. 112.

McFadden L.D., Eppes M.C., Gillespie A.R., Hallet B. Physical weathering in arid landscapes due to diurnal variation in the direction of solar heating // Geol. Soc. of America Bull. 2005. 117.

McGovern J.A., Bussey D.B., Greenhagen B.T., Paige D.A., Cahill J.T., Spudis P.D. Mapping and Characterization of non-polar permanent Shadows on the lunar Surface // Icarus. 2013. 223.

McKay D.S., Heiken G., Basu A., Blanford G., Reedy R. The lunar Regolith // Lunar Sourcebook. 1991. 7.

Melosh H.J. Planetary Surface Processes // Cambridge University Press. 2011.

Metivier L., Viron O. de, Conrad C.P., Renault S., Diament M., Patau G. Evidence of Earthquake Triggering by the solid Earth Tides // Earth and Planetary Science Letters. 2009. 278.

Metzger P.T., Anderson S., Colaprete A. Experiments indicate Regolith is looser in the lunar polar Regions than at the lunar Landing Sites // Biann. Int. Conf. on Eng., Science, Const., and Operations in Chall. Environ. 2018. 16.

Meyerhof G. The ultimate Bearing Capacity of Foundations // Geotechnique. 1951. 2.

Meyerhof G. The ultimate Bearing Capacity of Foundations on Slopes // Proc. Conf. on Soil Mech. and Found. Eng. 1957. 4.

Mitchell J.K., Bromwell L., Carrier W.D., Houston W., Scott R. Soil Mechanics Experiment // Apollo 15 Prel. Sci. Rep. 1972a. 7.

Mitchell J.K., Carrier W.D., Costes N., Houston W.N., Scott R., Hovland H.J. Soil Mechanics // Apollo 17 Prel. Sci. Rep. 1973. 8.

Mitchell J.K., Houston W., Carrier W.D., Costes N., Scott R. Apollo Soil Mechanics Experiment, S-200, Final Report // Space Sciences Lab. Series. 1974. 7.

Mitchell J.K., Houston W., Scott R., Costes N., Carrier W.D., Bromwell L. Mechanical Properties of lunar Soil: Density, Porosity, Cohesion and Angel of internal Friction // Lunar and Planetary Science Conference. 1972b.

Mohanty R., Kumar P.S., Raghukanth S.T.G., Lakshmi K.J.P. The long-lived and recent Seismicity at the lunar Orientale Basin: Evidence from Morphology and Formation Ages of Boulder Avalanches, Tectonics and seismic Ground Motion // Journal of Geophysical Research: Planets. 2020.

Mojzsis S.J., Brasser R., Kelly N., Abramov O., Werner S.C. Onset of Giant Planet Migration before 4480 Million Years ago // Astrophys. Jour. 2019. 881.

Molaro J., Hergenrother C.W., Chesley S.R., Walsh K.J., Hanna R.D., Haberle C.W., Ballouz R.-L., Schwartz S.R., Bottke W.F., Campins H.J., Lauretta D.S. Thermal fatigue as a mechanism for asteroid activity // Journal of Geophysical Research: Planets. 2019. 125.

Molaro J.L., Byrne S., J.-L-Le . Thermally induced Stresses in Boulders on airless Body Surfaces, and Implications for Rock Breakdown // Icarus. 2017. 294.

Moore H. J. Estimates of the mechanical properties of lunar surface using tracks and secondary impact craters produced by blocks and boulders // NASA Interagency Report: Astrogeology. 1970. 22.

Moore H.J., Vischer W.A., Martin G.L. Boulder tracks on the Moon and Earth // Geol. Surv. Res. Sci. Notes Summaries Invest. Geol. Hydrol. Rel. Fields. 1972. 800.

Morse Z.R., Osinski G.R., Tornabene L.L. Morphologic Mapping and Analysis of Tsiolkovsky Crater Ejecta // Lunar and Planetary Science Conference. 2018. 49.

Moseley B., Bickel V.T., Burelbach J., Relatores N. Unsupervised Learning for thermophysical Analysis on the lunar Surface // The Planetary Science Journal. 2020a. 1.

Moseley B., Bickel V.T., Lopez-Francos I., Rana L. Extreme low-Light environment-driven image denoising over permanently shadowed lunar regions with a physical noise model // IEEE CVPR. 2021.

Moseley B., Bickel V.T., Lopez-Francos I., Rana L., Olivares M., Wingo D., Zuniga A., Subtil N. Low-light image enhancement of permanently shadowed lunar regions with physics-based machine learning // Conf. on Neural Proc. Systems. 2020b. 34.

Muehlberger W.R., Batson R.M., Cernan E.A., Freeman V., Hait H.M., Holt H.E. Preliminary geologic Investigation of the Apollo 17 Landing Site // Apollo 17 Prel. Sci. Rep. 1973. 6.

NASA . Space Exploration Vehicle Concept // NASA fact sheet. 2010.

NASA . Apollo 11 Mission Overview // NASA. 2017.

NASA . NASA's Plan for sustained lunar Exploration and Development // NASA. 2020.

NRC . Earth Science and Applications from Space: National Imperatives for the Next Decade and Beyond // National Academies Press. 2007.

NSSDC . Surveyor/Apollo/Lunokhod // NSSDC. 2006.

Nagle-McNaughton T., McClanahan T., Scuderi L. PlaNet: A Neural Network for Detecting Transverse Aeolian Ridges on Mars // Remote Sensing. 2020. 12, 21.

Nahm A.L. A new Map of Graben on the lunar Nearside: Initial Observations and Classification // Lunar and Planetary Science Conference. 2016. 47.

Nahm A.L., Johnson M.B., Hauber E., Watters T.R., Martin E.S. New global Map and Classification of large-scale extensional Features // Lunar and Planetary Science Conference. 2018. 49.

Nakamura Y., Latham G.V., Dorman H.J., Ibrahim A.B.K., Koyama K., Horvath P. Shallow Moonquakes - Depth, Distribution and Implications as to the present State of the lunar Interior // Lunar and Planetary Science Conference. 1979. 10.

Needham D.H., Kring D.A. Lunar volcanism produced a transient atmosphere around the ancient Moon // Earth and Planetary Science Letters. 2017. 478. 175–178.

Nelson D.M., Koeber S.D., Daud K., Robinson M.S., Watters T.R., Banks M.E., Williams N.R. Mapping lunar Maria Extents and Lobate Scarps using LROC Image Products // Lunar and Planetary Science Conference. 2014. 45.

Neukum G., Ivanov B.A., Hartmann W.K. Cratering Records in the inner Solar System in Relation to the lunar Reference System // Space Sci. Rev. 2001. 96.

Newmark N.M. Effects of Earthquakes on Dams and Embankments // Geotechnique. 1965. 15.

Nunn C., Pike W.T., Stanley I.M., Kedar S., Panning M. Standing on Apollo's Shoulders: A Microseismometer for the Moon // The Planetary Science Journal. 2021. 2, 36.

O'Sullivan K.M., Tohout T., Thaisen K.G., Kring D.A. Calibrating several Key lunar stratigraphic Units representing 4 Billion Years of lunar History within Schroedinger Basin // Recent Adv. in Lunar Stratigraphy. 2011. 477.

Oberbeck V.R., Quaide W.L. Genetic Implications of lunar Regolith Thickness Variations // Icarus. 1968. 9.

Olhoeft G.R., Strangway D.W. Dielectric Properties of the first 100 Meters of the Moon // Earth and Planetary Science Letters. 1975. 24.

Otto K.A., Jaumann R., Krohn K., Matz K.D., Preusker F., Roatsch T., Schenk P. Mass-wasting features and processes in Vesta's south polar basin Rheasilvia // JGR: Planets. 2013. 118.

Paige D., Wood S.E., Vasavada A.R. The thermal Stability of Water Ice at the Poles of Mercury // Science. 1992. 258.

Paige D.A., Siegler M.A., Zhang J.A., Hayne P.O., Foote E., Bennett K.A. Diviner lunar Radiometer Observations of cold Traps in the Moon's south polar Regions // Science. 2010. 330.

Pasquon K., Gargani J., Masse M., Conway S.J. Present-day formation and seasonal Evolution of linear Dune Gullies on Mars // Icarus. 2016. 274.

Pierson H.A., Gashler M.S. Deep learning in robotics: a review of recent research // Robotics Society of Japan. 2017.

Pike R.J. Some Preliminary Interpretations of Lunar Mass Wasting Processes from Apollo 10 Photography // NASA Tech Rep. 1971. SP-232.

Piquette M., Horanyi M., Stern S.A. Laboratory Experiments to investigate sublimation rates of Water Ice in nighttime lunar Regolith // Icarus. 2017. 293.

Pitcher C., Koemle N., Leibniz O., Morales-Calderon O., Gao Y., Richter L. Investigation of the Properties of Icy lunar polar Regolith Simulants // Advances in Space Research. 2016. 57.

Polanskey C.A., Ahrens T.J. Impact Spallation Experiments: Fracture Patterns and Spall Velocities // Icarus. 1990. 87.

Popescu M.E. A suggested Method for Reporting Landslide Causes // Bull. of the Int. Ass. of Eng. Geol. 1994. 50.

Potts N.J., Gullikson A.L., Curran N.M., Dhaliwal J.K., Leader M.K., Rege R.N., Kring D.A. Robotic Traverse and Sample Return Strategies for a lunar Farside Mission to the Schroedinger Basin // Advances in Space Research. 2015. 55.

Povilaitis R.Z., Robinson M.S., Bogert C.H. van der, Hiesinger H., Meyer H.M., Ostrach L.R. Crater Density Differences: exploring regional Resurfacing, Crater Populations, and Crater Saturation Equilibrium on the Moon // Planet. Space Sci. 2017.

Prakash N., Manconi A., Loew S. Mapping landslides with a generalized convolutional neural network // Earth ArXiv. 2021.

Raack J., Reiss D., Appere T., Vincendon M., Ruesch O., Hiesinger H. Present-day seasonal Gully Activity in a South Polar Pit (Sysiphi Cavi), Mars // Icarus. 2015. 251.

Ravi S., Mahanti P., Meyer H., Robinson M.S. On the Usefulness of optical Maturity for relative Age Classification of fresh Craters // Am. Geophys. Union Fall Meeting. 2016. PS3A.

Raymond C.A., Ermakov A.I., Castillo-Rogez J.C., Marchi S., al. et. Impact-driven mobilization of deep crustal brines on dwarf planet Ceres // Nature Astronomy. 2020. 4, 741-747.

Ren S., He K., Girshick R., Sun J. Faster R-CNN: Towards Real-Time Object Detection with Region Proposal Networks // Advances in Neural Information Processing Systems. 2015.

Robbins S.J. A new global Database of lunar Impact Craters >1-2 km: Crater Locations and Sizes, Comparisons with published databases, and global Analysis // Journal of Geophysical Research: Planets. 2018. 124.

Roberts G.P., Matthews B., Bristow C., Guerrieri L., Vetterlein J. Possible evidence of paleomarsquakes from fallen boulder populations, Cerberus Fossae, Mars // Journal of Geophysical Research: Planets. 2012. 117.

Robinson M.S. ShadowCam: Seeing in the Shadows // Lunar Polar Volatiles Conf. 2018.

Robinson M.S., Brylow S.M., Tschimmel M., Humm D., NAC team the. Lunar Reconnaissance Orbiter Camera (LROC) Instrument Overview // Space Science Review. 2010. 150.

Rothe R., Guillaumin M., Gool L. van. Non-Maximum Suppression for Object Detection by Passing Messages between Windows // Proc. Asian Conf. Comput. Vision. 2014.

Russakovsky O., Deng J., Su H., Krause J., Satheesh S., Ma S., Huang Z., Karpathy A., Khosla A., Bernstein M., Berg A., Fei-Fei L. ImageNet Large Scale Visual Recognition Challenge // International Journal of Computer Vision. dec 2015. 115, 3. 211–252.

Russell P., Thomas N., Byrne S., Herkenhoff K. Seasonally active frost-dust avalanches on a north polar scarp of Mars captured by HiRISE // Geophysical Research Letters. 2008. 35.

Ryder G. The Moon // Rev. Geophys. 1987. 25.

Sanders G.B., Larson W.E. Progress made in lunar in Situ resource Utilization under NASA's Exploration Technology and Development Program // Jour. of Aerosp. Eng. 2013. 26.

Saran S., Sud V., Handa S. Bearing Capacity of Footings adjacent to Slopes // Jour. of Geotech. Eng. 1989. 115.

Sargeant H.M., Bickel V.T., Honniball C.I., Martinez S.N., Rogaski A., Bell S.K., Czaplinski E.C., Farrant B.E., Harrington E.M., Tolometti G.D., Kring D.A. Using Boulder Tracks as a Tool to Understand the Bearing Capacity of Permanently Shadowed Regions of the Moon // JGR: Planets. 2020. 125.

Sato H., Robinson M.S., Lawrence S.J., Denevi B.W., Hapke B., Jolliff B.L., Hiesinger H. Lunar Mare Tio2 Abundances estimated from UV/Vis Reflectance // Icarus. 2017. 296.

Scaioni M., Yordanov V., Brunetti M.T., Melis M.T., Zinzi A., Kang Z., Giommi P. Recognition of Landslides in lunar Impact Craters // Eur. Jour. Remote Sens. 2018. 51.

Schmidt F., Andrieu F., Costard F., Kocifaj M., Meresecsu A.G. Formation of Recurring Slope Lineae on Mars by rarefied gas-triggered granular Flows // Nature Geoscience. 2017. 10.

Scholten F., Oberst J., Matz K.D., Roatsch T., Waehlisch M., Speyerer E., Robinson M. GLD 100: The near-global lunar 100 raster DTM from LROC WAC stereo image data // Journal of Geophysical Research: Planets. 2012. 117.

Schorghofer N., Aharonson O., Gerstell M.F., Tatsumi L. Three Decades of Slope Streak Activity on Mars // Icarus. 2007. 191.

Schorghofer N., Aharonson O., Khatiwala S. Slope Streaks on Mars: Correlations with Surface Properties and the potential Role of Water // Geophys. Res. Letters. 2002. 29.

Schorghofer N., Taylor G.J. Subsurface Migration of H2O at lunar cold Traps // Journal of Geophysical Research. 2007. 112.

Schultz P.H., Hermalyn B., Colaprete A., Ennico K., Shirley M., Marshall W.S. The LCROSS cratering Experiment // Science. 2010. 330.

Scott R., Carrier W.D., Costes N., Mitchell J.K. Apollo 12 Soil Mechanics Investigation // Geotechnique. 1971. 21.

Shean D.E., Alexandrov O., Moratto Z., Smith B.E., Joughin I.R., Porter C., Morin P. An automated, open-source Pipeline for Mass Production of Digital Elevation Models (DEMs) from very-high-resolution commercial stereo satellite imagery // ISPRS. 2016. 116.

Shields D., Chandler N., Garnier J. Bearing Capacity of Foundations in Slopes // Jour. Geotech. Eng. 1990. 116.

Shill S., Hoque M. Comparison of Bearing Capacity Calculation Methods in designing shallow Foundations // Gazipur. 2015.

Shoemaker E.M., Gault D.E., Moore H.J., Lugn R.V. Hypervelocity Impact of Steel into Coconino Sandstone // Am. Journ. Sci. 1963. 261.

Shuratov Y.G., Bondarenko N.V. Regolith Layer Thickness Mapping of the Moon by Radar and optical Data // Icarus. 2001. 149.

Sidle R.C., Ochiai H. Landslides: Processes, Prediction, and Land Use // AGU. 2006. 18.

Siegler M., Keane J.T., Paige D.A. Subsurface Ice Stability on the Moon // Lunar Polar Volatiles Conf. 2018.

Siegler M., Paige D., Williams J.P., Bills B. Evolution of lunar polar Ice Stability // Icarus. 2015. 255.

Sierks H., Keller H.U., Jaumann R., Michalik H., FC team T. Behnke ans the. The Dawn Framing Camera // Space Science Reviews. 2011. 163.

Singh K.R. ESRI object detection challenge 2019 // GitHub. 2019.

Slyuta E. Physical and mechanical Properties of the lunar Soil (a Review) // Solar System Research. 2014. 48.

Space Room. Resource Prospector - A lunar Pathfinder // Room Space. n.d.

SpaceBok . The SpaceBok Project // ETHZ. 2017.

Spectrum IEEE. Forgotten soviet Rover beams Light back to Earth // IEEE Spectrum. 2010.

Speyerer E., Lawrence J., Stopar J.D., Glaeser P., Robinson M.S., Jolliff B.L. Optimized Traverse Planning for Future Polar Prospectors based on lunar Topography // Icarus. 2016. 273.

Spudis P., Bussey D., Baloga S., Cahill J., Glaze L., Patterson G. Evidence for Water Ice on the Moon: Results for anomalous polar Craters from the LRO Mini-RF imaging Radar // Journal of Geophysical Research: Planets. 2013a. 66.

Spudis P.D., McGovern P.J., Kiefer W. Large Shield Volcanoes on the Moon // Journal of Geophysical Research: Planets. 2013b. 118.

Steenstra E.S., Martin D.J., McDonald F.E., Paisarnsombat S., Venturino C., O'Hara S., Kring D.A. Analyses of robotic Traverses and Sample Sites in the Schroedinger Basin for the HERACLES human-assisted Sample Return Mission Concept // Advanced in Space Research. 2016. 58.

Stillman D.E., Bue B.D., Wagstaff K.L., Primm K.M., Michaels T.I., Grimm R.E. Evaluation of wet and dry recurring Slope Lineae (RSL) Formation Mechanisms based on quantitative Mapping of RSL in Garni Crater, Valles Marineris, Mars // Icarus. 2019. 335.

Strangway D., Pearce G., Olhoeft G. Magnetic and dielectric Properties of lunar Samples // In A.P. Vinogradov (Ed.). 1975.

Taylor J., Teanby N.A., Wookey J. Estimates of seismic Activity in the Cerberus Fossae Region of Mars // Journal of Geophysical Research: Planets. 2013. 118.

Tera F., Papanastassiou D.A., Wasserburg G.J. Isotopic Evidence for a terminal lunar Cataclysm // Earth Plan. Sci. Letters. 1974. 22.

Terzaghi K. Theoretical Soil Mechanics // Chapman and Hall Limited. 1951.

Tesson P.-A., Conway S.J., Mangold N., Ciazela J., Lewis S.R., Megea D. Evidence for thermal-stress-induced rockfalls on Mars impact crater slopes // Icarus. 2020. 342.

Thingiverse . Mars Curiosity Rover Wheel Assembly // Thingiverse. 2014.

Thompson T.J., Robinson M.S., Watters T.R., Johnson M.B. Global lunar Wrinkle Ridge Identification and Analysis // Lunar and Planetary Science Conference. 2017. 48.

Thor R.N., Kallenbach R., Christensen U.R:, Glaeser P., Stark A., Steinbruegge G., Oberst J. Determination of the lunar Body Tide by global Laser Altimetry Data // Journal of Geodesy. 2020.

Titley A. Seismic Energy as an Agent of morphologic Modification on the Moon // Astrogeologic Studies - Lun. and Plan. Inv. Ann. Prog. Rep. 1966.

Trask N.J., John E. Preliminary geologic Terrain Map of Mercury // Journal of Geophysical Research: Planets. 1975. 80.

Tubiana C., Guettler C., Kovacs G., Bertini I., Bodewits D., OSIRIS team the. Scientific assessment of the quality of OSIRIS images // Astronomy and Astrophysics. 2015. 583.

USGS . Lunar 5M Geologic Map Renovation // USGS. 2013.

USGS . Apollo Metric Camera // USGS. n.d.

USRA LPI. Lunar Orbiter Details // LPI. n.d.

Uijlings J.R.R, Sande K.E.A. van da, Gevers T., Smeulders A.W.M. Selective Search for Object Recognition // Int. Jour. Comp. Vision. 2013. 104.

Valantinas A., Schultz P.H. The Origin of Neotectonics on the lunar Nearside // Geology. 2020. 48.

Vesic A.S. Analysis of ultimate Loads of shallow Foundations // Jour. of Soil Mech. and Found. Div. 1973. 99.

WAC LRO. LRO WAC // LROC. n.d.

Wagner R.V., Speyerer E., Robinson M.S. New mosaicked Data Products from the LROC Team // Lunar and Planetary Science Conference. 2015. 46.

Wang X., Cai Z., Gao D., Vasconcelos N. Towards Universal Object Detection by Domain Attention // IEEE Conference on Computer Vision and Pattern Recognition. 2019.

Warren T., King O., Bowles N., Sefton-Nash E., Fisackerly R., Trautner R. The Oxford 3D thermophysical Model with Application to PROSPECT on the Luna-27 lunar Lander Mission // European Lunar Symposium. 2019.

Wasson J.T., Boynton W.V., Kallemeyn G.W., Sundberg L.L., Wai C.M. Volatile Compounds released during the lunar Lava Fountaining // Lunar Science Conference. 1976. 7.

Watson K., Murray B., Brown H. On the possible Presence of Ice on the Moon // Journal of Geophysical Research. 1961. 66.

Watters T.R., Robinson M.S., Beyer R.A., Banks M.E., Bell J.F., Pritchard M.E., Hiesinger H., Bogert C.H. van der, Thomas P.C., Turtle E.P., Williams N.R. Evidence of recent Thrust Faulting on the Moon revealed by the Lunar Reconnaissance Orbiter Camera // Science. 2010. 20.

Watters T.R., Weber R.C., Collins G.C., Howley I.J., Schmerr N.C., Johnson C.L. Shallow seismic Activity and young Thrust Faults on the Moon // Nature Geoscience. 2019. 12.

Weinstein B.G., Marconi S., Bohlman S., Zare A., White E. Individual Tree-Crown Detection in RGB Imagery Using Semi-Supervised Deep Learning Neural Networks // Remote Sensing. 2019.

Williams D.A., Jaumann R., McSween H.Y., Marchi S., Schmedemann N., Raymond C.A., Russell C.T. The chronostratigraphy of Protoplanet Vesta // Icarus. 2014. 244.

Williams J.P., Paige D., Greenhagen B., Sefton-Nash E. The global Surface Temperatures of the Moon as measured by the Diviner Lunar Radiometer Experiment // Icarus. 2017. 283.

Winkler E. Die Lehre von der Elastizitaet und Festigkeit mit besonderer Ruecksicht auf ihre Anwendung in der Technik // Verlag Dominicus. 1867.

Witze A. Meteorites pummel the Moon far more than expected // Nature News. 2018.

Wright J., Conway S.J., Morino C., Rothery D.A., Balme M.R., Fassett C.I. Modification of Caloris ejecta blocks by long-lived mass-wasting: A volatile-driven process? // Earth and Planetary Science Letters. 2020. 549.

Xiao Z., Zeng Z., Ding N., Molaro J. Mass wasting features on the Moon - how active is the lunar surface? // Earth and Planetary Science Letters. 2013. 376. 1–11.

Zhang J.A., Paige D.A. Cold-trapped organic Compounds at the Poles of the Moon and Mercury: Implications for Origins // Geophysical Research Letters. 2009. 36.

Zhang J.A., Paige D.A. Correction to: Cold-trapped organic Compounds at the Poles of the Moon and Mercury: Implications for Origins // Geophysical Research Letters. 2010. 37.

Appendix A

Supplementary Information

A.1 Using Boulder Tracks as a Tool to understand the Bearing Capacity of Permanently Shadowed Regions of the Moon

Published 2020 in the Journal of Geophysical Research: Planets
Sargeant, H.M., Bickel, V.T., Honniball, C.I., Martinez, S.N., Rogaski, A., Bell, S.K., Czaplinski, E.C., Farrant, B.E., Harrington, E.M., Tolometti, G.D., Kring, D.A., 2020
Contributions: study site selection, image and elevation model processing, implementation of bearing capacity equations, analysis and discussion of results, manuscript writing and revision.
https://doi.org/10.1029/2019JE006157

Abstract
Permanently shadowed regions (PSRs) are abundant at the lunar poles. They experience no direct sunlight and reach temperatures as low as 30 K. PSRs are of interest as evidence suggests that some may contain water ice (H_2O/OH-), which could provide a record of the evolution of volatiles in the inner solar system. This water ice is also a critical resource for life support systems and rocket propellant. A better understanding of mechanical properties of PSR regolith, such as its bearing capacity, will help optimize the design of future exploration rovers and landers. Thirteen boulder tracks were identified on the edge of, or inside, south polar lunar PSR enhanced imagery and used to estimate the strength of the PSR regolith at latitudes of 70° to 76° in sites with maximum annual temperatures of 65 to 210 K. PSR boulder track features are similar to those observed in highland, mare, and pyroclastic regions of the Moon, implying similar properties of the regolith. Measured features were used to estimate bearing capacity for PSR regolith at depths of ∼0.28 to 4.68 m. Estimated bearing capacity values suggest that these PSRs may be somewhat stronger than highland and mare regions at depths of 0.28 to 1.00 m. Bearing capacity in these PSRs is statistically the same as those in other regions of the Moon at depths of 1.00 to 2.00 m. The results of this study can be used to infer bearing capacity as one measure for the trafficability of lower-latitude PSRs of the type measured here.

Introduction

The International Space Exploration Coordination Group (ISECG) Global Exploration Roadmap outlines the shared goals of the ISECG space agencies to expand human presence in low Earth orbit, to the Moon, and finally to Mars. A critical step in achieving these goals is continued exploration of the Moon and identifying and harvesting its available resources. Of particular interest in this endeavor are the permanently shadowed regions (PSRs) at the lunar poles. These regions are considerably colder than the rest of the lunar surface, reaching temperatures below 30 K (Paige et al., 2010). As a result, it has been theorized that these PSRs could trap and accumulate stable water ice, as well as other volatiles, and retain them for hundreds of millions of years (Siegler et al., 2018; Watson et al., 1961). Indirect evidence and more recent direct evidence support these findings using data from the Lunar Crater Observation and Sensing Satellite (LCROSS) lunar impactor and the Moon Mineralogy Mapper, respectively (Colaprete et al., 2010; Li et al.,

2018). These volatiles have a range of important applications for in situ resource utilization (ISRU), such as life support systems and rocket propellant (Crawford, 2015). PSRs are also a valuable scientific target. The National Research Council outlined and ranked a series of scientific goals that should be considered when planning missions to the Moon (NRC, 2007). A future mission to a PSR would primarily address goals 4a, 4d, 7b, 7c, and 7d. These objectives pertain to the presence and behavior of volatiles on the Moon and the qualities of the regolith in which they reside. A robotic or human mission taking in situ measurements will be required to confirm volatile concentrations in the PSRs and assess the utility of any deposits for ISRU.

The success of a robotic mission is dependent on the ability of a rover to traverse the terrain. Thus, before planning a mission to a PSR, it is necessary to better understand the mechanical behavior of the regolith within these areas. Issues regarding extreme temperature lows, lack of solar energy, and static discharge (Jackson et al., 2011) in these regions are just a few of many concerns. Of particular concern for engineers is the soil behavior of the regolith in PSRs. The porosity of the regolith would influence the strength of the terrain and, thus, affect rover mobility. The porosity of PSR regolith has been inferred from the results of the LCROSS impactor where the resulting ejecta angles and flashes indicated highly porous material of ∼70% to equivalent depths of 2 to 3 m (Schultz et al., 2010). Meanwhile, far ultraviolet (FUV) reflectance properties of lunar PSRs showed FUV darkness, which could be a consequence of higher porosity, ∼70%, in the surface soil compared to regions outside PSRs with porosities of ∼40% (Gladstone et al., 2012). LRO Diviner indicates low thermal inertia values in the lunar high latitude regions, which suggest that the upper few centimeters of regolith are likely highly porous (Hayne et al., 2015). Laboratory studies have also shown that low thermal cycling in PSRs could result in higher porosity regolith (Metzger et al., 2018). As a result of these studies, one could assume that PSRs would be more difficult to traverse. If rovers and landers experience more sinkage into the regolith, becoming stuck could mean the end of a mission.

As it stands, the physical properties of the regolith in lunar polar PSRs are relatively unknown as there have been no in situ measurements taken to date. Experiments on lunar soil simulants have provided estimates of how the presence of water ice increases the soil strength (Gertsch et al., 2006; Pitcher et al., 2016). Gertsch et al. (2006) found that increasing water ice content in the simulant resulted in a stronger material, behaving like weak shale or mudstone at only 0.6% to 1.5% ice content. Similarly, the strength of icy rock has been studied and shown to be stronger than dry rock at equivalent temperatures (Atkinson et al., 2018). However, this experimental work did not provide estimates of trafficability. The following work will represent the first comprehensive study of trafficability in PSR regolith using data derived directly from lunar surface features.

Methods

This study investigates the geomechanical properties of regolith within and on the edge of south polar lunar PSRs using rockfalls and their associated boulder tracks, both of which are abundant on the Moon (Bickel et al., 2019; Kumar et al., 2016). A south polar PSR map generated by McGovern et al. (2013) was used to select images, taken by the Narrow Angle Camera (NAC) on board the Lunar Reconnaissance Orbiter (LRO), of PSRs that may host a rockfall. South polar images were processed to enhance the visibility of features within the PSRs so that boulders and their tracks could be measured. Those measured values were then used to estimate bearing capacities using the methodology of Bickel et al. (2019).

2.1 Image Processing and Digital Elevation Model Processing

It is not immediately evident that boulders and boulder tracks can be discerned within shadowed regions. However, we discovered that features within PSRs can be observed using secondary light diffusely scattered from an illuminated portion of a crater containing a PSR. Adjusting the brightness and contrast of Lunar Reconnaissance Orbiter Camera (LROC) NAC images, followed by image filtering, illuminates those features sufficiently well to be measured. Image filtering is necessary because raw NAC images are affected by semisystematic vertical and horizontal stripes as well as white noise. The noise was exasperated by contrast enhancement and greatly impedes accurate measurements of boulder tracks within these areas. To suppress or remove the noise content, two separate filtering methods were implemented. We outline those methods here, while referring readers to detailed workflows and filtering information in Figure A.62 and Table A.16 and Table A.17 in the supporting information. A total of 33 LROC NAC images were downloaded and processed by either of the following methods.

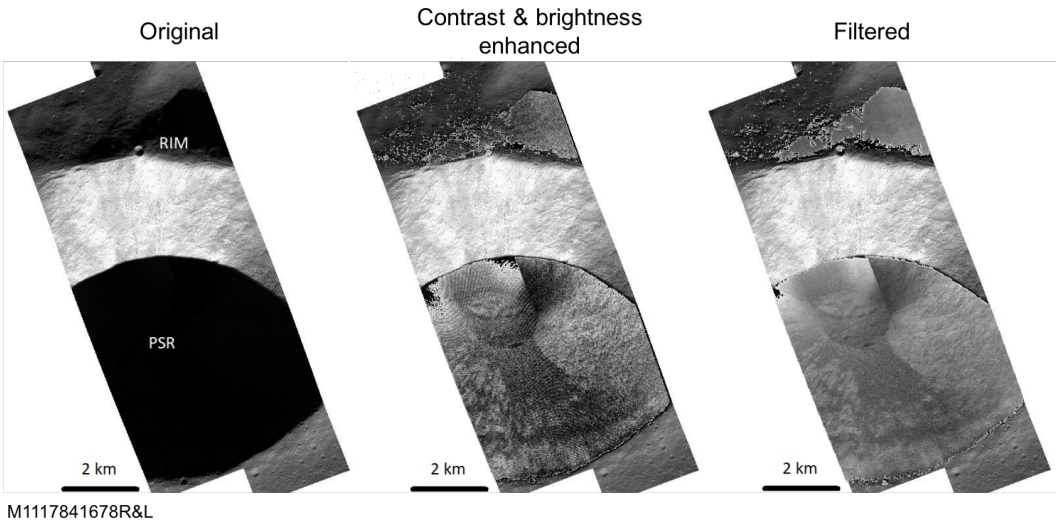


Figure A.1: (left) Lunar Reconnaissance Orbiter (LRO) Narrow Angle Camera (NAC) images M1117841678RE/LE contain a crater that hosts a permanently shadowed region (PSR) that is receiving a small amount of secondary sunlight being bounced from crater walls. (Middle) By altering the brightness and contrast, features within the PSR became visible. (Right) Further filtering in this work resulted in a reduction of image noise.

The first image processing method forced an exaggeration of the dominant vertical noise in echo corrected NAC images using a sliding rectangular kernel. This technique was designed to detect and mask vertical lines with a width of a single pixel. Subsequently, a Standard Hough Transform (SHT) (Hough, 1962) was applied to track the lines in the image and denote their beginning and end by using the SHT matrix. Next, these marked lines were removed from the image, and the resulting gaps in the image were interpolated using the values of the neighboring pixels. To minimize interference between adjacent lines, the filter was only run for lines that were not adjacent to another line. Once the lines were removed and interpolated, the filter was run again. This process was repeated for a specified number of times that was dependent on the noise level in the image. The resulting images were further refined with a two pass 2 D median filter using a 3 x 3 pixel kernel to suppress the remaining white noise content. The filtered images were up sampled using a bicubic interpolation in a 4 x 4 neighborhood to further increase image quality.

The second method was performed in ISIS3.5.1 and applied a low pass filter kernel (1x vertical image dimension) to the echo corrected NAC images to calculate a global column average of the images. The resulting low frequency image was then high pass filtered (1x horizontal image dimension), which produced a global albedo suppressed average noise image. This image was then subtracted from the original input. Subsequently, a standard 2 D median filter within a sliding 3 x 3 pixel kernel was used to suppress the remaining white noise content. Although all applied filter routines were nonaggressive, a small amount of local artifacts were observed (en echelon and cone shaped noise patches), but they did not interfere with the performed measurements. Of these two methods, both filters were used on a case by case basis depending on which method produced a superior view into the PSR. Lastly, all optimized images were warped to a planetocentric polar stereographic projection and translated and exported for utilization in ArcGIS10.1. An example of a raw NAC image of a PSR and the resultant filtered image is shown in Figure A.1. Depending on local illumination conditions and spatial resolution of a NAC raw image, the quality of the filtered products was sufficient to produce digital elevation models (DEMs) within PSRs with spatial resolutions of 2 to 3 m/pixel using the Ames Stereo Pipeline (Shean et al., 2016). Details about the produced DEMs can be found in Table A.18.

2.2 Identifying Boulder Tracks

In order to see boulder tracks within a PSR, there must be some secondary illumination of the PSR when the NAC images were obtained. At latitudes ~70° to 76°, there is sufficient secondary illumination of craters so that processing of the high resolution LRO NAC images (~0.5 m/pixel) reveals boulders and their associated tracks within the PSRs (Figure A.2). Although higher latitude PSRs have been

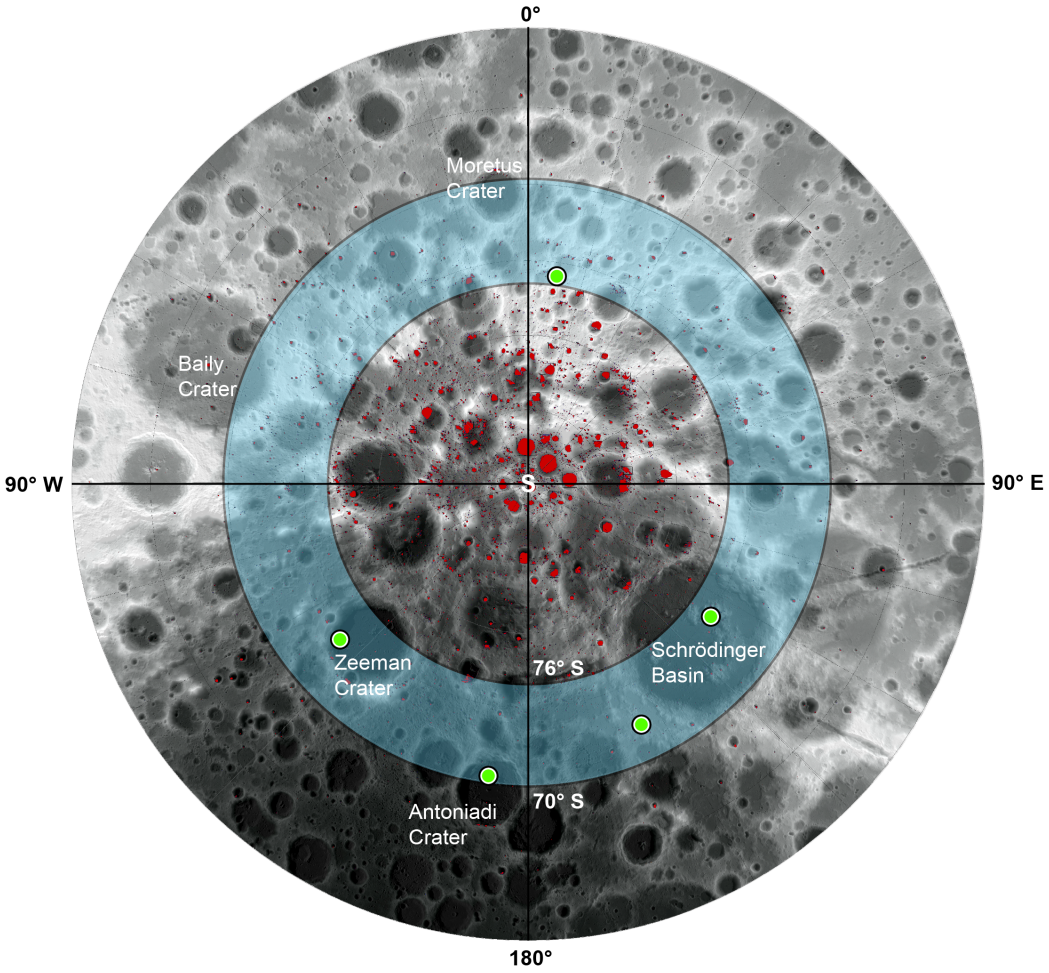


Figure A.2: A south polar view of the Moon with permanently shadowed regions (PSRs) highlighted in red (per McGovern et al. (2013)) and the location of identified PSR boulder tracks in green. The blue band area represents the region where boulder tracks were observed in PSRs, located between ∼70° and 76° latitude, that is, the region where secondary illumination and image processing still allow to use NAC images without compromising spatial resolution.

imaged (Haruyama et al., 2008) using data from Selene's Terrain Camera and Multispectral Imager, both those instruments have spatial resolution well below that of LRO's NAC. For example, the Terrain Camera imagery used to view the floor of Shackleton crater had a resolution of 10 by 10 m, far too coarse to measure boulder shape, boulder track width, and boulder track depth. A complete survey of that geographic band was performed so that all measurable boulder tracks were identified. All boulders identified as "in shadow" in NAC images were then compared to the PSR map produced by McGovern et al. (2013), derived from ray tracing techniques applied to a topographic data set from the LRO, to confirm that the boulders lie within a PSR or on a boundary. Ultimately 11 boulder tracks were measured inside PSRs, with two boulder tracks being identified as seasonally shadowed regions, SSRs (Kloos et al., 2019). In this work, SSRs are defined as areas of shadow, which are extensions of PSR shadows, but do not fall within the PSR boundaries identified by McGovern et al. (2013). An example of a boulder track identified inside a PSR is shown in Figure A.3. We recognize that secondary illumination has been mapped in PSRs closer to the pole (Cisneros et al., 2017; Koeber, Robinson, 2013; Koeber et al., 2014); however, the spatial resolution of the images has to be artificially reduced to account for the blurring introduced by the satellite's motion in combination with longer camera exposure times. Consequently, this method would not be suitable for higher latitude PSRs with current orbital imagers.

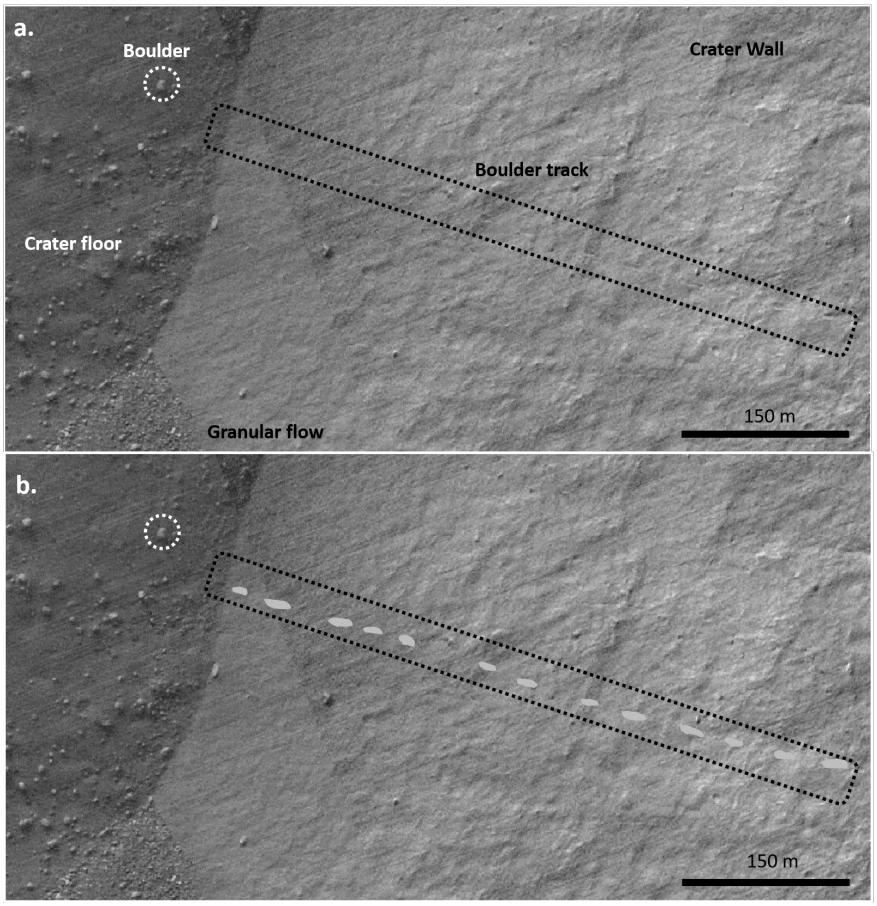


Figure A.3: An example of a boulder track and boulder identified in a permanently shadowed region. The entire image is inside a permanently shadowed region that covers the crater floor and wall. The image is a detail of a filtered Narrow Angle Camera (NAC) image M1117841678R inside an unnamed crater at latitude -72.219° and longitude 154.671°. Image (a) shows the unmarked track, and image (b) shows the highlighted track.

Calculating Bearing Capacity

Measurements of the boulders and their associated tracks are used to estimate ultimate bearing capacity. Bickel et al. (2019) compared two methods for estimating ultimate bearing capacity based on work by Terzaghi (Terzaghi, 1951) and Hansen (Hansen, 1970). An analytical solution provided by Hansen (Hansen, 1970) for shallow foundations provides a better and more realistic estimate of bearing capacity, because it allows for the adaptation of the bearing capacity estimation to the local slope and boulder shape (Bickel et al., 2019). Here we apply the Hansen (Hansen, 1970) equation for bearing capacity, q_f, with the same assumptions used by Bickel et al. (2019) for other regions of the Moon:

$$q_f = cN_c s_c d_c i_c b_c g_c + q_0 N_q s_q d_q i_q b_q g_q + 0.5\gamma B_H N_\gamma s_\gamma d_\gamma i_\gamma b_\gamma g_\gamma \tag{A.1}$$

where c is the cohesion of the soil; q_0 is the vertical stress within the soil; γ is the unit weight of the soil; B is the width of footing; N(c,q,γ) are the bearing capacity factors, which are derived from the angle of internal friction, ϕ; and d(c,q,γ) are the depth factors, s(c,q,γ) are the shape factors, g(c,q,γ) are the local slope inclination factors, and i(c,q,γ) and b(c,q,γ) are the load and foundation inclination factors, respectively. The unit weight of the soil is defined as $\rho * g$, where ρ is the density of the soil and g is the gravity of the Moon. For a detailed explanation of the Hansen (Hansen, 1970) equation and its assumptions, see Bickel et al. (2019).

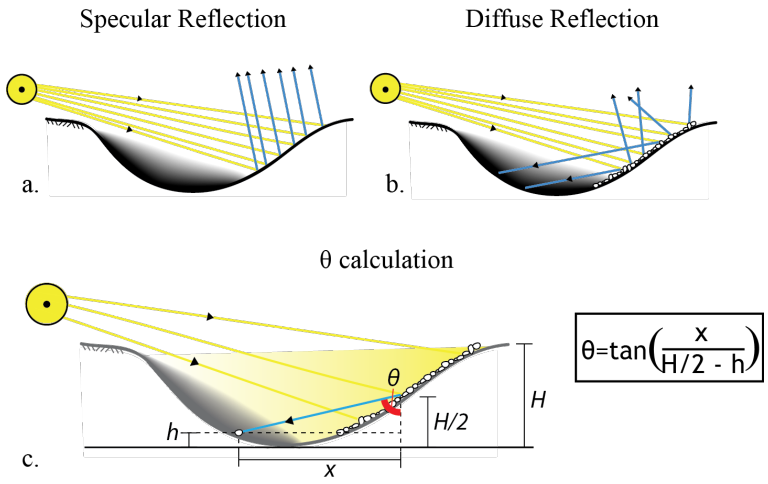


Figure A.4: (a) Schematic showing specular reflection from an illuminated crater wall. (b) Schematic showing diffuse reflection from an illuminated crater wall, likely caused by large scale roughness such as boulders and by small scale roughness of the regolith itself. (c) Schematic of the determination of the effective incidence angle θ as a result of diffuse reflection.

Density, cohesion, and internal friction angle are essential properties for understanding the behavior of the lunar regolith. These properties have been estimated through several studies; however, the values are highly varied in literature (Carrier et al., 1991; Mitchell et al., 1972a). Calculated bearing capacities in other works vary depending on the values pulled from the literature (Hovland, Mitchell, 1969b, 1973; Mitchell et al., 1973; Moore, 1970). Using the same conservative assumptions as Bickel et al. (2019), a cohesion value of 1 kPa (Mitchell et al., 1972a) was used for this work. As in situ measurements have yet to be taken for PSRs, highland bulk density values of 1.39 and 1.66 g/cm^3 were applied for shallow (<30 cm) and deep (>30 cm) PSR soil, respectively (Mitchell et al., 1972b), as PSRs occur in highland terranes with feldspathic composition and relatively low iron abundances (Lawrence et al., 2002; Spudis et al., 2013a). The angle of internal friction (29°) was estimated from granular flow features at their static angle of repose on slopes within PSRs evaluated with high resolution DEMs. For details on the production of those DEMs from filtered NAC images, see Table A.18; for details about the determination of the static angle of repose, see Bickel et al. (2019).

Measurements

From the 33 NAC images that were processed, a total of 13 boulder tracks were identified in or on the edge of 5 PSRs that were found to be suitable for measurements needed to calculate the ultimate bearing capacity q_f (see Table A.19). Measurements were made on the long L and short B diameters of the boulder, the width of the associated track W, the length of shadows cast within the track S, and the local slope α. All measurements were made near the boulder responsible for the track (subscript b) and near the beginning of the track (subscript s). Taking measurements at the start and end of the track allowed for the approximation of a static system, as the boulders will have little kinetic energy (Bickel et al., 2019). Thus, in general, each track produced two data points for analysis.

The width and shadow length measurements were repeated three times for each of the individual tracks whenever possible in order to calculate an average and to minimize the influence of variations in track appearance, a consequence of irregular boulder shapes forming tracks of changing widths. Shadow length and track width measurements were performed in the same area of the boulder track. Accurate measurements of the shadow length required determination of the illumination direction; the measurement was then made parallel to that direction. The measurement was most accurate when the shadow length was perpendicular to the track (Bickel et al., 2019).

Generally, the depth of a boulder track D was derived from the shadow length L and the incidence angle i

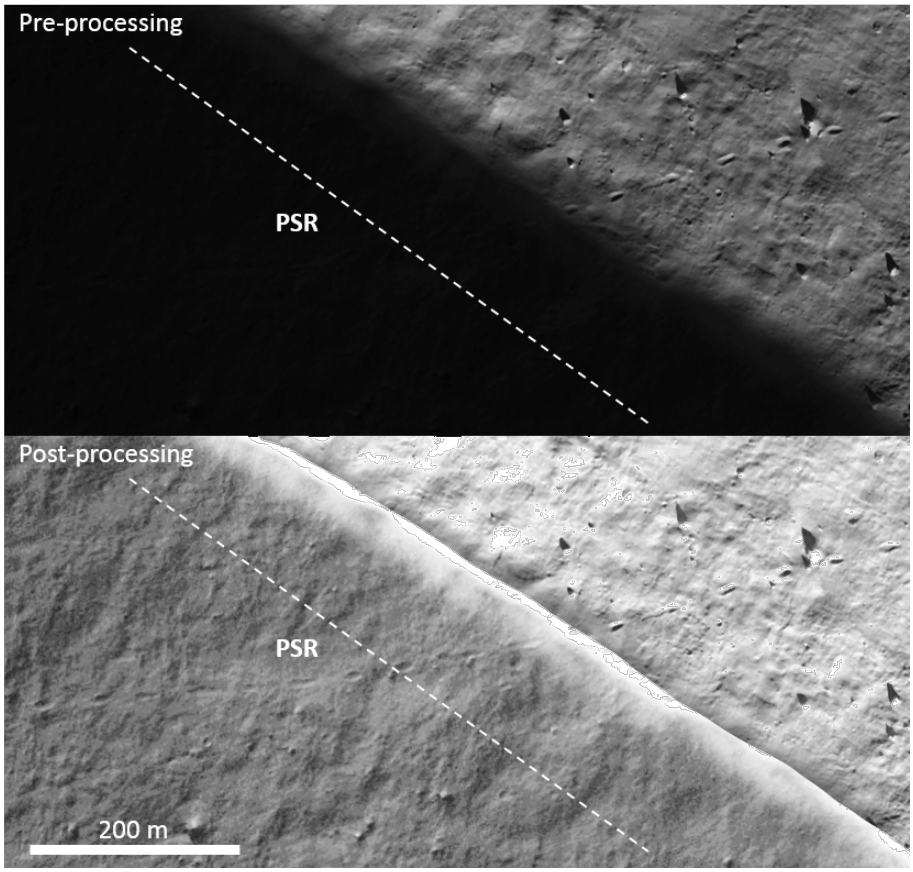


Figure A.5: Example boulder track which crosses the boundary from outside to inside a permanently shadowed region (PSR) as identified in a detail of image M1117841678LE/RE. Image processing allowed the identification of the track within the shadowed region. The PSR boundary is defined by McGovern et al. (2013). No obvious changes to track morphology were identified as the track enters the PSR.

of the Sun where

$$D = L\tan(i) \tag{A.2}$$

Determining the track depth in a PSR is challenging as the incidence angle of sunlight is not directly responsible for the length of shadows; instead, the shadow is produced from light reflected from an illuminated face of a crater. If specular reflection was wholly occurring (Figure A.4a), sunlight should be reflected out of the crater. As some sunlight is clearly being reflected into the PSR, diffuse reflection is occurring (Figure A.4b), likely as a result of surface roughness on these slopes. Assuming that diffuse reflection results in a broad beam of light from the illuminated crater wall into the PSR, the effective incidence angle θ can be derived (Figure A.4c). The illumination source was taken as the midpoint of the illuminated section of the crater wall H/2, which was derived from a 100 m resolution LRO Wide Angle Camera (WAC) stereo derived DEM. Using the elevation difference between this reflecting surface and the location of the boulder h, as well as the horizontal distance between these points x, the effective incidence angle can be calculated:

$$\theta = \tan\left(\frac{x}{\left(\frac{H}{2} - h\right)}\right) \tag{A.3}$$

The boulder track depth D in PSRs can therefore be calculated as follows:

$$D = L\tan(\theta) \tag{A.4}$$

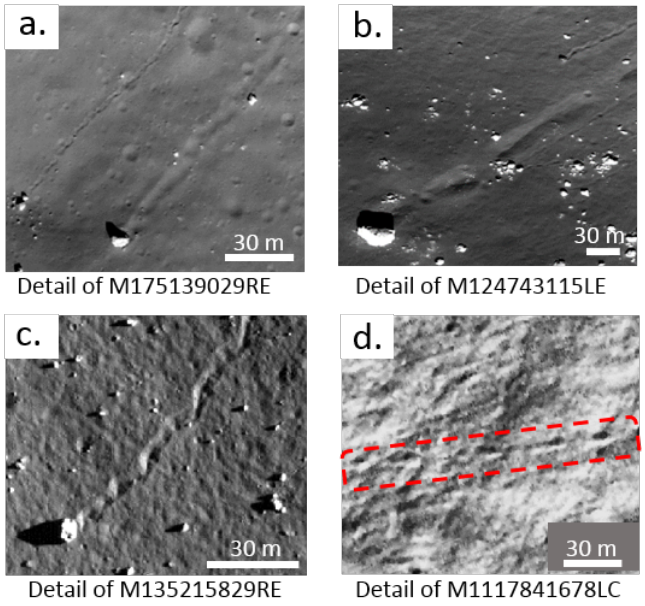


Figure A.6: Example boulder tracks as seen in (a) highland regions, (b) mare regions, (c) pyroclastic regions, and (d) permanently shadowed regions. The highland, mare, and pyroclastic images were taken from Bickel et al. (2019). A qualitative analysis of these tracks shows that there is no significant difference in mechanical properties of permanently shadowed region regolith compared to the other regions considered; that is, the boulders do not sink particularly deeply into the regolith.

Results

We began with a qualitative study of PSR boulder tracks in NAC images. Boulder tracks that crossed the boundary from sunlit regions into PSRs (e.g., M1117841678LE/RE) show no significant difference in track morphology, suggesting similar geomechanical properties (Figure A.5). Additionally, when compared to the tracks identified by Bickel et al. (2019) in highland, mare, and pyroclastic regions (Figure A.6), the tracks do not show any significant difference in morphology. Boulders rolling into PSRs penetrate sufficiently deep to leave measurable tracks but do not completely sink into the regolith as might be expected if the regolith was unusually porous and weak. If there is a large density contrast between sunlit and PSRs, then the track size would be significantly different. Yet no difference is observed. Once all measurements were obtained, Hansen's bearing capacity formula (Equation A.1) was applied. Estimated bearing capacity values for each terrane (PSRs, highland, mare, and pyroclastics) were plotted with respect to the slope angle where the measurements were taken. The data are presented as distinct ranges for depth of track ($\leq$1 m, 1 to 2 m, and 2 to 6 m) comparable to those of Bickel et al. (2019). A least squares fit was applied with a shaded error bar derived from an estimate of the standard deviation of the error (Figure A.7). Potential slope limits are also shown. Bearing capacity tends to decrease as the slope angle increases, a result of the reduced soil volume bearing the boulder (Castelli, Lentini, 2012; Meyerhof, 1957) and potentially a reduction of physical soil strength due to slow downslope movement (Bickel et al., 2019; Carrier et al., 1991). In addition, the bearing capacity is shown to be higher in deeper material, which would be expected as the vertical stress and bearing soil volume increases over depth. Generally all the regions plotted follow a similar trend.

A plot of bearing capacity with depth is shown in Figure A.8 for PSRs compared to highland, mare, and pyroclastic data from Bickel et al. (2019). As in Figure A.7, Figure A.8 also shows that the bearing capacity of the regolith appears to increase with depth, which is consistent with Apollo data (Mitchell et al., 1973). Calculated bearing capacities increase with depth for all terranes, with PSR and pyroclastic regolith being generally somewhat stronger than highland and mare regolith at equivalent depths. However, there also appears to be a lot of scatter in the bearing capacities and overlap of values among terranes, which might be connected to varying slope angles at the respective measurement locations. The trends produced in Figure A.7 were used to estimate bearing capacity for each associated depth range as a function of slope

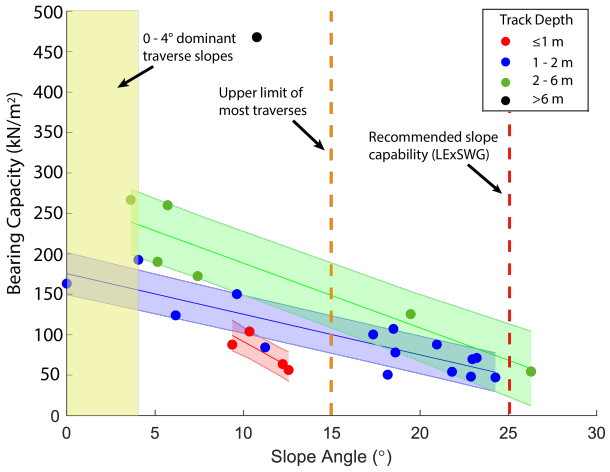


Figure A.7: Estimated bearing capacity values from permanently shadowed regions are shown here as a function of slope angle. The data are separated by the track depth at each measurement (≤1 m, 1-2 m, and 2-6 m) as in Bickel et al. (2019). Slope traverse values are taken from the final report of the Lunar Exploration Science Working Group (LExSWG, 1995).

(Table A.1). The uppermost regolith that has been measured with this technique in PSRs (0.28 to 1.00 m) appears to have higher average bearing capacities than highland and mare material at ≤1 m but ranges overlap. The greatest variability in bearing capacity at shallow depths lies with PSRs, while at greater depths the greatest variability lies with pyroclastics. The data obtained from the boulder tracks in SSRs fit the same trend as those obtained from PSRs, with no noticeable anomalies, indicating that the soil strength properties in the SSRs and PSRs measured at these 70-76° latitude locations are similar.

A statistical analysis of the spread of calculated bearing capacities over depth was performed to determine if there are significant differences between terranes (see Table A.20). A two sample T test assuming unequal variances (two tail) was applied to the calculated PSR values from this work and each data set from highland, mare, and pyroclastic calculations from Bickel et al. (2019) for the ≤1 and 1 to 2 m depth range providing p values based on a 95% confidence interval. The 2 to 6 m depth range could not be considered as there were too few data points for PSRs at this depth. Two analyses were performed, the first considered

Bearing capacity using Hansen's method at a range of slope angles (kN/m^2)					
Location	**Depth of track (m)**	**0°**	**10°**	**20°**	**30°**
PSRs	≤ 1 (n=8)	127 ± 29	84 ± 22	41 ± 24	-
∼	1-2 (n=13)	194 ± 29	134 ± 26	75 ± 26	16 ± 29
∼	2-6 (n=5)	271 ± 63	192 ± 53	112 ± 55	32 ± 68
Highlands	≤ 1 (n=12)	52 ± 14	39 ± 10	25 ± 7	11 ± 7
∼	1-2 (n=17)	166 ± 24	119 ± 21	72 ± 20	24 ± 22
∼	2-6 (n=51)	314 ± 63	228 ± 58	143 ± 57	57 ± 59
Mare	≤ 1 (n=15)	85 ± 12	57 ± 9	29 ± 7	1 ± 9
∼	1-2 (n=30)	167 ± 19	108 ± 18	50 ± 18	-
∼	2-6 (n=35)	276 ± 50	201 ± 47	126 ± 47	51 ± 50
LPD	≤ 1 (n=22)	131 ± 21	86 ± 20	41 ± 20	-
∼	1-2 (n=28)	200 ± 30	144 ± 28	89 ± 28	33 ± 30
∼	2-6 (n=32)	336 ± 79	261 ± 74	186 ± 73	111 ± 78

Table A.1: Estimated bearing capacity values and associated uncertainty (as derived from the distribution of the data) for each location type at the specified depth ranges of ≤ 1 m, 1-2 m, and 2-6 m, and for slope values of 0, 10, 20, and 30°. The highland, mare, and pyroclastic data were obtained from Bickel et al. (2019). Data were omitted where the estimated bearing capacity values fall below 0 kN/m^2 or where a trend line with uncertainty could not be obtained (≤ 3 data points). Due to Hansen's (Hansen, 1970) assumptions, estimated bearing capacity approaches zero when local slope angles approach the angle of internal friction; thus, data are sparse in the 30° bin.

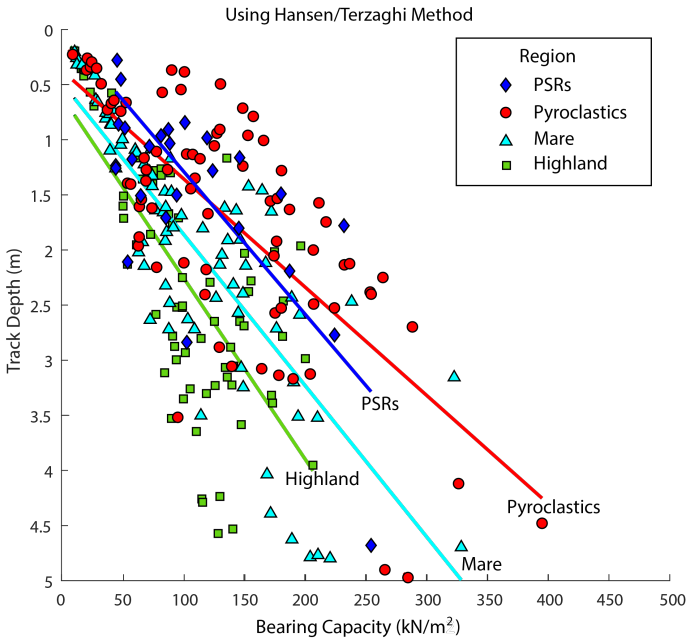


Figure A.8: Estimated bearing capacity values for each terrane are presented as a function of track depth. Linear fits are only indicative (for comparison between the terranes); they do not represent the actual bearing capacity values at shallow depth, as they do not consider slope angle.

all bearing capacity values in the depth range of $\leq$1 and 1 to 2 m across all slope angles. However, as there are no data for relatively shallow slope angles in the $\leq$1 m depth range in the highland and mare regions, a second T test was performed for bearing capacity data that are obtained at slope angles of $>15^\circ$ only for the $\leq$1 m depth range. This allowed for a comparison of shallow data without a bias associated with slope angle dependence. The analysis showed that for all data in the depth range of $\leq$1 m, the estimated bearing capacity in PSRs, as determined by the distribution of data, is statistically similar to lunar pyroclastic deposits, and statistically stronger than both highland and mare regions. However, the analysis performed in the $>15^\circ$ slope angle range indicated that PSRs are statistically stronger than pyroclastic deposits, highland, and mare regolith. Meanwhile, at the depth range of 1 to 2 m, PSRs have statistically similar bearing capacities to pyroclastic deposits, highland, and mare regions when considering all slope angles and slope angles of $>15^\circ$ only. In contrast, there is some indication that the bearing capacity is weaker at greater depths. For example, an estimated value of 271 kN/m^2 at 2 to 6 m in a PSR is lower than 314 kN/m^2 in highlands and 336 kN/m^2 in pyroclastic material at that same depth. We note, however, that there are not sufficient measurements from those depths to be statistically significant. It is important to note that there is considerable variation in any single terrane at all depths.

Discussion

6.1 Likelihood of Ice in Lower Latitude PSRs

Models indicate that water ice will be stable and form on the surface of PSRs at temperatures below ~100 to 112 K (Hayne et al., 2015; Paige et al., 1992; Siegler et al., 2015; Zhang, Paige, 2009, 2010). To understand whether water ice could be present in the PSRs studied here, a maximum (~240 m/pixel) temperature map derived from the Diviner Radiometer data (Williams et al., 2017) was evaluated. The PSRs in this study have maximum surface temperatures of ~65 to 210 K (see Table A.21). Four of the boulders studied in this work, distributed between two PSRs, are found in locations that have temperatures that would be suitable for surficial surface ice to be stable, although it is not observed. The presence of CO_2 ice is unlikely in the PSRs studied here as they require temperatures of $<$55 K to be stable (Hayne et al., 2019; Zhang, Paige, 2009) and, therefore, these "warmer" PSRs may be more desirable targets for those wishing to obtain water ice without CO_2 impurities. A lunar polar ice map derived from Moon Mineralogy Mapper reflectance spectra (Li et al., 2018) suggests that surficial water ice (within a few millimeters of

the surface) is not present at any of the studied boulder locations, suggesting that if ice has formed in the past, it would likely have redistributed deeper as a result of gardening of the upper regolith (Hurley et al., 2012). It should be noted that the PSRs studied here do not represent the PSRs found at higher latitudes that do have evidence to suggest surficial water ice.

The absence of surficial ice does not preclude the presence of subsurface ice. Water can thermally migrate through the regolith where it may remain trapped (Schorghofer, Taylor, 2007). The Oxford 3D Thermophysical Model (Warren et al., 2019) was applied to the PSRs studied in this work to estimate the temperature of the regolith with depth. The model analyzes a grid at each location with 8 ppd in the longitude direction and 16 ppd in the latitude direction. If the maximum temperature below the surface remains below 112 K, it is assumed that stable water ice could be found. The results show that water ice can be found at depths below 0.05 m in one PSR, and below 0.10 m in three further PSRs in this study (see Figure A.5 and Table A.21). The remaining PSR in this study was too small for the Oxford 3D Thermophysical model to be applied without the illuminated regions being included in the analysis. The estimated ice stability depths combined with the bearing capacity data suggest that low latitude PSRs that have the potential to contain buried water are likely traversable. Further work will be needed to assess bearing capacities and, thus, trafficability in the higher latitude, colder PSRs. In situ analyses are also needed to confirm whether water ice is present at such locations and how it is distributed.

6.2 Technique Limitations

It is important to understand the limitations of the measurements and the application of the Hansen (Hansen, 1970) bearing capacity equation, which were discussed in detail in Bickel et al. (2019). A number of assumptions were made when determining the effective incidence angle, θ, of secondary illumination of PSRs, which affects estimated track depths and bearing capacity (see Figure A.64). The uncertainty in θ is not well defined, but to illustrate the consequences of that uncertainty, an error analysis was performed assuming 5° and 10° errors in θ. For depths <6 m, a 5° and 10° uncertainty in θ results in a maximum uncertainty in our calculated bearing capacity values of q_{f-95}^{+107} kN/m^2 and q_{f-51}^{+59} kN/m^2, respectively. The largest impact of an uncertainty in θ occurs when measurements were taken at low slope angles, where the resulting θ is small. This is a consequence of the trigonometric nature of the θ estimations (see Figure A.4c).

Two additional sources of potential uncertainty lie with the track depth estimations. (1) When estimating track depth, a first order approximation was made, which assumes a flat bottomed track. However, boulder tracks are likely to be irregular in shape, particularly as lunar boulders are particularly angular (Bickel et al., 2019; Kumar et al., 2016). As a consequence, the track depth estimations may be shallower than the actual tracks. (2) At very high incidence angles, the rim of boulder tracks might cast a very long shadow that covers a majority of the track. These long shadows do not allow for an estimate of depth at the center of the track as desired, but toward the opposite rim, ultimately resulting in inaccurate track depth estimates. The consequence is a bearing capacity that is associated with a track on average 23% deeper than originally thought.

6.3 Implications for PSR Regolith Processes

Boulder track depths measured in this work range from 0.28 to 4.68 m, and, therefore, the estimated bearing capacity results are only directly applicable in that range. When comparing the measurements reported here in PSRs with those in mare and highland regions (Bickel et al., 2019), the bearing capacities are statistically the same in all regions in the 1 to 2 m depth, which indicates that regolith processes at this depth are unaffected by temperature differences at the surface. The bearing capacities are statistically higher for PSRs at the shallowest depths (≤1 m) as compared to highland and mare regions. Interestingly, the bearing capacities in the PSRs at ≤1 m are similar to those in pyroclastic deposits at equivalent depths. One might posit that extra strength is due to surficial or cohesive intergrain ice present in PSRs. Although remote sensing evidence suggests that there is no surficial water ice, there could be ice at depths of >10 cm as suggested by the Oxford 3D Thermophysical model. Water could have migrated beneath the surface as a consequence of impact bombardment and regolith overturn (Hurley et al., 2012). Providing water has migrated deeply enough into the regolith, perhaps the presence of water ice connects the grains forming a rigid matrix structure. If the PSRs studied in this work do not contain water ice, then an explanation is required for the statistically higher bearing capacity of PSR regolith in the upper meter. The specific location of measurements may be a factor in the increased PSR regolith strength calculated using this method. It is presumed that PSR regolith is porous; however, this study considers boulders and tracks, which are generally located on a slope. Slow downslope movement of regolith over time (Bickel et al., 2019; Carrier et al., 1991) might have resulted in a modified porosity and density of the regolith on the slopes.

These modified properties might vary from those at or closer to the center of PSRs. In situ measurements would be required to understand how representative the bearing capacity results are as compared to other locations within and around PSRs at different latitudes.

If subsurface ice existed at relatively shallow depths when the tracks were produced, the ice may have ablated from the walls of the tracks. Based on studies of boulder tracks elsewhere (Hurwitz, Kring, 2016; Kumar et al., 2016), tracks are obliterated by regolith processes on time scales of 20 to 35 Ma, although icy regolith may result in different track aging rates. Experimental data suggest that ice sublimates from hydrated lunar regolith simulants at a rate of $\leq$2% in 5 days at temperatures of $\sim$100 K (Piquette et al., 2017). Therefore, any ice exposed by the rolling boulders may have ablated before the tracks were observed by LROC.

The dimensions of the boulders measured in this work range from 4.2 to 16.3 m. This is a significantly smaller range than that found in highland, mare, and pyroclastic regions (Bickel et al., 2019), which contain boulders of 1 to 31 m in diameter (see Figure A.63). The lack of small boulders in PSRs may be an artifact of image noise, which makes it difficult to identify small features. The reason for a smaller proportion of larger boulders, relative to that seen in mare and highland regions, is less clear.

6.4 Implications for PSR Traverses

The observations indicate that rovers with wheel radii of $\geq\sim$28 cm should be able to traverse PSRs of the type studied here. It remains possible that the upper few centimeters of regolith are physically different than deeper regolith analyzed in this study. For example, the upper few centimeters of lunar regolith are generally very porous at $\sim$52% (Carrier et al., 1991); however, if water ice is present, then the porosity could be decreased if the ice fills the pore spaces. Additional work may, therefore, be needed to determine if vehicles with wheel diameters $<$28 cm can traverse these regions. The comparative assessment of average PSR bearing capacities with those of other terranes used highland and mare measurements obtained mostly at high slope angles ($>15^\circ$). Because slope affects bearing capacity, that may have produced a bias toward lower bearing capacity values in highland and mare terranes. That prompts a second comparison of PSR properties with those of highland and mare using only those observations made on slopes $>15^\circ$ (see Table A.20). On those surfaces, PSR regolith appears to be statistically stronger in the $\leq$1 m range, with the caveat that the result is based on only two data points. Both comparative approaches have weaknesses but point to similar conclusions: that PSRs appear to be stronger than highland and mare regions at equivalent depths and slope angles. When comparing the results of PSRs with pyroclastic deposits, pyroclastic deposits appear to be statistically similar in strength to PSRs when all slope angles are considered, but statistically weaker when considering higher slope angles only. As the pyroclastic data have a less variable distribution across all slope angles, it is more appropriate to consider the statistical analysis for all slope angles, which indicates that pyroclastic deposits are similar in strength to PSRs at $\leq$1 m. Despite those trends, it is also true that there is a range of bearing capacities in any terrane.

6.5 Implications of Regolith Relative Density on Bearing Capacity

The value for bulk density of PSR regolith used in this work (1.66 g/cm^3 for regolith $>$30 cm deep) was selected because the lunar polar regolith is thought to be mostly feldspathic "highland like" material. Therefore, the bulk density value is taken (Mitchell et al., 1972b), which analyzed highland material. However, it has also been theorized that PSRs are highly porous (Gladstone et al., 2012), which would equate to a lower relative and bulk density. Bulk density, ρ (g/cm^3), and porosity, n, are related as follows (Carrier et al., 1991):

$$\rho = G\rho_w(1-n) \tag{A.5}$$

where G is the specific gravity of regolith taken to be 3.1 and ρ_w is the density of water (1 g/cm^3). When using a bulk density of 1.66 g/cm^3, the estimated porosity would therefore be $\sim$46%. As evidence suggests that PSRs could have porosities as high as 70% (Gladstone et al., 2012), the equivalent bulk density is calculated to be 0.93 g/cm^3. As illustrated by Carrier et al. (1991) using a basaltic regolith simulant, an increase in porosity and a decrease in relative and bulk density will result in reduced cohesion and friction angle values of the respective soil. However, as the input parameters for cohesion and friction angle adopted from Bickel et al. (2019) are already conservative assumptions, particularly the angle of internal friction (29°), a further reduction would likely result in unrealistic bearing capacity estimates. A comparison of the bearing capacities as calculated using this lower limit value for bulk density is shown in Figure A.65 and Table A.22 and Table A.23. The results show that the bearing capacity is reduced at

higher porosities (e.g., from 127 ± 29 to 73 ± 14 kN/m^2 in PSRs at depths of ≤1 m and on a 0° slope for densities of 1.66 and 0.93 g/cm^3, respectively); however, the upper meter of regolith in PSRs is still estimated to be as strong as highland regolith and equally as strong as mare and pyroclastic regolith. At depths >1 m, the bearing capacity of regolith in PSRs is calculated to be significantly lower (∼34-45% lower) than highland, mare, and pyroclastic regolith for the lowest bulk density scenario; for example, PSRs have a bearing capacity of 110 ± 16 kN/m^2 when applying a density of 0.93 g/cm^3 as compared to bearing capacity values calculated for highland, mare, and pyroclastic regions of 166 ± 24, 167 ± 19, and 200 ± 30 kN/m^2, respectively, at depths of ≤1 m and on a 0° slope. As a consequence, the PSR regolith may be somewhat weaker at depths of >1 m, as compared to other regions of the Moon.

6.6 Requirements for Increasing the PSR Boulder Data Set

Although the data support a self consistent set of conclusions, we recognize that it needs to be confirmed. Now that the methodology has been demonstrated, the data set could be expanded. In this work, 13 boulders across five locations were analyzed. It seems reasonable that more boulders and boulder tracks can be located and measured within the north polar region in a similar latitude range of ∼70-75°. That will allow an assessment of heterogeneities that may exist in PSRs of different ages, composed of different lithologies. Some progress should be possible with the existing set of LROC NAC images, but we envision that a number of boulder tracks will be captured in some of the darkest and coldest PSRs once ShadowCam is deployed (Robinson, 2018). However, as the spatial resolution of ShadowCam will be lower than the LROC imager, it will likely only be able to resolve large boulder tracks, which cannot be used to estimate bearing capacity at shallow depths.

Conclusions

A method was developed to study boulder tracks in NAC images of lunar south polar PSRs from which the bearing capacities of PSR regolith could be assessed qualitatively and quantitatively. Boulders that traveled from sunlit regions into PSRs are seemingly unaffected. They do not disappear into an overly porous or weak regolith. Rather, the dimensions of the boulder tracks remain unchanged suggesting that there are no large bearing capacity contrasts between the regolith in sunlit and permanently shaded regions. Those track dimensions can also be used to estimate bearing capacities. When compared with bearing capacities determined in other terranes (Bickel et al., 2019), regolith in PSRs appear to be as strong as the regolith in highland and mare regions, and similar to that in pyroclastic deposits within the upper ∼0.28 to 1 m of regolith across all slope angles. Those qualitative and quantitative results seem to contradict reports of very high porosity in PSRs (Gladstone et al., 2012; Hayne et al., 2019; Metzger et al., 2018; Schultz et al., 2010) or require those proposed high porosity conditions be limited to the uppermost 28 cm or the presence of water ice provides additional strength in a porous regolith. In either case, trafficability of PSRs may be possible with rovers of wheel radii >28 cm with sufficient traction. In situ analyses are still required to verify these results and to establish the distribution of regolith strength within the uppermost centimeters and meters, and the lateral heterogeneity of the regolith, of PSRs.

Acknowledgments

The authors would like to acknowledge the support of the Lunar and Planetary Institute (LPI) in Houston, TX, and the Universities Space Research Association. Funding was provided by the NASA Solar System Exploration Research Virtual Institute (NNXA14AB07A, PI David A. Kring). The research was performed as part of the Exploration Science Summer Intern Program hosted by the LPI and the NASA Johnson Space Center in Houston, TX. The authors would like to thank Julie D. Stopar of the LPI for her willingness to provide insights about the LROC system. The authors would also like to thank Tristram Warren of Oxford University for his work with the Oxford 3D Thermophysical model and its application to the PSRs studied in this work. H. S. would like to acknowledge the support of the Science and Technology Facilities Council studentship grant (Grant ST/N50421X/1). V. T. B. gratefully acknowledges the financial support by the International Max Planck Research School at the Max Planck Institute for Solar System Research at the University of Goettingen (IMPRS) and the Engineering Geology group, Department of Earth Sciences, Swiss Federal Institute of Technology Zurich (ETHZ). This research has made use of the USGS Integrated Software for Imagers and Spectrometers (ISIS) and the Ames Stereo Pipeline (ASP). The described PSR image filtering routines of method one, that is, the line exaggeration, the SHT, and the "fillmissing" algorithm, have been written and/or implemented in Matlab R2018a. Used data can

be retrieved from Sargeant et al. (2020), the cited references, or from the LROC image archive (http://wms.lroc.asu.edu/lroc/search). All used NAC image IDs can be found in Table A.19. This is LPI Contribution No. 2247. LPI is operated by USRA under a cooperative agreement with the Science Mission Directorate of the National Aeronautics and Space Administration. The study was conceived by D. A. K and implemented by H. M. S., V. T. B., C. I. H., S. N. M., and A. R. with D. A. K. ISRU issues were addressed by C. I. H., A. R., and H. M. S., while V. T. B., C. I. H., S. N. M., A. R., and H. M. S. selected sites of interest. V. T. B. processed imagery and DEMs; V. T. B. and H. M. S. conceived the implementation of bearing capacity equations; S. N. M. and A. R. built the GIS and performed measurements. H. M. S., V. T. B., C. I. H., S. N. M., and A. R. analyzed the results and wrote the paper. All authors contributed to a discussion of findings, their implications for future missions, and editing the paper.

A.2 SUP: Detection and Mapping of Rockfalls

Automated Detection of Lunar Rockfalls Using a Convolutional Neural Network
Published 2018 in IEEE Transactions on Geoscience and Remote Sensing
Bickel, V.T., Lanaras, C., Manconi, A., Loew, S., Mall, U., 2018
https://doi.org/10.1109/TGRS.2018.2885280

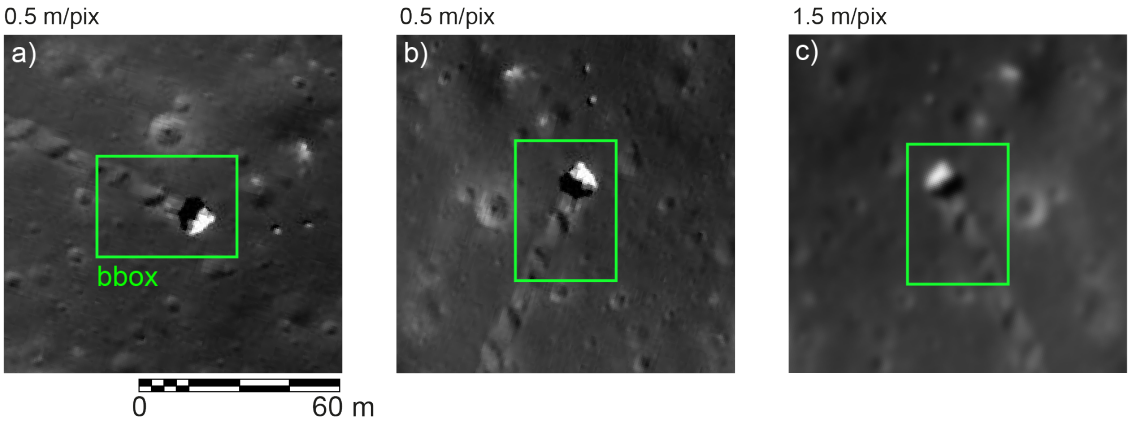


Figure A.9: RetinaNet training input image augmentation methods: green bboxes indicate rockfall features for the network to train on, a) original training image, detail taken from M111422030LC_pyr, b) augmented image using rotation by 90°counterclockwise, c) augmented image using a left-right flip as well as downsampling. In subset a) North is down.

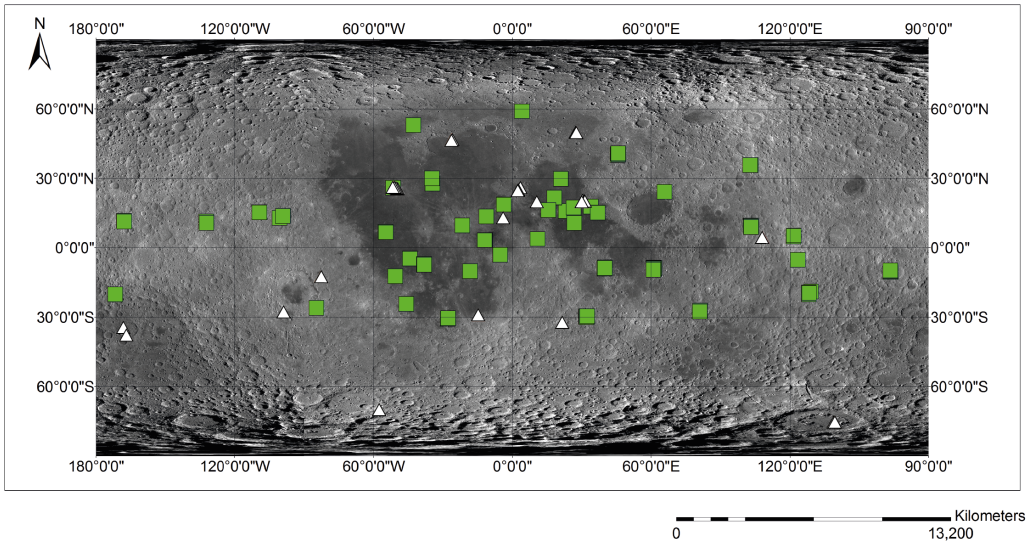


Figure A.10: Distribution of the used images that contain rockfalls across the lunar surface used for RetinaNet training and validation (green squares), and used for neural network testing (white triangles); equirectangular projection of WAC global mosaic.

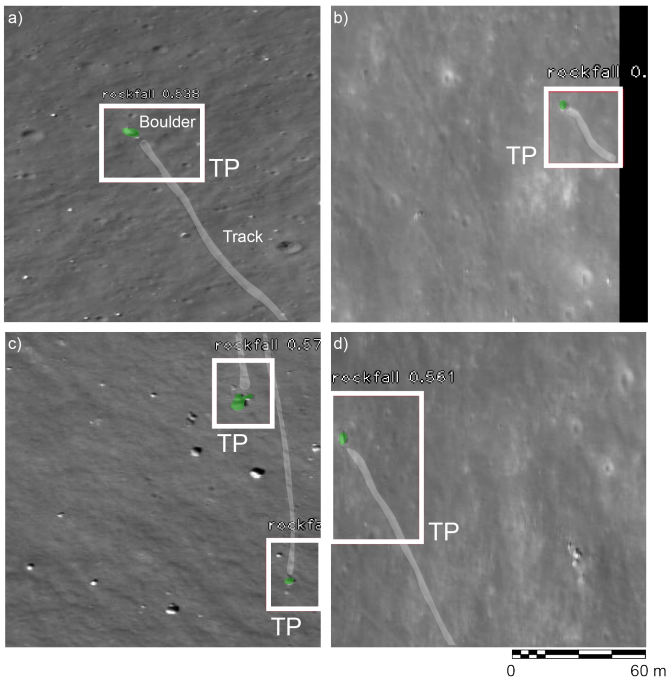


Figure A.11: Examples of successful rockfall (green shapes) detections (TPs) with activated NMS, further indicating the different bbox shapes used by the network, CT of 0.5. Tracks are slightly enhanced with a white signature. Black box in b) represents the border of a NAC image that has been padded to match the input patch size requirements of 844x844 pixel. CNN is able to pick up features close to or at the edge of NAC images. Details taken from M111422030LC_pyr, M175139029RC_pyr, and M1136354411LC_pyr. North is up.

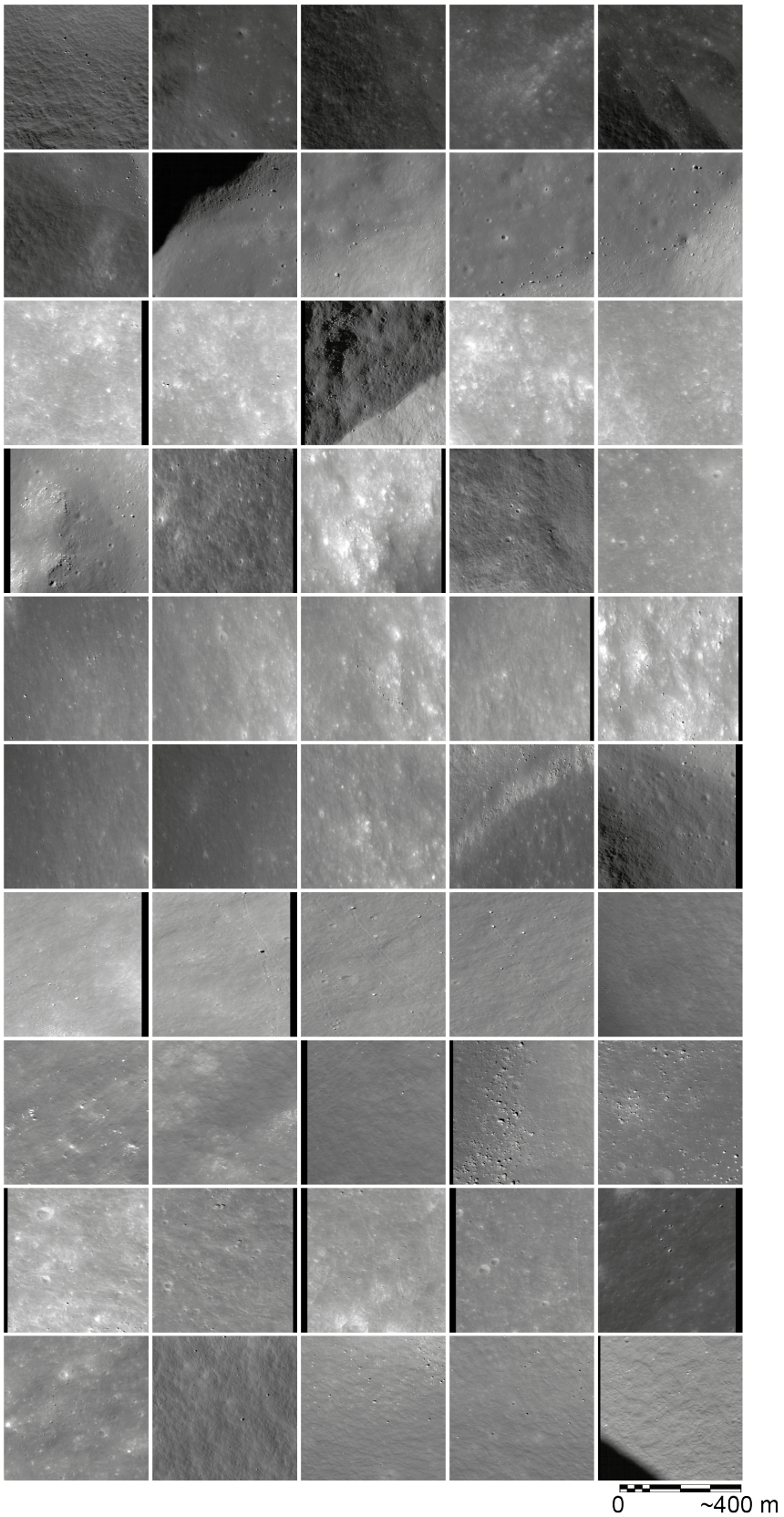


Figure A.12: Overview thumbnails for all 50 image patches used for testing, with rockfalls. Thumbnails illustrate the differences in illumination conditions and surface properties within the testing patches. North is up.

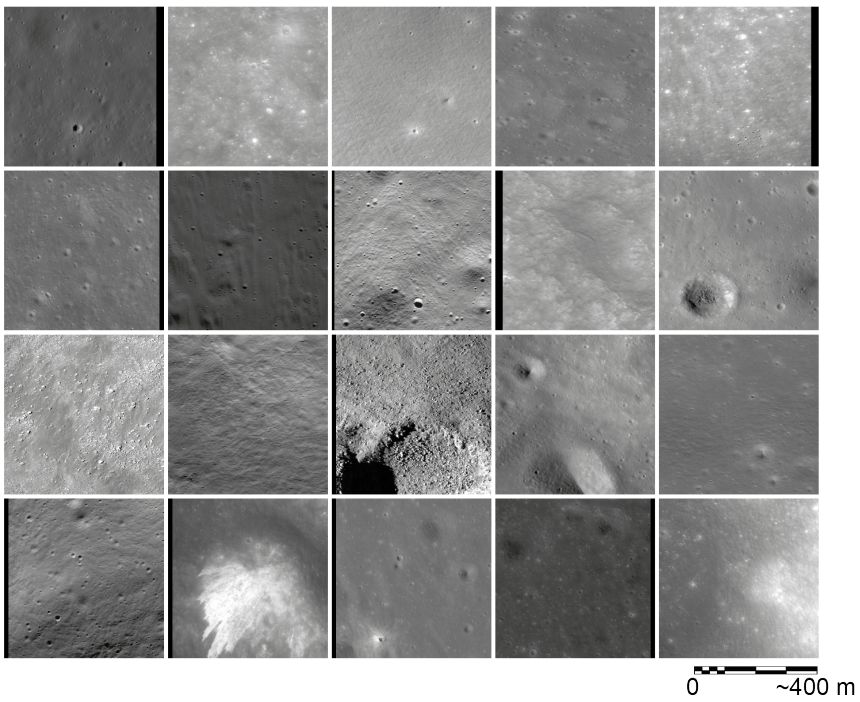


Figure A.13: Overview thumbnails for all 20 image patches used for testing, without rockfalls. Thumbnails illustrate the differences in illumination conditions and surface properties within the testing patches. North is up.

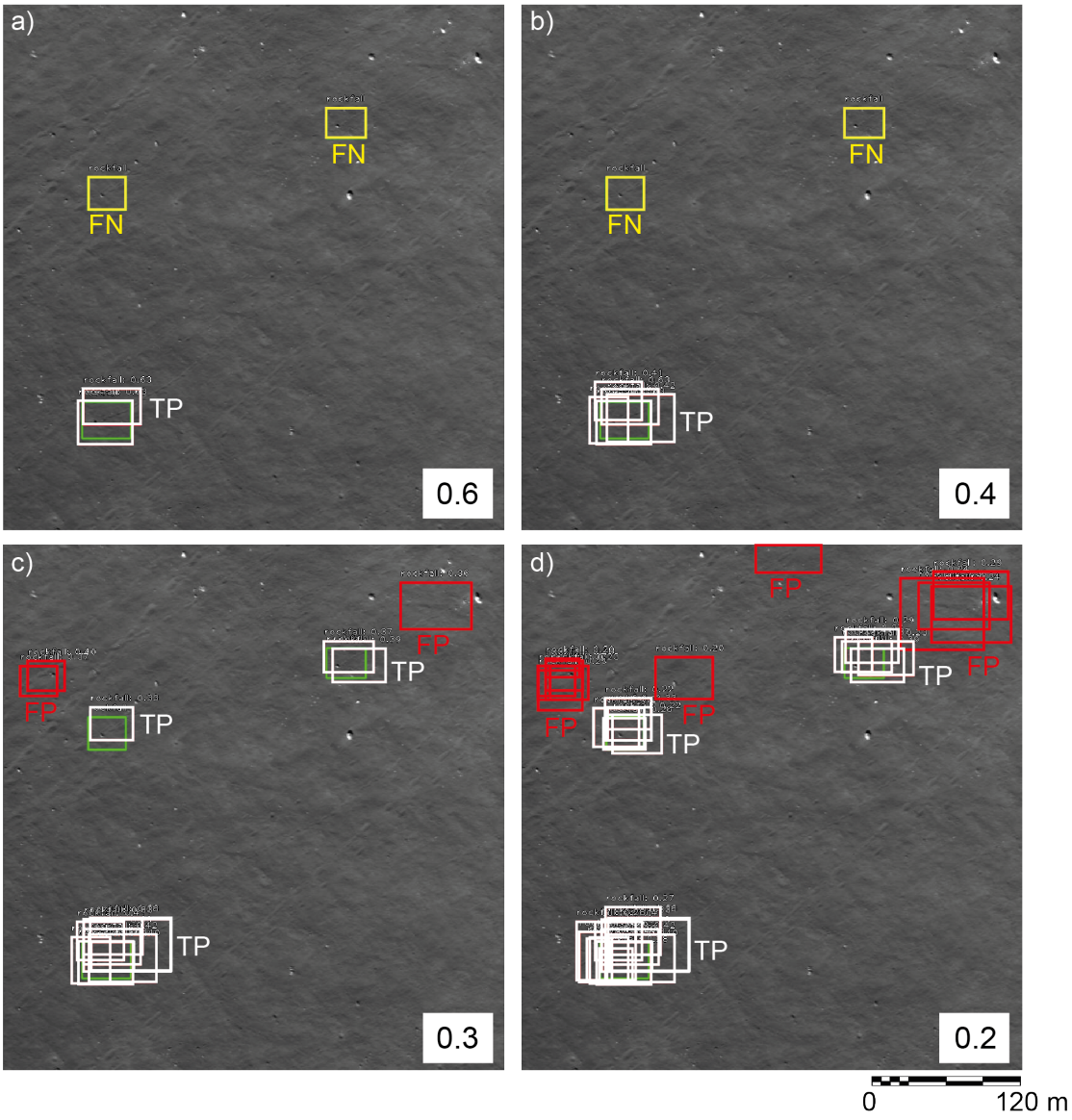


Figure A.14: Effect of varying CT on object detection, using a) 0.6, b) 0.4, c) 0.3, and d) 0.2 (CT value). Green boxes indicate labels created by a human operator (3 rockfalls are present in the tile), white boxes mark true positives (TP), yellow boxes indicate false negatives (FN), red boxes mark false positives (FP). NMS is deactivated to illustrate the increase in predictions per feature with decreasing CT. Detail taken from M170727953LC_pyr. North is up.

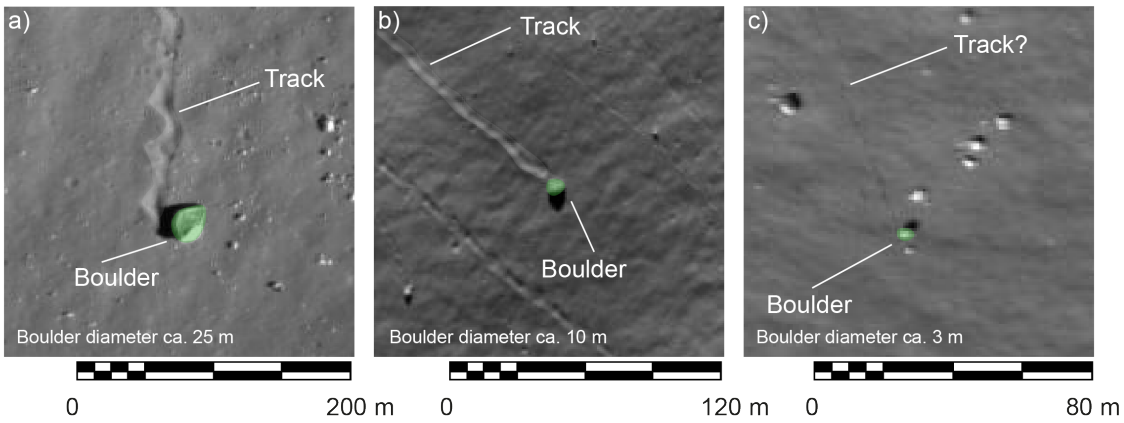


Figure A.15: Examples of different rockfall/boulder sizes (green shapes), a) large boulder (i.e. ∼25 m) with distinct track, detection very likely, b) intermediate-sized boulder (i.e. ∼10 m) with clear track, detection likely, c) small boulder (∼3 m) with ambiguous track, detection unclear. As feature size and spatial resolution decrease, the detection of rockfalls becomes less likely and reliable, for both human operators and the neural network. Details taken from M111422030LC_pyr, M113242798RC_pyr, and M1234588088LC_pyr. North is up.

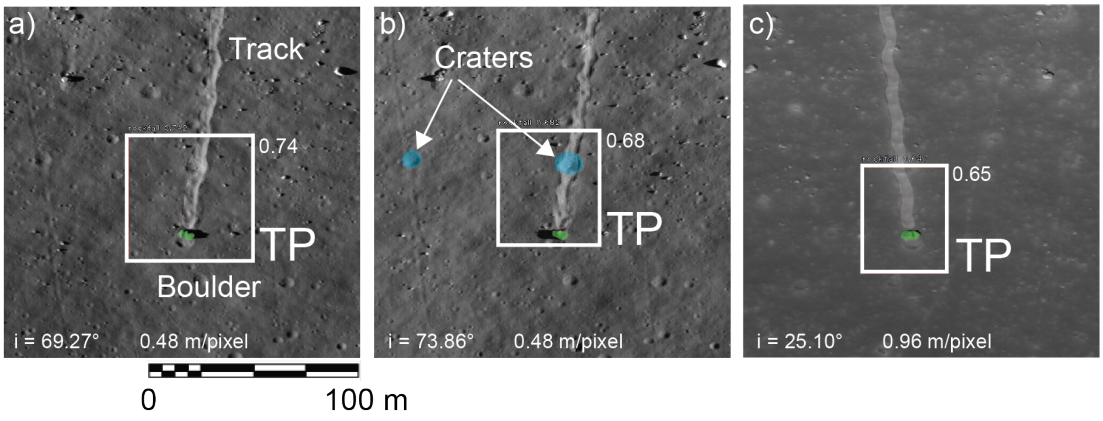


Figure A.16: Three acquisitions of the same rockfall in Taurus Littrow (green shape), tracks are slightly enhanced with a white signature. Illumination direction is W-E (a), E-W (b), and sub-nadir (c). The trained CNN is able to detect the identical rockfall in imagery with different spatial resolutions and illumination conditions (incidence angles, i). Network CT varies only by ∼9%. Small impact craters on the track (blue shapes) do not influence the performance and are not detected as FPs. Image orientation changes as NACs have been taken in ascending and descending orbits and as PTIFs are not projected. Details taken from M162107606LC_pyr, M165645700RC_pyr, and M172717297RC_pyr. North is up.

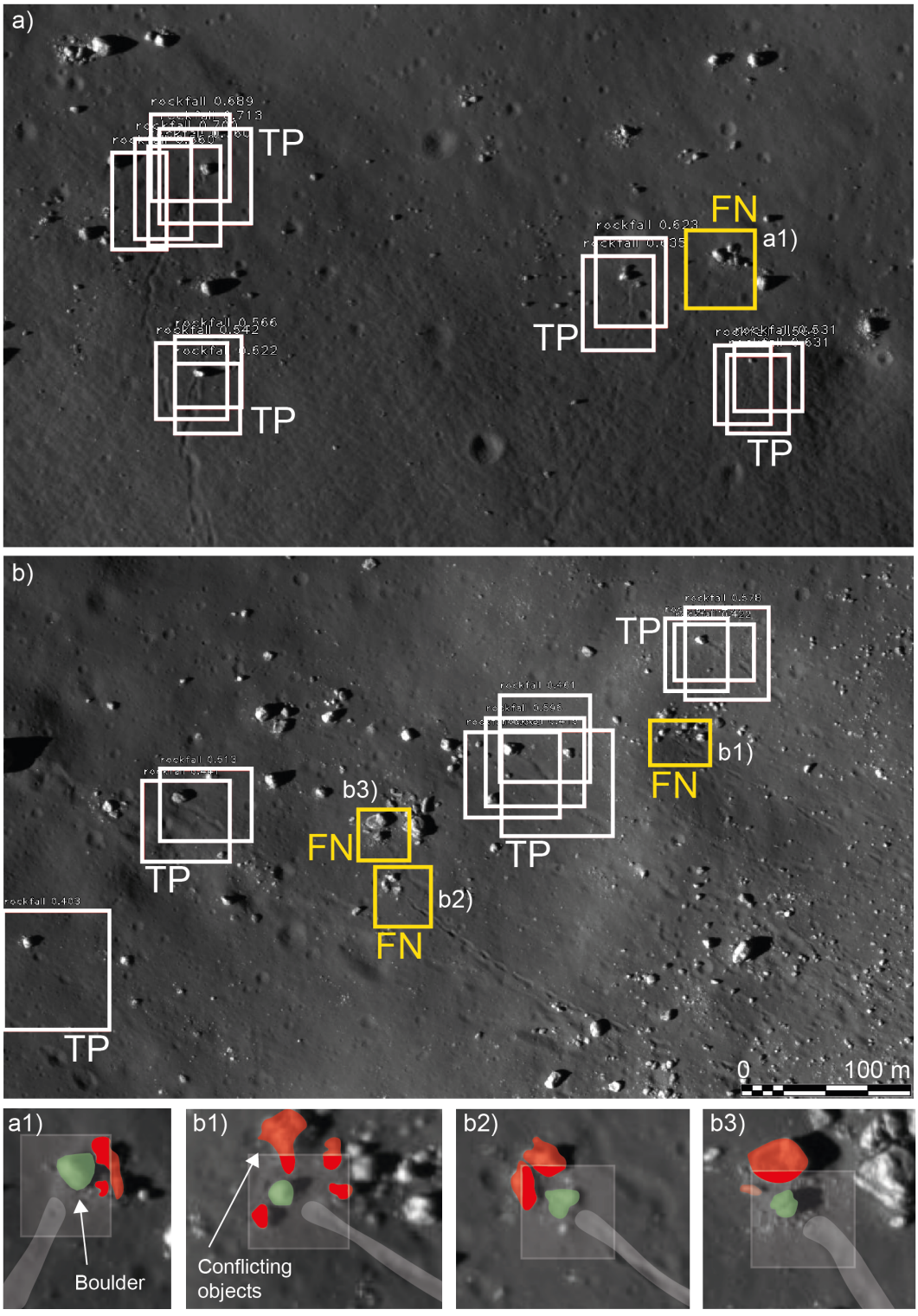


Figure A.17: CNN performance in boulder clusters. Conflicting objects very close to rockfalls (red shapes) potentially inhibit a successful detection of the feature (green shapes) (a1 through b3). In a1 to b3, the desired bboxes are indicated in gray and the overlap with conflicting objects in red. Tracks are slightly enhanced with a white signature. NMS is deactivated to better illustrate network performance. Details taken from M192109542LC_pyr and M169717752RC_pyr. North is up.

Patch ID	Region	Resolution (m/pixel)	Incidence (°)	Emission (°)	Phase (°)	Rockfall Y/N
M1252208394RC_4_38	LPD	0.9384111	39.11	1.17	38.11	Y
M1252208394RC_4_43						
M1252208394RC_4_13						
M1252208394RC_3_33						
M1252208394LC_4_15						
M1234588088LC_5_40	LPD	1.1872368	66.6	1.75	68.31	Y
M1234588088LC_4_43						
M1234588088LC_3_43						
M1234588088LC_2_44						
M1225813672RC_6_52	Mare/LPD	0.9516051	24.66	1.17	24.2	Y
M1225813672RC_4_50						
M1225813672RC_3_48						
M1225813672RC_3_49						
M1225813672RC_3_50						
M1207094593LC_2_46	LPD	0.6714386	46.57	1.66	47.79	Y
M1154306917LC_1_47	Mare	1.6846306	72.24	1.72	73.93	Y
M1137658694LC_1_31	LPD	0.7653549	57.59	1.71	59.16	Y
M1136356411LC_6_36	Mare/LPD	0.9918338	39.51	1.76	41.06	Y
M1136356411LC_6_8						
M1136356411LC_6_4						
M1136356411LC_6_9						
M1136356411LC_5_7						
M1136356411LC_5_4						
M1136356411LC_5_6						
M1136356411LC_4_6						
M1136356411LC_4_5						
M1136356411LC_3_43						
M1129816126LC_4_6	LPD	1.0170395	47.25	1.77	48.84	Y
M1121876217RC_6_17	Highland	0.7230762	55.87	1.15	54.79	Y
M1117933950RC_1_48	LPD	0.7493133	76.84	1.13	76.97	Y
M175139029RC_6_29	Highland	0.4258476	49.6	1.13	48.59	Y
M175139029RC_6_28						
M175139029RC_5_23						
M175139029RC_5_22						
M170727953LC_2_47	Mare	0.5199534	48.69	1.69	49.08	Y
M170727953LC_2_42						
M170727953LC_2_41						
M170727953LC_1_44						
M142251741RC_1_29	Mare/LPD	0.4972838	32.65	1.14	31.99	Y
M142244931RC_5_8	LPD	0.497364	33.6	3.25	35.77	Y
M142068699RC_1_34	Mare/LPD	0.4890287	27.94	0.92	28.61	Y
M142068699LC_6_31						
M142068699LC_1_31						
M142068699LC_1_28						
M126724656RC_6_12	Mare/LPD	0.4832478	31.49	1.13	30.6	Y
M126724656RC_5_33						
M111422030LC_2_26	LPD	0.4858976	55.62	1.69	56.52	Y
M111422030LC_3_21						
M111422030LC_4_21						
M113242798RC_2_30	Highland	0.6252425	48.22	1.15	47.09	Y
M104848322RC_1_1	LPD	1.45170952	53.87	1.2	52.73	N
M106676354RC_1_33	Mare/LPD	1.46716717	35.32	1.2	34.29	N
M110670656RC_1_61	LPD	0.6365209	74.72	2.98	73.73	N
M111422030LC_4_23	LPD	0.48589755	55.62	1.69	56.52	N
M114280746RC_4_56	LPD	0.49920562	63.48	1.14	62.4	N
M114498609RC_1_14	LPD	0.51406264	62.57	1.12	61.45	N
M124743115LC_5_35	Mare	0.46194609	45.16	1.68	45.29	N
M126955161RC_4_31	Mare/LPD	0.46748107	30.37	3.17	27.44	N
M144558374LC_2_24	LPD	0.49384812	50.66	4.23	54.67	N
M157934151RC_6_56	Mare/LPD	0.46958831	34.82	0.94	34.18	N
M170727953LC_1_38	Mare	0.51995335	48.69	1.69	49.08	N
M175610199LC_5_57	Mare/LPD	0.40653477	53.18	1.67	54.7	N
M1117933950RC_1_1	LPD	0.74931329	76.84	1.13	76.97	N
M1180447923LC_3_77	Highland	1.16486495	72.6	1.7	73.14	N
M1207094593LC_6_1	LPD	0.67143863	46.57	1.66	47.79	N
M1225813672RC_2_56	Mare/LPD	0.95160507	24.66	1.17	24.2	N
M1234243503RC_6_34	Mare/LPD	1.17293962	70.03	1.18	68.86	N
M1252222450LC_5_7	LPD	0.94064753	39.15	1.73	40.57	N

Table A.2: List of image patches used for RetinaNet testing, including various details. Patch ID consists of NAC image ID (MnnnnR/LC_pyr) and patch ID (_patch_N_M). N/A denotes images without any available information at the time of manuscript submission.

Deep Learning-Driven Detection and Mapping of Rockfalls on Mars
Published 2020 in IEEE Journal of Selected Topics in Applied Earth Observations and Remote Sensing
Bickel, V.T., Conway, S., Tesson, P.-A., Manconi, A., Loew, S., Mall, U., 2020
https://doi.org/10.1109/JSTARS.2020.2991588

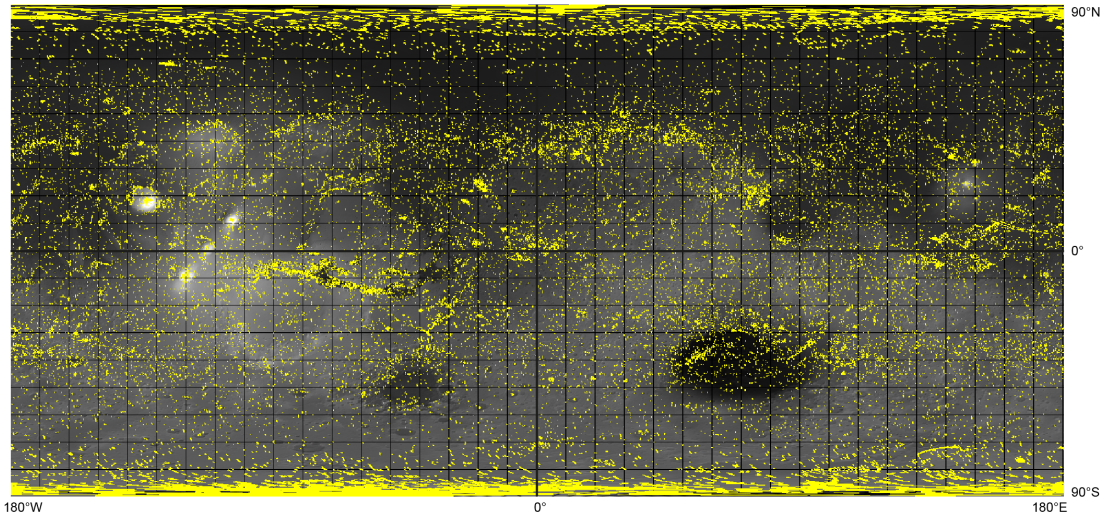


Figure A.18: Spatial distribution of all available HiRISE images over the surface of Mars (yellow footprints) as of February 12th 2020. Coverage is not complete, but widespread over the entire surface and across various different geomorphological settings. Plot created with JMars by Christensen et al. (2009).

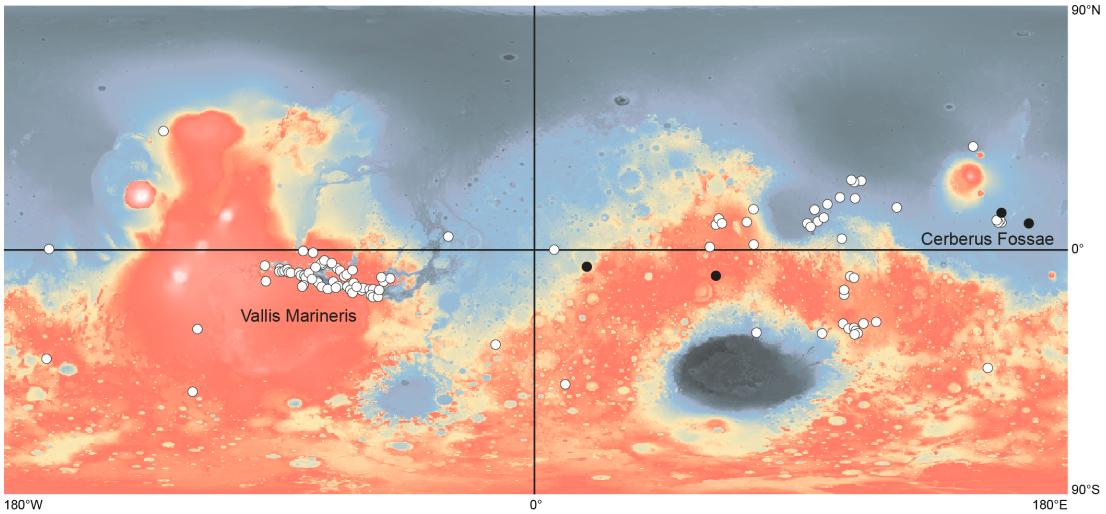


Figure A.19: Footprint locations of all used HiRISE images for training (white dots) and for testing (black dots), plotted on a Mars MOLA DEM in an equirectangular projection, black shows low, red and white show high altitudes (MOLA, 2014; Fergason et al., 2017).

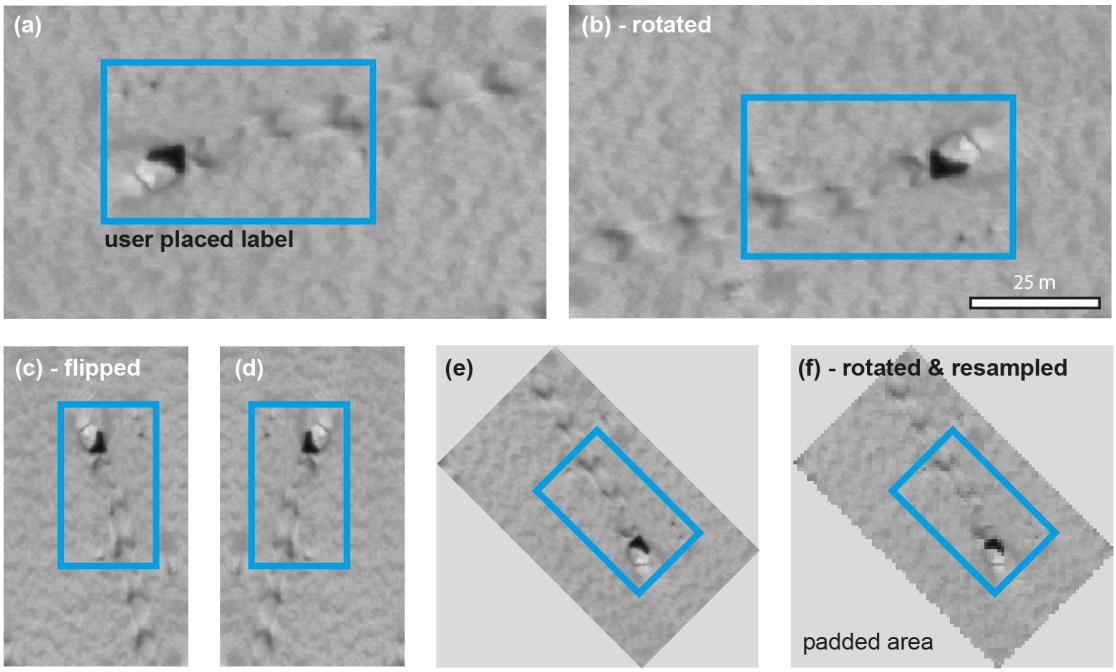


Figure A.20: Example of rockfall label placement and training data augmentation, following the workflow from Bickel et al. (2018). The label contains a boulder and its track to prevent detections of boulders without tracks or tracks without boulders. As discussed in section 2.2, the reduction of ambiguity using a relatively large label box comes to the cost of an increased background, which could potentially influence the training. Please refer to Figure A.21 c) for a box with a particularly complex background. Here, some of the performed data augmentation operations are visualized, such as rotation (a to b), left right/up down flip (c to d), and resampling (e to f). If the rotation angle is not equal to 90, 180, or 270°, the remaining area is padded to maintain a rectangular image. Detail of HiRISE image ESP_043293_1740. Image credits: NASA/JPL/UofA.

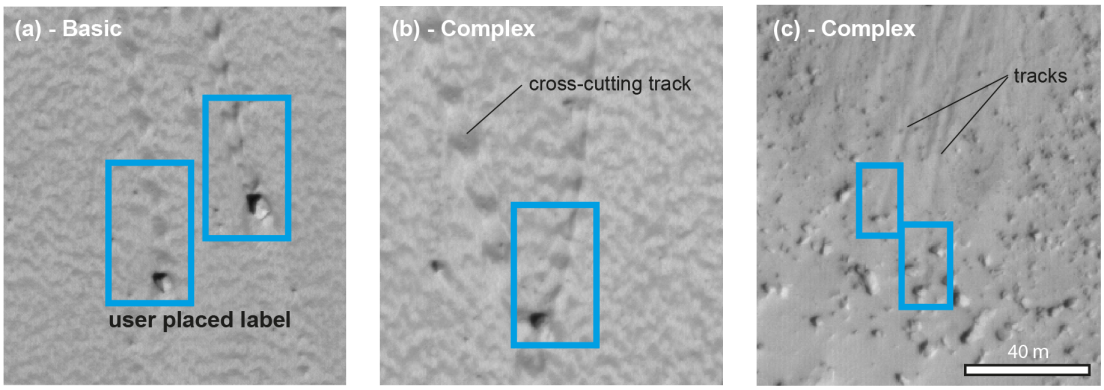


Figure A.21: Examples for Basic-type (a) and Complex-type (b and c) labels (not part of the actual training data). a) features large boulders and clearly visible tracks in combination with a clean background (smooth slope substrate); b) features a similar target, but increases complexity by a cross-cutting track (in the label box); c) features less visible tracks and small boulders in a debris field, where other, static boulders are included in the label box. Note the difference in label bounding box size that is later used to estimate a boulder size in meters: small box, small boulder; big box, big boulder (see Figure 2.12).

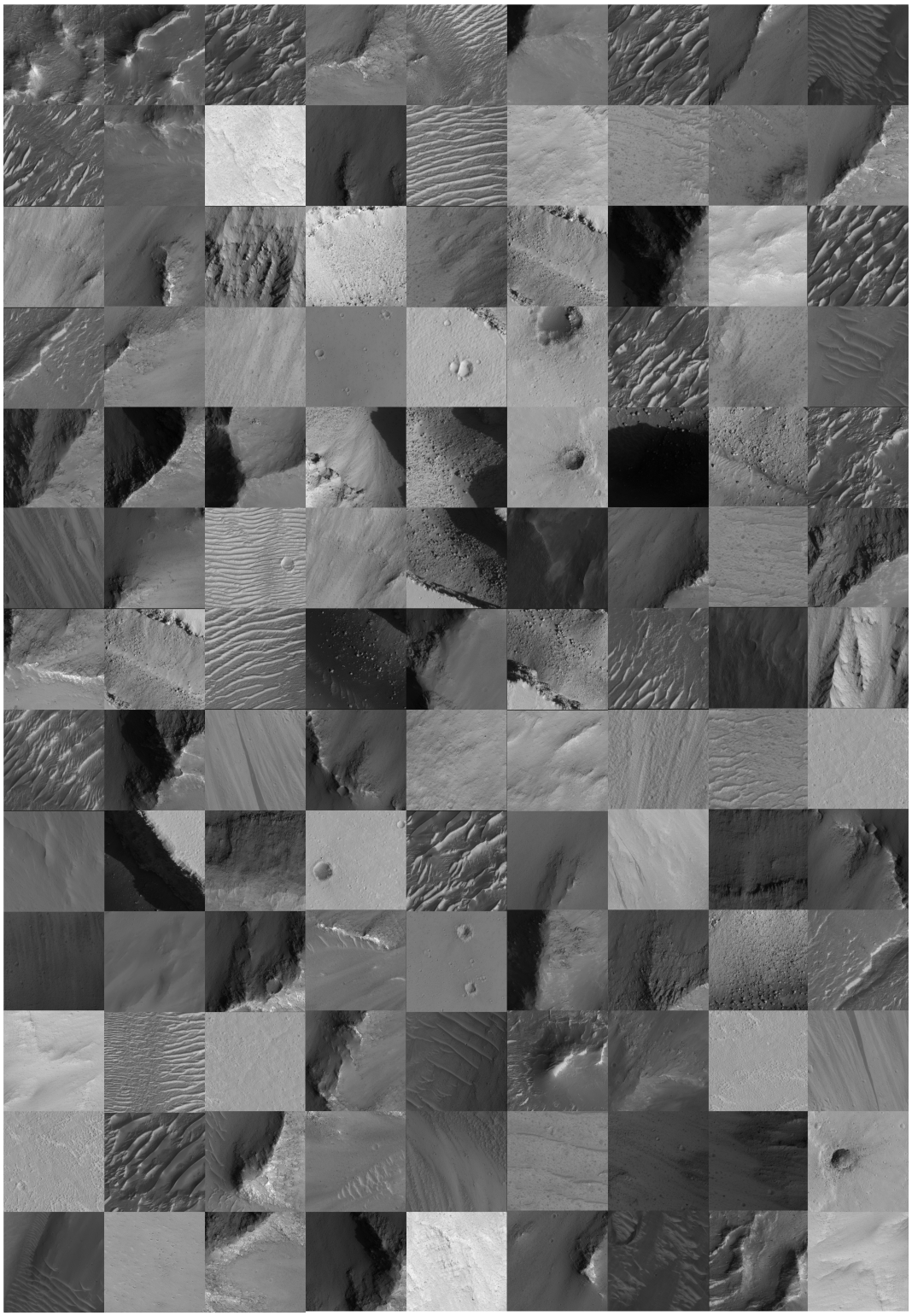


Figure A.22: Overview of some of the 5048 HiRISE patches used for CNN testing, taken from the HiRISE images ESP_025011_1965, ESP_037700_1710, ESP_038250_1880, and ESP_043293_1740. The variation in surface type, illumination conditions, surface albedo, geomorphological setting, etc. are clearly visible. Image credits: NASA/JPL/UofA.

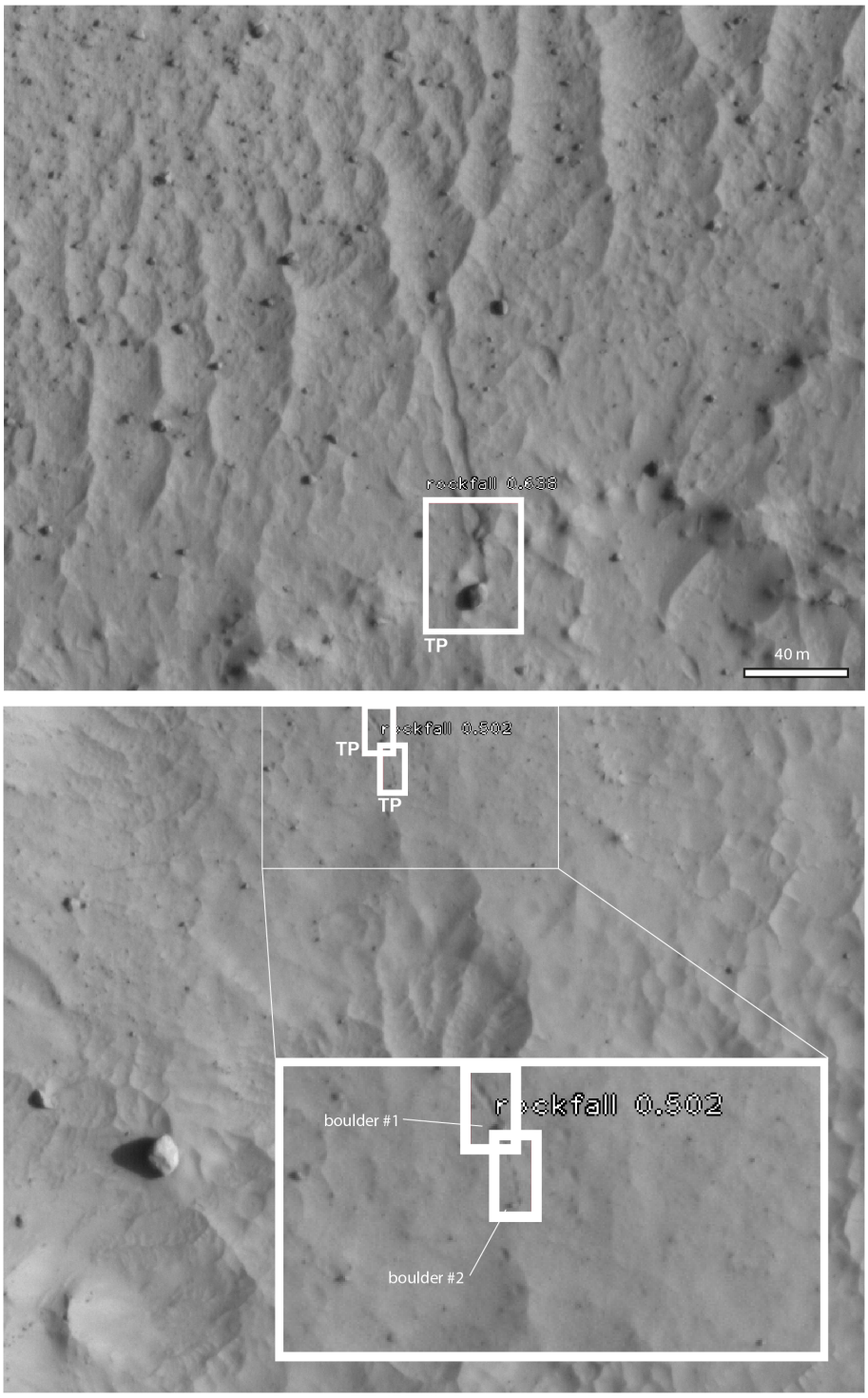


Figure A.23: More examples of rockfalls that have been detected by Ma/M Complex$_{101}$ (TPs). Note the highly complex environment with dunes, boulders, and a variety of other morphologic features that can potentially cause FPs. Also note the TPs that are located directly at the edge of the patch (bottom figure) and very close to each other, proving that the CNNs are able to detect the feature of interest directly or very close to the edge of an image patch, as well as when they are located right next to each other. These examples also show that the CNN is able to discard all other objects, such as sand ripples without boulders, boulders without tracks, and craters. Note that the "rockfall CT score" label is missing for one of the detections, as it falls outside of the patch. Details of HiRISE images ESP_036624_1720 and ESP_043293_1740. Image credits: NASA/JPL/UofA.

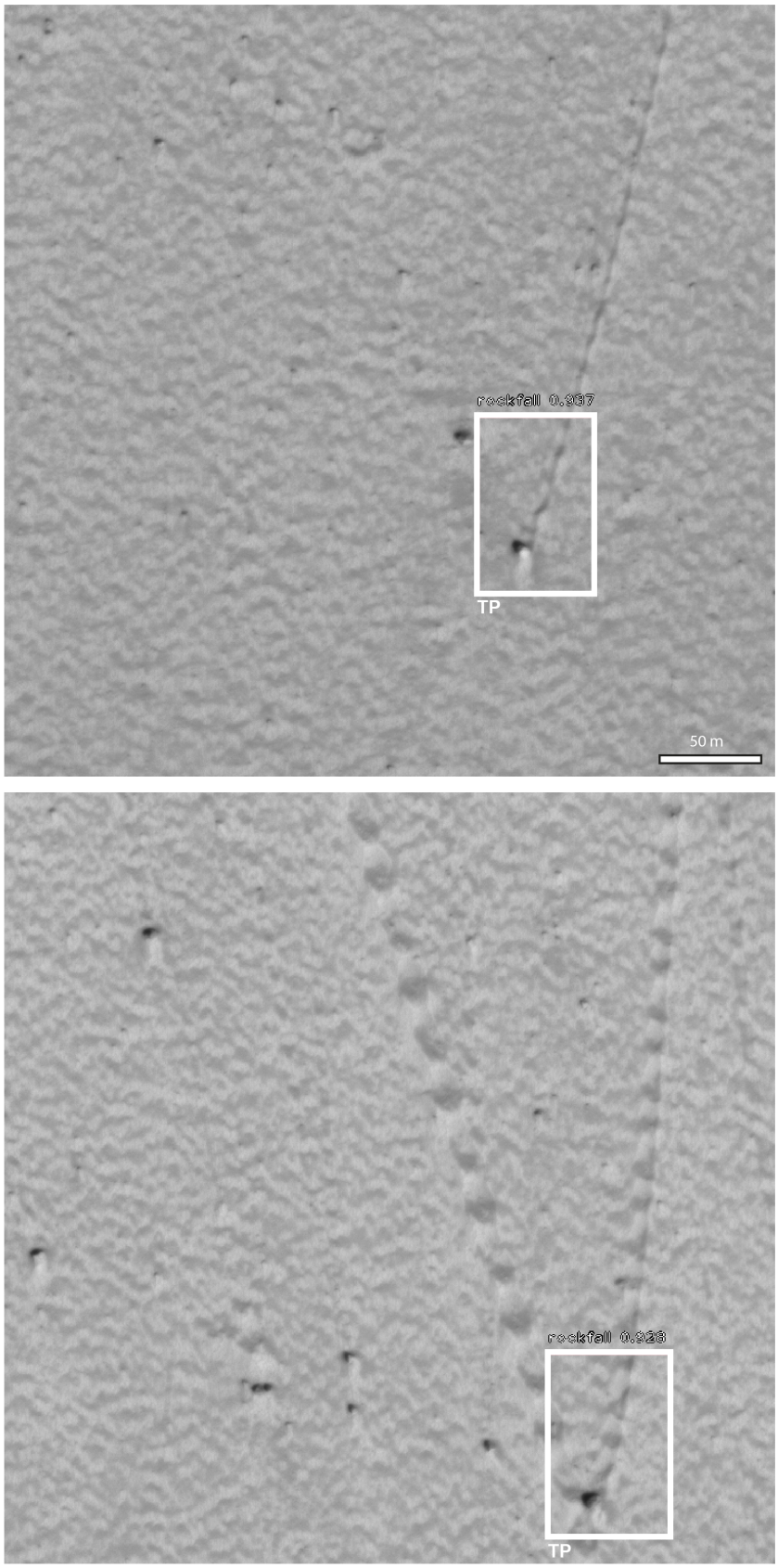


Figure A.24: More examples of very high confidence (> 0.9) rockfall detections made by Ma/M Complex$_{101}$ (TPs). Note that the CNN is not confused by the cross-cutting track in the bottom figure, indicating the value of the Complex-type labels, as shown in Figure A.21. Details of HiRISE image ESP_043293_1740. Image credits: NASA/JPL/UofA.

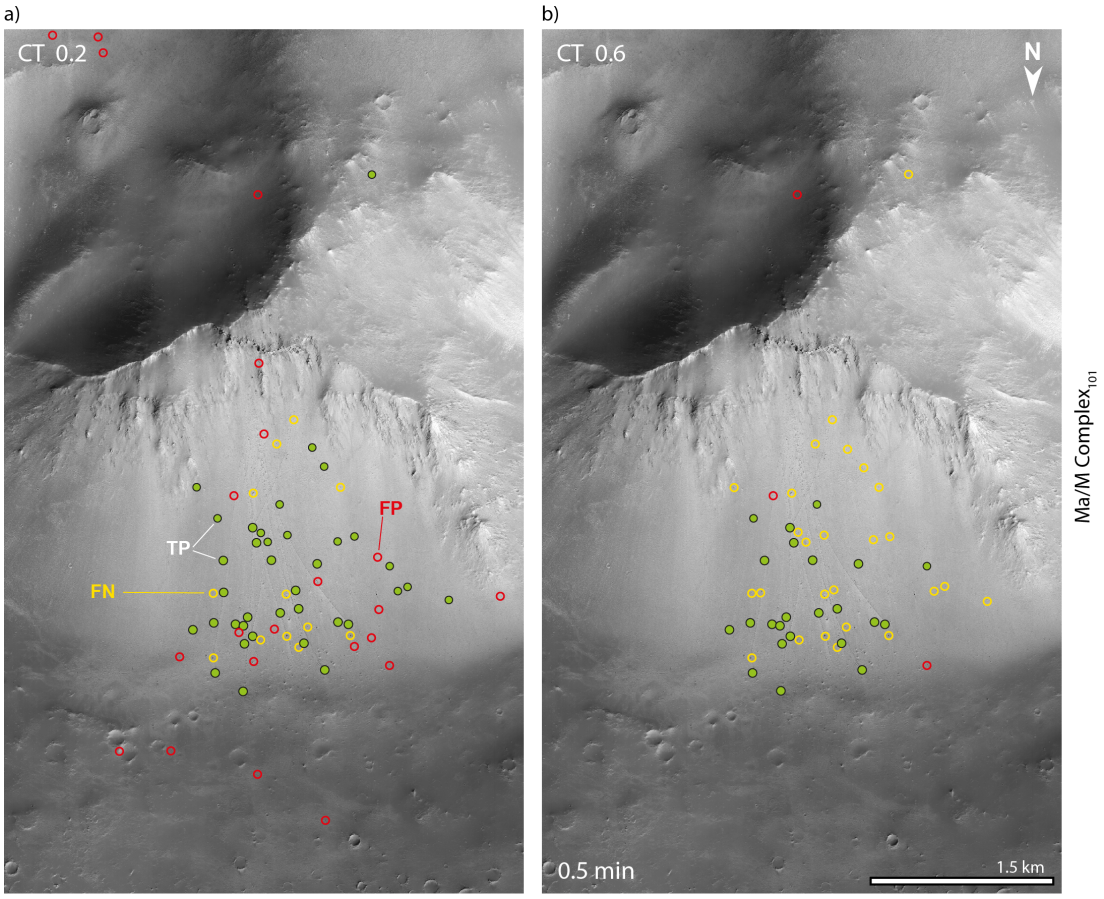


Figure A.25: CNN-driven rockfall mapping with a full-scene HiRISE image in Terra Meridiani by Ma/M Complex$_{101}$ with a) CT 0.2 and b) 0.6. Green dots are TPs, red indicates FPs, and yellow indicates FNs. The increase of the CT to 0.6 removes the vast majority of the FPs from the output, while slightly reducing the recall as well. Only FNs with distinct boulder and track combination are shown. Processing time for the full image is 30 seconds (CNN). Full HiRISE image ESP_043293_1740. Image credits: NASA/JPL/UofA.

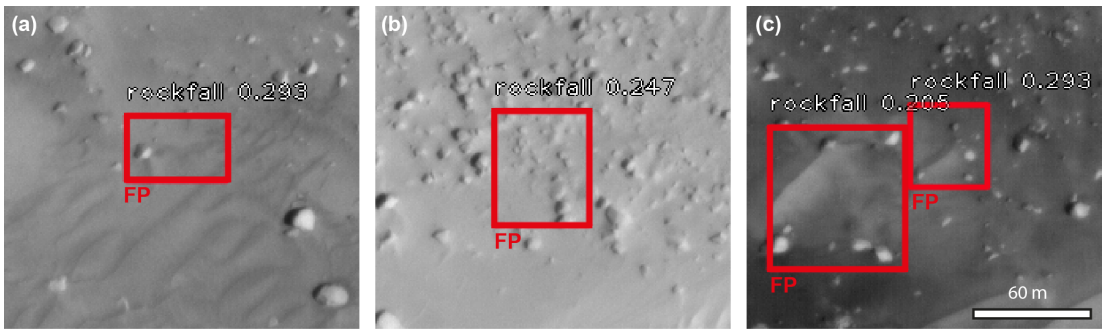


Figure A.26: Examples for FPs on Mars taken from the test set: (a) aeolian features such as sand scour and ripples in the lee of boulders, (b) linear lineup of boulders, and (c) a variation of aeolian deposits. All FPs have a low confidence score (< 0.3), which facilitates their removal. Details of HiRISE image ESP_025011_1965. Image credits: NASA/JPL/UofA.

Patch HiRISE ID			
ESP_011926_1720	ESP_029384_1665	ESP_016146_1730	ESP_030374_1725
ESP_012585_1755	ESP_031283_1715	ESP_016211_1655	ESP_033195_1710
ESP_018770_1730	ESP_034382_1695	ESP_016647_1725	ESP_033393_1750
ESP_019165_1765	ESP_036004_1710	ESP_017280_1725	ESP_034923_1735
ESP_019829_1900	ESP_037256_1650	ESP_020259_1670	ESP_036109_1675
ESP_024576_1900	ESP_038061_1755	ESP_025679_1755	ESP_037046_1725
ESP_025639_1660	ESP_039248_1675	ESP_027332_1900	ESP_037248_1900
ESP_025982_1675	PSP_005662_1700	ESP_028598_1900	ESP_037415_1705
ESP_026259_1675	PSP_008682_1770	ESP_028954_1900	ESP_039051_1725
ESP_028461_1665	PSP_009222_1660	ESP_028962_1645	ESP_042571_1675
ESP_014260_1675	ESP_016726_1720	ESP_017372_1710	ESP_018255_1680
ESP_024286_1910	ESP_025640_1730	ESP_025798_1675	ESP_026101_1750
ESP_026997_1660	ESP_037204_1710	ESP_030703_1675	ESP_033279_1905
ESP_038681_1745	ESP_035186_1670	ESP_039063_1660	PSP_001377_1685
PSP_005057_1695	PSP_008946_1715	PSP_010501_1645	PSP_001660_1950
PSP_007146_2085	ESP_019038_2170	ESP_016513_1850	PSP_003939_1420
PSP_007115_1505	ESP_032201_1515	ESP_037571_1475	ESP_030428_1315
ESP_039662_1400	ESP_037280_1795	ESP_022762_1335	ESP_036434_1890
ESP_035590_1895	ESP_011972_1665	ESP_045558_1665	PSP_010772_1520
ESP_046415_1520	ESP_047549_1520	ESP_027545_1530	ESP_047338_1705
ESP_044160_1705	ESP_030024_1540	ESP_017563_1525	ESP_033162_1565
ESP_044358_1540	PSP_005749_1510	ESP_033215_1840	ESP_036525_1930
ESP_024908_1885	ESP_043567_1880	ESP_018512_2015	ESP_026292_2045
ESP_025870_2045	ESP_035681_1920	ESP_026056_1820	ESP_024355_1900
ESP_041036_1935	ESP_031819_1820	ESP_012791_1910	ESP_036591_1945
ESP_030578_1965	ESP_026490_1990	ESP_026683_2205	ESP_011543_1665
ESP_012018_1750	ESP_012242_1725	ESP_012638_1700	ESP_012769_1645
ESP_012809_1725	ESP_012836_1720	ESP_012848_1705	ESP_012994_1700
ESP_013191_1660	ESP_013231_1690	ESP_013587_1685	ESP_013719_1665
ESP_013732_1690	ESP_014114_1665	ESP_014154_1730	ESP_016000_1670
ESP_016171_1700	ESP_016198_1695	ESP_016528_1705	ESP_016699_1715
ESP_017121_1690	ESP_017253_1765	ESP_018018_1705	ESP_018348_1730
ESP_018664_1785	ESP_018743_1750	ESP_018796_1790	ESP_019033_1750
ESP_019389_1725	ESP_019666_1730	ESP_019969_1730	ESP_020181_1750

Table A.3: List of HiRISE images used for network training (PSP = primary science phase, ESP = extended science phase).

Patch HiRISE ID			
ESP_037700_1710	ESP_038250_1880	ESP_025156_1965	ESP_043293_1740

Table A.4: List of HiRISE images used for network testing (ESP = extended science phase).

Transfer Learning for Enhanced Rockfall Mapping in Known and Unknown Planetary Domains
Submitted to the ISPRS Journal of Photogrammetry and Remote Sensing
Bickel, V.T., Mandrake, L., Doran, G., in review - might be subject to change



Figure A.27: All image tiles used for the Mars experiments (testing), showcasing the variation of the local geomorphology. Taken from RMaM–2020 (Bickel et al., 2021c).

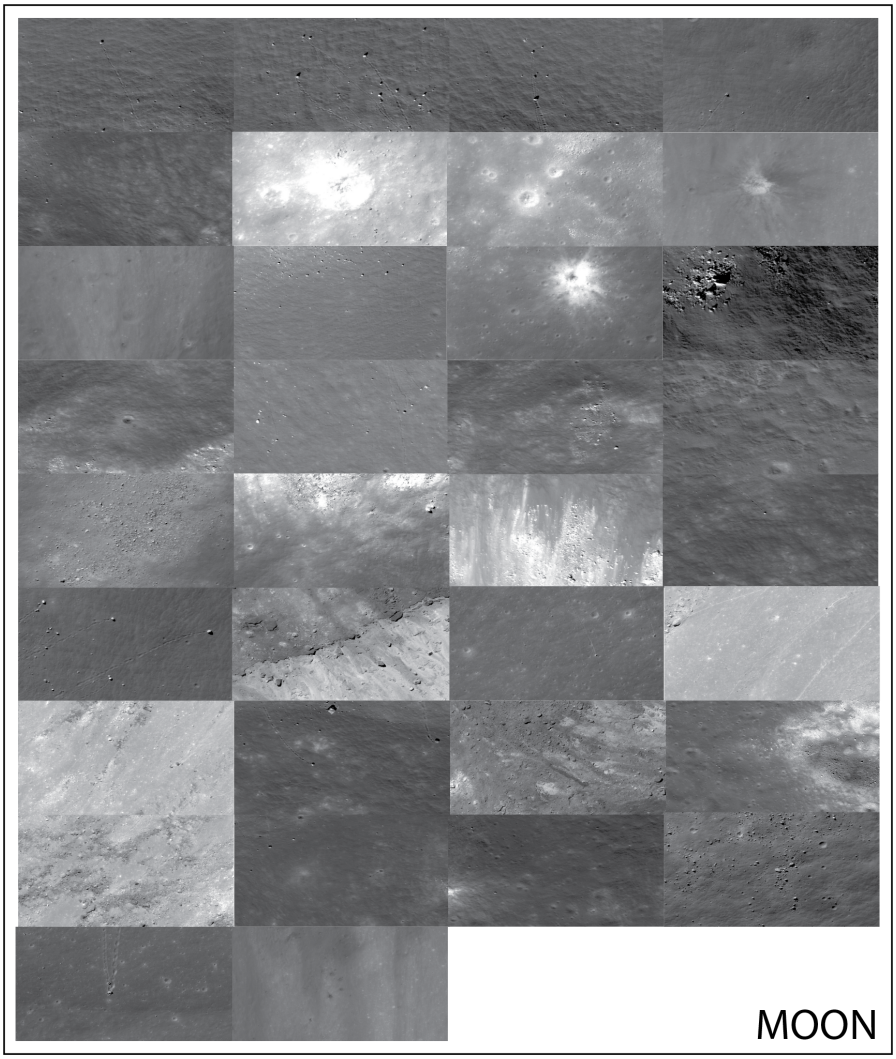


Figure A.28: All image tiles used for the Moon experiments (testing), showcasing the variation of the local geomorphology. Taken from RMaM–2020 (Bickel et al., 2021c).

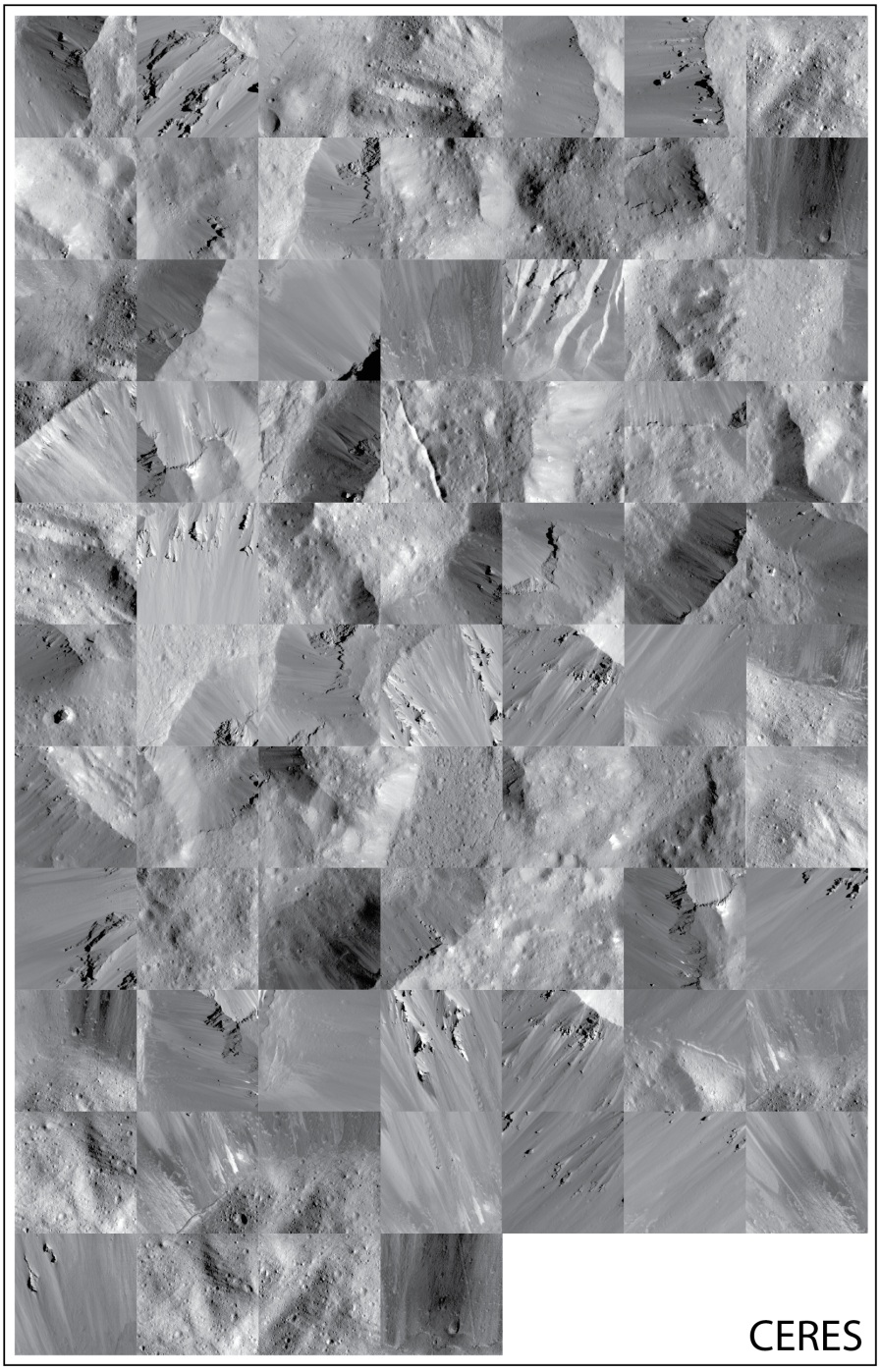


Figure A.29: All image tiles used for the Ceres experiments (testing), showcasing the variation of the local geomorphology.

A labeled image dataset for deep learning-driven rockfall detection on the Moon and Mars
Published 2021 in Frontiers in Remote Sensing
Bickel, V.T., Mandrake, L., Doran, G., 2021
https://doi.org/10.3389/frsen.2021.640034

HiRISE image ID				
ESP_014260_1675	ESP_016726_1720	ESP_017372_1710	ESP_018255_1680	ESP_024286_1910
ESP_025640_1730	ESP_025798_1675	ESP_026101_1750	ESP_026997_1660	ESP_029319_1730
ESP_030703_1675	ESP_033279_1905	ESP_034980_1910	ESP_035186_1670	ESP_036624_1720
ESP_037204_1710	ESP_037797_1665	ESP_038681_1745	ESP_039063_1660	PSP_001377_1685
PSP_005057_1695	PSP_007944_1735	PSP_008946_1715	PSP_009913_1910	PSP_010501_1645
ESP_011926_1720	ESP_012585_1755	ESP_018770_1730	ESP_019165_1765	ESP_019829_1900
ESP_016146_1730	ESP_016211_1655	ESP_016647_1725	ESP_017280_1725	ESP_020259_1670
ESP_021520_1550	ESP_037700_1710	ESP_062655_1670	ESP_027775_1675	ESP_038250_1880
ESP_025156_1965	ESP_043293_1740	ESP_024576_1900	PSP_009222_1660	

Table A.5: All HiRISE image IDs used for RMaM–2020.

NAC image ID				
M139348293LC	M126724656LC	M111422030LC	M122191322RC	M172730399LC
M101313293LC	M102493519LC	M103717945RC	M103831840RC	M103983419LC
M104305550LC	M104806008LC	M105614904RC	M105637059RC	M105801850LC
M106209806RC	M109026539LC	M110784724RC	M111293210LC	M111735067RC
M111843992RC	M112312113LC	M113934119LC	M114254548LC	M117419913RC
M121539000LC	M121987140RC	M124416659LC	M124797072RC	M127009259RC
M129621462LC	M133111610RC	M135222913LC	M137340408LC	M137340408RC
M137665718RC	M137727162LC	M138107059LC	M142625106LC	M144849957RC
M147055119LC	M148184487LC	M149724048LC	M152445210RC	M157330070RC
M158463234LC	M162969274LC	M164777545RC	M170865005RC	M180329337LC
M180994913RC	M183703084RC	M183710231RC	M186133886LC	M187571006RC
M189115113LC	M189929928LC	M1095658447LC	M1095815085RC	M1098452076LC
M1098608807LC	M1099102248LC	M1102495759RC	M1105396233RC	M1107889593LC
M1107889593RC	M1108925446LC	M1109783643LC	M1114050328LC	M1115854283LC
M1116422710LC	M1118617174LC	M1119753979LC	M1120947515RC	M1122750954RC
M1122758066LC	M1123376589LC	M1126054875LC	M1128650716LC	M1128806612RC
M1129084350RC	M1131700619LC	M1135873231RC	M1136377906RC	M1136911243LC
M1138595822RC	M1138653725LC	M1138987659LC	M1144394872RC	M1148022168LC
M1148022168RC	M1150378215RC	M1151459843RC	M1153816152LC	M1153931039LC
M1162148129RC	M1166857082LC	M1169267345LC	M1169324597LC	M1173413880LC
M1179831840RC	M1181223882LC	M1182551704LC	M1184156745RC	M1184540887LC
M1187686867RC	M1187961349LC	M1190456337LC	M1196943961LC	

Table A.6: All NAC image IDs used for RMaM–2020.

A.3 SUP: Drivers of Rockfalls

Impacts drive Lunar Rockfalls over Billions of Years
Published 2020 in Nature Communications
Bickel, V.T., Aaron, J., Manconi, A., Loew, S., Mall, U., 2020
https://doi.org/10.1038/s41467-020-16653-3

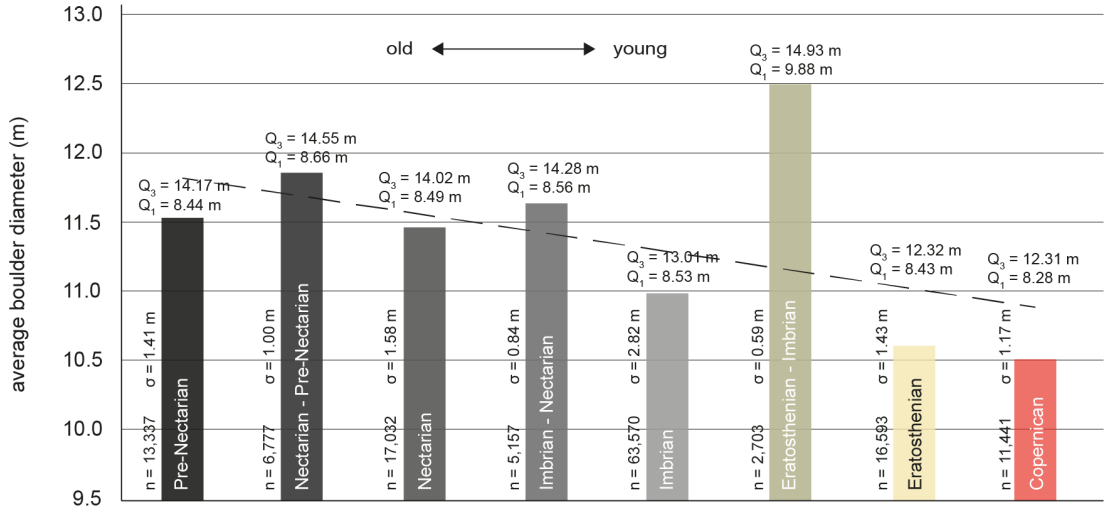


Figure A.30: Average boulder diameter as function of terrane age. Rockfalls in older terranes show systematically larger average boulder diameters, as highlighted by the linear fit. The used number of rockfalls (n), the standard deviation (σ), and the first and third quartiles ($Q1$ and $Q3$) of each age class are shown.

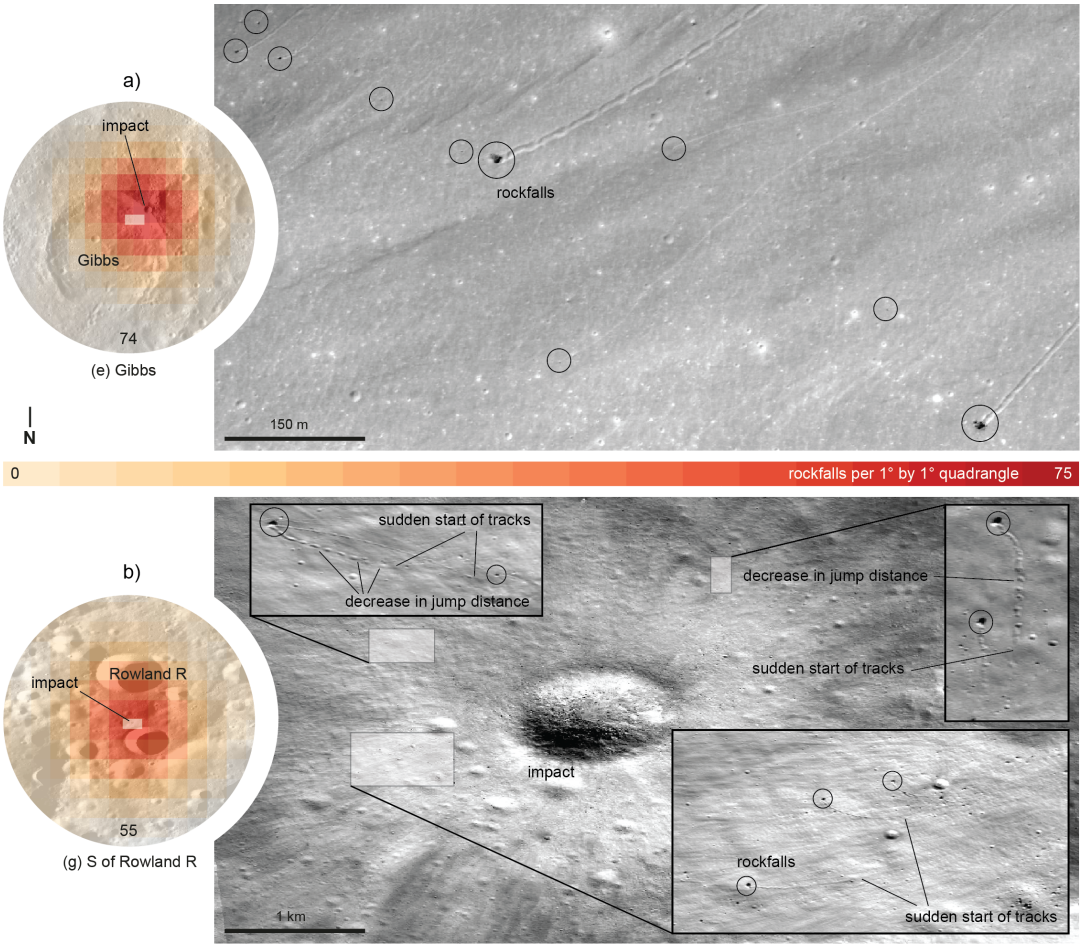


Figure A.31: Examples of impact-induced rockfalls. a) rockfalls (circled) triggered by recent impact on Gibbs crater's NE slope. b) rockfalls triggered by recent impact south of Rowland R crater. The three insets show tracks with sudden starts as well as gradually decreasing boulder jump distances, indicating that the boulders have initially been airborne. In both examples, the rockfalls radiate away from the respective recent impact craters, further supporting the hypothesis of an impact-induced boulder displacement. The white rectangles in the heat map insets indicate the location of the two background NAC images. The peak count of spatial rockfall density is shown in the heat map insets per 1 by 1°quadrangle. Details of LRO NAC (LROC) images M185325951RC, M187007205LC, and M128041655LC. NAC Image credits to LROC/ASU/NASA.

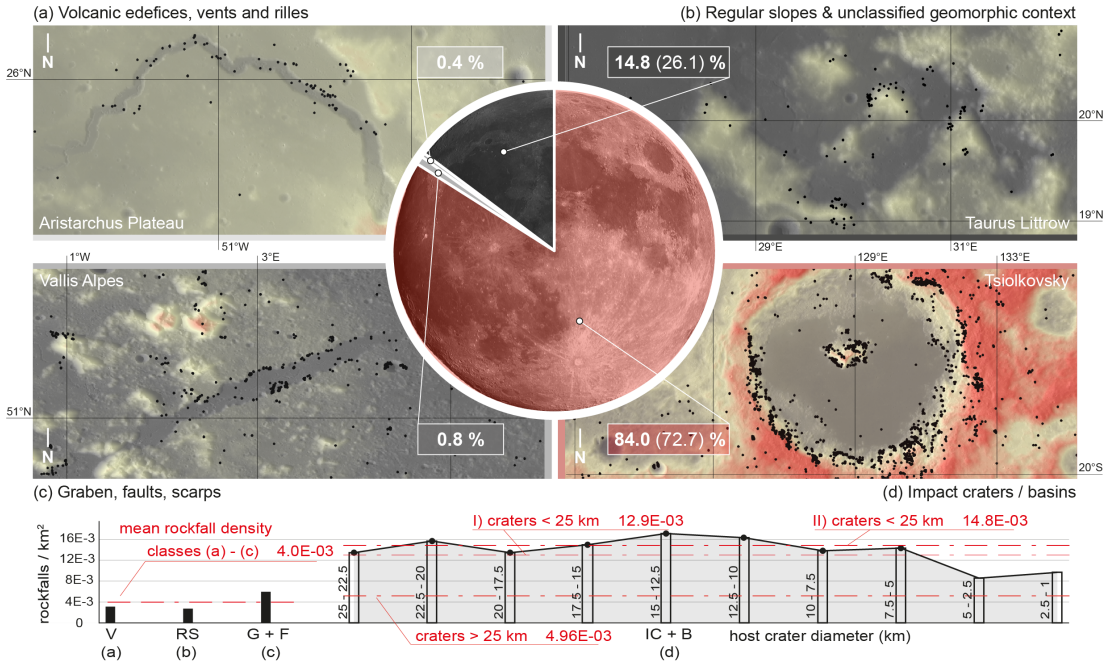


Figure A.32: Rockfall counts throughout the different geomorphic contexts. Geomorphic settings that host lunar rockfall features: impacts / basins, graben, faults, scarps, volcanic edifices, vents and rilles, and regular slopes & unclassified geomorphic context. Black dots indicate detected rockfalls. The vast majority of recent lunar rockfalls occur in impacts, basins, and on associated central peaks (see d). The pie chart and the bold percentages indicate the rockfall count with considering craters between 1 and 5 km in diameter (Robbins, 2018); the numbers in brackets indicate the count without considering the 1 to 5 km crater population. The box plot shows the (mean) rockfall density per square kilometer for classes (a) through (c) and for craters with diameters between 1 and 25 km (in 10 bins) as well as the overall averages (red lines and numbers); I) denotes an average with the 1 to 5 km crater population, II) without. Craters < 25 km generally feature higher rockfall densities and craters with sizes between 5 and 25 km have similar rockfall densities, while craters smaller 5 km show slightly reduced densities. The diameter range between 1 and 25 km has been chosen as craters in this size range mostly consist of 'slope area' (i.e., no or a small, flat crater floor), whereas larger craters feature increasingly less 'slope area' but more 'flat area' in the center of the crater, potentially biasing the area normalization. Elevation model (Scholten et al., 2012) and WAC mosaic in the background (Wagner et al., 2015), red colors indicate high and black colors low elevations (in the map insets).

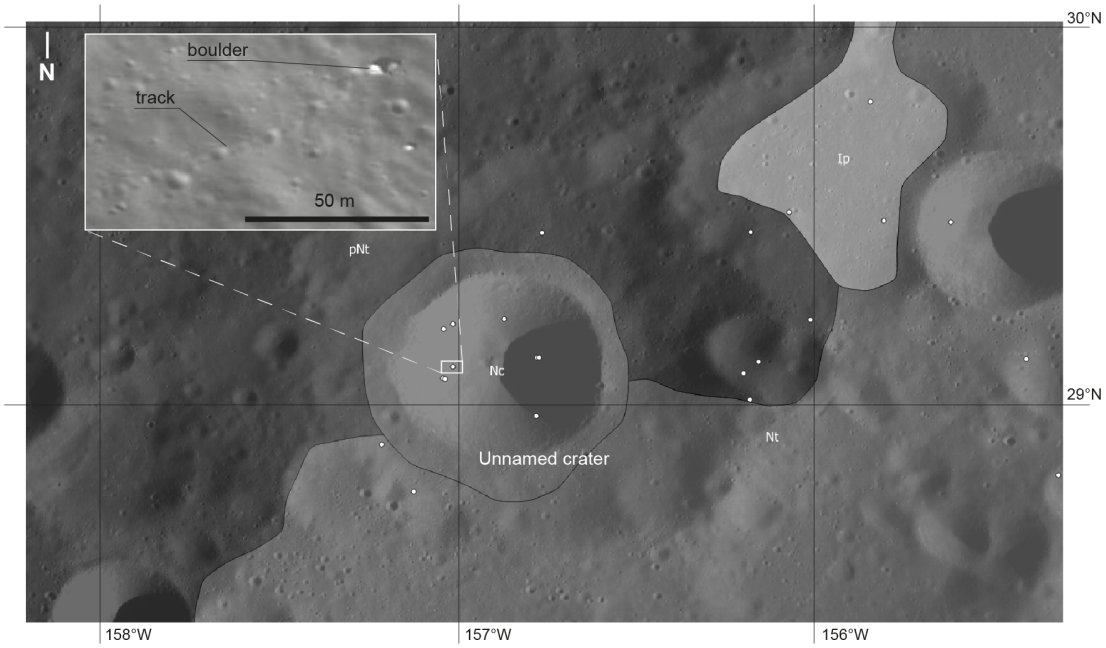


Figure A.33: Example for rockfalls in ancient (Nectarian) terranes. Rockfalls (white shapes) in a Nectarian crater (Nc) prove that these ancient terranes have been subject to geologically recent erosion or are still being eroded today. Other rockfalls are located in surrounding Nectarian (Nt), pre-Nectarian (pNt), and Imbrian terranes (Ip). Inset shows a detail of one of the rockfalls (the boulder and its track) in the unnamed crater. WAC mosaic in the background (Wagner et al., 2015), geological map taken from USGS (2013) and Fortezzo, Hare (2013).

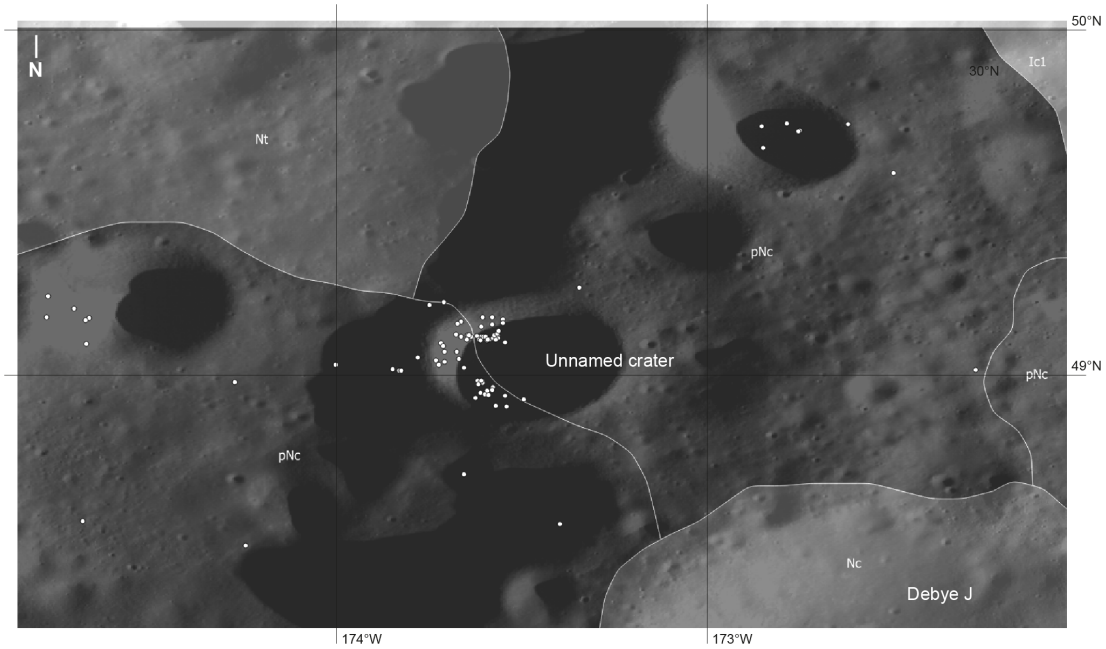


Figure A.34: Example for potentially mis-classified (epoch-wise) rockfalls. This example illustrates the influence of potentially mis-classified (epoch-wise) craters: The rockfalls (white shapes) in the unnamed crater are categorized as pre-Nectarian (pNc) although the crater might actually be younger. The map appears not to consider this particular crater as a geologic contact runs right through it (white line). WAC mosaic in the background (Wagner et al., 2015), geological map taken from USGS (2013) and Fortezzo, Hare (2013).

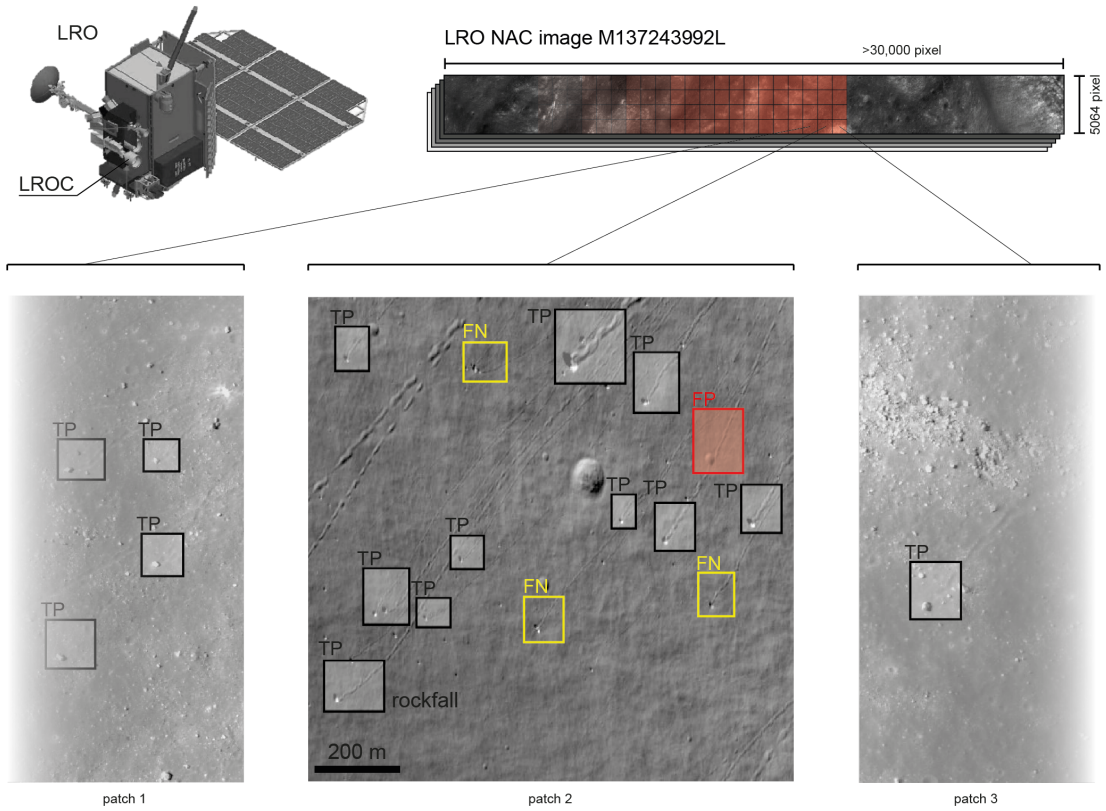


Figure A.35: CNN-driven detection pipeline. Detections made by the CNN in LRO NAC image M137243992L taken over Atlas crater, lunar nearside. True positives (correct detections, TP, black), false positives (false detections, FP, red), and false negatives (missed detections, FN, yellow) are indicated. The diameter of the CNN-inferred bounding box can be used to estimate the diameter of the detected rockfalls (Bickel et al., 2018). Detections and bounding boxes have been visually enhanced (colors, infill, labels) to help illustrate the underlying concept. NAC Image credits to LROC/ASU/NASA.

Global Drivers and Transport Mechanisms of Lunar Rockfalls
Submitted to the Journal of Geophysical Research: Planets
Bickel, V.T., Aaron, J., Manconi, A., Loew, S., in review - might be subject to change

This document includes additional figures that support the scientific findings and conclusions of the main paper, including maps (Figure A.36, Figure A.37, Figure A.38, Figure A.39, Figure A.40, and Figure A.41), plots (Figure A.42, Figure A.44, Figure A.46, Figure A.47, and Figure A.48), photographs (Figure A.43 and Figure A.45), and tables (Table A.7).

Dataset	Description	Reference/Source
Elevation	Topographic elevation	LOLA (n.d.)
Slope angle	Steepness of slopes	∼
Slope aspect	Direction of slopes	∼
Free-air gravity	Unprocessed gravity anomalies	Lemoine et al. (2014)
Bouguer gravity	Topography-removed gravity anomalies	∼
Tidal displacement	Radial displacement of the lunar crust	Thor et al. (2020)
Minimum temperature	Midnight temperature	Moseley et al. (2020a)
Maximum temperature	Noon temperature	∼
Temperature amplitude	Difference noon-midnight temperature	∼
Solar onset	Onset of the Sun over the lunar day	∼
Thermal conductivity	Heat conduction capability	∼
Effective albedo	Variation of albedo as a function of latitude	∼
Rock abundance	Rock fraction	Bandfield et al. (2011)
Nightside albedo	Far-UV (Lyman-alpha) surface reflectance	Gladstone et al. (2012)
Impact craters >20 km	Global catalog of craters larger than 20 km	Kadish et al. (2011)
Lunar graben	Global catalog of lunar graben	Nahm et al. (2018)
Lunar lobate scarps	Global catalog of lunar lobate scarps	Watters et al. (2019)
Lunar wrinkle ridges	Global catalog of lunar wrinkle ridges	Thompson et al. (2017)
Shallow moonquakes	Catalog of all recorded shallow moonquakes	Nakamura et al. (1979)

Table A.7: Summary of all used global, geophysical, auxiliary datasets, as discussed in chapter 3.2.

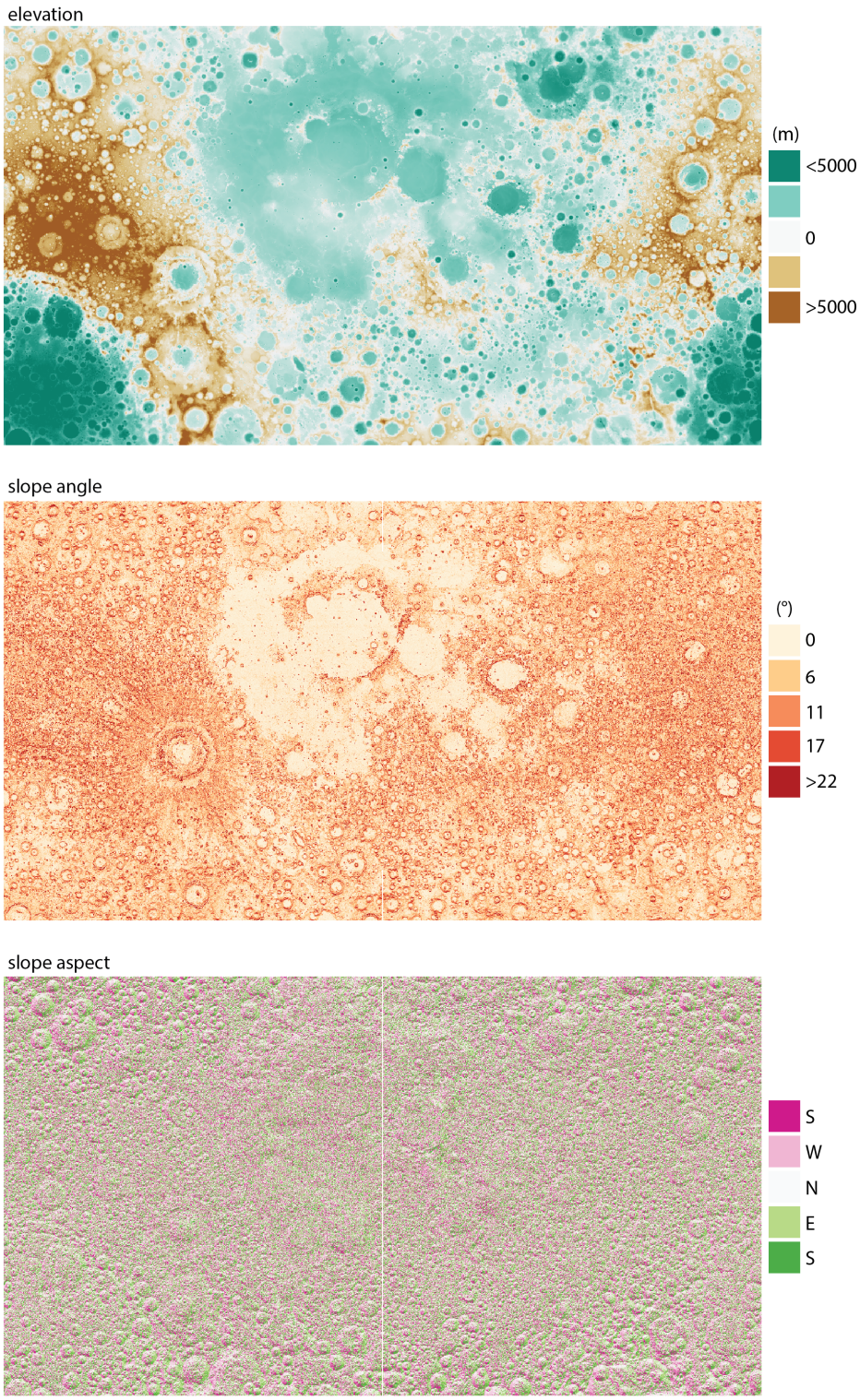


Figure A.36: Auxiliary maps (elevation, slope angle, slope aspect) as used for this study (Mercator projections, 70°N to 70°S, 180°W to 180°E, for visualization only). Please refer to the references cited in section 3.2 (main paper) and Table A.7 for more details.

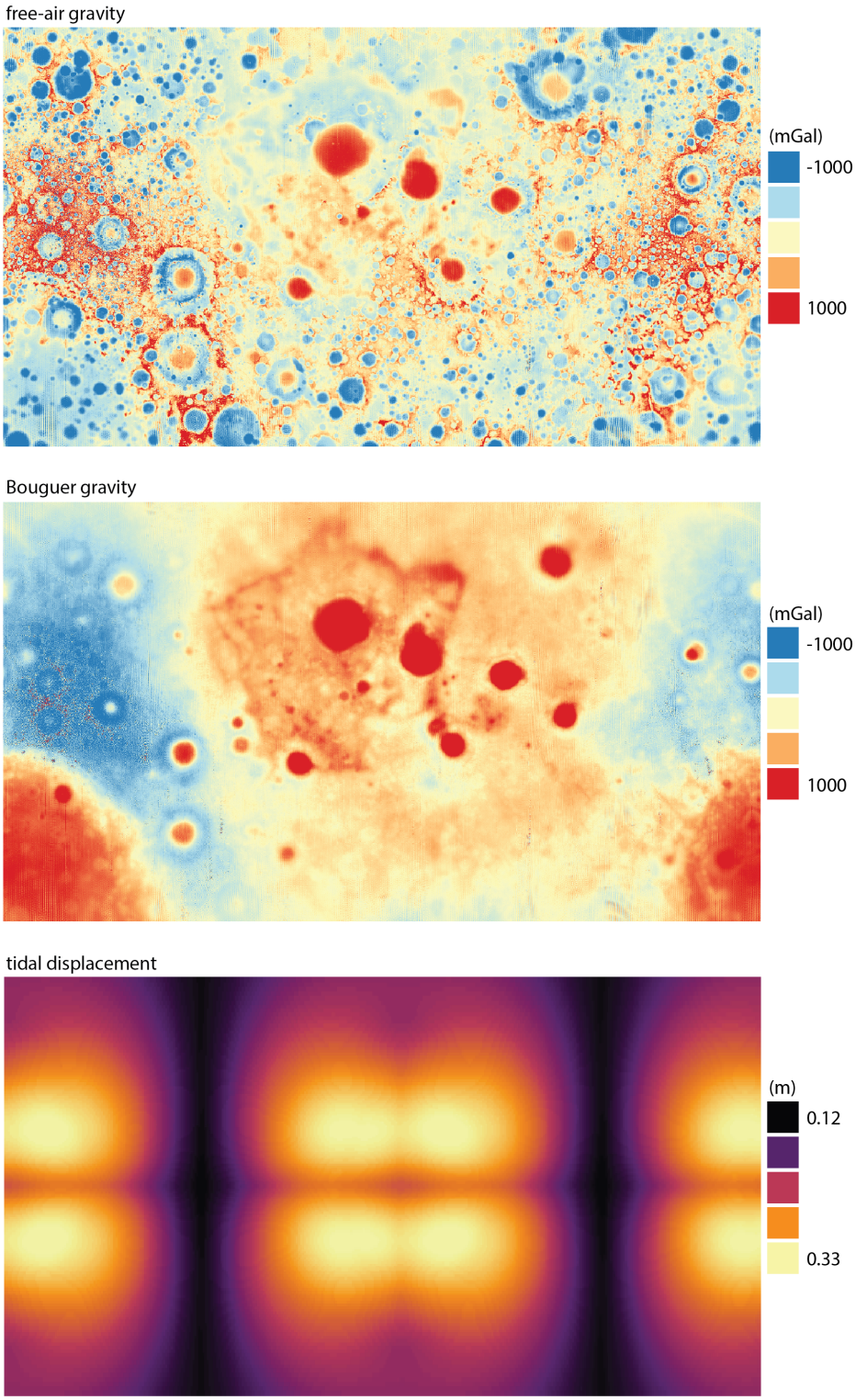


Figure A.37: Auxiliary maps (free-air gravity, Bouguer gravity, tidal displacement) as used for this study (Mercator projections, 70°N to 70°S, 180°W to 180°E, for visualization only). Please refer to the references cited in section 3.2 (main paper) and Table A.7 for more details.

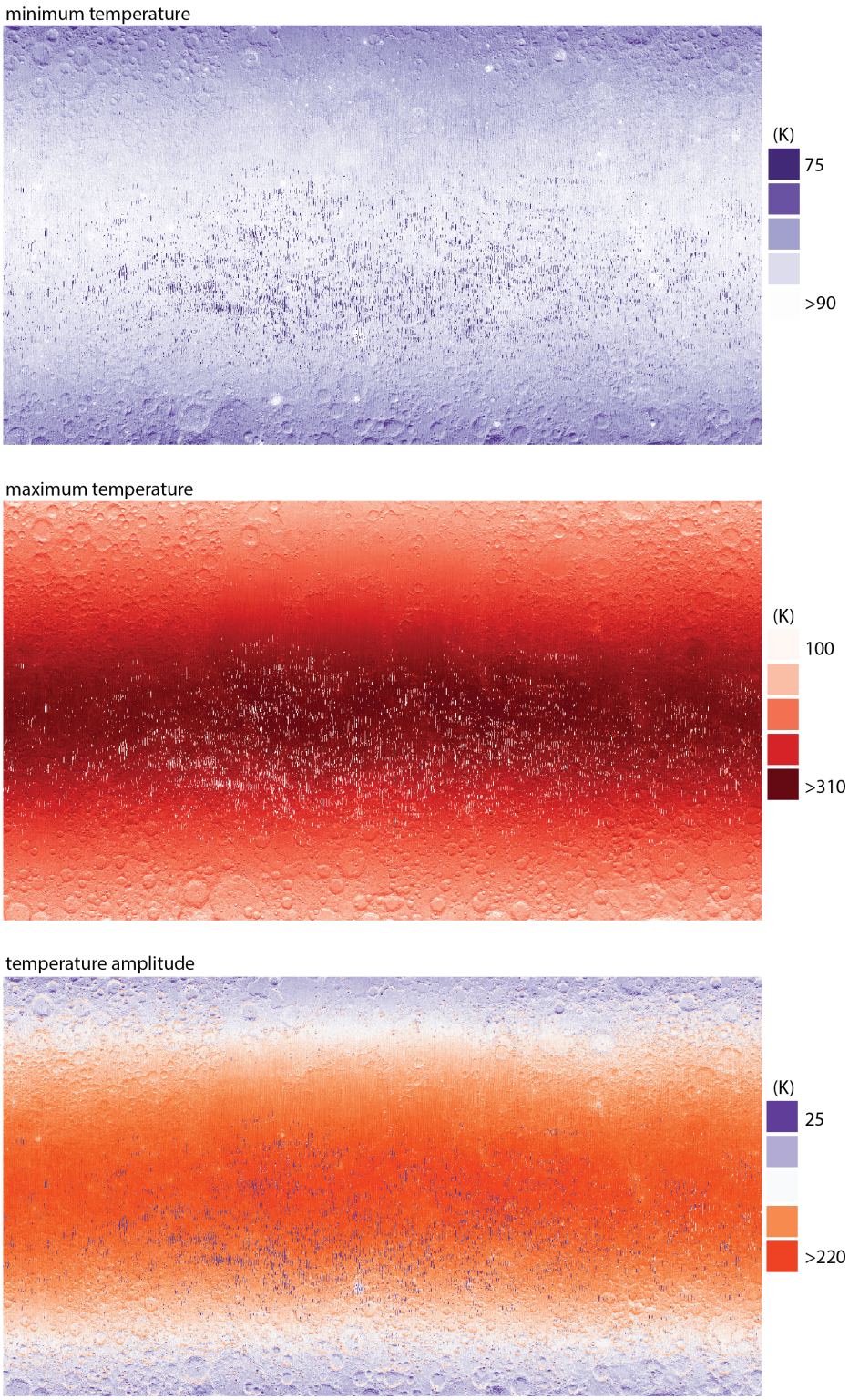


Figure A.38: Auxiliary maps (minimum temperature, maximum temperature, temperature amplitude) as used for this study (Mercator projections, 70°N to 70°S, 180°W to 180°E, for visualization only). Please refer to the references cited in section 3.2 (main paper) and Table A.7 for more details.

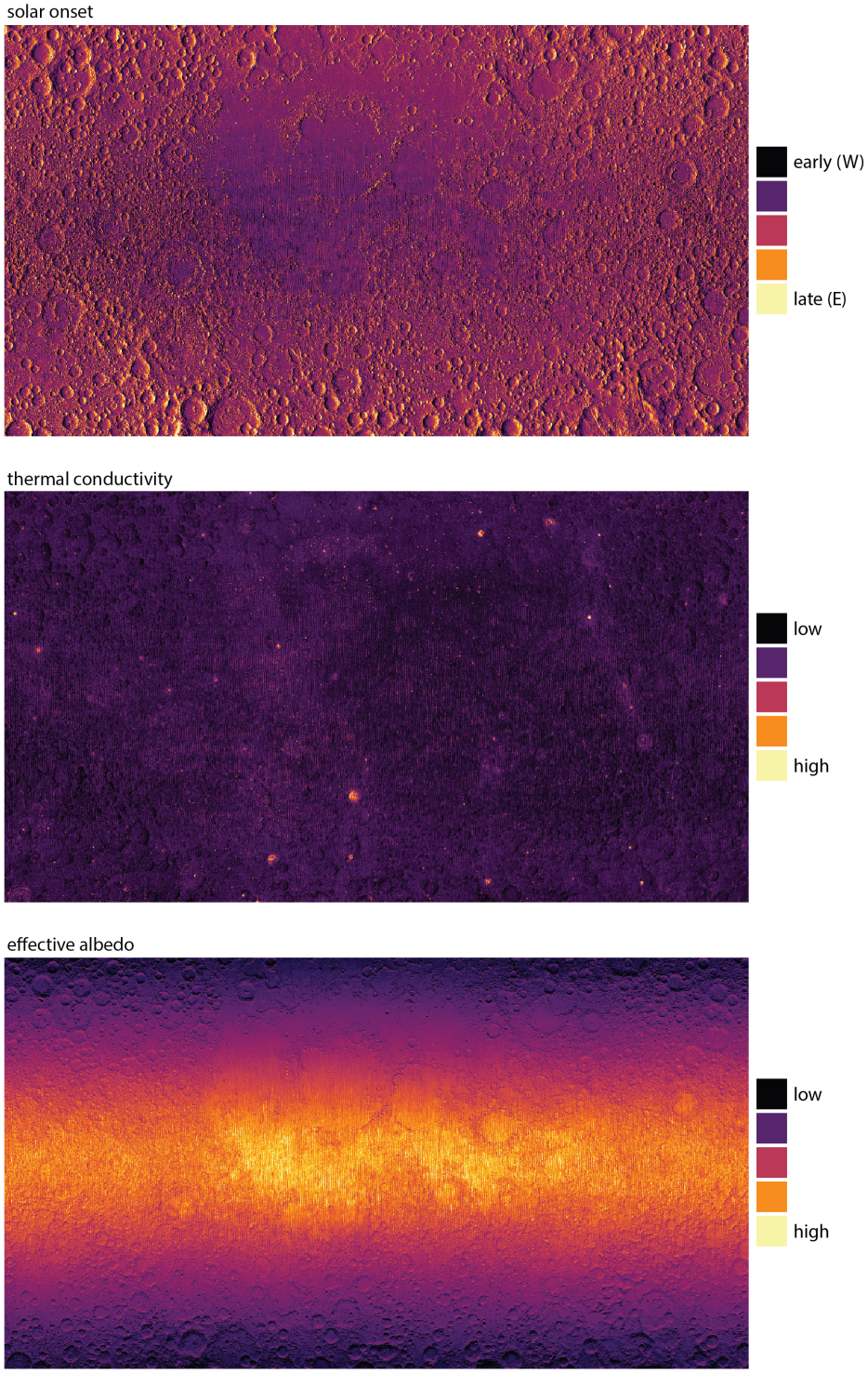


Figure A.39: Auxiliary maps (solar onset, thermal conductivity, effective albedo) as used for this study (Mercator projections, 70°N to 70°S, 180°W to 180°E, for visualization only). Please refer to the references cited in section 3.2 (main paper) and Table A.7 for more details.

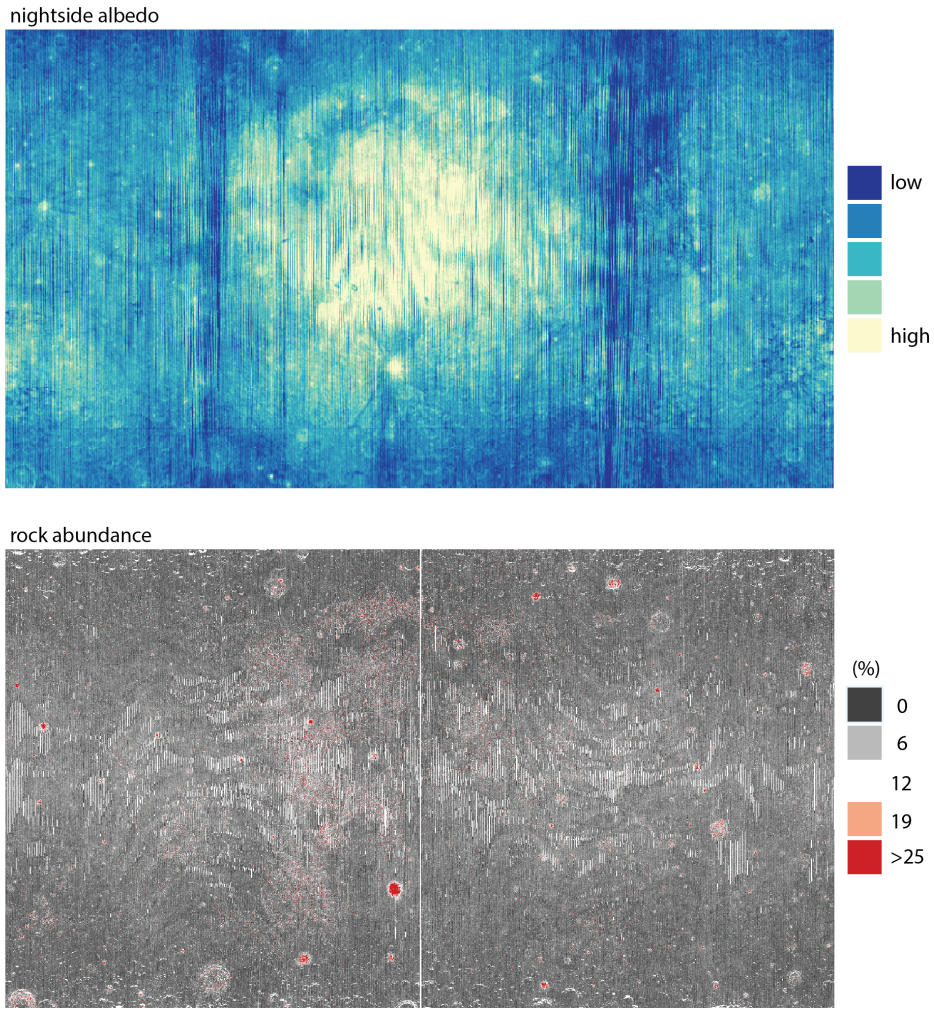


Figure A.40: Auxiliary maps (nightside albedo, rock abundance) as used for this study (Mercator projections, 70°N to 70°S, 180°W to 180°E, for visualization only). Please refer to the references cited in section 3.2 (main paper) and Table A.7 for more details.

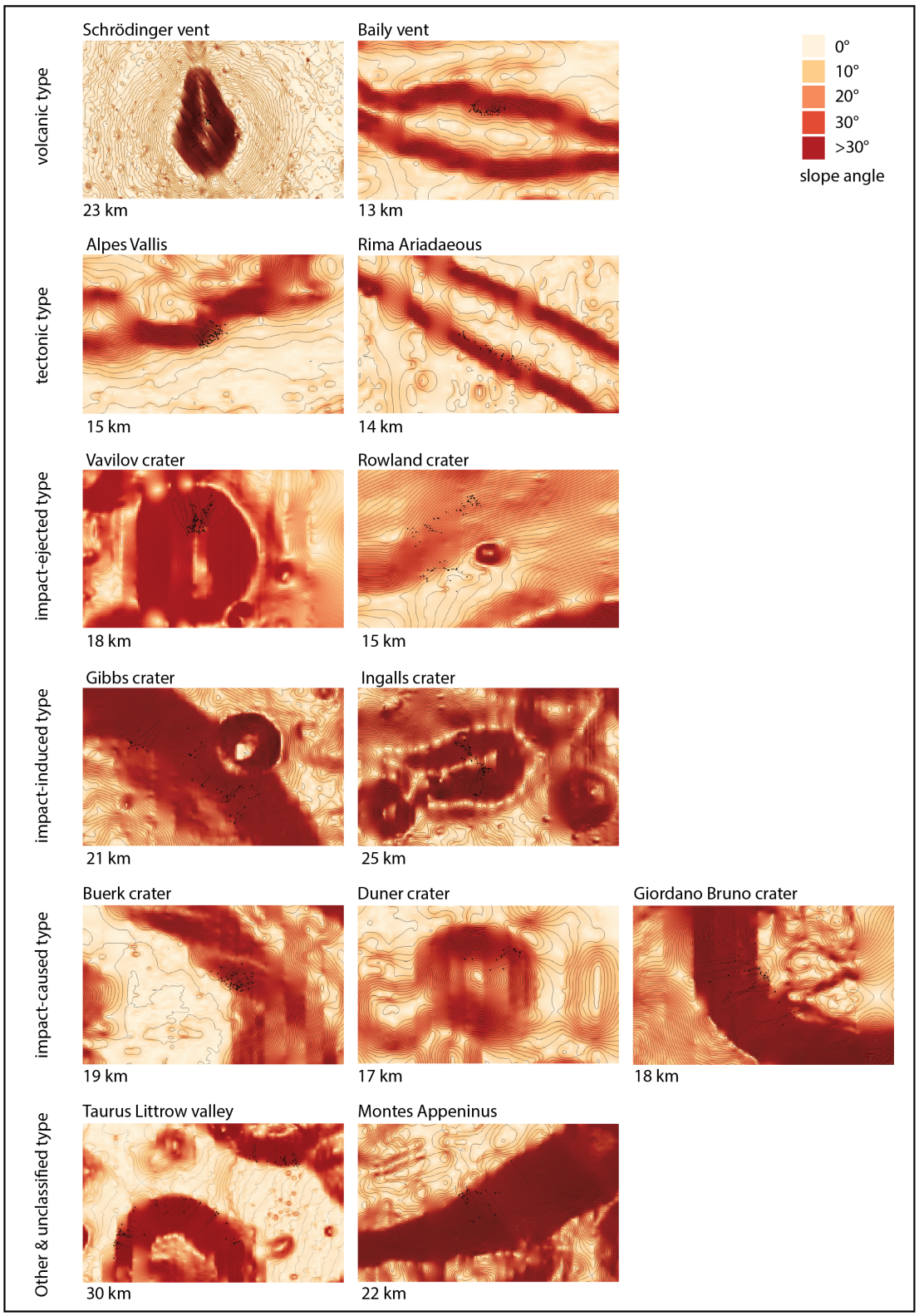


Figure A.41: Overview of all 13 AoIs, featuring elevation contour lines (LOLA DEM) and slope angles. AoIs are sorted according to their geomorphic context (type). AoI width is shown at the bottom of each inset.

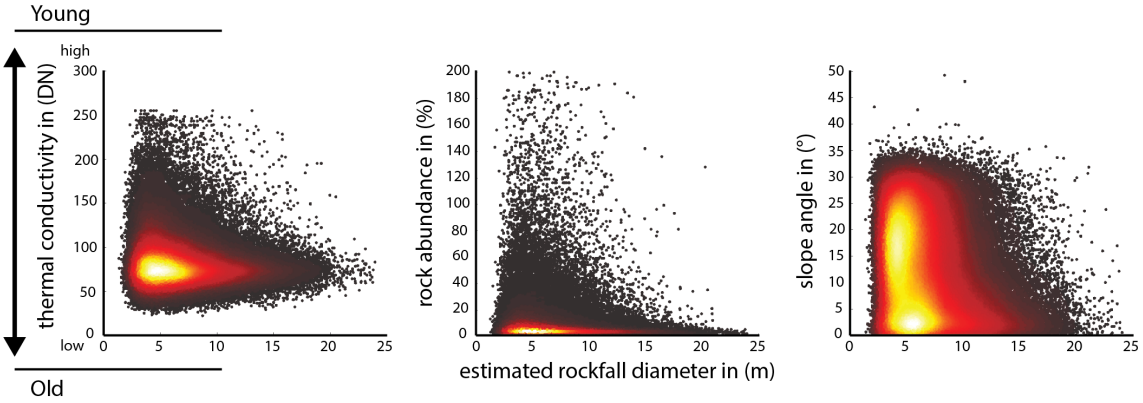


Figure A.42: Relation of estimated boulder diameter and thermal conductivity (left), rock abundance (center), and slope angle (right), indicating that rougher and younger terranes host smaller boulder sizes. Thermal conductivity is given in DN (digital number), not in physical numbers.

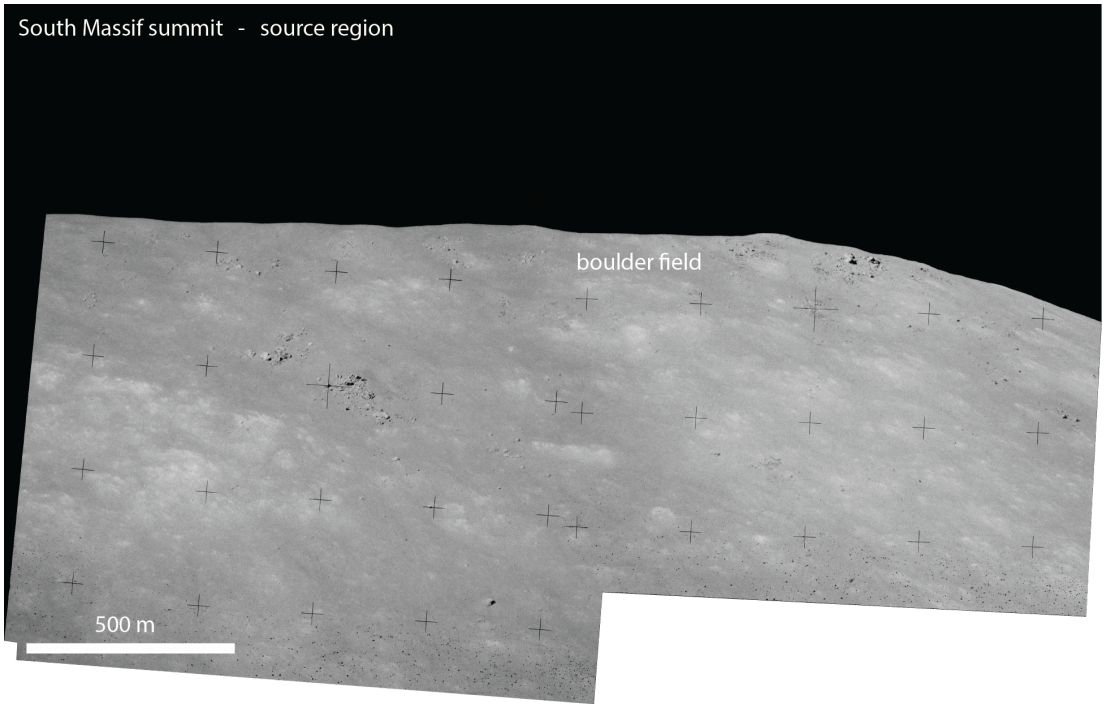


Figure A.43: Apollo 17 Hasselblad frames AS17-139-21208-09 and 21211 taken from Station 6 (bottom of Taurus Littrow valley) towards the southwest, showing the NE-facing summit region of the South Massif (20°N, 30.5°E). The area features a source region type we classify as boulder field-type. Due to the viewing geometry the scale bar only represents an approximation. Modified from a panorama originally assembled by Syd Buxton, retrieved from the Apollo Image Archive: https://www.hq.nasa.gov/alsj/a17/images17.html.

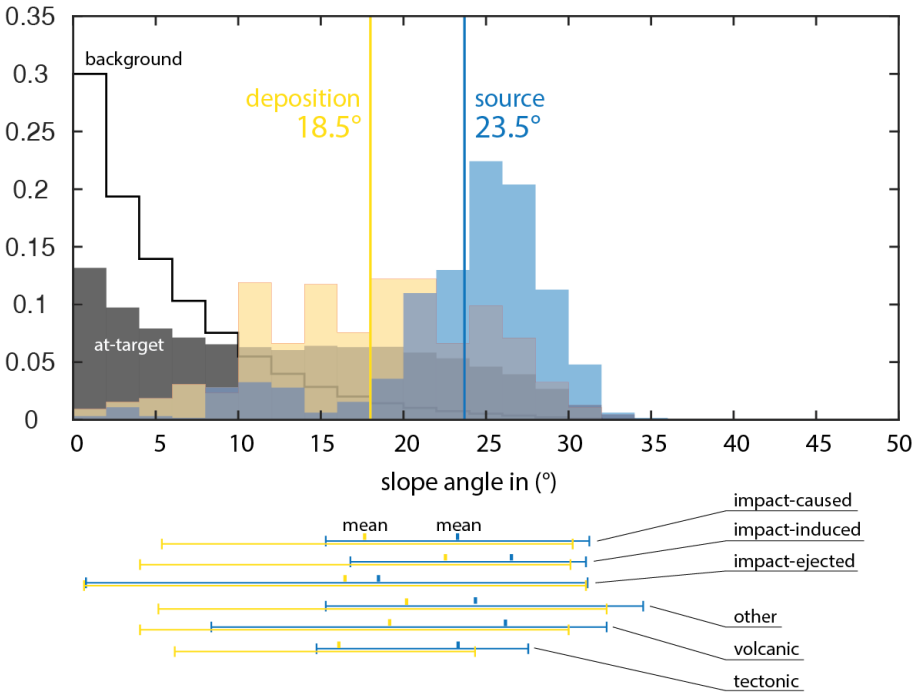


Figure A.44: Distribution of background and at-target deposition area slope angles, as well as local source (blue) and deposition (yellow) region slope angles. The vertical colored lines (top) indicate the distribution mean values; the horizontal colored lines (bottom) represent the range and mean of the deposition and source region slope angles for all geomorphic contexts.

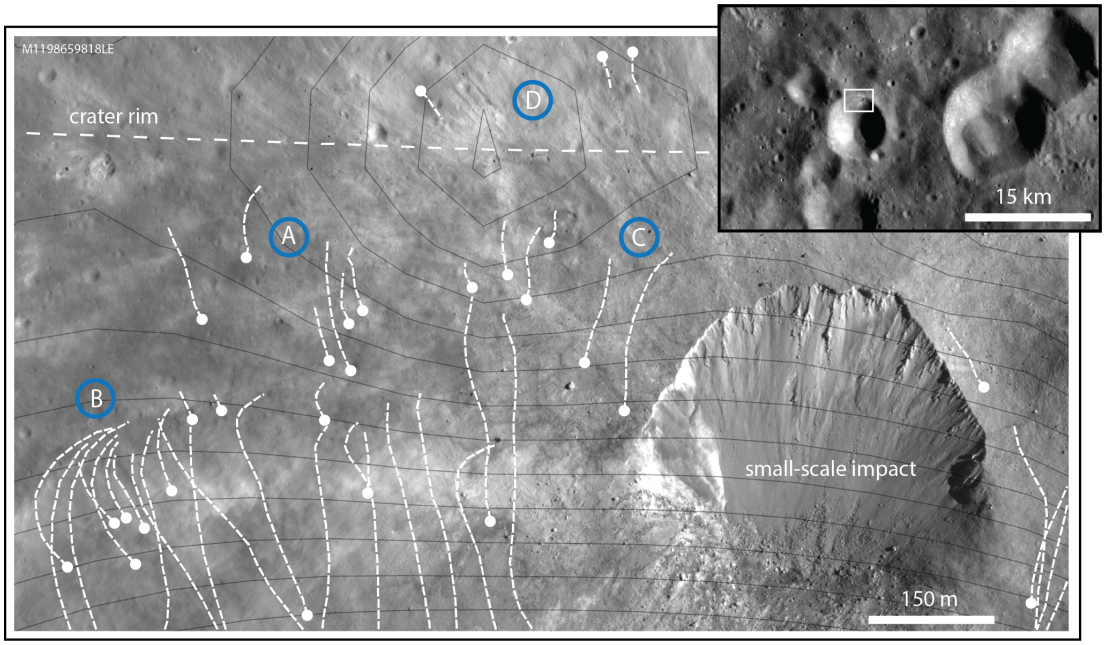


Figure A.45: LRO NAC image of rockfalls (boulders and tracks, white points and lines) in the Vavilov crater AoI (0.8°S, 138°W), where a small-scale impact (indicated) hit the northern crater wall of a larger, older crater (see WAC mosaic overview), close to its rim (represented by dashed white line), i.e., the slope dips towards the North and the South (North is up). We note: A) rockfalls that are likely impact-induced (co-impact), B) rockfalls that either are impact-induced and received a lateral push from the impactor (co-impact) or that represent low-velocity impact-ejecta that hit the slope at an angle (co-impact), C) rockfalls that run towards the impact (white shapes), i.e., are either impact-induced and from higher up the crater slope or are post-impact, i.e., have not been triggered by the small-scale impact, D) potentially impact-induced rockfalls that are located beyond the crater rim. Elevation changes are indicated by black contour lines. Image credits LROC/ASU/GSFC.

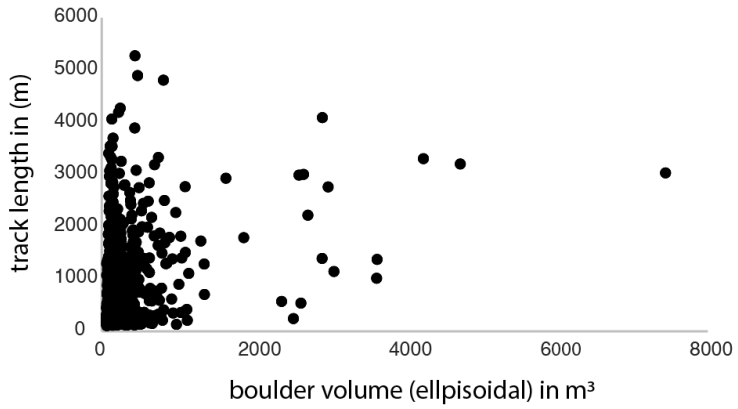


Figure A.46: Ellipsoidal boulder volume vs track length for all thirteen investigated AoIs. The scatter plot does not indicate any obvious relation between the two properties.

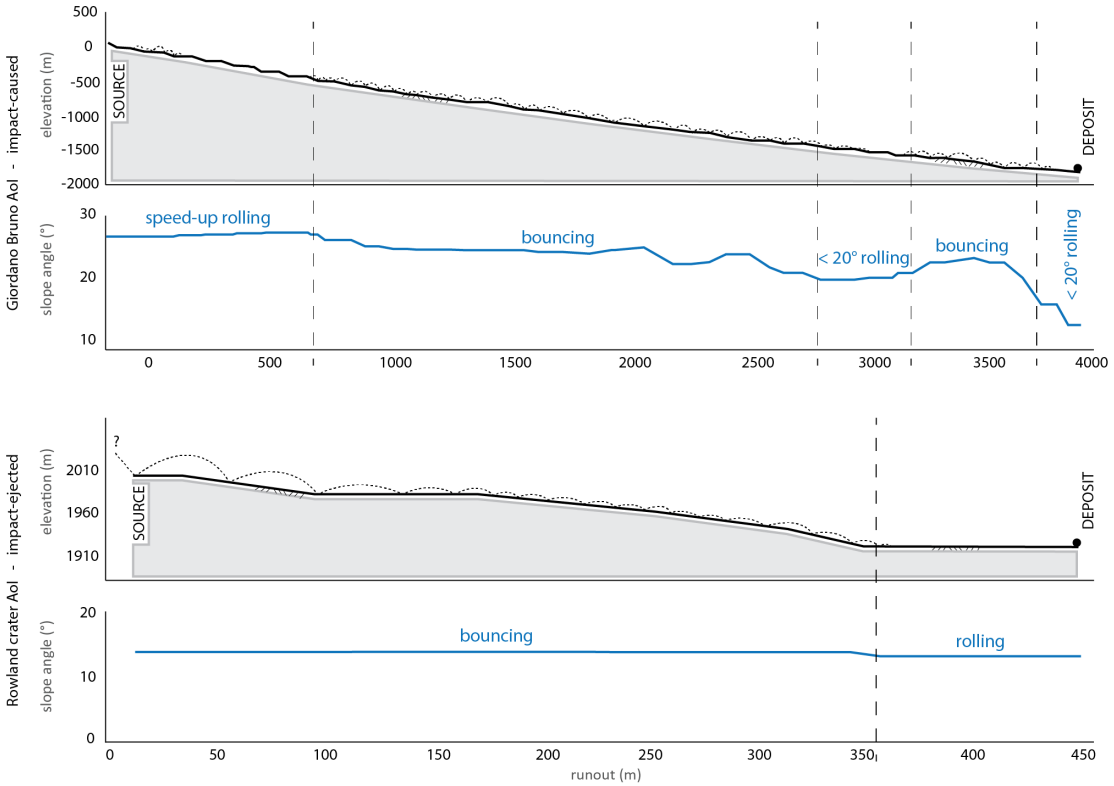


Figure A.47: Example rockfall trajectories from the Giordano Bruno (impact-caused) and Rowland crater (impact-ejected) AoIs. Top: topographic cross-section, bottom: slope angle along the trajectory. The dashed black line represents the trajectory of the rockfall. Bounce widths represent real observations, bounce heights are reconstructed. The x and y axes are not to scale.

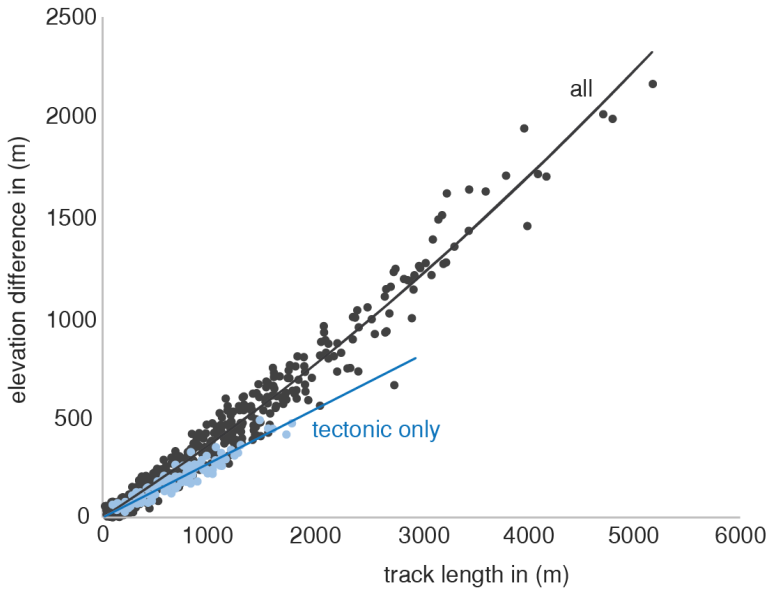


Figure A.48: Relation between track length and elevation drop for the cumulative (black, non-linear) and tectonic (blue, quasi-linear) rockfall populations as measured in the thirteen studied AoIs.

A.4 SUP: Exploration Applications of Rockfalls

Analysis of Lunar Boulder Tracks: Implications for Trafficability of Pyroclastic Deposits
Published 2019 in the Journal of Geophysical Research: Planets
Bickel, V.T., Honniball, C.I., Martinez, S.N., Rogaski, A., Sargeant, H.M., Bell, S.K., Czaplinski, E.C., Farrant, B.E., Harrington, E.M., Tolometti, G.D., Kring, D.A., 2019
https://doi.org/10.1029/2018JE005876

This appendix contains detailed information about the methods and results of this work. Figure A.49 through Figure A.52 present information about the spatial distribution of the measured boulder tracks on the lunar surface, the Isis3 processing steps to produce NAC images for the GIS database, the performed boulder track measurements, as well as details of the wheels and footpads of the investigated vehicles. Figure A.53 through Figure A.58 display all investigated vehicle concepts, details about the performed measurements with regard to the illumination conditions, a characterization of the boulder track database in histograms, a direct comparison between bearing capacity results derived with Terzaghi (Terzaghi, 1951) and Hansen (Hansen, 1970), a plot that shows the calculated N-factors for Terzaghi and Hansen versus the used internal friction angle, as well as a graphical representation of estimated unconsolidated regolith thickness in the areas of interest. Figure A.59, Figure A.60, and Figure A.61 show bearing capacity in relation to geomorphology and slope or depth, respectively, as well as photographs of LRV tracks in different lunar regions. Equations A.6 to A.19 describe additional factors that have been used in Hansen's bearing capacity framework. Table A.8 through Table A.10 describe the selected LPD sites of interest for this study, detailed rover specifications, and provide more information about soil mechanical parameters used for the bearing capacity calculations. Table A.11 through Table A.14 show details of the produced high-resolution DEMs produced with the Ames Stereo Pipeline, provide background information about the used unconsolidated regolith thickness estimates as well as more information about the statistical comparison between mare, highland, and LPD bearing capacities, and provide numerical bearing capacity results for specific depth ranges and slope inclinations. Table A.15 contains the IDs of all used NAC images.

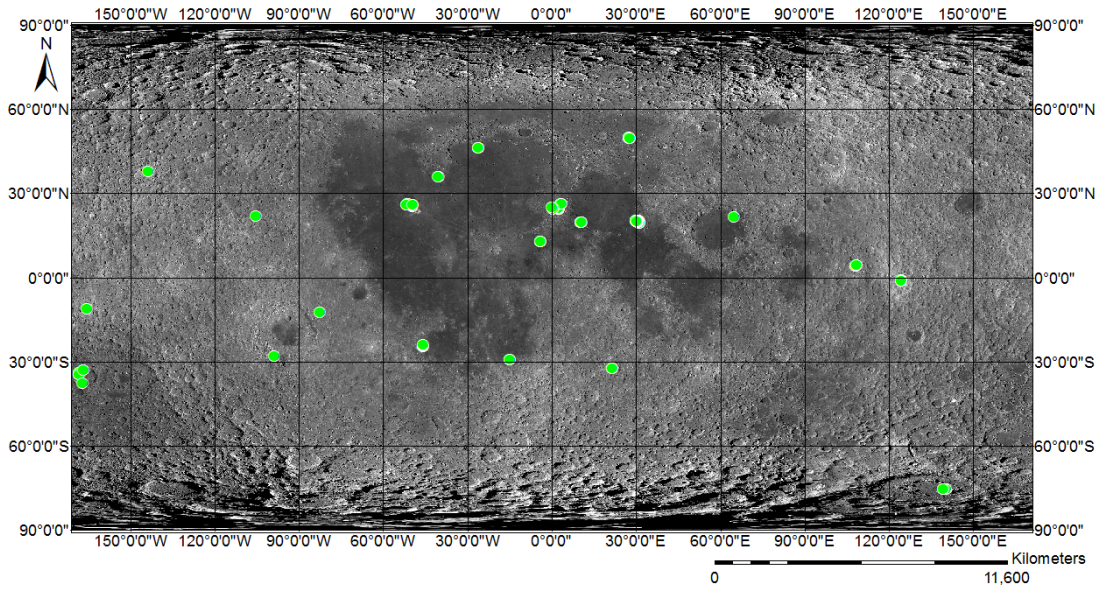


Figure A.49: Locations of all 149 investigated boulder tracks (filled green circles), WAC mosaic in equirectangular map projection.

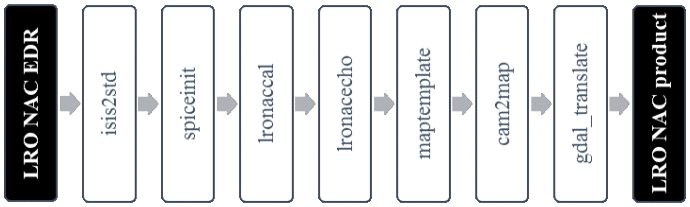


Figure A.50: Isis3 NAC processing pipeline commands: NAC EDRs are processed using these commands.

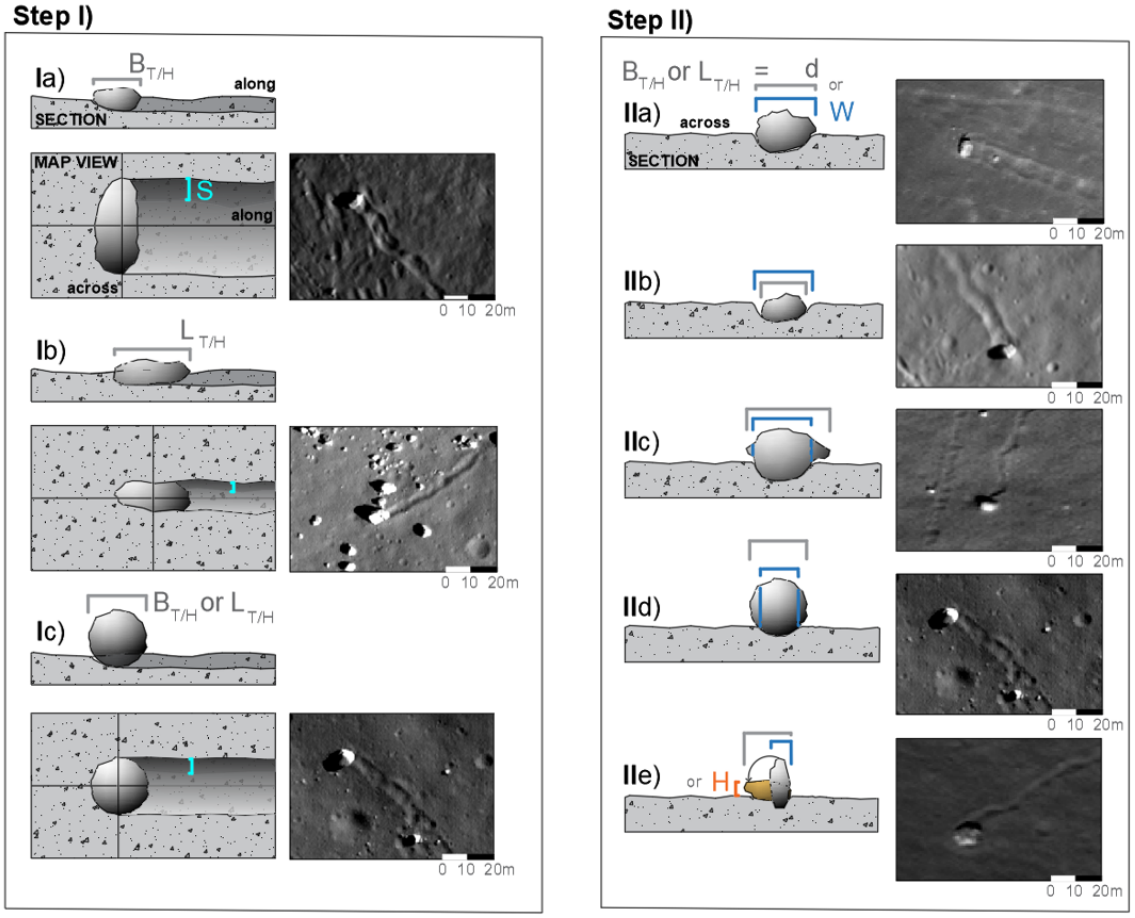


Figure A.51: Determination of each boulder's effective footing dimensions BT/H , LT/H (grey) , track width (blue) and in-track shadow length S (cyan) for usage in Equation 4.1 (Terzaghi, T), Equation 4.2, Equation 4.6, and Equation A.7 to Equation A.17 (Hansen, H), schematic displays map- and section views, as well as examples in map view. Step I: determine the along-track footing dimension, either BT/H for case Ia) or LT/H for case Ib), or one of both for case Ic). Step II: determine the across-track footing dimension (i.e. the missing BT/H or LT/H value) using cases IIa) through IIe). For I) BT/H or LT/H is always the respective boulder diameter; for II) BT/H or LT/H is dependent on the case, i.e. for IIa) with boulder diameter across-track (d) and track width (W) being equal, either one can be used, for IIb) with d $<$ W, the average of d and W is being used, for IIc) and IId) with d $>$ W, the track width W is being used. For IIe), a special case where boulder falls to one side after displacement, the boulder height H is being used, derived using the shadow length of the boulder. Case IIb) has been observed before by Hovland, Mitchell (1971) using Lunar Orbiter Images: as the passing boulder transfers a momentum in the shearing soil, the increased width of the track could be caused by the soil's inertia, which is more pronounced on the Moon due to a lower gravitational acceleration (Hovland, Mitchell, 1971).

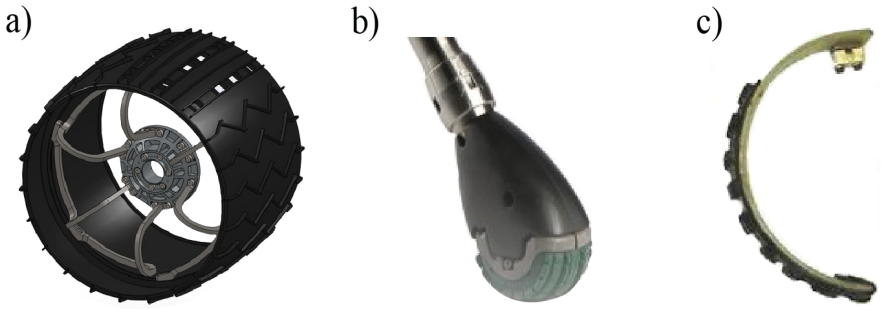


Figure A.52: Wheel and footpad types of investigated rover/robots. a) a wheel, b) a footpad that has been treated like a wheel for the contact area calculation, c) a curved footpad that has also has been treated like a wheel, but with a 'simulated' larger wheel diameter to account for the curvature. Images taken from Boston-Dynamics (2019) and Thingiverse (2014).

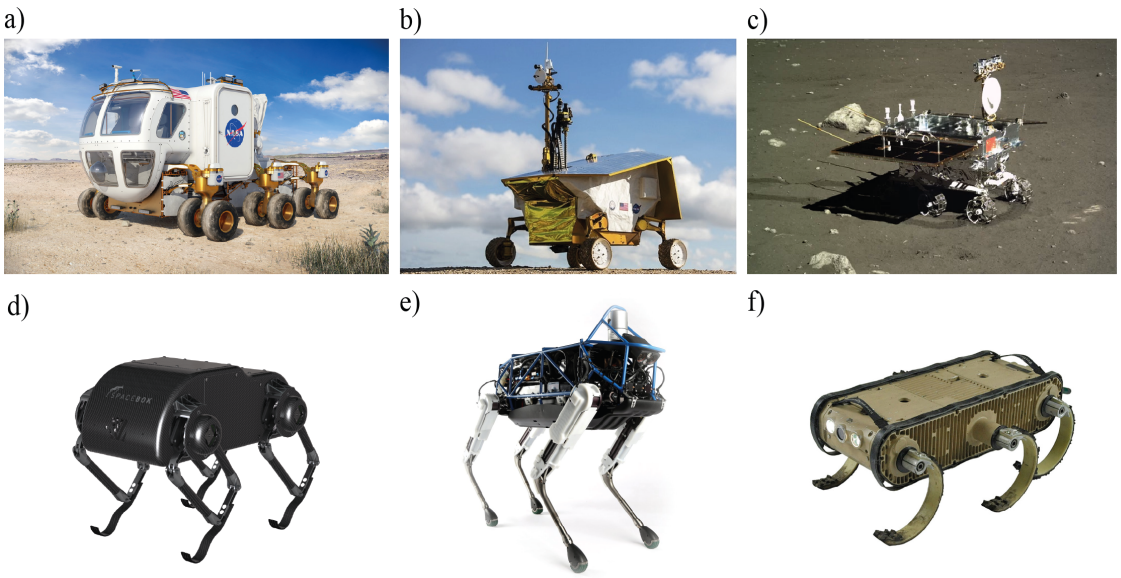


Figure A.53: Investigated rover/robot concepts. a) LER, b) RP, c) Yutu (a-c wheeled), d) SpaceBok, e) Spot, and f) RHex (d-f legged or hybrids). Images taken from Boston-Dynamics (2019), SpaceBok (2017), ESA (n.d.b), Space (n.d.), and CG (2014).

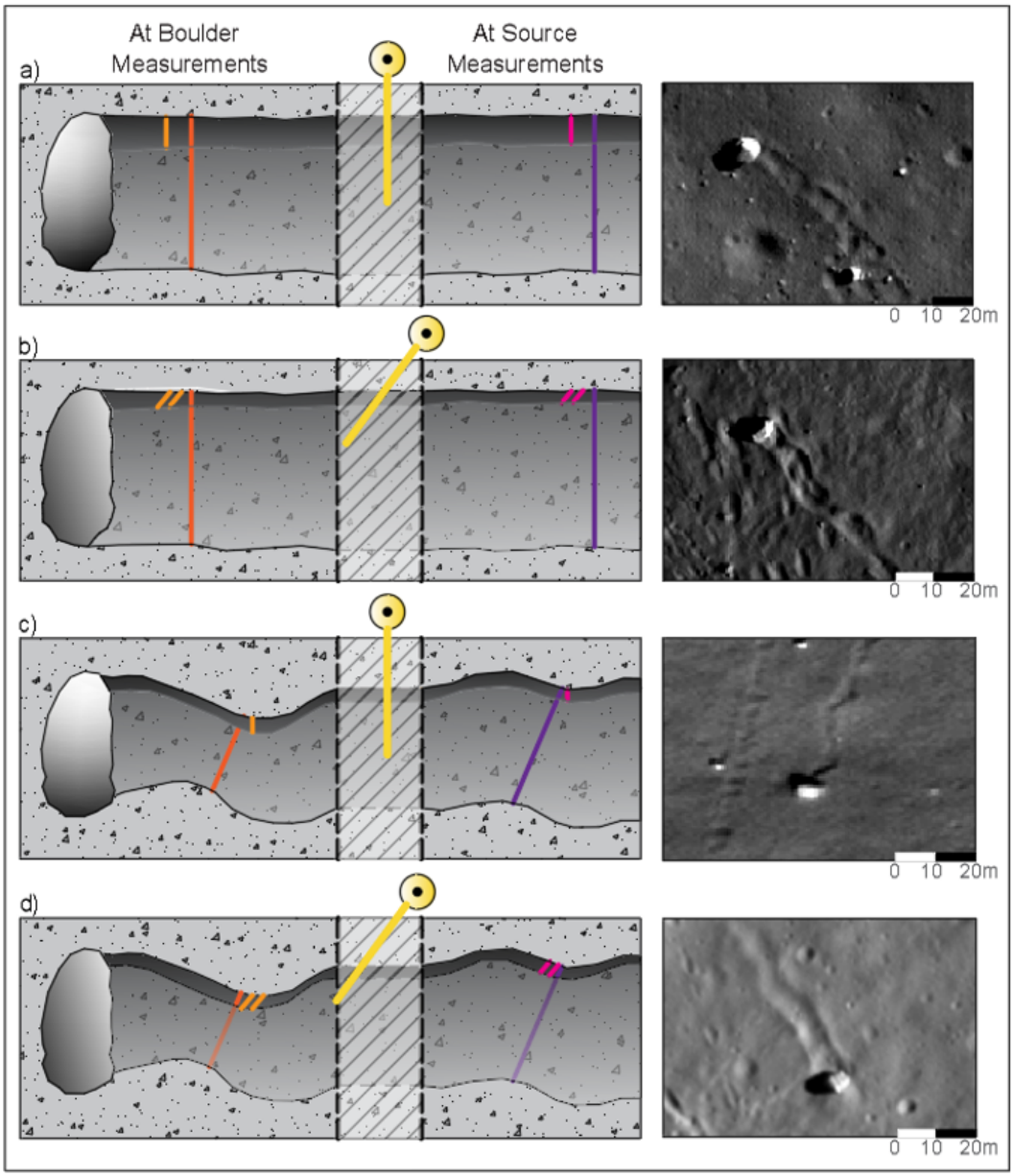


Figure A.54: Overview of all measurements made at the boulder tracks in map/plan view; yellow indicates the Sun illumination direction, dark orange denotes the track width measurement at boulder, light orange the shadow length at boulder, dark purple represents the track width measurement at source, light purple the shadow length at source. Examples are shown on the right.

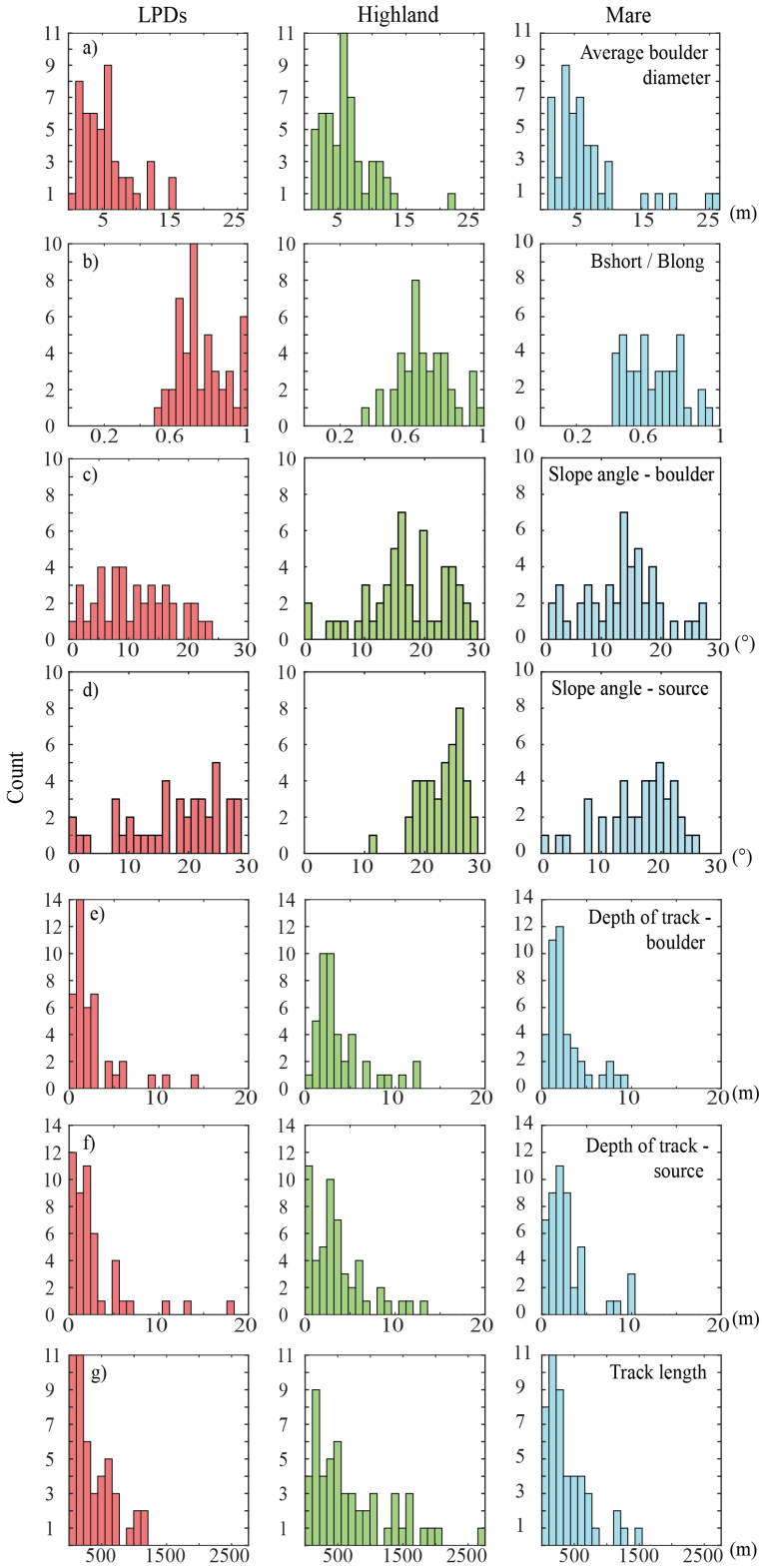


Figure A.55: Dataset characterization with histograms, a) average boulder diameter, b) short over long boulder diameter, i.e. mapview boulder shape, c) slope angle at boulder terminus, d) slope angle at boulder source, e) depth of track at boulder terminus, f) depth of track at boulder source, and g) length of track. In general, data taken from all regions are consistent, but the plots suggest that more boulders in highland areas detach at steeper slope angles and come to rest at steeper slopes angles. In contrast to mare and pyroclastic areas, most boulders in highland areas have been found in impact craters, which tend to be steeper than regular slopes, potentially explaining this observation.

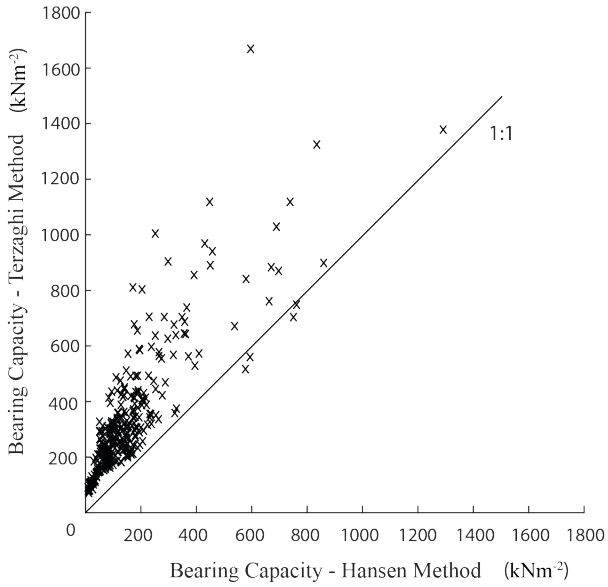


Figure A.56: Bearing capacities for regolith calculated from the Hansen and Terzaghi equations. The degree of correlation indicates the amount of variation between the two approaches. A boulder that plots directly on the 1:1 line indicates that both methods gave identical results. Points above the line give higher values with Terzaghi, while those below the line give higher values with Hansen. Correlation decreases with increasing bearing capacity values.

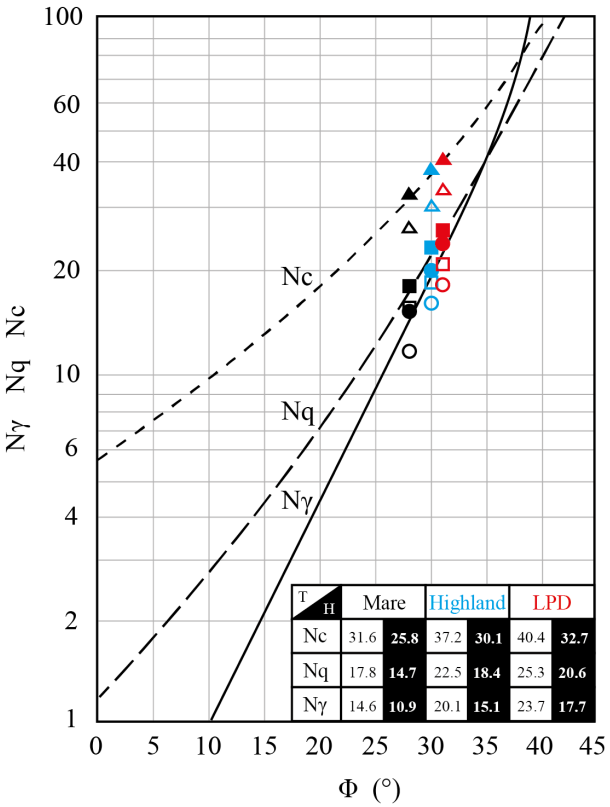


Figure A.57: Calculated N-factors for Terzaghi and Hansen versus the used internal friction angle (Phi) in comparison to Terzaghi N-factor envelopes (black lines). Hollow shapes are values derived with Hansen (1970) and Bowles (1997), filled shapes are values calculated using Terzaghi (1951) and Coduto et al. (2011). Circles denote N_γ, squares denote N_q, diamonds denote N_c. Terzaghi N-factor envelopes derived from Coduto et al. (2011) and EDU (n.d.).

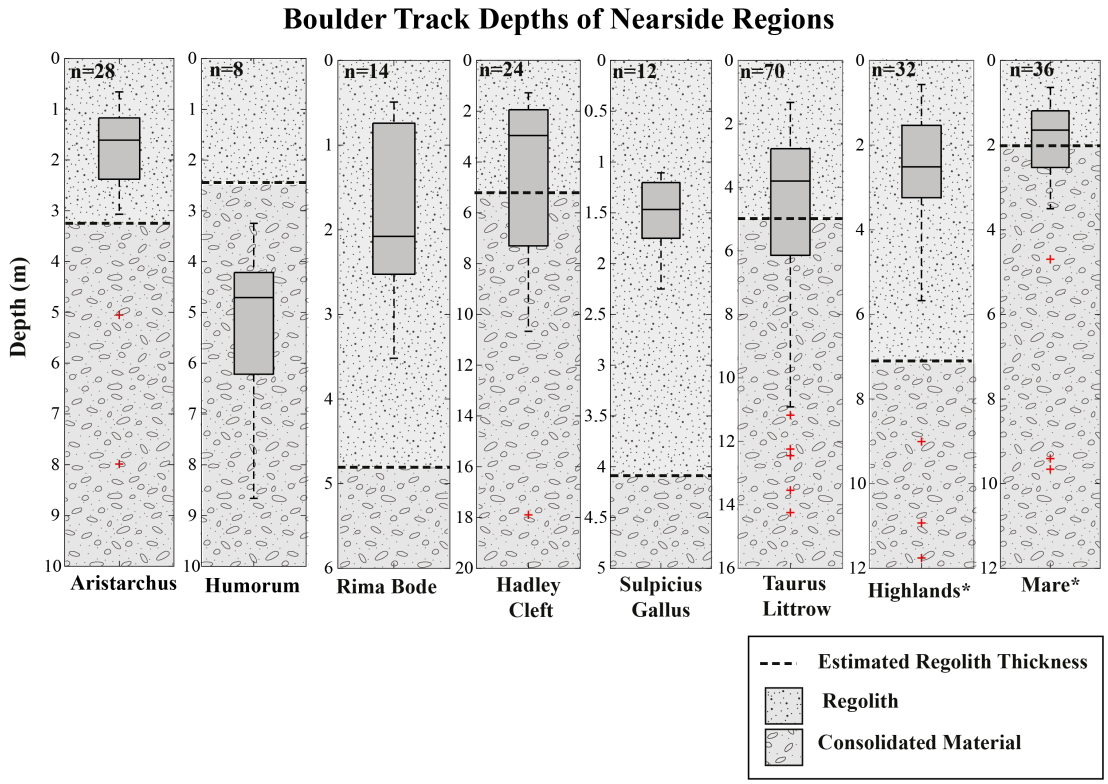


Figure A.58: Comparison of measured boulder track depth and estimated mean unconsolidated regolith thickness in different locations based on work of authors in Table A.12, in section view, surface on top. The dotted line represents the contact between un- and consolidated regolith, the solid horizontal line indicates the median of the measured track depths, red crosses suggest outliers. N values denotes number of boulder tracks in respective region. Boulders reach varying depths and locally penetrate beyond the estimated mean consolidated regolith contact; this could indicate that the depth of the contact is not homogeneously distributed or could locally be situated deeper than suggested by the mean estimates. *Highland and mare data are taken from widespread locations and the average regolith thicknesses within those materials, from the literature, are used to constrain estimated regolith thickness. This explains overlap in sample numbers.

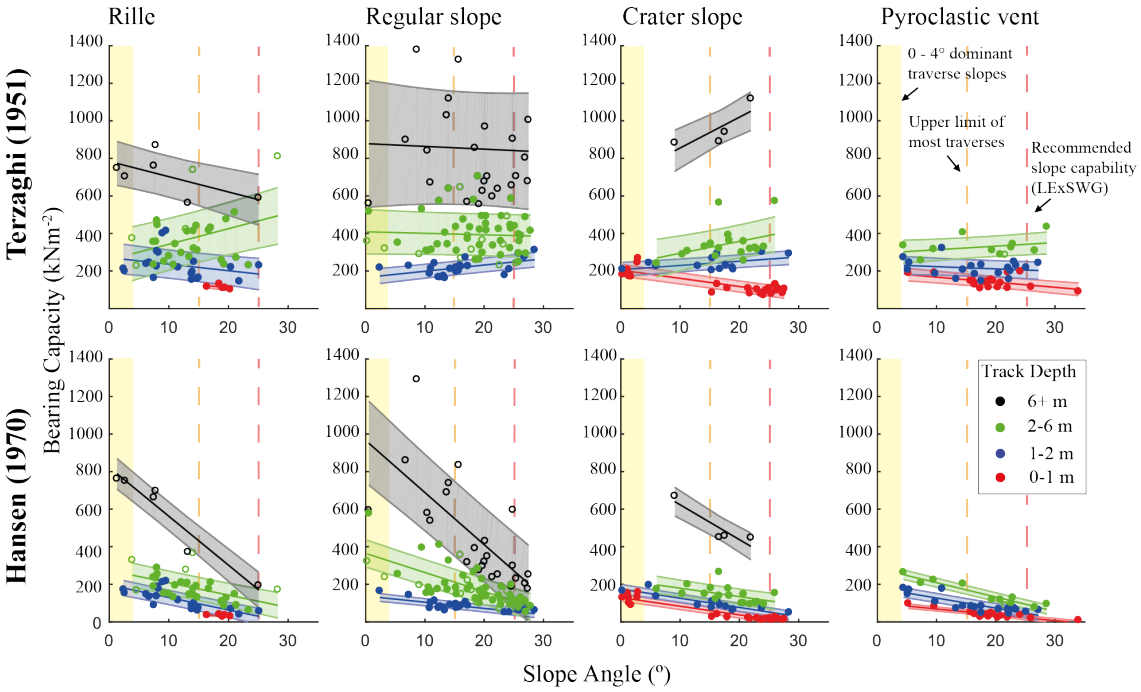


Figure A.59: Bearing capacity values are shown as a function of slope angle in relation to the geomorphological context. Values are provided from Terzaghi and Hansen calculations. Colors correspond to the depth of track from which the values are derived. Hollow circles indicate track depths that exceed local regolith thickness estimates. Bearing capacity is higher for deeper tracks and decreases at steeper slopes. Slope traverse values taken from LExSWG (1995).

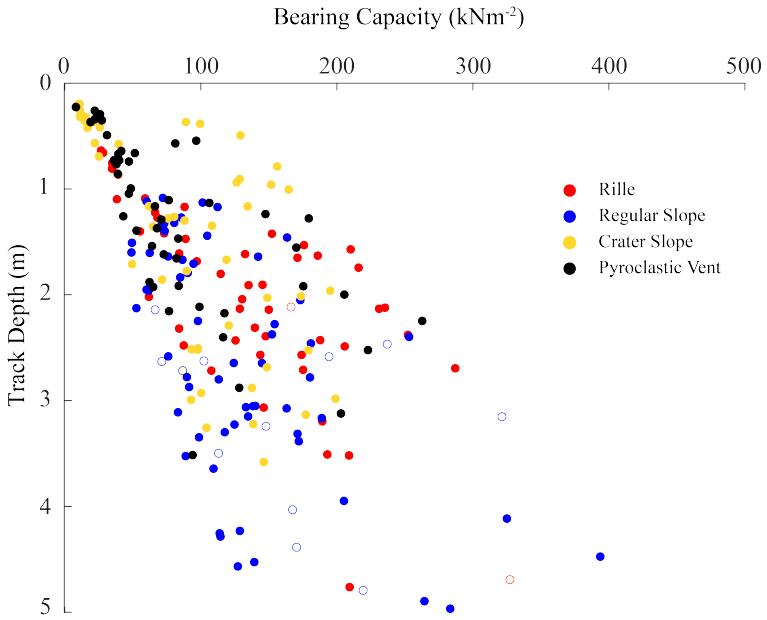


Figure A.60: The bearing capacity values for each boulder site in geomorphological context are presented as a function of track depth. Hollow shapes indicate boulders that are believed to have cut through the regolith at their location based on estimated taken from sources listed in Table A.12/ Figure A.56.

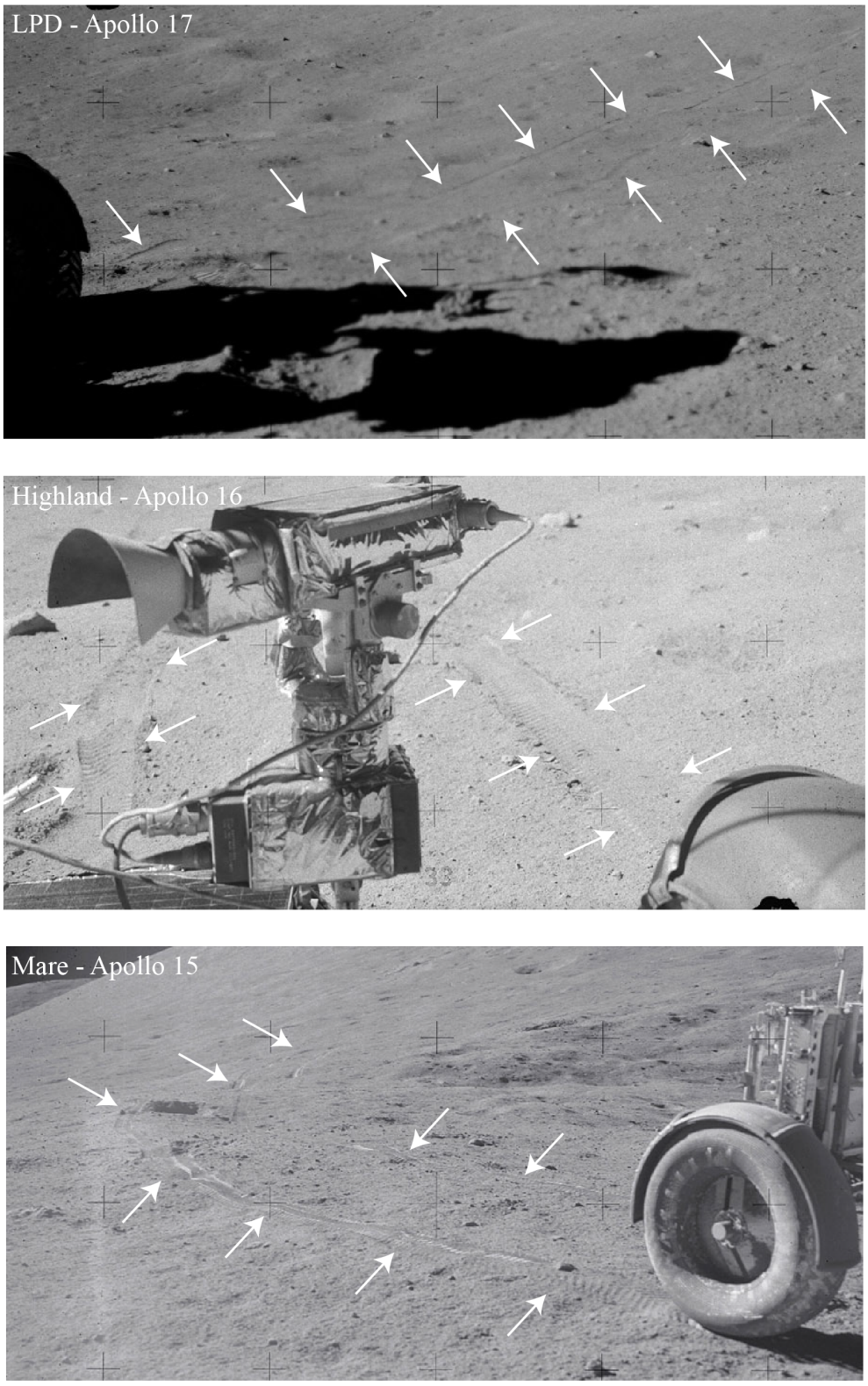


Figure A.61: Photographs of LRV tracks in pyroclastic, highland, and mare regolith, showing no substantial qualitative differences in track appearance and wheel sinkage. The photograph of the tracks in pyroclastic material has been taken at Apollo 17 station 4, "Shorty Crater"; the regolith there might not entirely reflect LPD material as encountered on large-scale pyroclastic deposits. Photographs AS17-133-20251, AS16-106-17360, and AS15-90-12216.

Additional equations for Hansen(Hansen, 1970)
In Figure S3, the longer boulder diameter is perpendicular to the track (case Ia). Hansen defines the depth factors as:

$$d_\gamma = 1 \tag{A.6}$$

If D $\leq$ B_H:

$$d_c = 0.4 * \frac{D}{B_H} \tag{A.7}$$

$$d_q = 1 + 2 * tan(\phi) * (1 - sin\phi))^2 * \frac{D}{B_H} \tag{A.8}$$

If D $>$ B_H:

$$d_c = 0.4 * arctan * \frac{D}{B_H} \tag{A.9}$$

$$d_q = 1 + 2 * tan(\phi) * (1 - sin(\phi))^2 arctan * \frac{D}{B_H} \tag{A.10}$$

In Figure A.51 the longer boulder diameter is parallel to the track (case Ib), both factors are defined as:

If D $\leq$ L_H:

$$d_c = 0.4 * \frac{D}{L_H} \tag{A.11}$$

$$d_q = 1 + 2 * tan(\phi) * (1 - sin\phi))^2 * \frac{D}{L_H} \tag{A.12}$$

If D $>$ L_H:

$$d_c = 0.4 * arctan * \frac{D}{L_H} \tag{A.13}$$

$$d_q = 1 + 2 * tan(\phi) * (1 - sin(\phi))^2 arctan * \frac{D}{L_H} \tag{A.14}$$

Shape factors are defined as following by Hansen (Hansen, 1970) and Bowles (Bowles, 1997), where B_H and L_H have been previously selected based on the criteria in Equation A.7 to Equation A.14:

$$s_c = (1 + \frac{N_q}{N_c} * \frac{B_H}{L_H}) \tag{A.15}$$

$$s_q = 1 + \frac{B_H}{L_H} * sin(\phi) \tag{A.16}$$

$$s_\gamma = 1 - 0.4 * \frac{B_H}{L_H} \tag{A.17}$$

Slope inclination factors are defined as (Hansen, 1970; Bowles, 1997):

$$g_c = (1 - \frac{\beta}{147^\circ}) \tag{A.18}$$

$$g_q = g_\gamma = (1 - 0.5 * tan(\beta))^5 \tag{A.19}$$

with the angle of the local slope as β.

LPD	Area (km^2)	# of tracks	TiO_2 cont.*	Water ilmenite (wt.%)	Water Fe^{2+} (wt.%)
Aristarchus	49013	14	Low	0.3 ±0.1	29.2 ±2.4
Rima Bode	6620	7	High	1.2 ±1.2	23.5 ±27.8
Sulpicius Gallus	4322	6	Intermediate	0.9 ±0.2	29.5 ±15.2
Taurus-Littrow	2940	35	High	1.1 ±0.4	28.8 ±9.6
Humorum	1472	4	Low	0.4 ±0.1	27.5 ±3.1
Hadley Cleft	898	12	Intermediate	0.4 ±0.1	27.6 ±2.4
Schrödinger	819	5	-	0.1 ±0.2	16.2 ±10.4
Oppenheimer	674	7	Intermediate	0.4 ±0.2	28.2 ±4.5
Mare +	n/a	21	High		
Highland +	n/a	16	Low		

Table A.8: LPD locations of interest for trafficability and Mare/Highland *Giguere et al. (2010); *Sato et al. (2017); + Used for comparison to LPDs). These deposits potentially present a larger source of material for future ISRU. A TiO_2 map, produced from Clementine data and methods outlined by Lucey et al. (2000), was used to estimate the mean ilmenite content in the selected pyroclastic deposits (Lucey, 2004). Assuming hydrogen reduction of ilmenite, the potential water that could be produced is shown as theoretical wt. % water from ilmenite. Meanwhile an FeO map, also produced from Clementine data and methods outlined by Lucey et al. (2000), was used to estimate the mean amount of iron bearing minerals, such as ilmenite, agglutinitic and pyroclastic glass, olivine, and pyroxene. Using experimental results from Allen et al. (1996), the potential water produced from all iron bearing minerals in this region is shown as experimental wt. % water from Fe^{2+} minerals.

Vehicle	Mass (kg)	Wheel diam. (m)	Wheel wid. (m)	Class *	Thrust +	Area (m^2)	Wheels
LRV	210	0.82	0.23	0.28 (III)	191.29	-	4
MET	75	0.41	0.10	0.24 (∼IV)	-	-	2
LER	4000	0.99	0.305	0.31 (III)	3643.59	-	12
RP	300	0.47	0.15	0.32 (III)	273.27	-	4
Lunokhod	800	0.51	0.20	0.39 (III)	728.72	-	8
Yutu	120	0.34	0.18	0.53 (II)	177.20	-	6
Spot	45	0.08#	0.05^	0.63 (∼II)$	-	-	4
SpaceBok	32	0.08#	0.04^	0.5 (∼II)$	-	-	4
RHex	12	0.10#	0.025^	0.25 (∼IV)$	-	-	6
Surveyor	292	-	-	-	-	0.34	3
A-LM	16400	-	-	-	-	3.14	4

Table A.9: Rover and lander design (A-LM = Apollo Lunar Module) specifications according to or inferred from Carrier et al. (1991), Asnani et al. (2009), ESA (n.d.a), ESA (n.d.b), Bluethmann (2018, pers. comm), NASA (2010), Boston-Dynamics (2019), SpaceBok (2017) and photographs/blueprints (where information was not directly accessible). Curved footpads of RHex- and SpaceBok-type robots are calculated like wheels with increased 'simulated' diameters to account for the curvature of the pads. Spot-type pads are approximated as regular wheels (see inlets in Figure 4.5 for details). *after Bekker (1956), class I describes a round ground-wheel contact area, class 4 a highly elongated contact area; +maximum horizontal soil thrust, applying Bekker (1960) using wheel contact area at estimated wheel sinkage (default design) and assuming no cleats, # foot contact length, ^ footpad width, $ class only given as approximation, as curved pads/footpads are not the same as wheels.

Location Type	Density layer	Sample #	ρ (g cm^{-3}) Literature	ρ (g cm^{-3}) Used
Pyroclastic Deposits	Top	15010	1.69[a]	1.63
		76001	1.57[a]	
	Bottom	15010	1.79-1.91[a]	1.85
Highland	Top	64002	1.38-1.4[b]	1.39
	Bottom	64001	1.66[b]	1.66
Mare	Top	12010	1.98[c]	1.86
		12013	1.74[c]	
	Bottom	12012	1.96[c]	1.96

Table A.10: Density values obtained from literature for depths <30 cm (Top) and >30 cm (Bottom) and the average values used in this work ([a] Apollo 15 Preliminary Science report and [b] Apollo 16 Preliminary Science report (Mitchell et al., 1972a); [c] (Scott et al., 1971)).

Region	Spatial res. (m/pixel)	Mean intersection error (m)	Used for
Aristarchus	2	0.78	WAC DEM error est.
Oppenheimer	10	3.58	WAC DEM error est.
Taurus Littrow	3	2.14	WAC DEM error est.
Highland #1	10	5.88	Phi determination
Highland #2	4	1.95	Phi determination
Mare #1	10	4.2	Phi determination
Mare #2	6	3.57	Phi determination
LPD #1	5	3.16	Phi determination
LPD #2	4	1.98	Phi determination

Table A.11: DEM spatial resolution and intersection error table, for Scholten et al. (2012) WAC DEM error estimation and for friction angle (Phi) determination; DEMs produced with ASP (Shean et al., 2016).

Region	Regolith depth (m)	Method	Source
Average Mare	5.2	Radar and Optical Model	Shuratov, Bondarenko (2001)
	4 to 5	-	McKay et al. (1991)
	2 to 4+	Small Crater Morphology	Bart et al. (2011)
	4.5	Multi-channel brightness temperature inversion	Fa, Jin (2010)
Apollo 17[a]	7	Surface Probing	Strangway et al. (1975)
	8.5	Seismic Profiling	Olhoeft, Strangway (1975)
	5.5+	Multi-channel brightness temperature inversion	Fa, Jin (2010)
Apollo 15[b]	5+	Multi-channel brightness temperature inversion	Fa, Jin (2010)
Average Highland	11	Radar and Optical Model	Shuratov, Bondarenko (2001)
	10 to 15	-	McKay et al. (1991)
	7.6+	Multi-channel brightness temperature inversion	Fa, Jin (2010)
	6.1	Radar and Optical Model	Shuratov, Bondarenko (2001)
Sinus Aestum[c]	4.7+	Multi-channel brightness temperature inversion	Fa, Jin (2010)
Oceanus Procellarum[d]	4.6	Crater Morphology	Oberbeck, Quaide (1968)
	3.3+	Crater Morphology	Oberbeck, Quaide (1968)
	4.2	Multi-channel brightness temperature inversion	Fa, Jin (2010)
	4.1+	Radar and Optical Model	Shuratov, Bondarenko (2001)
Mare Serenitatis[e]	4.6	Multi-channel brightness temperature inversion	Fa, Jin (2010)
Mare Humorum	4.1	Radar and Optical Model	Shuratov, Bondarenko (2001)
	2.5+	Small Crater Morphology	Bart et al. (2011)
	6	Multi-channel brightness temperature inversion	Fa, Jin (2010)

Table A.12: Unconsolidated regolith thickness table, containing region, estimated thickness of unconsolidated regolith, method, and source; + denotes potentially larger numbers, [a] Taurus Littrow, [b] Hadley Cleft, [c] Rima Bode, [d] Aristarchus, [e] Sulpicius Gallus.

Depth steps	LPD to Highland	LPD to Mare	Mare to Highland
0 - 1 m	Significantly higher	Significantly higher	No significant difference
1 - 2 m	Significantly higher	No significant difference	No significant difference
2 - 6 m	Significantly higher	Significantly higher	No significant difference
6+ m	Significantly higher	No significant difference	No significant difference

Table A.13: Statistical bearing capacity analysis in the investigated depth range, LPDs in comparison to highland and mare regions. T-test, two-sample assuming unequal variances (two-tail) for all 4 depth ranges, providing 12 p-values based on a 95% confidence interval.

Location	Depth of track	Bearing capacity on varying slope angles (kN/m^2)			
		0 °	10 °	20 °	30 °
All regions	0 - 1 cm	5.4 ±4.5	-	-	-
	1 - 2 cm	5.8 ±4.5	-	-	-
	2 - 3 cm	6.2 ±4.5	-	-	-
	3 - 4 cm	6.5 ±4.5	-	-	-
	4 - 5 cm	6.9 ±4.5	-	-	-
	5 - 6 cm	7.3 ±4.5	-	-	-
	6 - 7 cm	7.7 ±4.5	-	-	-
	7 - 8 cm	8.1 ±4.5	-	-	-
	8 - 9 cm	8.5 ±4.5	-	-	-
	9 - 10 cm	8.8 ±4.5	-	-	-
Pyroclastics	0 - 1 m	131 ±21	86 ±20	41 ±20	-
	1 - 2 m	200 ±30	144 ±28	89 ±28	33 ±30
	2 - 6 m	336 ±79	261 ±74	186 ±73	111 ±78
	6+ m	1143 ±333	861 ±262	579 ±267	296 ±345
Highlands	0 - 1 m	52 ±14	39 ±10	25 ±7	11 ±7
	1 - 2 m	166 ±24	119 ±21	72 ±20	24 ±22
	2 - 6 m	314 ±63	228 ±58	143 ±57	57 ±59
	6+ m	708 ±101	528 ±87	349 ±82	169 ±86
Mare	0 - 1 m	85 ±12	57 ±9	29 ±7	1 ±9
	1 - 2 m	167 ±19	108 ±18	50 ±18	-
	2 - 6 m	276 ±50	201 ±47	126 ±47	51 ±50
	6+ m	826 ±68	563 ±61	301 ±64	38 ±75

Table A.14: Report of the interpolated as well as calculated ultimate bearing capacity values and associated error (as derived above) for each location type at the specified depth ranges and for slope values of 0°, 10°, 20°and 30°. Interpolated values are only available for 0°. Data is omitted where the predicted values fall below 0 kN/m^2 (Figure 4.2), or where a trendline with error could not be obtained ($\leq$ 3 data points). For mare regions at depth 6+ m bearing capacity is lower than at 2-6 m depth due to the particular steep best-fit line - the reason for that is the fit of the 6+ m line and probably not a physical reason.

NAC image ID				
M1137658694LE	M114280746RE	M142061915LE	M168007359RE	M1116707457RE
M110670656RE	M114294313RE	M142068699LE	M170727953LE	M1118887721LE
M128378531LE	M114498609RE	M142068699RE	M170727953RE	M1120819351RE
M1099953065LE	M119666985RE	M142244931RE	M170865005RE	M1121876217RE
M1207094593LE	M124450712RE	M142251741RE	M172724086LE	M1129816126LE
M108313384RE	M124743115LE	M144422670RE	M175139029RE	M1136356411LE
M1117933950RE	M125658595LE	M144558374LE	M175375107LE	M1142447286LE
M154309391LE	M125658595RE	M144558374RE	M175610199LE	M1154306917LE
M104848322RE	M126724656RE	M157920577RE	M175610199RE	M1213101614RE
M104855480RE	M126955161RE	M157934151LE	M176210536LE	M1225813672RE
M106676354RE	M129086118LE	M157934151RE	M181509714RE	M1234243503RE
M111422030LE	M129234847LE	M159168880RE	M190401948RE	M1234588088LE
M111422030RE	M129282939RE	M159929419RE	M192760872LE	M1252208394LE
M112284817LE	M130836314LE	M165645700RE	M1098651578RE	M1252208394RE
M113242798RE	M135215829RE	M165828808LE	M1101009474RE	M1252222450LE
M113941548LE	M135452859LE	M166936042RE	M1103366626RE	

Table A.15: Table of all NAC image IDs that have been used for this study, as EDR (raw) versions.

Using Boulder Tracks as a Tool to understand the Bearing Capacity of Permanently Shadowed Regions of the Moon
Published 2020 in the Journal of Geophysical Research: Planets
Sargeant, H.M., Bickel, V.T., Honniball, C.I., Martinez, S.N., Rogaski, A., Bell, S.K., Czaplinski, E.C., Farrant, B.E., Harrington, E.M., Tolometti, G.D., Kring, D.A., 2020
https://doi.org/10.1029/2019JE006157

Additional information about the methods and results of this work. Figure A.62 outlines the NAC pipeline commands whilst Figure A.63 shows the range of boulder diameters found in PSRs as compared with those identified in other regions of the Moon by Bickel et al. (2019). Figure A.64 shows the effects of errors in the e-angle on bearing capacity calculations. Figure A.65 shows the effects of a change in bulk density of soil on bearing capacity calculations. Table A.16 and Table A.17 contain kernel weights for image filtering. Table A.18 contains details of the DEM production and errors. Table A.19 contains the key identification information and measurements for each boulder track analyzed in this work. Table A.20 contains the p-values of a two-tail statistical analysis of our results as compared to the data obtained by Bickel et al. (2019). Table A.21 contains the average and maximum temperatures experienced at the lunar south pole as derived from Diviner Radiometer data, with the estimated ice depth also shown, as derived from the Oxford 3D Thermophysical model (Warren et al., 2019). Table A.22 shows the change in bearing capacity values as a result of a change in bulk density. Finally, Table A.23 shows the change in p-values as a result in a change in bulk density.

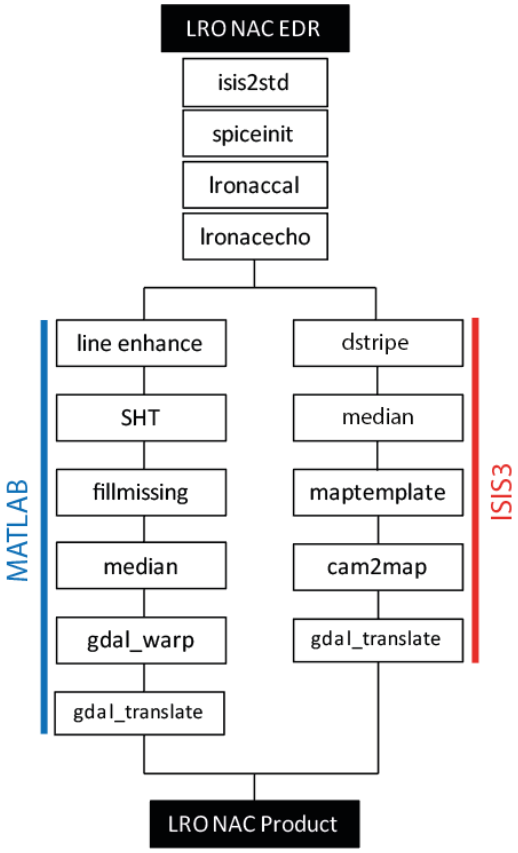


Figure A.62: NAC processing pipeline commands: NAC EDRs are processed using these commands.

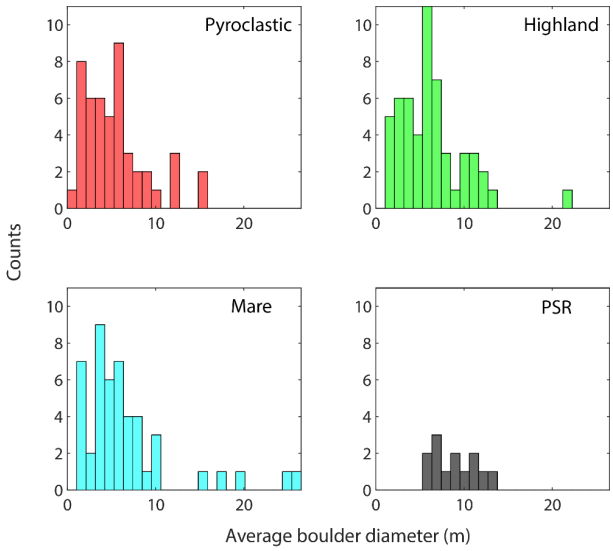


Figure A.63: Histogram of the average boulder diameters found in PSRs for this work as compared with that of the pyroclastic, highland, and mare boulders identified in Bickel et al. (2019). The range of boulder diameters measured in PSRs is significantly smaller than those measured in other regions.

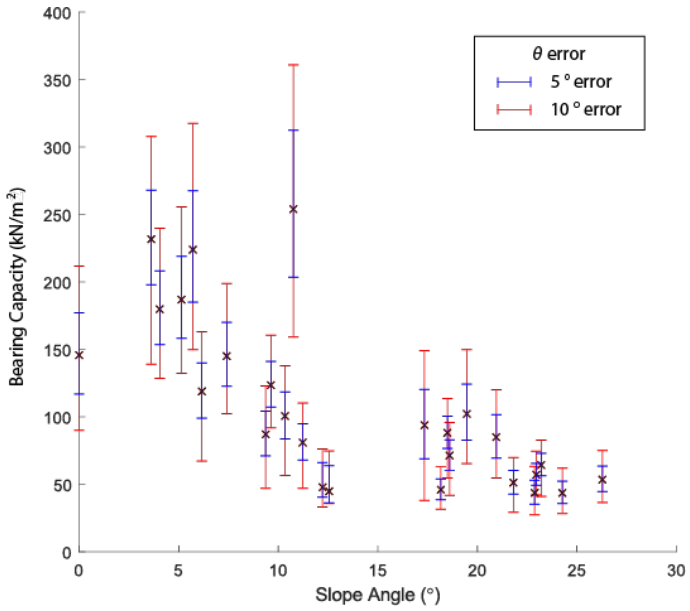


Figure A.64: A plot to show the resulting uncertainty in bearing capacity from 5°and 10°uncertainties in effective incidence angle, θ. A negative uncertainty in θ corresponds to an over-estimation of bearing capacity whilst a positive uncertainty in θ corresponds to an under-estimation in bearing capacity.

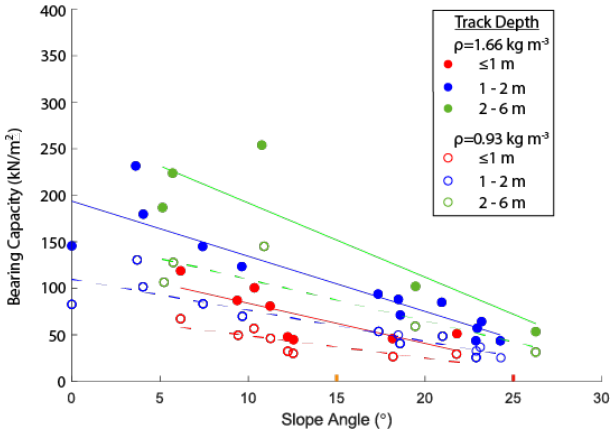


Figure A.65: Bearing capacity values from PSRs are shown here as a function of slope angle. The data is separated by the track depth at each measurement (≤1, 1-2, and 2-6 m). A comparison of results calculated from a predicted bulk density of soil of 1.66 g cm^{-3} and 0.93 g cm^{-3}

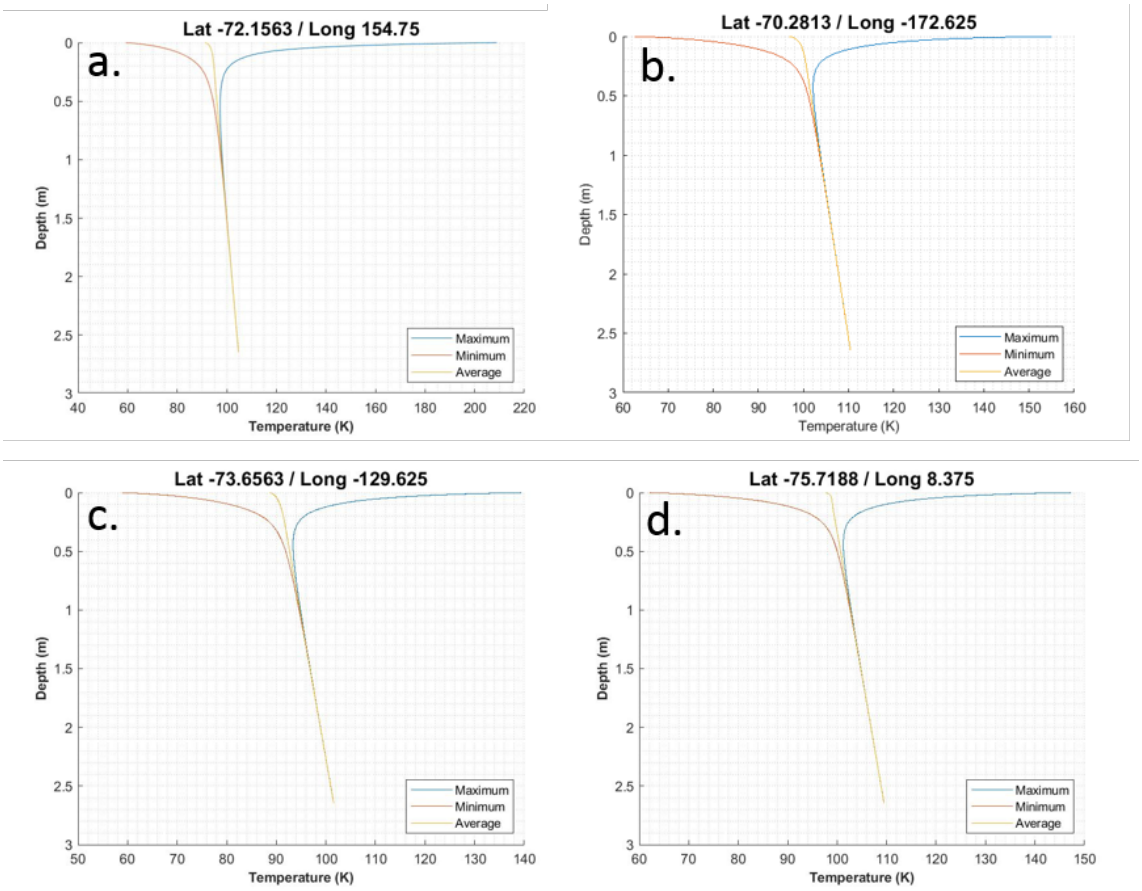


Figure A.66: Estimated ice depth plots as calculated from the Oxford 3D Thermophysical model (Warren et al., 2019) for the PSRs studied in this work. Plots are shown for 4 PSRs; a.) contains boulders PSR-001 and PSR-002, b.) contains boulders PSR-003 and PSR-005, c.) contains boulders PSR-004, PSR-006, PSR-007, PSR-008, PSR-009, and PSR-010, and d.) contains boulders PSR-012 and PSR-013. The remaining PSR containing boulder PSR-011, was too small for the model to be correctly applied.

-1	2	-1
-1	2	-1
-1	2	-1
-1	2	-1
-1	2	-1
-1	2	-1
-1	2	-1
-1	2	-1

Table A.16: Vertical noise exaggeration kernel weights; noise is marked with positive values.

1/2	pixel of interest	1/2

Table A.17: Removed pixel interpolation kernel weights (used by external fillmissing algorithm).

NAC DEM Region	Spatial res. (m/pixel)	Mean intersection error (m)	Used for
E of Schrödinger Crater	2	13.54	ϕ determination
SE of Baily Crater	3	1.13	ϕ determination

Table A.18: DEM spatial resolution and intersection error table, for friction angle, ϕ, determination; DEMs produced with ASP (Shean et al., 2016). The high intersection error of the first DEM is the result of local correlation errors that are caused by the difficult illumination conditions within PSRs.

ID	Lat	Lon	NAC ID	TL (m)	TD_S (m)	TD_B (m)	SA_S (°)	SA_B (°)	$\frac{B_S}{B_L}$	BAD (m)
001	-72.25	154.71	M1117841678RE	831	2.11	2.84	26.27	19.47	0.67	6.76
002	-72.23	154.68		1853	0.84	1.51	10.34	23.20	0.73	10.65
003	-70.34	-172.58	M141032202RE	2256	1.50	0.98	17.34	6.16	0.80	8.68
004	-73.71	-129.66	M1132733267LE	393	1.16	1.23	0.00	24.27	0.77	6.43
005	-70.37	-172.33	M138670911RE	287	1.26	0.86	22.88	18.16	0.54	6.03
006	-73.71	-129.66	M1132733267LE	1124	1.71	1.49	20.95	4.05	0.67	10.29
007	-73.71	-129.66		805	0.91	0.96	9.37	11.23	0.60	6.11
008	-73.71	-129.66		764	0.89	1.06	21.81	18.60	0.72	11.58
009	-73.71	-129.66		1047	1.03	1.78	18.49	3.62	0.63	12.88
010	-73.71	-129.66		533	1.18	1.28	22.96	9.63	0.55	12.64
011	-74.83	125.84	M159113056LE	590	0.28	0.45	12.55	12.22	0.63	9.06
012	-75.94	7.99	M139851557LE	516	4.68	1.80	10.76	7.41	0.66	8.15
013	-75.94	7.95		189	2.77	2.19	5.71	5.14	0.53	6.67

Table A.19: List of all PSR boulders identified and used for bearing capacity calculations in this work. The location, NAC image ID, track length (TL) and depth (TD), slope angle (SA), and boulder dimensions are listed (boulder average diameter, BAD), at source (S) and boulder (B).

Slope angle range	Region comparison	0-1 m range		1-2 m range	
		n	P-value	n	P-value
0-30°	PSR-Highland	8-12	0.001	13-17	0.230
	PSR-Mare	8-15	0.003	13-30	0.455
	PSR-Pyroclastic	8-22	0.997	13-28	0.621
>15°	PSR-Highland	2-12	0.004	8-13	0.807
	PSR-Mare	2-15	0.003	8-8	0.786
	PSR-Pyroclastic	2-12	0.007	8-15	0.404

Table A.20: The number of data points, n, for each region as calculated in this work (PSRs), and in Bickel et al. (2019) (highland, mare and pyroclastic). P values are calculated from a two-tail T-test for the comparison of bearing capacity values of PSRs to the highland, mare and pyroclastic regions of the Moon. The two-sample T-test assumes unequal variances for the depth ranges 0-1 and 1-2 m, based on a 95% confidence interval. The depth range 2-6 m is not considered as a result of limited data points in PSRs. When $P<0.05$ there is a statistically significant difference in the data sets. Data from all slope angles are considered, then data from slope angles >15°are considered.

Boulder ID	Annual Max. Temperature (K)	Estimated depth for stable water ice (m)
PSR-001	201	0.10
PSR-002	78	0.10
PSR-003	154	0.10
PSR-004	65	0.05
PSR-005	205	0.10
PSR-006	148	0.05
PSR-007	71	0.05
PSR-008	74	0.05
PSR-009	148	0.05
PSR-010	169	0.05
PSR-011	210	No Data
PSR-012	195	0.10
PSR-013	196	0.10

Table A.21: Annual maximum temperature of boulder locations as derived from Diviner Radiometer data with a resolution of ∼240 m/pixel respectively at the lunar south pole (Paige et al., 2010; Williams et al., 2017). The estimated depth of stable water ice as derived from Warren et al. (2019) is also shown.

Location	Depth of track (m)	Bearing Capacity using Hansen at a range of slope angles (kN/m^2)			
		0°	10°	20°	30°
PSRs	≤1	73±14	49±10	25±11	-
	1-2	110±16	76±15	43±15	10±16
	2-6	155±36	110±30	65±31	20±39

Table A.22: Estimated bearing capacity values and associated uncertainty (as derived from the distribution of the PSR data) at the specified depth ranges of ≤1 m, 1-2 m and 2-6 m, and for slope values of 0°, 10°, 20°and 30°when applying a bulk density value of 0.93 g cm^{-3}. Data was omitted where the predicted bearing capacity values fall below 0 kN/m^2.

Slope angle range	Region comparison	0-1 m range		1-2 m range	
		n	P-value	n	P-value
0-30°	PSR-Highland	8-12	0.004	13-17	0.072
	PSR-Mare	8-15	0.041	13-30	0.007
	PSR-Pyroclastic	8-22	0.019	13-28	0.000
>15°	PSR-Highland	2-12	0.015	8-13	0.000
	PSR-Mare	2-15	0.989	8-8	0.007
	PSR-Pyroclastic	2-12	0.465	8-15	0.000

Table A.23: The number of data points, n, for each region as calculated in this work (PSRs with a bulk density of 0.93 g cm^{-3}), and in Bickel et al. (2019) (highland, mare and pyroclastic). P values are calculated from a two-tail T-test for the comparison of bearing capacity values of PSRs to the highland, mare and pyroclastic regions of the Moon. The two-sample T-test assumes unequal variances for the depth ranges 0-1 and 1-2 m, based on a 95% confidence interval. The depth range 2-6 m is not considered as a result of limited data points in PSRs. When P<0.05 there is a statistically significant difference in the data sets. Data from all slope angles are considered, then data from slope angles >15°are considered.

Lunar South Pole Boulders and Boulder Tracks: Implications for Crew and Rover Traverses
Published 2020 in Icarus
Bickel, V.T., Kring, D.A., 2020
https://doi.org/10.1016/j.icarus.2020.113850

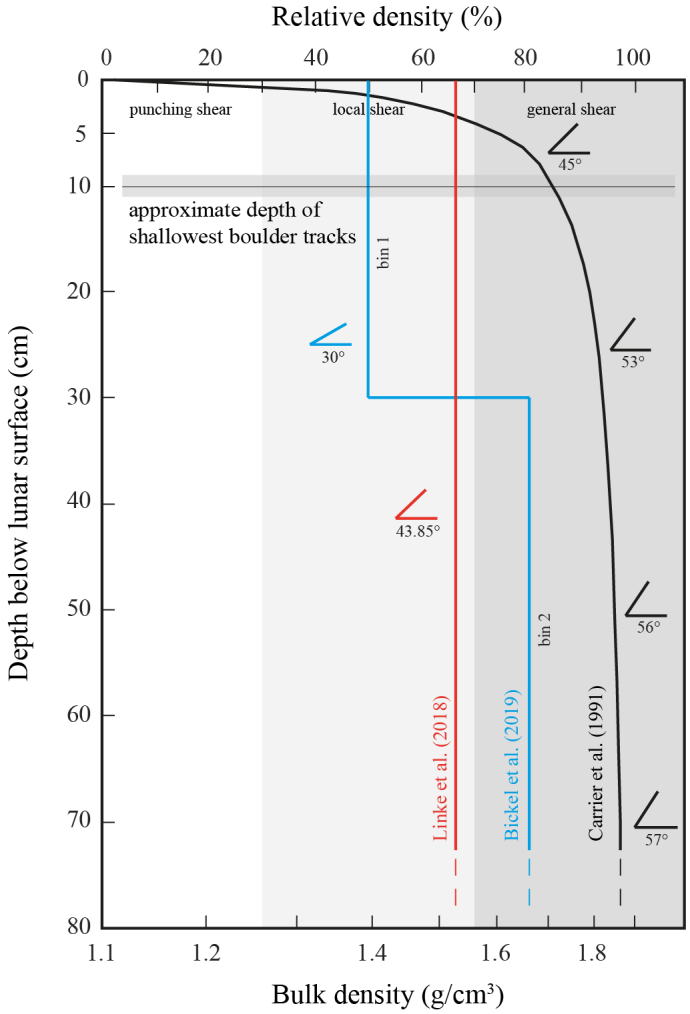


Figure A.67: Soil mechanical input parameters used for this study: blue represents the conservative values (see low angle of internal friction). Cohesion plays a minor role in the bearing capacity calculations and has not been plotted here (see Table A.25 for the used cohesion values). At extremely shallow depths ($<$ $\sim$1.5 cm), the blue envelope would produce slightly higher input parameters compared to the black envelope. The relative density controls the occurrence of general, local, or punching shear, as indicated (based on Vesic (1973)). This figure assumes that depth of foundation / width of foundation is equal or smaller 1 (Terzaghi, 1951), i.e., the precondition for the application of shallow foundation theory is met. This figure is based on Fig. 9.19 (Carrier et al., 1991) from the Lunar Source Book, Chapter 9, and has been modified with permission of the corresponding author.

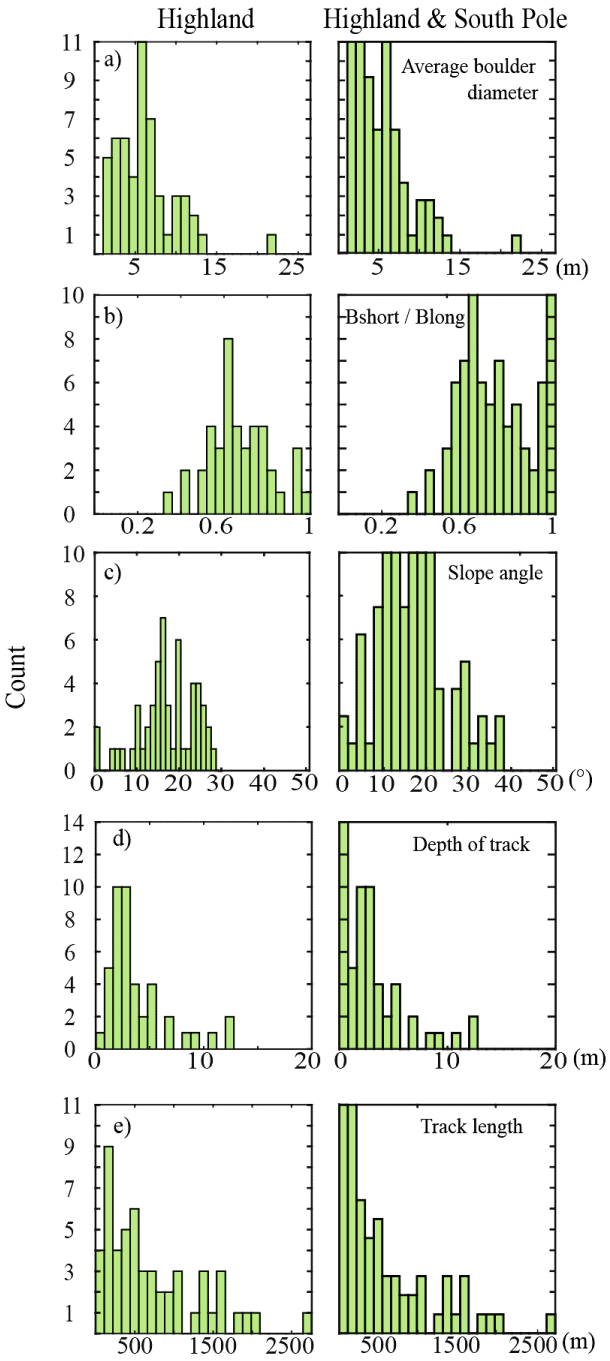


Figure A.68: Various histograms comparing boulder and track properties measured in multiple equatorial highland regions across the lunar surface (Bickel et al., 2019) with south pole and equatorial highland features combined. In general, south pole rockfalls are smaller, appear to be rounder, occur on steeper slopes, have shallow tracks, and short runouts. However, these observations could be biased, as PSRs impede measurements at the bottom of slopes - only features on the rims and upper flanks of topographic heights can be observed, which will likely be not representative for the entire rockfall population at the lunar south pole.

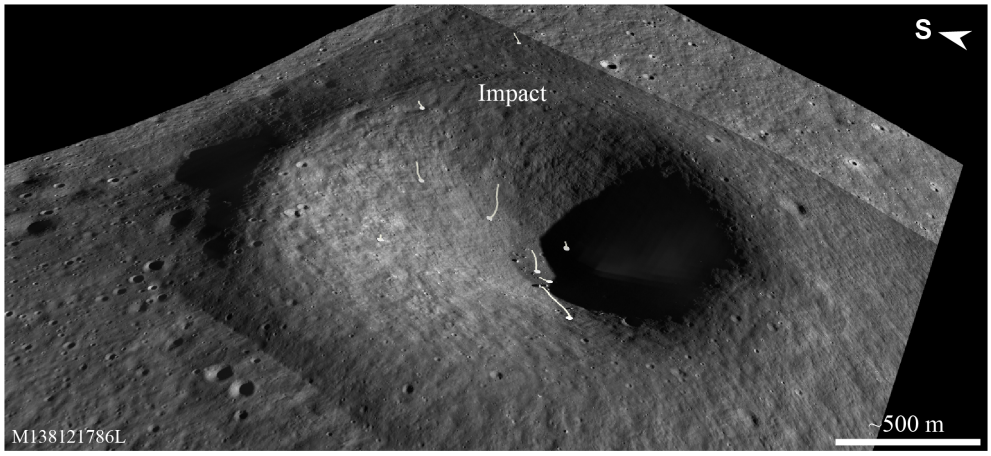


Figure A.69: Rolling boulders on the northern flank of Mons Malapert in a 2.5D view. Rockfalls have no clear source region, but appear to be associated with the impact crater. Detail of NAC M138121786L.

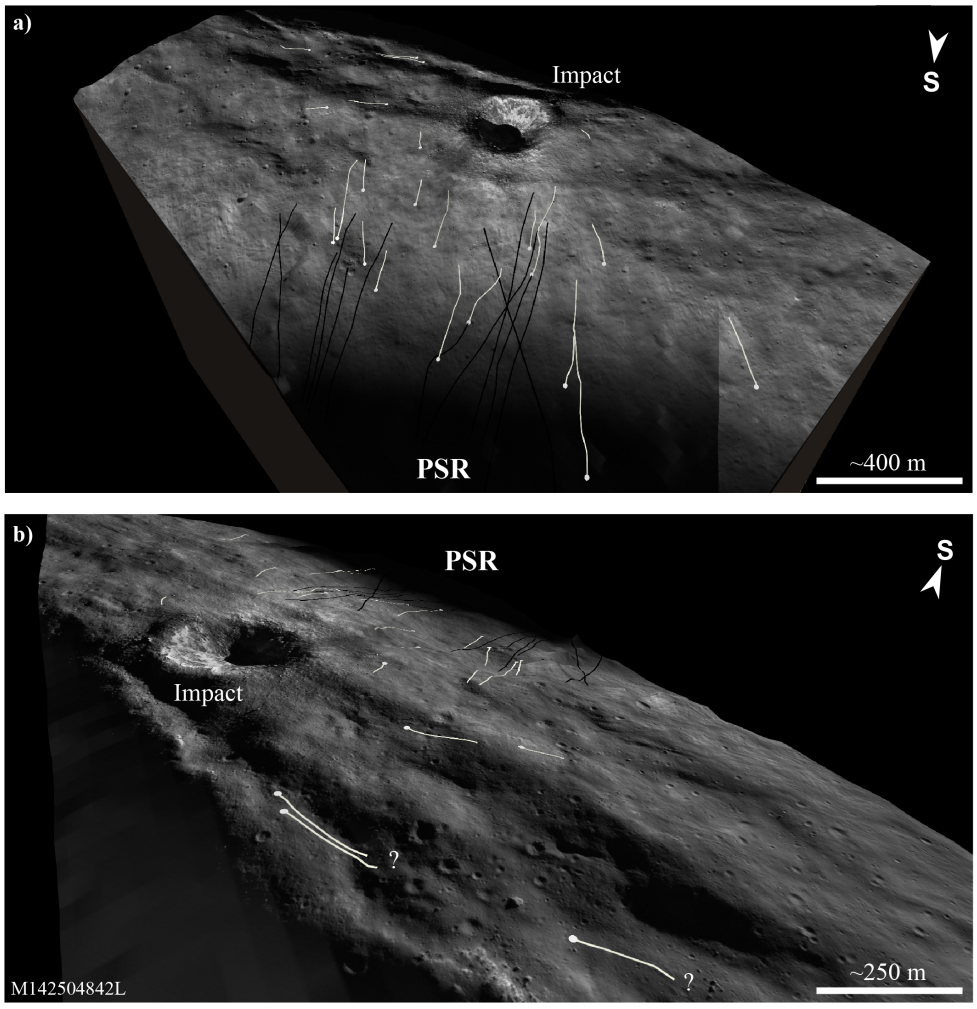


Figure A.70: Rolling boulders on the rim of the northern wall of Shackleton Crater in a 2.5D view. a) view from S to N, rockfalls appear to be associated with a recent impact crater (trigger). Thirteen tracks disappear in Shackleton's PSR (black lines). b) view from N to S (into the crater), boulders that rolled along the rim are visible, but their source region and trigger remains ambiguous. Detail of NAC M142504842L.

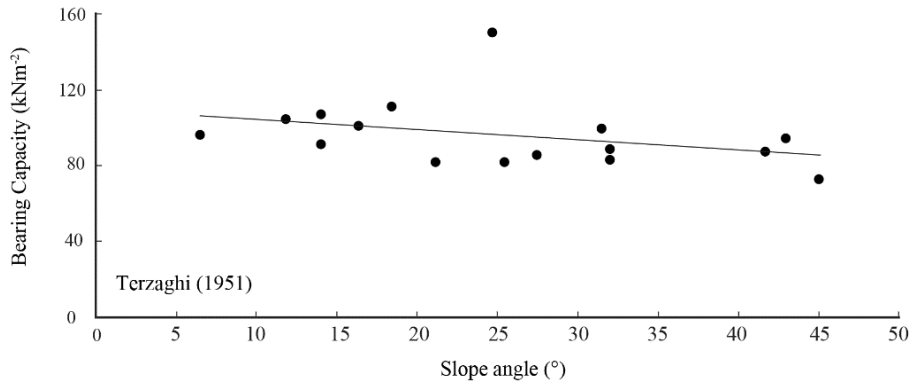


Figure A.71: Bearing capacity vs. slope angle, using Terzaghi (Terzaghi, 1951) and south polar tracks (depth range ∼0.10 to ∼0.52 m). Estimated values compare well with previous work (Carrier et al., 1991). The results indicate a slight but constant physical drop in strength with increasing slope angles, potentially indicating a shallow colluvium with altered mechanical properties on lunar inclines. Terzaghi (Terzaghi, 1951) assumes a circular foundation shape and has been applied as described and discussed in Bickel et al. (2019).



Figure A.72: Rover concepts used for this study: a) LER, b) VIPER (former RP), and c) SpaceBok. Images taken from NASA (2010), Colaprete (2016), and ETH Zurich's RSL webpage: https://rsl.ethz.ch/.

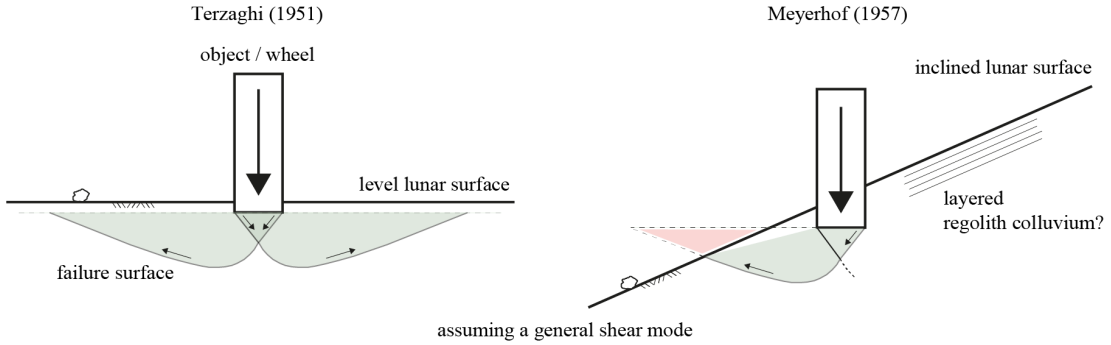


Figure A.73: Shear failure surface under an object on level (Terzaghi, 1951) and inclined terrain (Meyerhof, 1957), assuming a general shear mode (cross-section of object and terrain). On inclined terrain the bearing capacity is reduced due to a reduction of the bearing soil volume.

NAC image ID				
M138121786LE	M142450586RE	M114527087LE	M128738066LE	M128738066RE
M137558576RE	M117560736LE	M105029384LE	M117581091RE	M128738066LE
M170621836LE	M142450586RE	M105029384LE	M117581091RE	M138148932LE
M137450046RE	M142450586LE	M102638882RE	M117560736LE	M187776525LE
M179806189LE	M142450586LE	M102638882LE	M142464150LE	M142518406LE
M179806189LE	M142213197LE	M1148611029LE	M142477713LE	M142518406LE
M137450046LE	M141046118RE	M142559106LE	M142491277LE	M128751644LE
M130902574RE	M141046118LE	M142545534LE	M141046118RE	M139424245LE
M128751644LE	M142531971LE	M144838646LE	M141046118LE	M142504842LE
M139437820RE	M142504842LE	M128751644RE	M142545534LE	M142531971LE

Table A.24: NAC images (50) used for the estimation of south pole bearing capacities (EDR versions). Images have been processed from EDR level using ISIS3. Processing workflow is detailed in Bickel et al. (2019).

Parameter	Depth of layer	Sample #	Literature	Used
Bulk density	< 30 cm	64002	1.38 - 1.4 g/cm^3 [a]	1.39 g/cm^3
	> 30 cm	64001	1.66 g/cm^3 [a]	1.66 g/cm^3
Cohesion	-	-	1 kN/m^2	1 kN/m^2
Friction angle	-	RS*	-	30°
Bulk density [b]	-	-	1.53 g/ cm^3	1.53 g/ cm^3
Cohesion [b]	-	-	0.43 - 0.59 kN/m^2	0.51 kN/m^2
Friction angle [b]	-	-	41.9 - 45.8°	43.85°
Bulk density [c]	5 cm	-	1.6 g/cm^3	1.6 g/cm^3
	25 cm	-	1.8 g/cm^3	1.8 g/cm^3
	50 cm	-	1.85 g/cm^3	1.85 g/cm^3
	100 cm	-	1.86 g/cm^3	1.86 g/cm^3
Cohesion [c]	5 cm	-	1 kN/m^2	1 kN/m^2
	25 cm	-	1.1 kN/m^2	1.1 kN/m^2
	50 cm	-	1.3 kN/m^2	1.3 kN/m^2
	100 cm	-	1.4 kN/m^2	1.4 kN/m^2
Friction angle [c]	5 cm	-	45°	45°
	25 cm	-	53°	53°
	50 cm	-	56°	56°
	100 cm	-	57°	57°

Table A.25: Soil parameters obtained from literature for depths <30 cm and >30 cm and the average values used in this work ([a] Apollo 16 Preliminary Science report, Mitchell et al. (1972a)), as well as values ([b] Linke et al. (2018); [c] Carrier et al. (1991)) used for comparison; values for [c] are exemplary (see Figure A.67). RS* denotes values that have been derived with remote sensing by Bickel et al. (2019) using shallow granular flows at their angle of repose. This aims to refine and adapt this decisive input parameter to the local conditions (worst case scenario), rather than using values derived at distal sites. Usage of these values is based on the observation that the south pole is a highland-type terrane with a feldspathic regolith composition.

Vehicle	Mass (kg)	Wheel diam. (m)	Wheel wid. (m)	Class*	Area (m^2)	Wheels
LRV	210 (708)	0.82	0.23	0.28 (III)	-	4
LER	4000	0.99	0.305	0.31 (III)	-	12
VIPER	225	0.50	0.20	0.4 (II - III)	-	4
Apollo LM	16400	-	-	-	3.14	4

Table A.26: Rover specifications according to or inferred from Carrier et al. (1991), Bluethmann (2018, pers. comm.), Shirley (2019, pers. comm.), and NASA (2010). *after Bekker (1956), class I describes a round ground-wheel contact area, class 4 a highly elongated contact area (standard wheels).

Appendix B

Declaration of Originality

Eidgenössische Technische Hochschule Zürich
Swiss Federal Institute of Technology Zurich

Declaration of originality

The signed declaration of originality is a component of every semester paper, Bachelor's thesis, Master's thesis and any other degree paper undertaken during the course of studies, including the respective electronic versions.

Lecturers may also require a declaration of originality for other written papers compiled for their courses.

I hereby confirm that I am the sole author of the written work here enclosed and that I have compiled it in my own words. Parts excepted are corrections of form and content by the supervisor.

Title of work (in block letters):

Analysis of Lunar Rockfalls

Authored by (in block letters):

For papers written by groups the names of all authors are required.

Name(s):	**First name(s):**
Bickel	Valentin Tertius

With my signature I confirm that

- I have committed none of the forms of plagiarism described in the 'Citation etiquette' information sheet.
- I have documented all methods, data and processes truthfully.
- I have not manipulated any data.
- I have mentioned all persons who were significant facilitators of the work.

I am aware that the work may be screened electronically for plagiarism.

Place, date	**Signature(s)**
Goettingen, 17 January 2021	

For papers written by groups the names of all authors are required. Their signatures collectively guarantee the entire content of the written paper.